

Faculty of Physics
Adam Mickiewicz University
Poznań, Poland

Ph.D. Thesis

**The influence of magnetic field on the
superconducting properties and the BCS-BEC
crossover in systems with local fermion pairing**

Agnieszka Cichy

Supervisor
Prof. dr hab. Roman Micnas
Adam Mickiewicz University
Solid State Theory Division

Poznań 2012

To my Parents

Contents

Acknowledgements	7
List of abbreviations	8
Introduction	9
1 Principles of superconductivity and superfluidity	13
1.1 Historical perspective	13
1.2 Basics of the BCS-BEC crossover physics	16
1.3 The new possibilities	19
2 The Hubbard model	23
2.1 Introduction	23
2.2 The Hubbard Hamiltonian	23
2.3 The Spin-Polarized extended Hubbard model	25
2.4 The Hartree-Fock approximation	26
3 Kosterlitz-Thouless Transition	35
3.1 The XY model	35
3.2 The Kosterlitz-Thouless critical temperature determination	37
4 Superconducting properties in the presence of a Zeeman magnetic field: Weak and intermediate coupling	43
4.1 Ground state	44
4.1.1 Phase diagrams	49
4.2 Finite temperatures	51
4.2.1 The superfluid density	58
4.2.2 Phase diagrams	61
4.3 The influence of the pure d-wave pairing symmetry on the polarized super- conducting phase stability	67
5 The BCS-BEC crossover at $T = 0$ in the spin-polarized Attractive Hub- bard Model with spin independent hopping integrals	79
5.1 2D square lattice	80

5.2	3D simple cubic lattice	82
5.3	The influence of different lattice geometries (densities of states) on the stability of the magnetized superfluid phase	89
6	The BCS-BEC crossover at finite temperatures in the spin-polarized AHM with spin independent hopping integrals	97
6.1	2D square lattice. The Kosterlitz-Thouless scenario	97
6.2	3D simple cubic lattice. T-matrix approach	102
6.2.1	Formalism	102
6.2.2	Numerical results	111
7	The influence of spin dependent hopping integrals (mass imbalance) on the BCS-BEC crossover	119
7.1	The large- U limits	120
7.2	AAHM on 2D square lattice	126
7.2.1	Ground state phase diagrams	127
7.2.2	Finite temperature phase diagrams	132
7.3	AAHM on 3D simple cubic lattice	137
	Conclusions and prospects	143
	Streszczenie w języku polskim pracy doktorskiej pt. <i>Wpływ pola magnetycznego na własności nadprzewodzące i przejście BCS-BEC w układach z lokalnym parowaniem fermionów</i>	149
A	Attraction-repulsion Symmetry	157
B	Zero-temperature equations	159
C	The analysis of the quasiparticle excitations spectrum: gapless region	161
D	T-matrix approach. Functional derivatives technique	165
D.1	Functional derivatives technique	165
D.2	T-matrix scheme	172
D.3	T-matrix approach for $h \neq 0$	176
E	Density of states	179
	Bibliography	183
	List of publications	200
	List of conferences and schools	201

Acknowledgements

I would like to thank my supervisor Roman Micnas, who introduced me to condensed matter physics and was always patient in answering all my questions and sharing his great experience.

I thank Stanisław Robaszkiewicz for many insightful discussions and constant support in my work.

I would like to thank all the people from the Solid State Theory division for useful discussions and very friendly atmosphere during my PhD thesis work.

I thank Piotr Tomczak who contributed a lot to my education in numerical methods, which was of utmost importance for this work.

I am very grateful to Karl Jansen thanks to whom I could learn the principles of Lattice QCD and do some work in this fascinating field. I also thank DESY for hospitality during my stays in Zeuthen.

I acknowledge useful discussions with: Maciej Bąk, Ravindra Chhajlany, Krzysztof Cichy (who is my husband now), Przemysław Grzybowski, Andrzej Koper and Tomasz Polak.

This work was partly financed from Ministry of Science and Higher Education grant nr. N N0305/B/H03/2011/40.

Last but not least, I thank my family and friends who supported me over many years – especially my husband Krzysztof and my parents. My son Filip provided great motivation in the final months of writing this thesis. I also thank Monika Rudnicka, Alina Piwowarczyk, Gosia and Maciej Niemir, Małgorzata Mrowińska, Ania and Marcin Makowscy, Asia and Dominik Niedzielscy, Wojtek Kowalewski, Ania Dyrdał, Piotr Trocha for their support and care.

List of abbreviations

AAHM	Asymmetric Attractive Hubbard Model
AHM	Attractive Hubbard Model
BCC	Body-Centered Cubic
BCS	Bardeen-Cooper-Schrieffer (theory)
BEC	Bose-Einstein Condensation
BP	Breached Pair
BP-1	Breached Pair with 1 Fermi surface
BP-2	Breached Pair with 2 Fermi surfaces
CC	Chandrasekhar-Clogston (limit)
CDW	Charge Density Wave
CO	Charge Ordering
DMRG	Density Matrix Renormalization Group
DOS	Density Of States
FCC	Face-Centered Cubic
FFLO	Fulde-Ferrell-Larkin-Ovchinnikov
FS	Fermi Surface
GS	Gapless
HFA	Hartree-Fock Approximation
HTSC	High- T_c superconductivity
KM	Kadanoff-Martin
KT	Kosterlitz-Thouless
LP	Local Pair
LPU	Large-Positive- U
MF	Mean-Field
NO	NOrmal (phase)
NO-I	partially polarized NOrmal (phase)
NO-II	fully polarized NOrmal (phase)
NSR	Nozières-Schmitt-Rink
PG	Pseudo-Gap
PS	Phase Separation
PS-I	partially polarized Phase Separation (SC_0 +NO-I)
PS-II	fully polarized Phase Separation (SC_0 +NO-II)
PS-III	Phase Separation (SC_M +NO-II)
QCP	Quantum Critical Point
QMC	Quantum Monte Carlo
RT	Reentrant transition
SC	SuperConducting
SC_0	unpolarized SuperConducting (phase)
SC_M	homogeneous magnetized SuperConducting (phase)
SDW	Spin Density Wave
TCP	TriCritical Point

Introduction

The immense development of experimental techniques in cold atomic Fermi gases in the last years has allowed investigation of not only strongly correlated systems in condensed matter physics, but also in high energy physics and even astrophysics (neutron stars) systems. The ability to control the interactions via the Feshbach resonance in ultracold fermionic gases sets new perspectives for experimental realization and study of many different unconventional systems, including: spin-polarized superfluidity (with population imbalance), superconductivity with nontrivial Cooper pairing, Bose-Fermi mixtures, mixtures of fermions with unequal masses and mixtures of fermions with three hyperfine states (in analogy to quantum chromodynamics). The possibility to control the population imbalance has also motivated the attempts to understand the BCS-BEC crossover phase diagrams at zero and finite temperatures in the presence of spin polarization.

The aim of the thesis was to investigate superconducting properties in the presence of Zeeman magnetic field in systems with local fermion pairing on the lattice. The study also concerned the evolution from the weak coupling (BCS-like) limit to the strong coupling limit of tightly bound local pairs (BEC) with increasing attraction, both in the ground state and at finite temperatures, within the spin-polarized extended Hubbard model. The analysis was also extended to the case of spin dependent hopping integrals (mass imbalance), with special attention paid to the BCS-BEC crossover physics in the ground state. The methods used included: the mean field approximation (BCS-Stoner type) and the estimation of the phase coherence temperature within the Kosterlitz-Thouless (KT) scenario in two dimensions. The BCS-BEC crossover was also analyzed in three dimensions, at finite temperatures, within the spin polarized Attractive Hubbard Model (AHM), going beyond the mean field approximation. In this case, the critical temperatures of the superconducting transition were determined within the self-consistent T-matrix method. The strong coupling expansion was applied to map the spin polarized AHM onto the model of hard-core bosons on the lattice.

The thesis is organized as follows.

In **chapter 1**, the theoretical principles of superconductivity and superfluidity are reviewed, beginning with a historical introduction. The fundamentals of the BCS-BEC crossover physics are given, including the characteristic features of the BCS and BEC limits. We also show new experimental and theoretical possibilities of studying cold atomic Fermi gases.

Chapter 2 gives a discussion of the spin-polarized extended Hubbard model. The Hamiltonian is introduced and its symmetries are discussed. Next, applying the broken

symmetry Hartree approximation, the set of self-consistent equations for the superconducting gap parameter, the number of particles and magnetization are obtained. From the partition function, the grand canonical potential of the superconducting and normal state are determined.

In **chapter 3**, some theoretical aspects of the KT transition in 2D systems are outlined, followed by a brief discussion of the two-dimensional XY model. This model is a good example of a system which does not have the long range order at finite temperatures but it exhibits a phase transition. Finally, the superfluid density in a general case is calculated and further used to determine the KT temperature from a universal relation.

In **chapter 4**, the influence of the Zeeman term on the superfluid characteristics of the attractive Hubbard model with spin independent hopping integrals is analyzed, for the square and simple cubic lattices. Within the mean-field approach, we construct phase diagrams in two ways: by fixing the chemical potential or the electron concentration, and show the relevant differences resulting from these possibilities. The importance of the Hartree term in the broken symmetry Hartree-Fock approximation is indicated. For the two-dimensional case, the KT transition in the weak coupling regime is investigated. Finally, the influence of the pure d-wave pairing symmetry on the superconducting phases stability in a 2D system is analyzed.

In **chapter 5**, the influence of magnetic field on the BCS-BEC crossover in the ground state for the square and simple cubic lattices is analyzed, within the spin-polarized AHM. The development of experimental techniques in cold atomic Fermi gases with tunable attractive interactions (through the Feshbach resonance) allowed a study of the BCS-BEC crossover and the properties of exotic states in these systems.

In **chapter 6**, the BCS-BEC crossover analysis is extended to finite temperatures in 2D within the Kosterlitz-Thouless scenario. We also investigate the effects of pairing fluctuations using self-consistent T-matrix approach to study the BCS-BEC crossover in 3D. The T-matrix approach goes beyond the standard mean field, since it includes the effects of non-condensed pairs and allows a description of the BEC side of the crossover. The crossover diagrams include the pseudogap state. We make a comparison of the results obtained within the so-called $(GG_0)G_0$ and $(GG)G_0$ schemes, both for the 3D continuum model with contact attraction and for the AHM, for a simple cubic lattice. We also discuss a generalization of the T_c equations in non-zero Zeeman magnetic field case and show numerical solutions.

Chapter 7 presents the results concerning the effects of spin-dependent hopping integrals ($t^\uparrow \neq t^\downarrow$) on the stability of the superfluid phases. We study the evolution from the weak to strong coupling limit, within the AHM in magnetic field with spin-dependent hopping integrals, for square and simple cubic lattices. We also construct the BCS-BEC crossover phase diagrams in finite temperatures in 2D, taking into account the Kosterlitz-Thouless transition. The strong coupling expansion is applied to map the spin polarized AHM onto the model of hard-core bosons on the lattice. We show the occurrence of competition between charge ordering and superconducting phases for any particle concentration in the spin dependent hopping integrals case. This mapping is specific to the lattice fermion model.

Appendices A-E contain additional material.

Chapter 1

Principles of superconductivity and superfluidity

1.1 Historical perspective

Superconductivity, superfluidity and Bose-Einstein condensation (BEC) are among the most interesting phenomena of condensed matter physics. They have been a scientific mystery for many years of the 20th century and they still provide many theoretical and experimental challenges. The properties of superconductors and superfluids are seemingly very different, but they are similar in many respects, e.g. both evince frictionless flow and contain quantized vortices. The appearance of these effects depends upon whether the system in question is electrically neutral (superfluids) or charged (superconductors).

The phenomenon of superconductivity, i.e. the ability of some materials to conduct the electric current without resistance, was discovered in 1911 by Kamerlingh-Onnes [1] in a mercury (Hg) sample which was cooled to 4.2 K. Two years after this spectacular discovery, superconductivity was found in lead (Pb) with critical temperature $T_c = 7.2$ K and in 1930 in niobium (Nb) at $T_c = 9.2$ K.

In 1933 Meissner and Ochsenfeld [2] discovered that magnetic flux is canceled from the inside of a sample when it is cooled below its superconducting transition temperature in a weak external magnetic field. Therefore, a characteristic feature of superconducting materials is perfect diamagnetism. Twenty years after this discovery, with advent of the Ginzburg-Landau theory, superconductors were proposed to be divided into two classes – those from which magnetic field is fully canceled were named **type-I superconductors**, while those from which strong magnetic field is only partly canceled were named **type-II superconductors**.

At around the same time (1924), Indian physicist Satyendra Bose sent to Albert Einstein a paper in which he derived the Planck black-body radiation formula with the use of exclusively statistical arguments [3]. Bose was a relatively unknown scientist and his earlier papers had been ignored. However, Einstein realized that there were spectacular novel ideas in Bose's letter and helped him to publish the results in *Zeitschrift für Physik* [4]. He was also interested in this topic and wrote two papers in which a complete theory of

bosonic particles was included. The statistics that governs the behavior of such particles has been named **Bose-Einstein statistics**.

In one of his papers, Einstein noticed [5] that if the number of particles is conserved, the system of non-interacting particles undergoes a thermodynamic phase transition at sufficiently low temperatures, called the **Bose-Einstein condensation (BEC)**. The condensation discovered by Einstein results from the fact that the total number of states at decreasing energy becomes very low in the thermodynamic limit, and there is no space for all particles when temperature decreases. Thus, the system can accumulate particles only in the ground state.

However, for a long time no physical system was known to actually have shown Bose-Einstein condensation. In 1938 F. London suggested [6] that the superfluidity phenomenon which was discovered earlier in ^4He by Allen, Misener and Kapitza [7, 8] can be a manifestation of bosonic condensation. The absence of superfluidity in ^3He (the fermionic helium isotope), whose nuclei are fermions, supported this thesis. However, much later ^3He turned out to be superfluid at a yet much lower temperature than ^4He (by Osheroff, Richardson, Lee) [9]. For many years, the nature of relation between the superfluid properties and Bose-Einstein condensation was unclear. The breakthrough took place in the 1950s when O. Penrose and L. Onsager found the connection between superfluidity and the long-range order present in highly-correlated bosonic systems [10]. It permitted an estimation of the number of condensed atoms in the liquid ^4He as 8%. The number is relatively small in contrast to the BEC theory which describes the case of an ideal gas and neglects any interactions between the particles. However, the interactions are strong in liquid helium and hence can not be neglected.

Strong interactions in ^4He made it impossible to carry out the *ab initio* calculations of its properties. However, superfluidity itself (the lack of viscosity in a liquid) was explained within the Landau phenomenological theory in 1941 [11, 12]. In this theory, superfluidity results from the fact that when the accessible energy is very low, only long-wavelength phonons can be excited. In 1947 N. Bogoliubov extended this approach by introducing the low-energetic spectrum of phonons and assuming that the dynamics of the system is dominated by the atoms which constitute the condensate [13, 14]. In this paper, the Bogoliubov canonical transformation was introduced, which turned out to be very useful for the description of many phenomena, such as: *superconductivity*, *atomic condensates* and also in *nuclear physics*. The weakly interacting systems were studied also in perturbation theory by K. Huang in the 1950s [15].

In 1957, the mechanism of superconductivity was finally explained in the framework of quantum mechanics by J. Bardeen, L. Cooper and R. Schrieffer [16]-[18]. **The BCS theory** clarifies that the interaction of electrons with the crystalline lattice (electron-phonon coupling) in a superconductor leads to an attractive interaction and the creation of pairs of electrons with opposite momenta and spins (Cooper pairs). Cooper has shown that even a very weak attractive interaction causes a Fermi sea instability. Therefore, the formation of Cooper pairs is more energetically favorable for superconducting systems than the occupation of allowed single particle states. The BCS theory based on the above background explains consistently many physical properties of phonon superconductors.

The theory predicted (among other things) the formation of a minimum excitation energy (or energy gap) in a superconductor below the critical temperature (T_c). The energy gap increases gradually with decreasing temperature. The Cooper pairs are well-defined objects in momentum space. The BCS theory describes conventional superconductors, for which the critical temperature is of order 10^4 times weaker than the Fermi energy (E_F) (strictly speaking $k_B T_c \sim 10^{-4}$).

In 1986 Bednorz and Müller [19] obtained a ceramic material consisting of lanthanum (La), barium (Ba), copper (Cu) and oxygen (O) (LaBaCuO), which exhibits the phase transition from the superconducting to the normal state at $T_c = 35$ K. From this time on, many materials have been discovered with yet higher transition temperatures. These compounds have been named High- T_c superconductors (HTSC) and this phenomenon – High- T_c superconductivity. High- T_c superconductors are anisotropic ionic crystals which are, depending on doping, antiferromagnetic insulators or superconductors with very untypical properties in the normal state. They have critical temperatures $T_c \sim 100$ K, i.e. an order of magnitude higher than conventional superconductors. They are also extreme II-type superconductors, i.e. they have considerably shorter coherence length ($\xi \sim 10$ Å) than conventional superconductors and large penetration depth ($\lambda \sim 3000$ Å). A very important feature of unconventional superconductors is a linear dependence between the superconducting transition temperature and the inverse square of penetration depth (extrapolated to $T = 0$ K). The plot of this dependence has been named Uemura plot [20].

Although it is known that conventional phonon mechanism plays some role, there is still no complete microscopic theory to describe unconventional superconductivity. Therefore, many hypotheses on the source of occurrence of this phenomenon have been put forward.

As mentioned before, in the weak coupling limit the fermion superfluid or superconducting (charged fermion superfluid) system is described within the Bardeen-Cooper-Schrieffer theory. With increasing attraction, the system can evolve to the Bose-Einstein condensation limit of preformed fermionic pairs (pairing in real space). Already in 1980 A. Leggett showed that when attraction between two fermions with opposite spins is weak, the BCS superfluid is stable, but when the attraction becomes strong, the system is on the BEC side at $T = 0$ [21]. Leggett considered the zero-range attractive potential (the contact interaction). In 1985 Leggett's analysis was extended to non-zero temperatures (especially the critical temperature for the emergence of superfluidity) by P. Nozières and S. Schmitt-Rink (NSR) [22]. They used a diagrammatic method for a model of fermions with a finite-range attractive interaction.

The most interesting and promising ideas assume that the properties of High- T_c superconductors (and also other unconventional superconductors) place them between two regimes: BCS and BEC [23]-[33]. **The BCS-BEC crossover phenomenon** is also used: (a) to describe superfluidity in ultracold atomic gases, (b) to describe the insulator-superconductor transition in disordered systems, (c) to study Bose condensation of excitons, (d) in high-energy physics (quantum chromodynamics on a lattice (lattice QCD)), (e) in astrophysics (neutron stars).

The physics of the BCS-BEC crossover will be described in section 1.2.

1.2 Basics of the BCS-BEC crossover physics

As mentioned before, there has been a broad agreement that the physics of BCS-BEC crossover is crucial for unconventional superconductivity.

The properties of a fermionic system with attractive interaction are very different in the extreme BCS and BEC limits, especially in the normal state.

The characteristic features of **the BCS limit** are the following:

- pairs form and condense at the same temperature (T_c),
- pairing takes place in momentum space and only a small number of electrons in the vicinity of the Fermi surface form the Cooper pairs,
- attractive interaction between fermions ($|U|$) is weak,
- pair size in the condensate is much larger than the average distance between them (hence the pairs strongly overlap),
- the energy gap decreases monotonically with increasing T and vanishes at T_c ,
- the critical temperature and the thermodynamics are determined by single particle excitations – broken Cooper pairs with exponentially small gap,
- above the critical temperature the normal state is described by the Fermi liquid theory.

On the other hand, **the BEC limit (or the local pair limit (LP))** is characterized by the following features:

- pairs are formed at a temperature T_p , much higher than the critical temperature ($T_p \gg T_c$) in which the long-range phase coherence occurs and phase transition to the superconducting state takes place,
- pairs form in real space and all electrons are paired,
- attractive interaction between fermions is strong,
- pairs are much smaller than the average distance between them,
- pair binding energy is proportional to $|U|$, pairs exist above T_c up to T_p ,
- the critical temperature and thermodynamics are determined by collective modes,
- the normal state is described by the Bose liquid of tightly bound and phase incoherent pairs (in the range of $T_c < T < T_p$).

For intermediate couplings, the normal state can have a so-called *pseudo-gap* (PG) in the single particle energy spectrum and deviations from the standard Landau theory of the Fermi liquids occur.

A schematic phase diagram for systems in which the evolution from the BCS to BEC limit takes place is presented in Fig. 1.1. The solid lines corresponds to the border between the superconducting and the normal state ($T_c \sim t \exp(-1/N(0)|U|)$, where $N(0)$ – density of states at Fermi level) – in the weak coupling regime and $T_c \sim t^2/|U|$ – in the strong coupling limit). The intermediate region (the dashed part of the diagram) between the Fermi liquid and the Bose liquid regimes is the area in which the pairs are formed ($T_p \sim |U|$). The continuation of T_c , determined within continuum model, is denoted by the dashed line in the phase diagram.

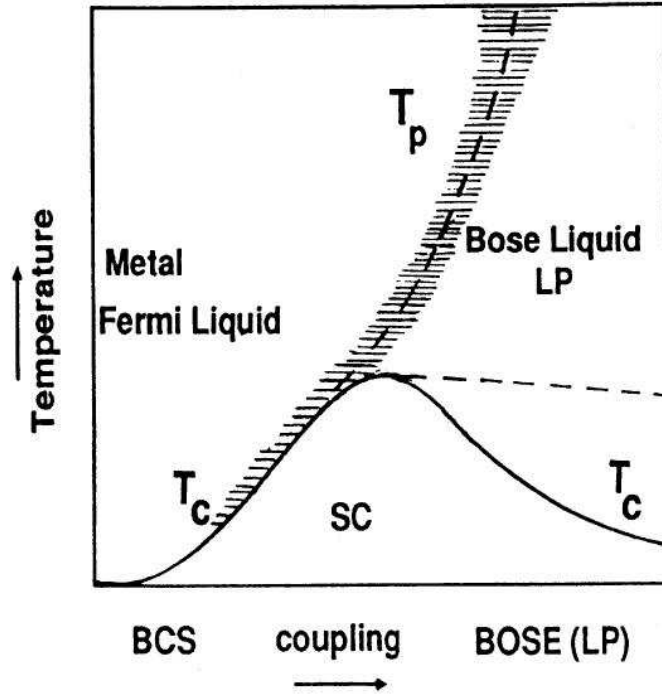


Figure 1.1: Schematic phase diagram for systems in which the BCS-BEC crossover takes place [34] (see also chapter 6.2.2).

The effects of the BCS-BEC crossover are clearly visible in the behavior of chemical potential μ at $T = 0$. In the weak coupling limit, $\mu = E_F$ (E_F – Fermi energy) and the conventional BCS theory is valid. At a suitably strong coupling, the chemical potential drops to $\mu = 0$ and becomes negative ($\mu < 0$) in the BEC limit. The point at which $\mu = 0$ is the BCS-BEC crossover point [21]. However, the behavior of the system does not resemble neither the BCS nor the BEC regime near $\mu = 0$, so one can speak of a whole crossover region, not only of one crossover point. When $\mu \simeq E_F$, the Fermi surface is present in the system and we deal with a Cooper pairs condensate. On the other hand,

when μ becomes negative, the Fermi surface vanishes and the bosonic regime appears.

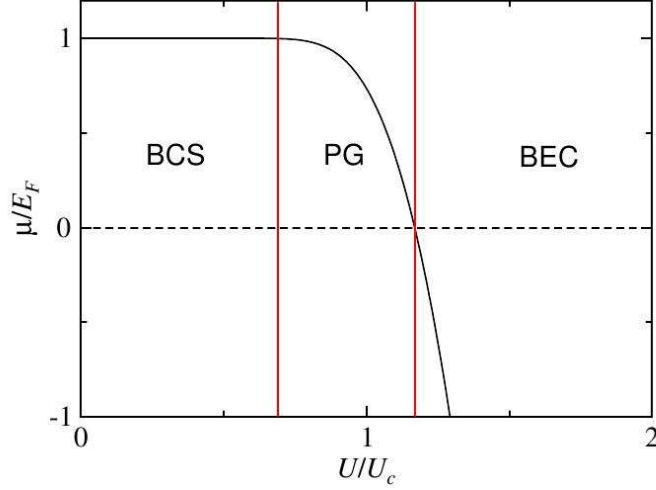


Figure 1.2: Chemical potential behavior in units of the Fermi energy at $T = 0$ in three regimes: BCS, BCS-BEC crossover (PG) and BEC [35].

The evolution from the BCS superfluid to the Bose-Einstein condensation limit of preformed fermionic pairs cannot be directly examined experimentally by tuning the interaction strength in superconductors, nuclear matter or in neutron stars. However, the BCS-BEC crossover in superconductors can be analyzed experimentally by changing particle concentration (doping). The tuning of interactions itself, in turn, is feasible in ultracold Fermi atoms through **Feshbach resonances** [36, 37]. These resonances take place when the energy difference ΔE between a bound state with energy E_{res} (the closed channel) and the threshold energy E_{th} of scattering states (the open channel) goes to zero, by using an external magnetic field B_0 . The Feshbach resonance is characterized by a divergence in the scattering length a_s . The BCS limit occurs when the dimensionless scattering parameter: $1/k_F a_s \rightarrow -\infty$, while the BEC limit corresponds to $1/k_F a_s \rightarrow \infty$, where k_F is the Fermi momentum.

In 2003 three experimental groups observed a condensation of pairs of fermionic atoms of ultracold gases in the region of the BCS-BEC crossover. M. Grimm et al. [38, 39] and also W Ketterle et al. [40, 41] used ^6Li atoms. D. S. Jin et al. [42, 43] cooled down the trapped atom gas of ^{40}K to a temperature of the order of $5 \cdot 10^{-8}$ K. Afterwards, the interactions between atoms were tuned through the Feshbach resonance. The appearance of the energy gap was shown on the basis of radiospectroscopic measurements [44, 45]. Years later the existence of the superfluid phase was eventually confirmed through the presence of quantized vortices [46].

1.3 The new possibilities

Unconventional superconductivity with nontrivial Cooper pairing in strongly correlated electron systems and spin-polarized superfluidity (in the context of cold atomic Fermi gases) are currently investigated and also widely discussed in the leading world literature. They lay down one of the most investigated directions of studies in the range of condensed matter physics and ultracold quantum gases.

Recently, experimental groups from MIT [47]-[49] and from the Rice University [50] have begun investigations of quantum Fermi gases (^6Li) with unequal numbers of fermions with down (\downarrow) and up (\uparrow) spins ($N_\downarrow \neq N_\uparrow$ – systems with *population imbalance*). The possibility to control the population imbalance has motivated the attempts to understand the BCS-BEC crossover phase diagrams at zero and finite temperatures.

Experiments have indicated the presence of an unpolarized superfluid core in the center of the trap and a polarized normal state surrounding this core in the density profiles of trapped Fermi mixtures with population imbalance. Hence, a phase separation appears between the unpolarized BCS and the polarized normal state.

Experiments in which the fermionic (or bosonic) gases are put on optical lattices have also been carried out [39, 51]. Both the depth of the periodic trapped potential and the geometry can be fully controlled. In this way, strongly correlated systems with different geometries of the lattice can be investigated. Atomic gases with tunable interactions on optical lattices allow experimental realization of the Hubbard model.

The possibility to create the population imbalance in conventional superconductors is to apply an external magnetic field, but this field is shielded by the orbital motion of electrons (the Meissner effect). However, a mixture with arbitrary population ratio can be prepared in atomic Fermi gases. Hence, the influence of the Zeeman magnetic field on superfluidity can be also investigated.

In the presence of the Zeeman magnetic field (h), the densities of states are different for the particles with spin down and spin up. The population imbalance introduces a mismatch between the Fermi surfaces. At stronger imbalance, in the weak coupling regime, superfluidity is destroyed and there is a first-order phase transition to the polarized normal state at a universal value of the critical magnetic field $h_c = \Delta_0/\sqrt{2} \approx 0.707\Delta_0$ (the Chandrasekhar-Clogston limit (CC) [52, 53]), where Δ_0 is the gap at $T = 0$, $h = 0$. Rather recently a behavior in accordance with the CC limit has been observed in population imbalanced atomic Fermi gases [54].

In the weak coupling limit, at a large difference in the occupation number (or at a strong magnetic field) states with nontrivial Cooper pairing can exist. An example of such pairing is the formation of Cooper pairs across the spin-split Fermi surface with non-zero total momentum ($\vec{k} \uparrow, -\vec{k} + \vec{q} \downarrow$), leading to the so-called Fulde-Ferrell [55] and Larkin-Ovchinnikov [56] (FFLO) state, which is favored [57]-[61] (against the normal state) up to $h_c^{FFLO} = 0.754\Delta_0$ in three dimensions. There are experimental and theoretical premises that the FFLO state can be found in heavy-fermion superconductors (e.g. CeCoIn_5). However, the observation of such a state is extremely difficult in superconducting systems because of the very strong destructive influence of the orbital effect on

the superconductivity, as mentioned above.

There has been much work on exact numerical studies (Quantum Monte Carlo (QMC) simulations and density-matrix renormalization group (DMRG)) of the 1D attractive Hubbard model with fermion population imbalance [62]–[66]. The results seem to suggest that the FFLO state can be obtained in one-dimensional systems, which is consistent with the fact that h_c^{FFLO} diverges as $T \rightarrow 0$ in $d = 1$.

Another kind of pairing and phase coherence is the spatially homogeneous spin-polarized superconductivity (breached pair (BP)) which has a gapless spectrum for the majority spin species [67, 68, 69]. The coexistence of the superfluid and the normal component in the isotropic state is characteristic of the BP phase. The state of this type was originally considered by Sarma [70]. He studied the case of a superconductor in an external magnetic field within the BCS theory. All orbital effects were neglected. He showed that self-consistent mean field solutions with gapless spectrum ($\Delta(h)$) are energetically unstable at $T = 0$, in contrary to the fully gapped BCS solutions. On the other hand, a non-zero temperature can lead to the stabilization of a spin-polarized state.

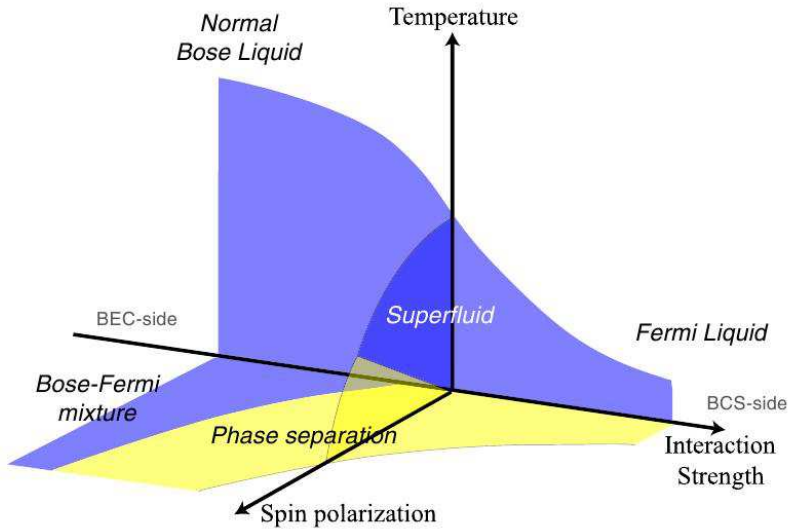


Figure 1.3: Schematic diagram (temperature-interaction strength-spin polarization) in which various possible phases of two-component Fermi gas are illustrated [71].

As shown in Fig. 1.3, one can expect at least three phases when the interaction is changed and the population imbalance is fixed. In the weak coupling region at $T = 0$, the superfluid BCS state with equal particle densities is spatially separated from the unpaired fermions. On the other hand, at $T = 0$, for strong attraction the two-component Fermi gas with population imbalance evolves into a coherent mixture of local pairs (LP's) and excess spin-up fermions (Bose-Fermi mixture).

New possibilities appear when one investigates mixtures of fermions with unequal masses. These systems are very interesting not only in the context of atomic physics,

but also in that of condensed-matter physics and color superconductivity in high energy physics. If the number of hyperfine states is extended from two to three, there can be three types of s -wave pairing. Such pairs are analogous to quarks which can form pairs in different color states in the cores of neutron stars [72].

First theoretical studies of Fermi condensates in systems with spin and mass imbalances have shown that the BP state can have excess fermions with two Fermi surfaces (BP-2 or interior gap state) [73]-[80]. However, the problem of stability of the BP-2 state is still open. According to some investigations, the interior gap state proposed by Liu and Wilczek [73] is always unstable even for large mass ratio and the phase separation is favorable [81, 82]. On the other hand, at strong attraction the homogeneous magnetized superconducting phase can only have one Fermi surface (BP-1). Details concerning these exotic phases will be discussed later.

Chapter 2

The Hubbard model

2.1 Introduction

The Hubbard model is one of the most important models in solid state physics. Despite its simplicity, it describes many interesting phenomena, such as: metal-superconductor transition, antiferromagnetism, ferrimagnetism, ferromagnetism and superconductivity in strongly correlated systems [83]. The Hubbard model is the simplest many-body Hamiltonian which allows a description of two opposing tendencies: (a) the kinetic energy leading to the delocalization of electrons (metal-like behavior), (b) the Coulomb repulsion leading to the localization of electrons on the lattice (metal-insulator transition – the Mott transition).

2.2 The Hubbard Hamiltonian

Let us consider the case of a partially filled s -band which contains n electrons per atom. Let $\Psi_{\vec{k}}$ be the Bloch functions of this band and $\epsilon_{\vec{k}}$ – the energies corresponding to the Bloch functions. The wave functions and the energies are calculated in the Hartree-Fock potential which represents the average s -band electrons interaction with the electrons of other bands and other s -band electrons.

The electrons dynamics can be described through the following Hamiltonian [84]:

$$\begin{aligned}
 H = & \sum_{\vec{k}, \sigma} \epsilon_{\vec{k}} c_{\vec{k}\sigma}^\dagger c_{\vec{k}\sigma} + \frac{1}{2} \sum_{\vec{k}_1, \vec{k}_2, \vec{k}'_1, \vec{k}'_2} \sum_{\sigma_1, \sigma_2} (\vec{k}_1 \vec{k}_2 | 1/r | \vec{k}'_1 \vec{k}'_2) c_{\vec{k}_1 \sigma_1}^\dagger c_{\vec{k}_2 \sigma_2}^\dagger c_{\vec{k}'_2 \sigma_2} c_{\vec{k}'_1 \sigma_1} \\
 & - \sum_{\vec{k}, \vec{k}'} \sum_{\sigma} \left(2(\vec{k} \vec{k}' | 1/r | \vec{k} \vec{k}') - (\vec{k} \vec{k}' | 1/r | \vec{k} \vec{k}') \right) \nu_{\vec{k}'} c_{\vec{k}\sigma}^\dagger c_{\vec{k}\sigma},
 \end{aligned} \tag{2.1}$$

where: sum over \vec{k} from the first Brillouin zone, $\nu_{\vec{k}}$ – band filling of electrons with momentum \vec{k}

$$(\vec{k}_1 \vec{k}_2 | 1/r | \vec{k}'_1 \vec{k}'_2) = e^2 \int \frac{\varphi_{\vec{k}_1}^*(\vec{x}) \varphi_{\vec{k}'_1}(\vec{x}) \varphi_{\vec{k}_2}^*(\vec{x}') \varphi_{\vec{k}'_2}(\vec{x}')}{|\vec{x} - \vec{x}'|} d\vec{x} d\vec{x}'. \tag{2.2}$$

1. Hamiltonian term – the band energies of electrons,
2. Hamiltonian term – the Coulomb interaction of electrons,
3. Hamiltonian term – prevents double counting of the electrons interactions within the band (they were included when $\epsilon_{\vec{k}}$ were calculated within the Hartree-Fock approximation (HFA)).

Here, we introduce the Wannier functions:

$$\phi(\vec{x} - \vec{R}_i) = \frac{1}{\sqrt{N}} \sum_{\vec{k}} e^{-i\vec{k} \cdot \vec{x}} \varphi_{\vec{k}}(\vec{x}), \quad (2.3)$$

where N is the number of atoms. Then, one can show that:

$$\varphi_{\vec{k}}(\vec{x}) = \frac{1}{\sqrt{N}} \sum_i e^{i\vec{k} \cdot \vec{R}_i} \phi(\vec{x} - \vec{R}_i), \quad (2.4)$$

where the sum goes over all positions of atoms \vec{R}_i . Let us introduce creation and annihilation operators of electrons with spin σ in the Wannier state $\phi(\vec{x} - \vec{R}_i)$:

$$c_{\vec{k}\sigma} = \frac{1}{\sqrt{N}} \sum_i e^{i\vec{k} \cdot \vec{R}_i} c_{i\sigma}, \quad (2.5)$$

$$c_{\vec{k}\sigma}^\dagger = \frac{1}{\sqrt{N}} \sum_i e^{-i\vec{k} \cdot \vec{R}_i} c_{i\sigma}^\dagger. \quad (2.6)$$

The Hamiltonian (2.1) can be rewritten using creation and annihilation operators:

$$\begin{aligned} H &= \sum_{i,j} \sum_{\sigma} t_{ij} c_{i\sigma}^\dagger c_{j\sigma} + \frac{1}{2} \sum_{i,j,k,l} \sum_{\sigma,\sigma'} (ij|1/r|kl) c_{i\sigma}^\dagger c_{j\sigma'}^\dagger c_{l\sigma'} c_{k\sigma} \\ &- \sum_{i,j,k,l} \sum_{\sigma} (2(ij|1/r|kl) - (ij|1/r|kl)) \nu_{jl} c_{i\sigma}^\dagger c_{k\sigma}, \end{aligned} \quad (2.7)$$

where:

$$t_{ij} = \frac{1}{N} \sum_{\vec{k}} \epsilon_{\vec{k}} e^{i\vec{k} \cdot (\vec{R}_i - \vec{R}_j)}, \quad (2.8)$$

$$(ij|1/r|kl) = e^2 \int \frac{\phi^*(\vec{x} - \vec{R}_i) \phi(\vec{x} - \vec{R}_k) \phi^*(\vec{x}' - \vec{R}_j) \phi(\vec{x}' - \vec{R}_l)}{|\vec{x} - \vec{x}'|} d\vec{x} d\vec{x}', \quad (2.9)$$

$$\nu_{jl} = \sum_{\vec{k}} \nu_{\vec{k}} e^{i\vec{k} \cdot (\vec{R}_j - \vec{R}_l)}. \quad (2.10)$$

Let us simplify the Hamiltonian (2.7). The Wannier functions resemble the atomic s functions, since we consider a narrow energy band. Then, the size of the atomic shell is much smaller than the inter-atomic distances. Hence, the largest integral among (2.9) is

($ii|1/r|ii$) $\equiv U$, suggesting that we can neglect all integrals (2.9), except for the integral U . Then, the Hamiltonian (2.7) takes the form:

$$H = \sum_{i,j} \sum_{\sigma} t_{ij} c_{i\sigma}^{\dagger} c_{j\sigma} + \frac{1}{2} U \sum_i \sum_{\sigma} n_{i\sigma} n_{i-\sigma} - U \sum_i \sum_{\sigma} \nu_{ii} n_{i\sigma}. \quad (2.11)$$

We get from eq. (2.2):

$$\nu_{ii} = \frac{1}{N} \sum_{\vec{k}} \nu_{\vec{k}} = \frac{1}{2} n \quad (2.12)$$

and the last term in (2.11) reduces to a constant so we can neglect it and obtain final form of the Hamiltonian:

$$H = \sum_{i,j} \sum_{\sigma} t_{ij} c_{i\sigma}^{\dagger} c_{j\sigma} + \frac{1}{2} U \sum_i \sum_{\sigma} n_{i\sigma} n_{i-\sigma}. \quad (2.13)$$

2.3 The Spin-Polarized extended Hubbard model

The Hubbard model can be extended by adding the intersite interaction term to the Hubbard Hamiltonian. One can also analyze the influence of the pure Zeeman effect on the superfluid characteristics within a lattice fermion model (the AHM). The Hamiltonian of such system takes the form:

$$\begin{aligned} H = & \sum_{ij} \sum_{\sigma} t_{ij}^{\sigma} c_{i\sigma}^{\dagger} c_{j\sigma} + \frac{1}{2} U \sum_{i\sigma} n_{i\sigma} n_{i-\sigma} + \frac{1}{2} \sum_{ij} \sum_{\sigma\sigma'} W_{ij} n_{i,\sigma} n_{j,\sigma'} \\ & - h \sum_i (n_{i\uparrow} - n_{i\downarrow}), \end{aligned} \quad (2.14)$$

where: t_{ij}^{σ} – nearest-neighbor spin-dependent hopping; $\sigma = \uparrow, \downarrow$ – spin index; $n_{i\sigma} = c_{i\sigma}^{\dagger} c_{i\sigma}$ – particle number operator; U – on-site interaction; W_{ij} – intersite interaction; h – Zeeman magnetic field¹.

The Hamiltonian (2.14) (the extended Hubbard model at $h = 0$, $t_{ij}^{\uparrow} = t_{ij}^{\downarrow} = t_{ij}$) has been proposed by Micnas, Ranninger and Robaszkiewicz while working on the problem of theoretical models in systems with local fermion pairing [27, 85]. This Hamiltonian describes a system of narrow band electrons which are strongly coupled with a bosonic field. The electrons polarize the bosonic field and, in this way, interact effectively with each other, creating excitations which exhibit a short-range Fröhlich type-interaction, which competes with the Coulomb interaction. These bosonic modes can be phonons, excitons, acoustic plasmons etc. The parameters of the Hamiltonian (2.14) – t_{ij} , U , W_{ij} are effective parameters.

¹In the case of ultracold Fermi gases, the role of the Zeeman field is played by the difference in chemical potentials for spin-up and spin-down fermions, i.e. $h \equiv (\mu_{\uparrow} - \mu_{\downarrow})/2$.

A typical microscopic mechanism which leads to the effective short-range attraction is the strong electron-lattice coupling. It causes the formation of polarons (the anharmonic modes can play an important role in this case) or the interaction of electrons with excitations – excitons, plasmons, magnons [85].

Two cases are considered most often within the extended Hubbard model [34]:

- $U_{eff} < 0$, $W_{eff} > 0$ – the induced local attraction plays a crucial role and dominates over the on-site repulsion. Therefore, this is the case of the on-site attraction (*negative- U extended Hubbard model*). In the strong coupling limit, electron pairs form. One can also consider the weak attraction limit. The Hubbard model with $U_{eff} < 0$ is the simplest lattice model of a superconductor with a short-range coherence length which exhibits the crossover between the regime of BCS-type superconductivity and Bose-Einstein condensation of local pairs. It is also an effective model which accounts for the properties of superconductivity and the charge ordering in the family of barium bismuthates ($Ba_{1-x}K_xBiO_3$, $BaPb_xBi_{1-x}O_3$), Chevrel phases and fullerenes. It can also be used for discussion of general properties (such as a pseudogap) cuprates.
- $W_{eff} < 0$, $U_{eff} > 0$ – this is the case of the intersite attraction. The induced attraction is strong enough to dominate over the intersite Coulomb repulsion. It is the model which describes the intersite pairing with various symmetries. In this case the Hamiltonian accounts for the properties of cuprates and heavy-fermion superconductors.

As mentioned before, the recent progress in experimental techniques gives new possibilities to observe various exotic phases appearing in strongly correlated systems. The properties of two-component Fermi mixtures with arbitrary population ratio ($n_\uparrow \neq n_\downarrow$) and spin dependent hopping integrals $t^\uparrow \neq t^\downarrow$ (mass imbalance) on optical lattices can be described by the extended Hubbard model (2.14).

In this thesis we focus on the analysis of the Zeeman term influence on the superfluid characteristics of the attractive Hubbard model ($U < 0$) for the square and simple cubic lattices (s -wave pairing). We also study the properties of the $t^\sigma - U - h$ model in which the spin-dependent hopping ($t^\uparrow \neq t^\downarrow$) is included. We analyze briefly the $t - W - h$ model in which the attractive interaction between the electrons on the neighboring sites is taken into account. In this way, we study the stability of various superconducting phases in an external magnetic field, with d -wave pairing symmetry.

2.4 The Hartree-Fock approximation

In this thesis we deal with the properties of two- and three dimensional systems in a Zeeman field, within the spin-polarized extended Hubbard model (in grand canonical

ensemble):

$$\begin{aligned}
H &= \sum_{i,j,\sigma} (t_{i,j}^\sigma - \mu \delta_{i,j}) c_{i,\sigma}^\dagger c_{j,\sigma} + U \sum_i n_{i,\uparrow} n_{i,\downarrow} + \frac{1}{2} \sum_{i,j,\sigma,\sigma'} W_{ij} n_{i,\sigma} n_{j,\sigma'} \\
&- h \sum_i (n_{i\uparrow} - n_{i\downarrow}),
\end{aligned} \tag{2.15}$$

where: μ – chemical potential. The Zeeman field (h) can originate from an external magnetic field (in $g\mu_B/2$ units) or from population imbalance in the context of the cold atomic Fermi gases with $\mu = (\mu_\uparrow + \mu_\downarrow)/2$ and $h = (\mu_\uparrow - \mu_\downarrow)/2$, where μ_σ is the chemical potential of atoms with (pseudo) spin- σ . This model allows inclusion of the influence of the Zeeman field on the superfluid properties not only for the isotropic pairing symmetry (s -wave) but also for the $s_{x^2+y^2}$ -wave and $d_{x^2-y^2}$ -wave pairing symmetries, which originate from the W term [25, 86, 87].

One should emphasize that the attractive Hubbard model ($U < 0$) in a Zeeman field, with spin independent hopping integrals ($t - U - h$) can be transformed to a doped repulsive Hubbard model (see Appendix A).

Let us Fourier transform the Hamiltonian (2.15) to the reciprocal space:

$$c_{j,\sigma}^\dagger = \frac{1}{\sqrt{N}} \sum_{\vec{k}} c_{\vec{k}\sigma}^\dagger e^{i\vec{r}_j \cdot \vec{k}}. \tag{2.16}$$

Then, one obtains:

$$\begin{aligned}
H &= \sum_{\vec{k},\sigma} (\epsilon_{\vec{k}}^\sigma - \mu) c_{\vec{k}\sigma}^\dagger c_{\vec{k}\sigma} + \frac{1}{N} \sum_{\vec{k}_1, \vec{k}_2, \vec{q}} \sum_{\sigma, \sigma'} \left(U \delta_{\sigma\sigma'} + \frac{W}{2} \gamma_{\vec{q}} \right) c_{\vec{k}_1\sigma}^\dagger c_{\vec{k}_1 - \vec{q}\sigma} c_{\vec{k}_2\sigma'}^\dagger c_{\vec{k}_2 + \vec{q}\sigma'} \\
&- h \sum_{\vec{k}} (c_{\vec{k}\uparrow}^\dagger c_{\vec{k}\uparrow} - c_{\vec{k}\downarrow}^\dagger c_{\vec{k}\downarrow}),
\end{aligned} \tag{2.17}$$

where: N – number of lattice sites. The electron dispersion is $\epsilon_{\vec{k}}^\sigma = \sum_{\vec{\delta}} t_{\vec{\delta}}^\sigma e^{i\vec{k} \cdot \vec{\delta}} = -2t^\sigma \Theta_{\vec{k}}$; $\Theta_{\vec{k}} = \sum_{l=1}^d \cos(k_l a_l)$ (here $d = 2, 3$ for two- and three-dimensional lattices, respectively); a_l is the lattice constant in the l -th direction (we set $a_l = 1$ in further considerations); $\gamma_{\vec{q}} = 2\Theta_{\vec{q}}$, $\gamma_{\vec{q}} = \gamma_{-\vec{q}}$, $\sum_{\vec{q}} \gamma_{\vec{q}} = 0$.

We will not consider alternative phases such as FFLO states, in which the $\vec{q} \neq 0$ pairs can occur.

Now, we use the Hartree-Fock approximation by separating the two-particle operators in such a way that:

$$A = \langle A \rangle + \delta A. \tag{2.18}$$

Hence:

$$\begin{aligned}
AB &= (\langle A \rangle + \delta A)(\langle B \rangle + \delta B) \simeq \langle A \rangle \langle B \rangle + \delta A \langle B \rangle + \delta B \langle A \rangle = \\
&= \langle A \rangle \langle B \rangle + A \langle B \rangle - \langle A \rangle \langle B \rangle + B \langle A \rangle - \langle A \rangle \langle B \rangle = \\
&= A \langle B \rangle + B \langle A \rangle - \langle A \rangle \langle B \rangle.
\end{aligned} \tag{2.19}$$

For example (if $\vec{k}_1 = -\vec{k}_2$), we get:

$$\begin{aligned}
& c_{\vec{k}_1\sigma}^\dagger c_{\vec{k}_1-\vec{q}\sigma} c_{\vec{k}_2\sigma'}^\dagger c_{\vec{k}_2+\vec{q}\sigma'} = c_{\vec{k}_1\sigma}^\dagger c_{\vec{k}_1-\vec{q}\sigma} c_{-\vec{k}_1\sigma'}^\dagger c_{-\vec{k}_1+\vec{q}\sigma'} = \\
& = -c_{\vec{k}_1\sigma}^\dagger c_{-\vec{k}_1\sigma'}^\dagger c_{\vec{k}_1-\vec{q}\sigma} c_{-\vec{k}_1+\vec{q}\sigma'} = -\langle c_{\vec{k}_1\sigma}^\dagger c_{-\vec{k}_1\sigma'}^\dagger \rangle c_{\vec{k}_1-\vec{q}\sigma} c_{-\vec{k}_1+\vec{q}\sigma'} \\
& - \langle c_{\vec{k}_1-\vec{q}\sigma} c_{-\vec{k}_1+\vec{q}\sigma'} \rangle c_{\vec{k}_1\sigma}^\dagger c_{-\vec{k}_1\sigma'}^\dagger + \langle c_{\vec{k}_1\sigma}^\dagger c_{-\vec{k}_1\sigma'}^\dagger \rangle \langle c_{\vec{k}_1-\vec{q}\sigma} c_{-\vec{k}_1+\vec{q}\sigma'} \rangle,
\end{aligned} \tag{2.20}$$

while if $\vec{k}_2 = \vec{k}_1 - \vec{q}$ then:

$$\begin{aligned}
& c_{\vec{k}_1\sigma}^\dagger c_{\vec{k}_1-\vec{q}\sigma} c_{\vec{k}_2\sigma'}^\dagger c_{\vec{k}_2+\vec{q}\sigma'} = c_{\vec{k}_1\sigma}^\dagger c_{\vec{k}_1-\vec{q}\sigma} c_{\vec{k}_1-\vec{q}\sigma'}^\dagger c_{\vec{k}_1\sigma'} = \\
& = -c_{\vec{k}_1\sigma}^\dagger c_{\vec{k}_1\sigma'}^\dagger c_{\vec{k}_1-\vec{q}\sigma} c_{\vec{k}_1-\vec{q}\sigma'} = -\langle c_{\vec{k}_1\sigma}^\dagger c_{\vec{k}_1\sigma'}^\dagger \rangle c_{\vec{k}_1-\vec{q}\sigma} c_{\vec{k}_1-\vec{q}\sigma'} \\
& - \langle c_{\vec{k}_1-\vec{q}\sigma} c_{\vec{k}_1-\vec{q}\sigma'} \rangle c_{\vec{k}_1\sigma}^\dagger c_{\vec{k}_1\sigma'}^\dagger + \langle c_{\vec{k}_1\sigma}^\dagger c_{\vec{k}_1\sigma'}^\dagger \rangle \langle c_{\vec{k}_1-\vec{q}\sigma} c_{\vec{k}_1-\vec{q}\sigma'} \rangle.
\end{aligned} \tag{2.21}$$

The anomalous averages have also been taken into account apart from the normal averages. The averages which describe the charge ordering (CO) and spin density waves (SDW ordering) have been neglected at this stage of the work. As a result, we obtain the following Hamiltonian in a bilinear form:

$$H = \sum_{\vec{k}\sigma} \bar{\epsilon}_k^\sigma c_{\vec{k}\sigma}^\dagger c_{\vec{k}\sigma} - \sum_{\vec{k}} (\Delta_{\vec{k}} c_{\vec{k}\uparrow}^\dagger c_{-\vec{k}\downarrow}^\dagger + H.c.) - \frac{1}{2} \sum_{\vec{k}\sigma} (\Delta_t^\sigma(\vec{k}) c_{\vec{k}\sigma}^\dagger c_{-\vec{k}\sigma}^\dagger + H.c.) + C, \tag{2.22}$$

where:

$$\bar{\epsilon}_k^\uparrow = \epsilon_k^\uparrow - p_\uparrow W \gamma_{\vec{k}} / \gamma_0 - \bar{\mu}_\uparrow - h, \tag{2.23}$$

$$\bar{\epsilon}_k^\downarrow = \epsilon_k^\downarrow - p_\downarrow W \gamma_{\vec{k}} / \gamma_0 - \bar{\mu}_\downarrow + h, \tag{2.24}$$

$$\bar{\mu}_\uparrow = \mu - U n_\downarrow - W \gamma_0 n, \tag{2.25}$$

$$\bar{\mu}_\downarrow = \mu - U n_\uparrow - W \gamma_0 n, \tag{2.26}$$

$$p_\uparrow = \frac{1}{N} \sum_{\vec{q}} \gamma_{\vec{q}} \langle c_{\vec{q}\uparrow}^\dagger c_{\vec{q}\uparrow} \rangle, \tag{2.27}$$

$$p_\downarrow = \frac{1}{N} \sum_{\vec{q}} \gamma_{\vec{q}} \langle c_{\vec{q}\downarrow}^\dagger c_{\vec{q}\downarrow} \rangle, \tag{2.28}$$

$$\Delta_{\vec{k}} = \frac{1}{N} \sum_{\vec{q}} V_{\vec{k}\vec{q}}^s \langle c_{-\vec{q}\downarrow} c_{\vec{q}\uparrow} \rangle, \tag{2.29}$$

$$V_{\vec{k}\vec{q}}^s = -U - W \gamma_{\vec{k}-\vec{q}}, \tag{2.30}$$

$$\Delta_t^\sigma(\vec{k}) = \frac{1}{N} \sum_{\vec{q}} V_{\vec{k}\vec{q}}^t \langle c_{-\vec{q}\sigma} c_{\vec{q}\sigma} \rangle, \tag{2.31}$$

$$V_{\vec{k}\vec{q}}^t = \frac{1}{2} W (\gamma_{\vec{k}+\vec{q}} - \gamma_{\vec{k}-\vec{q}}), \tag{2.32}$$

$$\begin{aligned}
C &= -\frac{U}{N} \sum_{\vec{k}\vec{q}} \langle c_{\vec{k}\uparrow}^\dagger c_{-\vec{k}\downarrow}^\dagger \rangle \langle c_{\vec{q}\downarrow} c_{-\vec{q}\uparrow} \rangle + \frac{1}{2N} \sum_{\vec{k}\vec{q}\sigma\sigma'} W \gamma_{\vec{k}-\vec{q}} \langle c_{\vec{k}\sigma}^\dagger c_{-\vec{k}\sigma'}^\dagger \rangle \langle c_{-\vec{q}\sigma} c_{\vec{q}\sigma'} \rangle \\
&+ \frac{1}{2N} \sum_{\vec{k}\vec{q}\sigma} W \gamma_{\vec{k}-\vec{q}} \langle c_{\vec{k}\sigma}^\dagger c_{\vec{k}\sigma} \rangle \langle c_{\vec{q}\sigma}^\dagger c_{\vec{q}\sigma} \rangle - UN n_\uparrow n_\downarrow - \frac{1}{2} W \gamma_0 N n^2.
\end{aligned} \tag{2.33}$$

$\Delta_{\vec{k}}$ is the order parameter for the singlet pairing, for which $\langle c_{-\vec{q}\downarrow} c_{\vec{q}\uparrow} \rangle = \langle c_{\vec{q}\downarrow} c_{-\vec{q}\uparrow} \rangle$. $\Delta_t^\sigma(k)$ – the order parameter for the triplet (equal spin) pairing, which describes the p -wave pairing symmetry. In this work we will restrict our analysis to the properties of the singlet pairing.

The following Bogoliubov transformation can be used to transform the Hamiltonian (2.22) to a diagonal form:

$$c_{\vec{k}\uparrow} = u_{\vec{k}}^* \gamma_{\vec{k}0} + \nu_{\vec{k}} \gamma_{\vec{k}1}^\dagger, \tag{2.34}$$

$$c_{-\vec{k}\downarrow}^\dagger = -\nu_{\vec{k}}^* \gamma_{\vec{k}0} + u_{\vec{k}} \gamma_{\vec{k}1}^\dagger. \tag{2.35}$$

The quasiparticle operators $\gamma_{\vec{k}0}$ and $\gamma_{\vec{k}1}$ are also the fermion operators. Therefore, the anticommutation condition takes the form:

$$|u_{\vec{k}}|^2 + |\nu_{\vec{k}}|^2 = 1. \tag{2.36}$$

Then, the Hamiltonian (2.22) can be rewritten:

$$\begin{aligned}
H &= \sum_{\vec{k}} [\bar{\epsilon}_{\vec{k}}^\uparrow (|u_{\vec{k}}|^2 \gamma_{\vec{k}0}^\dagger \gamma_{\vec{k}0} - |\nu_{\vec{k}}|^2 \gamma_{\vec{k}1}^\dagger \gamma_{\vec{k}1}) + \bar{\epsilon}_{\vec{k}}^\downarrow (|\nu_{\vec{k}}|^2 \gamma_{\vec{k}1}^\dagger \gamma_{\vec{k}1} - |u_{\vec{k}}|^2 \gamma_{\vec{k}0}^\dagger \gamma_{\vec{k}0}) \\
&+ (\bar{\epsilon}_{\vec{k}}^\uparrow + \bar{\epsilon}_{\vec{k}}^\downarrow) (\nu_{\vec{k}} u_{\vec{k}} \gamma_{\vec{k}0}^\dagger \gamma_{\vec{k}1}^\dagger + \nu_{\vec{k}}^* u_{\vec{k}}^* \gamma_{\vec{k}1} \gamma_{\vec{k}0}) + |\nu_{\vec{k}}|^2 (\bar{\epsilon}_{\vec{k}}^\uparrow + \bar{\epsilon}_{\vec{k}}^\downarrow)] \\
&+ \sum_{\vec{k}} [(\Delta_{\vec{k}} u_{\vec{k}} \nu_{\vec{k}}^* + \Delta_{\vec{k}}^* u_{\vec{k}}^* \nu_{\vec{k}}) (\gamma_{\vec{k}0}^\dagger \gamma_{\vec{k}0} + \gamma_{\vec{k}1}^\dagger \gamma_{\vec{k}1} - 1) \\
&+ (\Delta_{\vec{k}} \nu_{\vec{k}}^{*2} - \Delta_{\vec{k}}^* u_{\vec{k}}^{*2}) \gamma_{\vec{k}1} \gamma_{\vec{k}0} + (\Delta_{\vec{k}} \nu_{\vec{k}}^2 - \Delta_{\vec{k}}^* u_{\vec{k}}^2) \gamma_{\vec{k}0}^\dagger \gamma_{\vec{k}1}^\dagger].
\end{aligned} \tag{2.37}$$

We equate the non-diagonal terms of the Hamiltonian (2.37) to zero:

$$(\bar{\epsilon}_{\vec{k}}^\uparrow + \bar{\epsilon}_{\vec{k}}^\downarrow) u_{\vec{k}} \nu_{\vec{k}} + \nu_{\vec{k}}^2 \Delta_{\vec{k}}^* - u_{\vec{k}}^2 \Delta_{\vec{k}} = 0. \tag{2.38}$$

Hence:

$$\frac{\nu_{\vec{k}}}{u_{\vec{k}}} \Delta_{\vec{k}}^* = E_{\vec{k}\uparrow} - \bar{\epsilon}_{\vec{k}}^\uparrow = E_{\vec{k}\downarrow} - \bar{\epsilon}_{\vec{k}}^\downarrow, \tag{2.39}$$

where:

$$E_{\vec{k}\uparrow} = \frac{\bar{\epsilon}_{\vec{k}\uparrow} - \bar{\epsilon}_{\vec{k}\downarrow}}{2} + \sqrt{\left(\frac{\bar{\epsilon}_{\vec{k}\uparrow} + \bar{\epsilon}_{\vec{k}\downarrow}}{2}\right)^2 + |\Delta_{\vec{k}}|^2}, \tag{2.40}$$

$$E_{\vec{k}\downarrow} = \frac{\bar{\epsilon}_{\vec{k}\downarrow} - \bar{\epsilon}_{\vec{k}\uparrow}}{2} + \sqrt{\left(\frac{\bar{\epsilon}_{\vec{k}\uparrow} + \bar{\epsilon}_{\vec{k}\downarrow}}{2}\right)^2 + |\Delta_{\vec{k}}|^2}. \tag{2.41}$$

After simple mathematical transformations:

$$E_{\vec{k}\downarrow,\uparrow} = \pm(-t^\downarrow + t^\uparrow)\Theta_{\vec{k}} \pm \frac{UM}{2} \pm \frac{1}{2}W(p_\uparrow - p_\downarrow)\frac{\gamma_{\vec{k}}}{\gamma_0} \pm h + \omega_{\vec{k}}, \quad (2.42)$$

where:

$$\omega_{\vec{k}} = \sqrt{((-t^\uparrow - t^\downarrow)\Theta_{\vec{k}} - \bar{\mu} - p\frac{\gamma_{\vec{k}}}{\gamma_0}W)^2 + |\Delta_{\vec{k}}|^2}, \quad (2.43)$$

$$\bar{\mu} \equiv \frac{\bar{\mu}_\uparrow + \bar{\mu}_\downarrow}{2} = \mu - n(\frac{U}{2} + W\gamma_0), \quad (2.44)$$

$p \equiv \frac{p_\uparrow + p_\downarrow}{2}$, $M = n_\uparrow - n_\downarrow$ is the spin magnetization.

Defining the ratio $r \equiv t^\uparrow/t^\downarrow$, the quasiparticle energies (2.42) can be rewritten as:

$$E_{\vec{k}\downarrow,\uparrow} = \pm\left(\frac{1-r}{1+r}\right)\epsilon_{\vec{k}} \pm \frac{UM}{2} \pm \frac{1}{2}W(p_\uparrow - p_\downarrow)\frac{\gamma_{\vec{k}}}{\gamma_0} \pm h + \omega_{\vec{k}}. \quad (2.45)$$

The condition (2.36) with Eq. (2.39) allow calculation of the coefficients $u_{\vec{k}}$ and $\nu_{\vec{k}}$:

$$|\nu_{\vec{k}}|^2 = \frac{1}{2}\left(1 - \frac{\bar{\epsilon}_{\vec{k}\uparrow} + \bar{\epsilon}_{\vec{k}\downarrow}}{E_{\vec{k}\uparrow} + E_{\vec{k}\downarrow}}\right), \quad (2.46)$$

$$|u_{\vec{k}}|^2 = \frac{1}{2}\left(1 + \frac{\bar{\epsilon}_{\vec{k}\uparrow} + \bar{\epsilon}_{\vec{k}\downarrow}}{E_{\vec{k}\uparrow} + E_{\vec{k}\downarrow}}\right). \quad (2.47)$$

The remaining terms of the Hamiltonian (2.37) are reduced to:

$$H = \frac{1}{2} \sum_{\vec{k}} [(\bar{\epsilon}_{\vec{k}}^\uparrow + \bar{\epsilon}_{\vec{k}}^\downarrow) - (E_{\vec{k}\uparrow} + E_{\vec{k}\downarrow})] + \sum_{\vec{k}} [E_{\vec{k}\uparrow}\gamma_{\vec{k}0}^\dagger\gamma_{\vec{k}0} + E_{\vec{k}\downarrow}\gamma_{\vec{k}1}^\dagger\gamma_{\vec{k}1}] + C. \quad (2.48)$$

Knowing the coefficients $|u_{\vec{k}}|^2$ and $|\nu_{\vec{k}}|^2$, one can calculate the operator averages:

$$\langle c_{\vec{k}\uparrow}^\dagger c_{\vec{k}\uparrow} \rangle = |\nu_{\vec{k}}|^2 + \langle |u_{\vec{k}}|^2 \gamma_{\vec{k}0}^\dagger \gamma_{\vec{k}0} - |\nu_{\vec{k}}|^2 \gamma_{\vec{k}1}^\dagger \gamma_{\vec{k}1} \rangle. \quad (2.49)$$

Now, we substitute: $\langle \gamma_{\vec{k}0}^\dagger \gamma_{\vec{k}0} \rangle$ and $\langle \gamma_{\vec{k}1}^\dagger \gamma_{\vec{k}1} \rangle$ with the Fermi-Dirac distribution functions: $f(E_{\vec{k}\uparrow}) = 1/(e^{\beta E_{\vec{k}\uparrow}} + 1)$, $f(E_{\vec{k}\downarrow}) = 1/(e^{\beta E_{\vec{k}\downarrow}} + 1)$, respectively, where $\beta = 1/k_B T$. We obtain:

$$\langle c_{\vec{k}\uparrow}^\dagger c_{\vec{k}\uparrow} \rangle = |\nu_{\vec{k}}|^2 f(-E_{\vec{k}\downarrow}) + |u_{\vec{k}}|^2 f(E_{\vec{k}\uparrow}). \quad (2.50)$$

In a similar way:

$$\langle c_{\vec{k}\downarrow}^\dagger c_{\vec{k}\downarrow} \rangle = |u_{\vec{k}}|^2 f(-E_{\vec{k}\uparrow}) + |\nu_{\vec{k}}|^2 f(E_{\vec{k}\downarrow}). \quad (2.51)$$

These two expressions ((2.50)-(2.51)) can be written as:

$$n_\sigma = \frac{1}{N} \sum_{\vec{k}} \langle c_{\vec{k}\sigma}^\dagger c_{\vec{k}\sigma} \rangle = \frac{1}{N} \sum_{\vec{k}} (|u_{\vec{k}}|^2 f(E_{\vec{k},\sigma}) + |\nu_{\vec{k}}|^2 f(-E_{\vec{k},-\sigma})). \quad (2.52)$$

After simple transformations, the particle number equation takes the form:

$$n = 1 - \frac{1}{2N} \sum_{\vec{k}} \frac{-(t^\uparrow + t^\downarrow)\Theta_{\vec{k}} - \bar{\mu} - p\frac{\gamma_{\vec{k}}}{\gamma_0}W}{\omega_{\vec{k}}} \left(\tanh \frac{\beta E_{\vec{k}\uparrow}}{2} + \tanh \frac{\beta E_{\vec{k}\downarrow}}{2} \right), \quad (2.53)$$

where: $n = n_\uparrow + n_\downarrow$.

The equation for the magnetization is:

$$M = \frac{1}{2N} \sum_{\vec{k}} \left(\tanh \frac{\beta E_{\vec{k}\downarrow}}{2} - \tanh \frac{\beta E_{\vec{k}\uparrow}}{2} \right). \quad (2.54)$$

After calculating the anomalous averages, one obtains the following equation for the superconducting gap parameter:

$$\Delta_{\vec{k}} = \frac{1}{N} \sum_{\vec{q}} V_{\vec{k}\vec{q}}^s \Delta_{\vec{q}} F_{\vec{q}}(T), \quad (2.55)$$

where:

$$F_{\vec{q}}(T) = (2\omega_{\vec{q}})^{-1} \frac{1}{2} \left(\tanh \frac{\beta E_{\vec{q}\uparrow}}{2} + \tanh \frac{\beta E_{\vec{q}\downarrow}}{2} \right). \quad (2.56)$$

The pairing potential $V_{\vec{k}\vec{q}}^s$ can be separated for the two-dimensional square lattice into:

$$V_{\vec{k}\vec{q}}^s = -U + \frac{|W|}{4} (\gamma_{\vec{k}}\gamma_{\vec{q}} + \eta_{\vec{k}}\eta_{\vec{q}}) + 2|W|(\sin k_x \sin q_x + \sin k_y \sin q_y), \quad (2.57)$$

where: $\gamma_{\vec{k}} = 2(\cos k_x + \cos k_y)$, while $\eta_{\vec{k}} = 2(\cos k_x - \cos k_y)$.

Eq. (2.55) is separated into parts corresponding to the s , $s_{x^2+y^2}$ and $d_{x^2-y^2}$ pairing symmetry.

In this way:

$$\Delta_{\vec{k}} = \Delta_0 + \Delta_\gamma \gamma_{\vec{k}} + \Delta_\eta \eta_{\vec{k}}. \quad (2.58)$$

The self-consistent equations take the form:

$$\Delta_0 = -U\phi_1, \quad (2.59)$$

$$\Delta_\gamma = \frac{|W|}{4} \phi_\gamma \quad (2.60)$$

for the s -wave pairing symmetry, and:

$$\Delta_\eta = \frac{|W|}{4} \phi_\eta \quad (2.61)$$

for the d -wave pairing symmetry,

where:

$$\phi_1 = \frac{1}{N} \sum_{\vec{q}} \Delta_{\vec{q}} F_{\vec{q}}, \quad (2.62)$$

$$\phi_\gamma = \frac{1}{N} \sum_{\vec{q}} \Delta_{\vec{q}} \gamma_{\vec{q}} F_{\vec{q}}, \quad (2.63)$$

$$\phi_\eta = \frac{1}{N} \sum_{\vec{q}} \Delta_{\vec{q}} \eta_{\vec{q}} F_{\vec{q}}. \quad (2.64)$$

Inserting to the self-consistent equations (2.59), (2.60) and (2.61) the expression (2.58), we obtain a system of equations for the $s_{x^2+y^2}$ pairing:

$$\begin{pmatrix} 1 + U\phi_1(T) & U\phi_2(T) \\ -\frac{|W|}{4}\phi_2(T) & 1 - \frac{|W|}{4}\phi_\gamma(T) \end{pmatrix} \begin{pmatrix} \Delta_0 \\ \Delta_\gamma \end{pmatrix} = 0, \quad (2.65)$$

where:

$$\phi_1(T) = \frac{1}{N} \sum_{\vec{q}} F_{\vec{q}}(T), \quad (2.66)$$

$$\phi_2(T) = \frac{1}{N} \sum_{\vec{q}} \gamma_{\vec{q}} F_{\vec{q}}(T), \quad (2.67)$$

$$\phi_\gamma(T) = \frac{1}{N} \sum_{\vec{q}} \gamma_{\vec{q}}^2 F_{\vec{q}}(T). \quad (2.68)$$

For the d -wave pairing:

$$\frac{4}{|W|} = \frac{1}{N} \sum_{\vec{q}} \eta_{\vec{q}}^2 F_{\vec{q}}(T). \quad (2.69)$$

From these equations, the value of the order parameter for different types of pairing and the transition temperature can be determined.

As follows from eq. (2.65), the solution for the $s_{x^2+y^2}$ pairing depends both on U and on $|W|$. However, the solution (2.69) for the d -wave pairing is formally independent of U . Substitution of the form (2.58) neglects the relative phases of d - and s -waves order parameters and therefore it is not the most general. Such a coupling of phases can be relevant when we consider the mixed phases $s-d$ below the critical temperature [87].

The equations for the Fock parameters (2.27), (2.28) take the form:

$$p_\uparrow = \frac{1}{N} \sum_{\vec{q}} \frac{1}{2} \gamma_{\vec{q}} \left(|\nu_{\vec{q}}|^2 \tanh \frac{\beta E_{\vec{q}\downarrow}}{2} - |u_{\vec{q}}|^2 \tanh \frac{\beta E_{\vec{q}\uparrow}}{2} \right), \quad (2.70)$$

$$p_\downarrow = \frac{1}{N} \sum_{\vec{q}} \frac{1}{2} \gamma_{\vec{q}} \left(|\nu_{\vec{q}}|^2 \tanh \frac{\beta E_{\vec{q}\uparrow}}{2} - |u_{\vec{q}}|^2 \tanh \frac{\beta E_{\vec{q}\downarrow}}{2} \right). \quad (2.71)$$

If $p \equiv (p_\uparrow + p_\downarrow)/2$, we obtain:

$$p = -\frac{1}{N} \sum_{\vec{q}} \frac{1}{2} \gamma_{\vec{q}} \frac{-(t^\uparrow + t^\downarrow) \Theta_{\vec{q}} - \bar{\mu} - p_{\gamma_0}^{\gamma_{\vec{q}}} W}{\omega_{\vec{q}}} \left(\tanh \frac{\beta E_{\vec{q}\uparrow}}{2} + \tanh \frac{\beta E_{\vec{q}\downarrow}}{2} \right). \quad (2.72)$$

From the partition function, one can determine the grand canonical potential of the superconducting state:

$$\begin{aligned}
\frac{\Omega^{SC}}{N} &= \frac{1}{4}Un(2-n) - \mu + \frac{1}{4}UM^2 + W\gamma_0n - \frac{1}{2}W\gamma_0n^2 - Wp_{\uparrow}^2/2\gamma_0 - Wp_{\downarrow}^2/2\gamma_0 \\
&+ \frac{1}{N} \sum_{\vec{k}} \frac{|\Delta_{\vec{k}}|^2}{2\omega_{\vec{k}}} \frac{1}{2} \left(\tanh \frac{\beta E_{\vec{k}\uparrow}}{2} + \tanh \frac{\beta E_{\vec{k}\downarrow}}{2} \right) \\
&- \frac{1}{\beta N} \sum_{\vec{k}} \ln \left(2 \cosh \frac{\beta(E_{\vec{k}\uparrow} + E_{\vec{k}\downarrow})}{2} + 2 \cosh \frac{\beta(-E_{\vec{k}\uparrow} + E_{\vec{k}\downarrow})}{2} \right), \tag{2.73}
\end{aligned}$$

and also the free energy: $F^{SC}/N = \Omega^{SC}/N + \mu n$.

The equations for the superconducting gap parameter (2.55), the number of particles (determining μ) (2.53) and the magnetization (2.54) satisfy the following extremum conditions: $\frac{\partial F}{\partial \Delta} = 0$, $\frac{\partial F}{\partial \mu} = 0$, $M = -\frac{1}{N} \frac{\partial F}{\partial h}$, respectively.

The above equations take into account the spin polarization in the presence of a magnetic field and spin-dependent hopping ($t^{\uparrow} \neq t^{\downarrow}$) [75, 88]. This method includes the spin-dependent Hartree term and can be called the BCS-Stoner approach.

The equations for the normal phase ($\Delta = 0$) have the following form:

$$n = 1 - \frac{1}{2N} \sum_{\vec{k}} \left(\tanh \frac{\beta E_{\vec{k}\uparrow}^{NO}}{2} + \tanh \frac{\beta E_{\vec{k}\downarrow}^{NO}}{2} \right), \tag{2.74}$$

$$M = \frac{1}{2N} \sum_{\vec{k}} \left(\tanh \frac{\beta E_{\vec{k}\downarrow}^{NO}}{2} - \tanh \frac{\beta E_{\vec{k}\uparrow}^{NO}}{2} \right), \tag{2.75}$$

$$p = -\frac{1}{N} \sum_{\vec{k}} \frac{1}{2} \gamma_{\vec{k}} \left(\tanh \frac{\beta E_{\vec{k}\uparrow}^{NO}}{2} + \tanh \frac{\beta E_{\vec{k}\downarrow}^{NO}}{2} \right), \tag{2.76}$$

$$\begin{aligned}
\frac{\Omega^{NO}}{N} &= \frac{1}{4}Un(2-n) - \mu + \frac{1}{4}UM^2 + W\gamma_0n - \frac{1}{2}W\gamma_0n^2 \\
&- Wp_{\uparrow}^2/2\gamma_0 - Wp_{\downarrow}^2/2\gamma_0 - \frac{1}{\beta N} \sum_{\vec{k}} \ln \left(2 \cosh \frac{\beta(E_{\vec{k}\uparrow}^{NO} + E_{\vec{k}\downarrow}^{NO})}{2} \right) \\
&- \frac{1}{\beta N} \sum_{\vec{k}} \ln \left(2 \cosh \frac{\beta(-E_{\vec{k}\uparrow}^{NO} + E_{\vec{k}\downarrow}^{NO})}{2} \right), \tag{2.77}
\end{aligned}$$

where:

$$E_{\vec{k}\downarrow,\uparrow}^{NO} = \pm(-t^{\downarrow} + t^{\uparrow})\Theta_{\vec{k}} \pm \frac{UM}{2} \pm \frac{1}{2}W(p_{\uparrow} - p_{\downarrow})\frac{\gamma_{\vec{k}}}{\gamma_0} \pm h + \omega_{\vec{k}}^{NO}, \tag{2.78}$$

$$\omega_{\vec{k}}^{NO} = (-t^{\uparrow} - t^{\downarrow})\Theta_{\vec{k}} - \bar{\mu} - p\frac{\gamma_{\vec{k}}}{\gamma_0}W. \quad (2.79)$$

The equations for the superconducting gap parameter, the number of particles, the magnetization, the Fock parameter and the grand canonical potential at $T = 0$, both in the superconducting and in the normal state are presented in Appendix B.

Chapter 3

Kosterlitz-Thouless Transition

A two-dimensional superconductor at $h = 0$ can be classified in the same universality class as a 2D superfluid system or the 2D XY model. In these cases, no phase transition exists above $T = 0$, understood as the disappearance of a long-range order [89, 90]. However, there is some evidence that a **topological ordering** can occur in these systems [91, 92].

In the 2D XY model, the **Kosterlitz-Thouless (KT) transition** [91, 92] from the disordered to a topologically ordered system takes place. Below the KT transition temperature (T_c^{KT}), the system has a quasi-long-range (algebraic) order, which is characterized by a power law decay of the order parameter correlation function and non-zero superfluid stiffness (ρ_s). Below T_c^{KT} , bound vortex-antivortex pairs exist. These pairs get unbound when temperature increases above T_c^{KT} .

3.1 The XY model

As mentioned before, in statistical physics, the two-dimensional XY model is a good example of a system which does not have a long-range order (LRO), because it is unstable due to the low-energy excitations of spin waves at only finite temperatures [89]. This model is a system of spins which can rotate in the plane of the lattice and is defined by the Hamiltonian:

$$H = -J \sum_{\langle ij \rangle} \vec{S}_i \cdot \vec{S}_j = -J \sum_{\langle ij \rangle} \cos(\phi_i - \phi_j), \quad (3.1)$$

where: $J > 0$ – spin coupling constant, $\sum_{\langle ij \rangle}$ – sum over nearest neighbors. In its classical version, the spins \vec{S} are vectors of length 1 oriented in the $x - y$ plane, ϕ_i – angle between the i -th spin and the x axis. The spins are located in the nodes of the square lattice with lattice spacing a .

The XY model exhibits specific symmetries, which make it possible to study the ferro- and antiferromagnetic ordering. This model is also used to describe such systems as: (a) superconducting materials, (b) thin superfluid helium films [93], (c) Josephson junctions [94], (d) gaseous and liquid crystal systems, (e) melting in 2D (dislocations).

It is worth noting that the Hamiltonian (3.1) has a rotational symmetry, i.e.: the transformation $\phi_i \rightarrow \phi_i + \phi_0$, for all i leaves the Hamiltonian invariant.

At high temperatures, more spins flip randomly, because the interactions between the spins are weak compared to the thermal energy. As a consequence, the system is in a disordered state. At $T = 0$, all the spins align along a given direction. At low temperatures, the spins fluctuate weakly around this direction. If $|\phi_i - \phi_j| \ll 2\pi$ (the spin-wave approximation), the Hamiltonian (3.1) takes the form:

$$H = -\frac{zNJ}{2} + \frac{1}{2}J \sum_{\langle ij \rangle} (\phi_i - \phi_j)^2 = E_0 + \frac{1}{4}J \sum_{\vec{r}, \vec{a}} (\phi(\vec{r} + \vec{a}) - \phi(\vec{r}))^2, \quad (3.2)$$

where: z – the number of nearest neighbors, E_0 – the ground state energy. The sum over \vec{a} – the sum over nearest neighbors of site \vec{r} . If $\phi(\vec{r})$ does not vary a lot from site to site, one can write the Hamiltonian (3.2) in the continuum limit:

$$H = E_0 + \frac{1}{2}J \int d^2\vec{r} (\vec{\nabla} \phi(\vec{r}))^2, \quad (3.3)$$

where the finite differences and the sum over lattice sites in (3.2) are replaced by derivatives and an integral, respectively. The second term is the spin-wave energy.

Let us calculate the spin-spin correlation function:

$$g(r) = \langle \vec{S}(\vec{r}) \cdot \vec{S}(0) \rangle = \langle \exp(i(\phi(\vec{r}) - \phi(0))) \rangle, \quad (3.4)$$

where $\langle \dots \rangle$ is the thermal average.

In high temperatures, the correlation function takes the form: $g(r) \sim \exp(-r/\xi(T))$. It decays exponentially to zero at large distances and the system is disordered. On the other hand, if the correlation function decays to a constant value at $r \rightarrow \infty$, the system exhibits LRO.

At low temperatures, by using the spin-wave approximation (3.3), we find the correlation function which decays with the power law:

$$g(r) = \left(\frac{a}{\pi r} \right)^{\eta(T)}, \quad (3.5)$$

where: $\eta(T) = k_B T / 2J\pi$. This kind of ordering in the system, characterized by a power-law decay of the correlation function, is called the quasi-long-range order (qLRO). Therefore, there must exist some excitations in the system which can bring the system from its low-temperature phase to the high-temperature state.

In 1972, Kosterlitz and Thouless proposed a scenario in which these new excitations (called vortices) are unbound above the critical temperature T_c^{KT} . On the other hand, the vortices form tightly bound pairs at $T < T_c^{KT}$. It is worth emphasizing that the vortices can be positively or negatively charged (i.e. vortices or antivortices).

Let us consider an isolated vortex. In the continuum approximation $\phi(r, \theta) = n\theta$, where $\phi(r, \theta)$ – the spin orientation at a polar coordinates r, θ and n – the strength of

the vortex. Then: $\int d\vec{l} \cdot \nabla\phi = 2n\pi$ and $\nabla\phi = \frac{n}{r}$. One can easily show that the energy of the system with an isolated vortex takes the form:

$$E = \pi J n^2 \ln\left(\frac{L}{a}\right), \quad (3.6)$$

where L is the radius of the system. Therefore, the energy of the vortex increases logarithmically with the size of the system and is infinite in the thermodynamic limit.

In turn, the energy of the vortex-antivortex pair is given by:

$$E_{pair}(\vec{r}_1, \vec{r}_2) = -2\pi n_1 n_2 \ln \frac{|\vec{r}_1 - \vec{r}_2|}{a}, \quad (3.7)$$

where: n_1, n_2 – the strengths of the vortices. One can easily notice that the energy of an isolated vortex (3.6) is higher than the energy of the vortex-antivortex pair (3.7) if the radius of the system is much larger than the distance between two vortices which are oppositely charged. It means that the existence of bound vortex pairs is energetically favorable in low temperatures. However, vortex pair unbinding is much easier at a higher temperature, because of the thermal energy.

The entropy of an isolated vortex is given by:

$$S = k_B \ln\left(\frac{L}{a}\right)^2. \quad (3.8)$$

Then, the free energy of the system with an isolated vortex takes the form:

$$F = E - TS \approx (\pi J n^2 - 2k_B T) \ln\left(\frac{L}{a}\right). \quad (3.9)$$

As we can see, for:

$$k_B T_c = \frac{\pi}{2} J \quad (3.10)$$

the free energy changes its sign. Obviously, the free energy becomes more negative with increasing temperature. For sufficiently high T , the vortex-antivortex pairs are destroyed by the thermal energy.

3.2 The Kosterlitz-Thouless critical temperature determination

In Sec. 3.1 it has been shown that T_c^{KT} in the XY model is expressed by eq. (3.10).

As mentioned before, there is experimental evidence which confirms the nature of the phase transition in thin films of ^4He . It is worth mentioning that the experimental situation in trapped gases is different from theoretical predictions. Because of the presence of a trapping potential, the system is not uniform. Hence, the Bose-Einstein condensation is possible to occur in 2D systems [95, 96]. However, the KT transition is also observed in trapped systems [97, 98]. Recent works of the experimental group from Paris [99, 100]

have reported the observation of the KT transition in a trapped quantum degenerate gas of ^{87}Rb .

The attractive Hubbard Model, which describes the isotropic superconductivity, can be mapped into the XY model by means of the functional integration method [101, 102]. As mentioned above, the two-dimensional superconductor at $h = 0$ can be classified in the same universality class as a 2D superfluid system or the 2D XY model. Therefore, the KT temperature can be determined in the same way as in the previous case. Then, the KT critical temperature in the superconducting system takes the form [103]:

$$k_B T_c^{KT} = \frac{\pi \hbar^2 n_s^*}{2m^*} = \frac{\pi \rho_s (T_c^{KT})}{2}, \quad (3.11)$$

where: $n_s^* = n_s/2$ – the number of pairs in the condensate, $m^* = 2m$ – the mass of the pair, n_s – the density of the superconductor electrons, m – the mass of the electron, $\rho_s(T)$ – the superfluid density or the phase stiffness. ρ_s is equivalent of the spin stiffness in the XY model [104, 105].

The superfluid stiffness (or helicity modulus) can be determined from the change in the grand canonical potential ($\Omega_{\vec{q}}$) of the system in the response to the order parameter twist [106, 107, 108]. For this purpose, we have to determine $\Omega_{\vec{q}}$ with the phase twist.

We assume that the fluctuations of the order parameter are specified by the formula:

$$\Delta_l = |\Delta_l| e^{2i\vec{q} \cdot \vec{R}_l}, \quad (3.12)$$

where \vec{q} is the twist vector, \vec{R}_l – the position vector of site l . Then, the effective Hamiltonian (2.22) takes the form:

$$H_{eff} = \sum_{\vec{k}\sigma} \xi_{\vec{k}+\vec{q}}^\sigma c_{\vec{k}\sigma}^\dagger c_{\vec{k}\sigma} - \sum_{\vec{k}} (|\Delta| c_{\vec{k}\uparrow}^\dagger c_{-\vec{k}\downarrow}^\dagger + |\Delta| c_{-\vec{k}\downarrow} c_{\vec{k}\uparrow}) + C, \quad (3.13)$$

where: $\xi_{\vec{k}+\vec{q}}^{\downarrow,\uparrow} = \epsilon_{\vec{k}+\vec{q}}^{\downarrow,\uparrow} - \bar{\mu}_{\downarrow,\uparrow} \pm h$. We do not take into account the Fock term in further calculations.

The above Hamiltonian can be written as:

$$H_{eff} = \sum_{\vec{k}} \Psi_{\vec{k}}^\dagger \hat{M}_{\vec{k},\vec{q}} \Psi_{\vec{k}} + \sum_{\vec{k}} (\xi_{\vec{q}-\vec{k}}^\uparrow + \xi_{\vec{q}-\vec{k}}^\downarrow), \quad (3.14)$$

where: the matrix $\hat{M}_{\vec{k},\vec{q}}$:

$$\hat{M}_{\vec{k},\vec{q}} = \begin{pmatrix} \xi_{\vec{k}+\vec{q}}^\uparrow & -|\Delta| & 0 & 0 \\ -|\Delta|^* & -\xi_{\vec{q}-\vec{k}}^\downarrow & 0 & 0 \\ 0 & 0 & \xi_{\vec{k}+\vec{q}}^\downarrow & |\Delta| \\ 0 & 0 & |\Delta| & -\xi_{\vec{q}-\vec{k}}^\uparrow \end{pmatrix}, \quad (3.15)$$

the operator Ψ :

$$\Psi_{\vec{k}} = \begin{pmatrix} c_{\vec{k}\uparrow} \\ c_{-\vec{k}\downarrow}^\dagger \\ c_{\vec{k}\downarrow} \\ c_{-\vec{k}\uparrow}^\dagger \end{pmatrix}. \quad (3.16)$$

$\hat{M}_{\vec{k},\vec{q}}$ is a block diagonal matrix. To determine the quasiparticle energies (eigenvalues of the matrix $\hat{M}_{\vec{k},\vec{q}}$), we solve the equations:

$$\det \begin{pmatrix} \xi_{\vec{k}+\vec{q}}^\uparrow - E & -|\Delta| \\ -|\Delta|^* & -\xi_{\vec{q}-\vec{k}}^\downarrow - E \end{pmatrix} = 0, \quad (3.17)$$

$$\det \begin{pmatrix} \xi_{\vec{k}+\vec{q}}^\downarrow - E & |\Delta| \\ |\Delta| & -\xi_{\vec{q}-\vec{k}}^\uparrow - E \end{pmatrix} = 0. \quad (3.18)$$

As a result, we get:

$$E_{1,2}(\vec{k}, \vec{q}) = \frac{\xi_{\vec{k}+\vec{q}}^\uparrow - \xi_{\vec{q}-\vec{k}}^\downarrow}{2} \pm \sqrt{\left(\frac{\xi_{\vec{k}+\vec{q}}^\uparrow + \xi_{\vec{q}-\vec{k}}^\downarrow}{2}\right)^2 + |\Delta|^2}, \quad (3.19)$$

$$E_{3,4}(\vec{k}, \vec{q}) = \frac{\xi_{\vec{k}+\vec{q}}^\downarrow - \xi_{\vec{q}-\vec{k}}^\uparrow}{2} \pm \sqrt{\left(\frac{\xi_{\vec{k}+\vec{q}}^\uparrow + \xi_{\vec{q}-\vec{k}}^\downarrow}{2}\right)^2 + |\Delta|^2}, \quad (3.20)$$

It is easy to show that: $E_2(-\vec{k}, \vec{q}) = -E_3(\vec{k}, \vec{q})$ and $E_4(-\vec{k}, \vec{q}) = -E_1(\vec{k}, \vec{q})$.

After some transformations, the grand canonical potential with the phase twist takes the form:

$$\begin{aligned} \frac{\Omega_{\vec{q}}}{N} &= \frac{1}{N} \sum_{\vec{k} > 0} (\xi_{\vec{q}-\vec{k}}^\uparrow + \xi_{\vec{q}-\vec{k}}^\downarrow) - \frac{1}{\beta N} \sum_{\vec{k}} \ln \left[2 \cosh \left(\frac{\beta E_1(\vec{k}, \vec{q})}{2} \right) \right] \\ &- \frac{1}{\beta N} \sum_{\vec{k}} \ln \left[2 \cosh \left(\frac{\beta E_3(\vec{k}, \vec{q})}{2} \right) \right] + C, \end{aligned} \quad (3.21)$$

where C is a constant.

We Taylor-expand $\Omega_{\vec{q}}$ up to the q^2 term:

$$\frac{\Omega_{\vec{q}}}{N} = \frac{\Omega_{\vec{q}=0}}{N} + 2\rho_s q^2 + O(q^4). \quad (3.22)$$

On the other hand:

$$\Omega_{\vec{q}} = \Omega_{\vec{q}=0} + \frac{1}{2} q_x^2 \frac{\partial^2 \Omega_{\vec{q}}}{\partial q_x^2} + \frac{1}{2} q_y^2 \frac{\partial^2 \Omega_{\vec{q}}}{\partial q_y^2} + O(q^4). \quad (3.23)$$

On the square lattice $\frac{\partial^2 \Omega_{\vec{q}}}{\partial q_x^2} = \frac{\partial^2 \Omega_{\vec{q}}}{\partial q_y^2}$ and hence:

$$\Omega_{\vec{q}} = \Omega_{\vec{q}=0} + \frac{1}{2} q^2 \frac{\partial^2 \Omega_{\vec{q}}}{\partial q_x^2} + O(q^4). \quad (3.24)$$

Comparing the coefficients of q^2 in (3.23) and (3.24), we get:

$$2\rho_s = \frac{1}{2} \frac{\partial^2 \Omega_{\vec{q}}}{\partial q_x^2} \Big|_{\vec{q}=0}. \quad (3.25)$$

Calculating this derivative explicitly yields:

$$\begin{aligned} \rho_s(T) = & \frac{1}{4N} \sum_{\vec{k}} \left\{ \frac{\partial^2 \epsilon_{\vec{k}}^+}{\partial k_x^2} - \frac{1}{2} \left[\frac{\partial^2 \epsilon_{\vec{k}}^-}{\partial k_x^2} + \frac{\epsilon_{\vec{k}}^+}{\omega_{\vec{k}}} \left(\frac{\partial^2 \epsilon_{\vec{k}}^+}{\partial k_x^2} \right) + \left(\frac{\partial \epsilon_{\vec{k}}^-}{\partial k_x} \right)^2 \frac{|\Delta|^2}{\omega_{\vec{k}}^3} \right] \tanh \left(\frac{\beta E_{\vec{k}\uparrow}}{2} \right) \right. \\ & + \frac{1}{2} \left[\frac{\partial^2 \epsilon_{\vec{k}}^-}{\partial k_x^2} - \frac{\epsilon_{\vec{k}}^+}{\omega_{\vec{k}}} \left(\frac{\partial^2 \epsilon_{\vec{k}}^+}{\partial k_x^2} \right) - \left(\frac{\partial \epsilon_{\vec{k}}^-}{\partial k_x} \right)^2 \frac{|\Delta|^2}{\omega_{\vec{k}}^3} \right] \tanh \left(\frac{\beta E_{\vec{k}\downarrow}}{2} \right) \\ & \left. + \left[\frac{\partial \epsilon_{\vec{k}}^+}{\partial k_x} + \frac{\epsilon_{\vec{k}}^+}{\omega_{\vec{k}}} \left(\frac{\partial \epsilon_{\vec{k}}^-}{\partial k_x} \right) \right]^2 \frac{\partial f(E_{\vec{k}\uparrow})}{\partial E_{\vec{k}\uparrow}} + \left[\frac{\partial \epsilon_{\vec{k}}^+}{\partial k_x} - \frac{\epsilon_{\vec{k}}^+}{\omega_{\vec{k}}} \left(\frac{\partial \epsilon_{\vec{k}}^-}{\partial k_x} \right) \right]^2 \frac{\partial f(E_{\vec{k}\downarrow})}{\partial E_{\vec{k}\downarrow}} \right\}, \quad (3.26) \end{aligned}$$

where: $\epsilon_{\vec{k}}^+ = \frac{\xi_{\vec{k}\uparrow} + \xi_{\vec{k}\downarrow}}{2}$, $\epsilon_{\vec{k}}^- = \frac{\xi_{\vec{k}\uparrow} - \xi_{\vec{k}\downarrow}}{2}$, $\omega_{\vec{k}} = \sqrt{\epsilon_{\vec{k}}^2 + |\Delta|^2}$. Then, evaluating the derivatives with respect to k_x and using the trigonometric identities:

$$\tanh \left(\frac{x}{2} \right) \pm \tanh \left(\frac{y}{2} \right) = \frac{\sinh \left(\frac{x \pm y}{2} \right)}{\cosh \left(\frac{x}{2} \right) \cosh \left(\frac{y}{2} \right)}, \quad (3.27)$$

$$\frac{1}{\cosh^2 \left(\frac{x}{2} \right)} + \frac{1}{\cosh^2 \left(\frac{y}{2} \right)} = \frac{4 \left(1 + \cosh \left(\frac{x+y}{2} \right) \cosh \left(\frac{x-y}{2} \right) \right)}{\left(\cosh \left(\frac{x+y}{2} \right) + \cosh \left(\frac{x-y}{2} \right) \right)^2}, \quad (3.28)$$

$$\frac{1}{\cosh^2 \left(\frac{x}{2} \right)} - \frac{1}{\cosh^2 \left(\frac{y}{2} \right)} = \frac{4 \sinh \left(\frac{x+y}{2} \right) \sinh \left(\frac{y-x}{2} \right)}{\left(\cosh \left(\frac{x+y}{2} \right) + \cosh \left(\frac{x-y}{2} \right) \right)^2}, \quad (3.29)$$

the superfluid stiffness (3.26) can be rewritten as:

$$\begin{aligned}
\rho_s(T) = & \frac{1}{4N} \sum_{\vec{k}} \left((t^\uparrow \cos k_x - t^\downarrow \cos k_x) X_{\vec{k}}^a - \left(\frac{\xi_{\vec{k}\uparrow} + \xi_{\vec{k}\downarrow}}{2\omega_{\vec{k}}} (t^\uparrow \cos k_x + t^\downarrow \cos k_x) \right. \right. \\
& + (t^\uparrow \sin k_x - t^\downarrow \sin k_x)^2 \frac{|\Delta|^2}{\omega_{\vec{k}}^3} \Big) X_{\vec{k}}^b \\
& - \left((t^\uparrow \sin k_x + t^\downarrow \sin k_x)^2 + \left(\frac{\xi_{\vec{k}\uparrow} + \xi_{\vec{k}\downarrow}}{2\omega_{\vec{k}}} \right)^2 (t^\uparrow \sin k_x - t^\downarrow \sin k_x)^2 \right) Y_{\vec{k}}^a \\
& + 2 \left(\frac{\xi_{\vec{k}\uparrow} + \xi_{\vec{k}\downarrow}}{2\omega_{\vec{k}}} \right) ((t^\uparrow \sin k_x)^2 - (t^\downarrow \sin k_x)^2) Y_{\vec{k}}^b \Big), \tag{3.30}
\end{aligned}$$

where:

$$X_{\vec{k}}^a = \frac{\sinh(\beta\omega_{\vec{k}})}{\cosh(\beta((-t^\downarrow + t^\uparrow)\Theta_{\vec{k}} + h + \frac{UM}{2})) + \cosh(\beta\omega_{\vec{k}})}, \tag{3.31}$$

$$X_{\vec{k}}^b = \frac{\sinh(\beta((-t^\downarrow + t^\uparrow)\Theta_{\vec{k}}h + \frac{UM}{2}))}{\cosh(\beta((-t^\downarrow + t^\uparrow)\Theta_{\vec{k}} + h + \frac{UM}{2})) + \cosh(\beta\omega_{\vec{k}})}, \tag{3.32}$$

$$Y_{\vec{k}}^a = \beta \frac{\cosh(\beta((-t^\downarrow + t^\uparrow)\Theta_{\vec{k}} + h + \frac{UM}{2})) \cosh(\beta\omega_{\vec{k}}) + 1}{(\cosh(\beta((-t^\downarrow + t^\uparrow)\Theta_{\vec{k}} + h + \frac{UM}{2})) + \cosh(\beta\omega_{\vec{k}}))^2}, \tag{3.33}$$

$$Y_{\vec{k}}^b = \beta \frac{\sinh(\beta((-t^\downarrow + t^\uparrow)\Theta_{\vec{k}} + h + \frac{UM}{2})) \sinh(\beta\omega_{\vec{k}})}{(\cosh(\beta((-t^\downarrow + t^\uparrow)\Theta_{\vec{k}} + h + \frac{UM}{2})) + \cosh(\beta\omega_{\vec{k}}))^2}, \tag{3.34}$$

Δ , M , μ are found from a set of self-consistent equations (2.53)-(2.55).

If $t^\uparrow = t^\downarrow$, eq. (3.26) reduces to:

$$\begin{aligned}
\rho_s = & \frac{1}{4N} \sum_{\vec{k}} \left\{ \frac{\partial^2 \epsilon_{\vec{k}}}{\partial k_x^2} \left[1 - \frac{\bar{\epsilon}_{\vec{k}}}{2\omega_{\vec{k}}} \left(\tanh\left(\frac{\beta E_{\vec{k}\uparrow}}{2}\right) + \tanh\left(\frac{\beta E_{\vec{k}\downarrow}}{2}\right) \right) \right] + \right. \\
& + \left. \left(\frac{\partial \epsilon_{\vec{k}}}{\partial k_x} \right)^2 \left[\frac{\partial f(E_{\vec{k}\uparrow})}{\partial E_{\vec{k}\uparrow}} + \frac{\partial f(E_{\vec{k}\downarrow})}{\partial E_{\vec{k}\downarrow}} \right] \right\}, \tag{3.35}
\end{aligned}$$

where: $\bar{\epsilon}_{\vec{k}} = \epsilon_{\vec{k}} - \bar{\mu}$, $E_{\vec{k}\downarrow, \uparrow} = \pm \frac{UM}{2} \pm h + \omega_{\vec{k}}$.

Expression (3.35) can be written in a simple form:

$$\rho_s(T) = -\frac{t}{N} \sum_{\vec{k}} \left(\frac{\epsilon_{\vec{k}} - \bar{\mu}}{2\omega_{\vec{k}}} \cos k_x X_{\vec{k}}^a + t \sin^2 k_x Y_{\vec{k}}^a \right), \tag{3.36}$$

with $X_{\vec{k}}^a$ and $Y_{\vec{k}}^a$ for $t^\uparrow = t^\downarrow$.

Finally, if $h = M = 0$, $E_{\vec{k}\uparrow} = E_{\vec{k}\downarrow} = E_{\vec{k}}$, where $E_{\vec{k}}$ is given by the standard form, ρ_s is:

$$\rho_s = \frac{1}{2N} \sum_{\vec{k}} \left\{ \frac{1}{2} \frac{\partial^2 \epsilon_{\vec{k}}}{\partial k_x^2} \left[1 - \frac{\bar{\epsilon}_{\vec{k}}}{2\omega_{\vec{k}}} \tanh\left(\frac{\beta E_{\vec{k}}}{2}\right) \right] + \left(\frac{\partial \epsilon_{\vec{k}}}{\partial k_x} \right)^2 \frac{\partial f(E_{\vec{k}})}{\partial E_{\vec{k}}} \right\}. \tag{3.37}$$

Chapter 4

Superconducting properties in the presence of a Zeeman magnetic field: Weak and intermediate coupling

In this chapter we focus on the analysis of the influence of the Zeeman term on the superfluid characteristics of the attractive Hubbard model (AHM) with spin independent hopping integrals ($t^\uparrow = t^\downarrow$) for the square and simple cubic lattices. Within the mean-field (the BCS-Stoner) approach, we construct phase diagrams in two ways: by fixing the chemical potential (μ) or the electron concentration (n), and show the relevant differences resulting from these possibilities. The importance of the Hartree term in the broken symmetry Hartree-Fock approximation is indicated. A reentrant transition is observed for sufficiently high magnetic fields in the temperature phase diagrams in the weak coupling regime. However, we also find a region where the superfluid density (ρ_s) becomes negative on these diagrams, both for $d = 2$ and $d = 3$. For the two-dimensional case, we investigate the Kosterlitz-Thouless transition (KT) in the weak coupling regime. Finally, we also briefly discuss the influence of the pure d-wave pairing symmetry on the polarized superconducting phase stability in the 2D system. Some selected results have been published by us in Refs. [109, 110, 111].

Because of the fact that most of this chapter is devoted to the analysis of the superconducting characteristics of the spin-polarized AHM, we write its Hamiltonian explicitly. The Hamiltonian (2.15) is reduced to the form:

$$H = \sum_{ij\sigma} (t_{ij} - \mu\delta_{ij}) c_{i\sigma}^\dagger c_{j\sigma} + U \sum_i n_{i\uparrow} n_{i\downarrow} - h \sum_i (n_{i\uparrow} - n_{i\downarrow}), \quad (4.1)$$

where: $n_{i\uparrow} = c_{i\uparrow}^\dagger c_{i\uparrow}$, $n_{i\downarrow} = c_{i\downarrow}^\dagger c_{i\downarrow}$, t_{ij} – spin independent hopping integral.

The superconducting gap parameter for the s-wave pairing symmetry is defined by: $\Delta = -\frac{U}{N} \sum_i \langle c_{i\downarrow} c_{i\uparrow} \rangle = -\frac{U}{N} \sum_{\vec{k}} \langle c_{-\vec{k}\downarrow} c_{\vec{k}\uparrow} \rangle$.

The system of self-consistent equations for the s-wave pairing symmetry case ($W = 0$,

$U < 0$) in the presence of a Zeeman magnetic field is reduced to:

$$\Delta = -\frac{U}{N} \sum_{\vec{k}} \frac{\Delta}{2\omega_{\vec{k}}} \frac{1}{2} \left(\tanh \frac{\beta E_{\vec{k}\uparrow}}{2} + \tanh \frac{\beta E_{\vec{k}\downarrow}}{2} \right), \quad (4.2)$$

where:

$$E_{\vec{k}\downarrow,\uparrow} = \pm \frac{UM}{2} \pm h + \omega_{\vec{k}}, \quad (4.3)$$

$$\omega_{\vec{k}} = \sqrt{\epsilon_{\vec{k}}^2 - \bar{\mu}^2 + |\Delta|^2}, \quad \bar{\mu} = \mu - \frac{Un}{2}.$$

The particle number equation takes the form:

$$n = 1 - \frac{1}{2N} \sum_{\vec{k}} \frac{\epsilon_{\vec{k}} - \bar{\mu}}{\omega_{\vec{k}}} \left(\tanh \frac{\beta E_{\vec{k}\uparrow}}{2} + \tanh \frac{\beta E_{\vec{k}\downarrow}}{2} \right). \quad (4.4)$$

The equation for the magnetization is:

$$M = \frac{1}{2N} \sum_{\vec{k}} \left(\tanh \frac{\beta E_{\vec{k}\downarrow}}{2} - \tanh \frac{\beta E_{\vec{k}\uparrow}}{2} \right). \quad (4.5)$$

The grand canonical potential of the superconducting state:

$$\begin{aligned} \frac{\Omega^{SC}}{N} &= \frac{1}{4} Un(2-n) - \mu + \frac{1}{4} UM^2 - \frac{|\Delta|^2}{U} \\ &- \frac{1}{\beta N} \sum_{\vec{k}} \ln \left(2 \cosh \frac{\beta(E_{\vec{k}\uparrow} + E_{\vec{k}\downarrow})}{2} + 2 \cosh \frac{\beta(-E_{\vec{k}\uparrow} + E_{\vec{k}\downarrow})}{2} \right), \end{aligned} \quad (4.6)$$

and the free energy: $F^{SC}/N = \Omega^{SC}/N + \mu n$.

4.1 Ground state

The system of the above self-consistent equations was solved numerically for the 2D square and 3D simple cubic lattices. The sums over the first Brillouin zone were performed with the use of the density of states¹, whenever possible. First, the chemical potential was fixed. The first order transition lines were determined from the condition $\Omega^{SC} = \Omega^{NO}$. Then, these results were mapped onto the case of fixed n .

Let us start our analysis with the influence of a Zeeman magnetic field on the order parameter Δ , at fixed μ . As shown in Fig. 4.1(a), there are three different solutions for the order parameter at $T = 0$.

¹The density of states for the 2D square lattice is expressed by the complete elliptic integral of the first kind K [31], while the form of the density of states for a simple cubic lattice has been taken from Ref. [112] (see Appendix E).

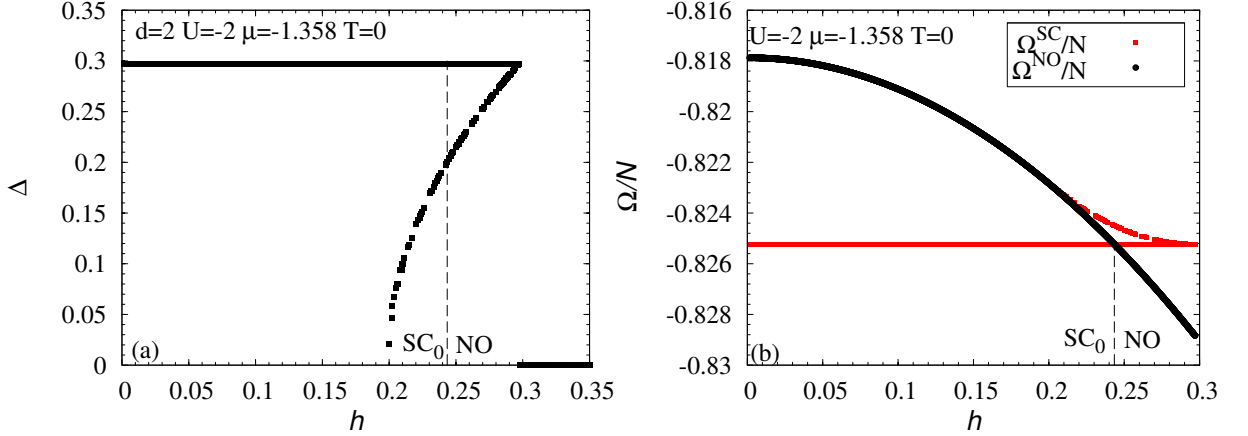


Figure 4.1: Dependence of the order parameter (a) and the grand canonical potential (b) on the magnetic field at $T = 0$, $d = 2$, $U/t = -2$, for a fixed $\mu \approx -1.358$. SC_0 – the superconducting phase without the spin polarization ($n_\uparrow = n_\downarrow$, $P = 0$), NO – the normal state. In Fig. (a) the lower branch is unstable (the grand canonical potential for this branch is higher than the grand canonical potential for the SC_0 branch – Fig. (b) – red squares). The vertical dashed lines mark the Hartee-Fock phase transition magnetic field – the first order phase transition to the normal state at $T = 0$. The chemical potential has been chosen to yield $n \approx 0.75$ at $h = 0$.

The first type of the solution is $\Delta \neq 0$ which is a constant function of the magnetic field. It means that $n_\uparrow = n_\downarrow$ and the spin polarization $P = 0$. Such solution will be marked $\Delta(h = 0) \equiv \Delta_0$ in further considerations. This is the unpolarized superconducting ground state (SC_0).

For higher magnetic fields, the densities of states are different for the particles with spin down and spin up ($n_\uparrow \neq n_\downarrow$, $P \neq 0$). Then, there appears a lower branch of solutions with $\Delta(h)$ and a gapless spectrum for the majority spin species. This is a polarized superconducting state with a magnetic field dependent order parameter. However, as follows from Fig. 4.1(b), this branch of Δ is energetically unstable, i.e. the grand canonical potential for this branch is higher than the grand canonical potential for the SC_0 branch.

At $h = \Delta_0$, there is a jump in the order parameter from a constant value to zero. Hence, one can distinguish a third solution with $\Delta = 0$ and $P \neq 0$. This is the Pauli paramagnetic state (normal phase (NO)).

If we investigate the behavior of the grand canonical potential vs. the order parameter (Fig. 4.2), for fixed h and $T = 0$, we find that at $h = 0$ (Fig. 4.2(a)) there is a global minimum for the solution from the upper branch (Δ_0 with $P = 0$), i.e. it is stable. When the magnetic field is increased, such a situation persists until $h \approx 0.2$. Up to this point, there are two solutions to the self-consistent equations ($\Delta = \Delta_0$ and $\Delta = 0$). For $h \in (0.2, 0.242)$ (Fig. 4.2(b)), we still find a global minimum for the solution from the upper branch, but there appears a third solution (the lower branch with $\Delta(h)$, $P \neq 0$), which is a local maximum, indicating that it is unstable. If h is larger than approx. 0.242,

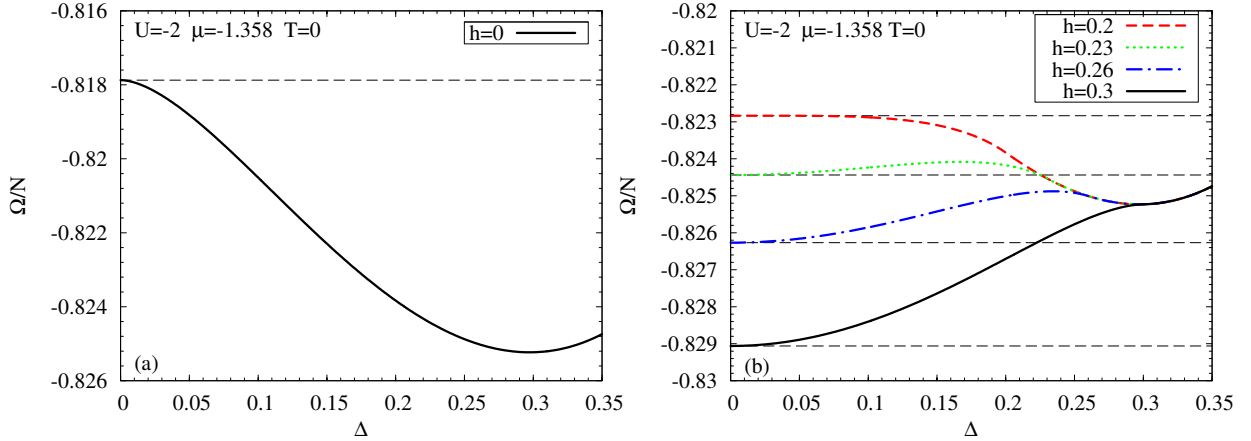


Figure 4.2: Dependence of the grand canonical potential on the order parameter at $T = 0$ and fixed $\mu \approx -1.358$. (a) $h = 0$, (b) $h = 0.2$ (red, dashed line), $h = 0.23$ (green, dotted line), $h = 0.26$ (blue, dash-dotted line) and $h = 0.3$ (black, solid line). t is used as the unit.

the global minimum for the solution from the upper branch becomes a local minimum, whereas the global minimum corresponds now to $\Delta = 0$ – the system undergoes a first-order phase transition to the NO state. Finally, for $h > \Delta_0$, there is no local minimum at $\Delta \neq 0$ and the self-consistent equations yield only one solution with $\Delta = 0$.

The influence of a Zeeman magnetic field on the superconducting phase is also manifested by changes in the density of states.

The spin-dependent density of states (DOS) in the superconducting ground state is determined from:

$$g_\sigma(E) = \frac{1}{N} \sum_{\vec{k}} \left[|u_{\vec{k}}|^2 \delta(E - E_{\vec{k}\sigma}) + |\nu_{\vec{k}}|^2 \delta(E + E_{\vec{k}-\sigma}) \right], \quad (4.7)$$

where: the coefficients $u_{\vec{k}}$ and $\nu_{\vec{k}}$ are given by Eqs. (2.46)-(2.47), $E_{\vec{k}\downarrow,\uparrow}$ are expressed in the general form by Eq. (2.42) and $\bar{\epsilon}_{\vec{k}\downarrow,\uparrow}$ – by Eqs. (2.23)-(2.24). The total density of states: $g(E) = g_\uparrow(E) + g_\downarrow(E)$. For numerical calculations, the Dirac delta function is expressed by: $\delta(x) = \frac{1}{\pi} \lim_{\eta \rightarrow 0} \frac{\eta}{x^2 + \eta^2}$, where $\eta = 10^{-3}$.

Apart from changes in the densities of states, the influence of a magnetic field on the superconducting phase is manifested by a change in the momentum distributions in the Brillouin zone. The momentum distribution at finite temperatures, in the Brillouin zone is given by:

$$n_{\vec{k}\sigma} = |u_{\vec{k}}|^2 f(E_{\vec{k}\sigma}) + |\nu_{\vec{k}}|^2 f(-E_{\vec{k}-\sigma}). \quad (4.8)$$

Above formula at $T = 0$ takes the form: $n_{\vec{k}\sigma} = |u_{\vec{k}}|^2 \Theta(-E_{\vec{k}\sigma}) + |\nu_{\vec{k}}|^2 \Theta(E_{\vec{k}-\sigma})$, where $\Theta(x)$ is the Heaviside step function: $\Theta(x) = 1$ if $x > 0$ and zero otherwise.

Fig. 4.3 shows the densities of states $g_\uparrow(E)$ (red dashed lines) and $g_\downarrow(E)$ (black solid lines), while Fig. 4.4 show momentum occupation numbers $n_{\vec{k}\uparrow}$ (red points), $n_{\vec{k}\downarrow}$ (black points) vs. $k \equiv |k_x| = |k_y|$ and the corresponding quasiparticle spectra (insets). The

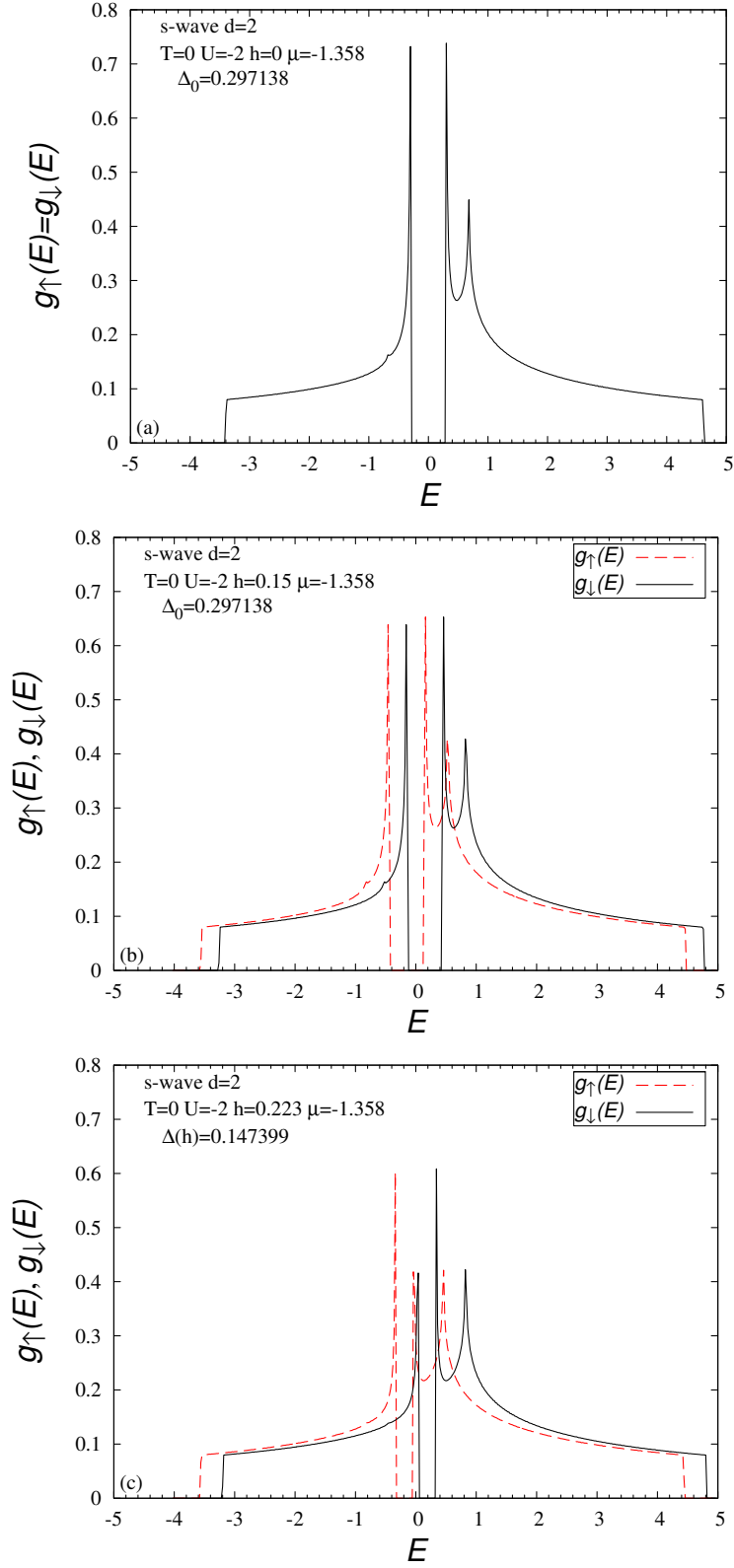


Figure 4.3: Density of states for two-dimensional s-wave pairing symmetry case, $T = 0$, $\mu \approx -1.358$, $U = -2$, (a) $h = 0$, (b) $h = 0.15$ (the stable branch solution), (c) $h = 0.223$ (the unstable branch solution).

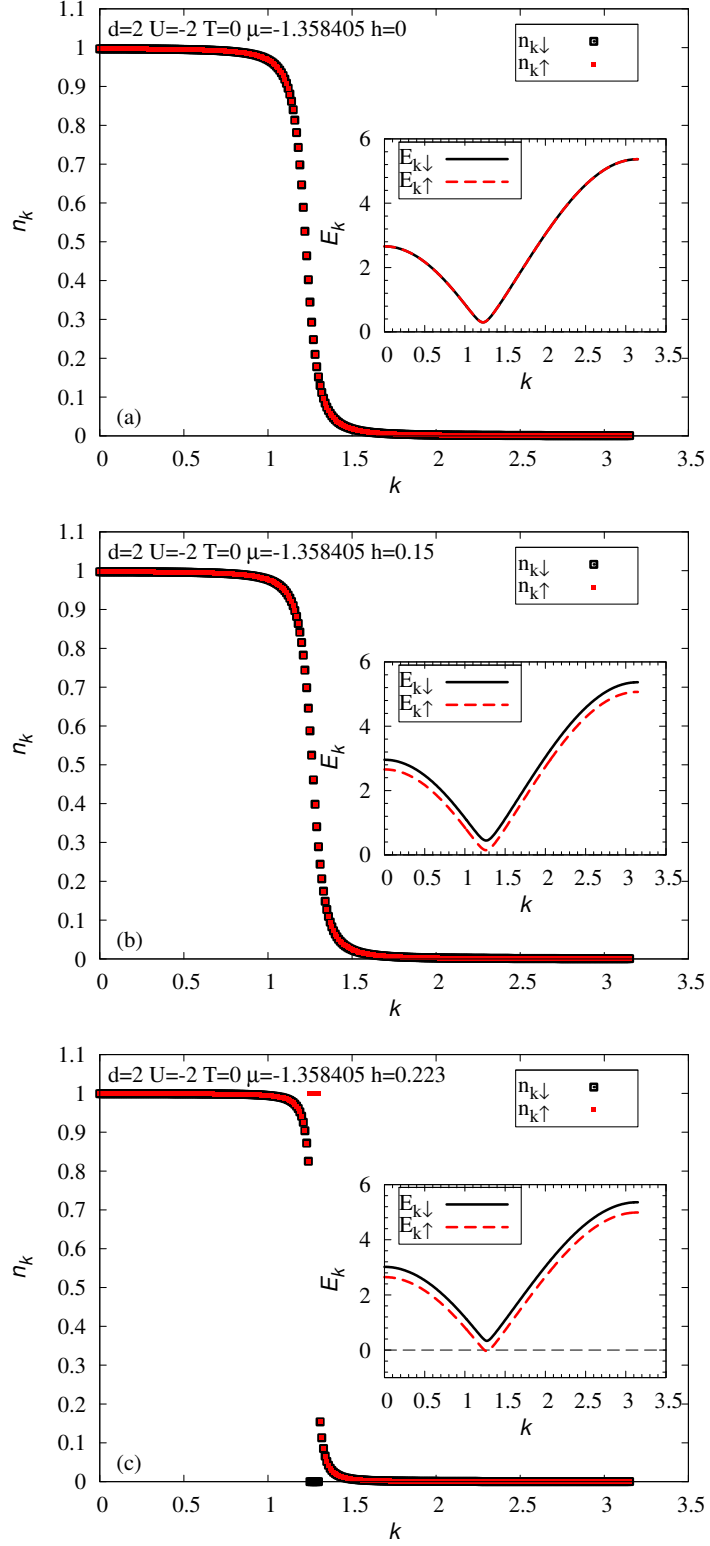


Figure 4.4: Plots of momentum occupation numbers $n_{\vec{k}\uparrow}$ (red points), $n_{\vec{k}\downarrow}$ (black points) vs. $k \equiv |k_x| = |k_y|$ and corresponding quasiparticle spectra $E_{\vec{k}\uparrow}$, $E_{\vec{k}\downarrow}$ (insets) for $U = -2$, $\mu \approx -1.358$, (a) $h = 0$, (b) $h = 0.15$, (c) $h = 0.223$.

excitation spectrum of the quasiparticles is given by Eq. (4.3). For both figures, we give results at a fixed $\mu \approx -1.358$, $h = 0$ and two values of the magnetic field.

If $h = 0$, the densities of states are equal for the particles with spin down and spin up ($g_{\uparrow}(E) = g_{\downarrow}(E)$). The energy gap (E_g) occurs in DOS, for the isotropic s-wave pairing symmetry (Fig. 4.3(a)). E_g is bounded by the location of the square root singularities. The width of the energy gap in the BCS limit is given by: $E_g = 2\Delta$. The energies of the quasiparticles are equal ($E_{\vec{k}\uparrow} = E_{\vec{k}\downarrow} \geq \Delta$), $n_{\vec{k}\uparrow} = n_{\vec{k}\downarrow}$ and we observe the characteristic smearing around the Fermi surface (Fig. 4.4(a)).

In the presence of the magnetic field, $g_{\uparrow}(E) \neq g_{\downarrow}(E)$. Let us assume $h > 0$. If we take into account the unpolarized solution ($P = 0$), then $g_{\uparrow}(E)$ moves to the left by h and $g_{\downarrow}(E)$ to the right by h (Fig. 4.3(b)). Since $h < \Delta$, the regions with $g_{\uparrow}(E) = 0$ and $g_{\downarrow}(E) = 0$ still have an overlap, hence the total density of states $g(E)$ is gapped. Accordingly (Fig. 4.4(b)), $E_{\vec{k}\uparrow}$ moves down by h , yielding a minimum excitation energy for quasiparticles with spin-up of $\Delta - h > 0$ and $E_{\vec{k}\downarrow}$ moves up by h , giving a minimum excitation energy for spin-down of $\Delta + h > 0$. There is still one Fermi surface in the system, since the momentum occupation numbers $n_{\vec{k}\uparrow} = n_{\vec{k}\downarrow}$ and thus $P = 0$.

If Δ is h -dependent and $h > \Delta$, $n_{\uparrow} \neq n_{\downarrow}$, the shift to the left of $g_{\uparrow}(E)$ and the shift to the right of $g_{\downarrow}(E)$ by h is such that the gapped regions in both $g_{\sigma}(E)$ do not overlap any more and thus the total density of states $g(E)$ becomes gapless (Fig. 4.3(c)). Moreover, the excitation energy $E_{\vec{k}\uparrow} = \Delta - h < 0$, i.e. the spectrum for the majority spin species becomes gapless (Fig. 4.4(c)). There are two Fermi surfaces in the system, which is manifested in the momentum occupation numbers by the appearance of a region with $n_{\vec{k}\uparrow} = 1$ and $n_{\vec{k}\downarrow} = 0$. However, as shown above, the spatially homogeneous polarized superconducting phase, characterized by the gapless spectrum for the majority spin species is unstable at $T = 0$, on the BCS side and in the s-wave pairing symmetry case.

4.1.1 Phase diagrams

In this subsection, we consider the ground state phase diagrams for the square and simple cubic lattices. The weak and intermediate couplings are analyzed at $r = 1$.

As mentioned above, in the absence of a magnetic field, in the weak coupling regime, the usual superconducting state (BCS-type state) is stable at $T = 0$.

The Zeeman magnetic field destroys superfluidity at weak and intermediate couplings through the paramagnetic effect (or by population imbalance). In consequence, there is a first order phase transition from the unpolarized superconducting to the polarized normal state, both for $d = 2$ and $d = 3$.

Fig. 4.5 shows the $h - \mu$ phase diagram for the (a) square and (b) simple cubic lattices, at $T = 0$. These diagrams are symmetric with respect to the sign change of $\mu - U/2$ or h . For the sake of clarity, we only show the range of $\mu - U/2$ from -4 to 0 (for $d = 2$), from -6 to 0 (for $d = 3$) and for $h \geq 0$. The solid lines denote the first order phase transition to the NO phase. The range of stability of the SC_0 state depends on the value of the attractive interaction, i.e. it widens with increasing attraction. For the weak and intermediate attraction, $\bar{\mu}$ does not drop below the lower band edge in the three

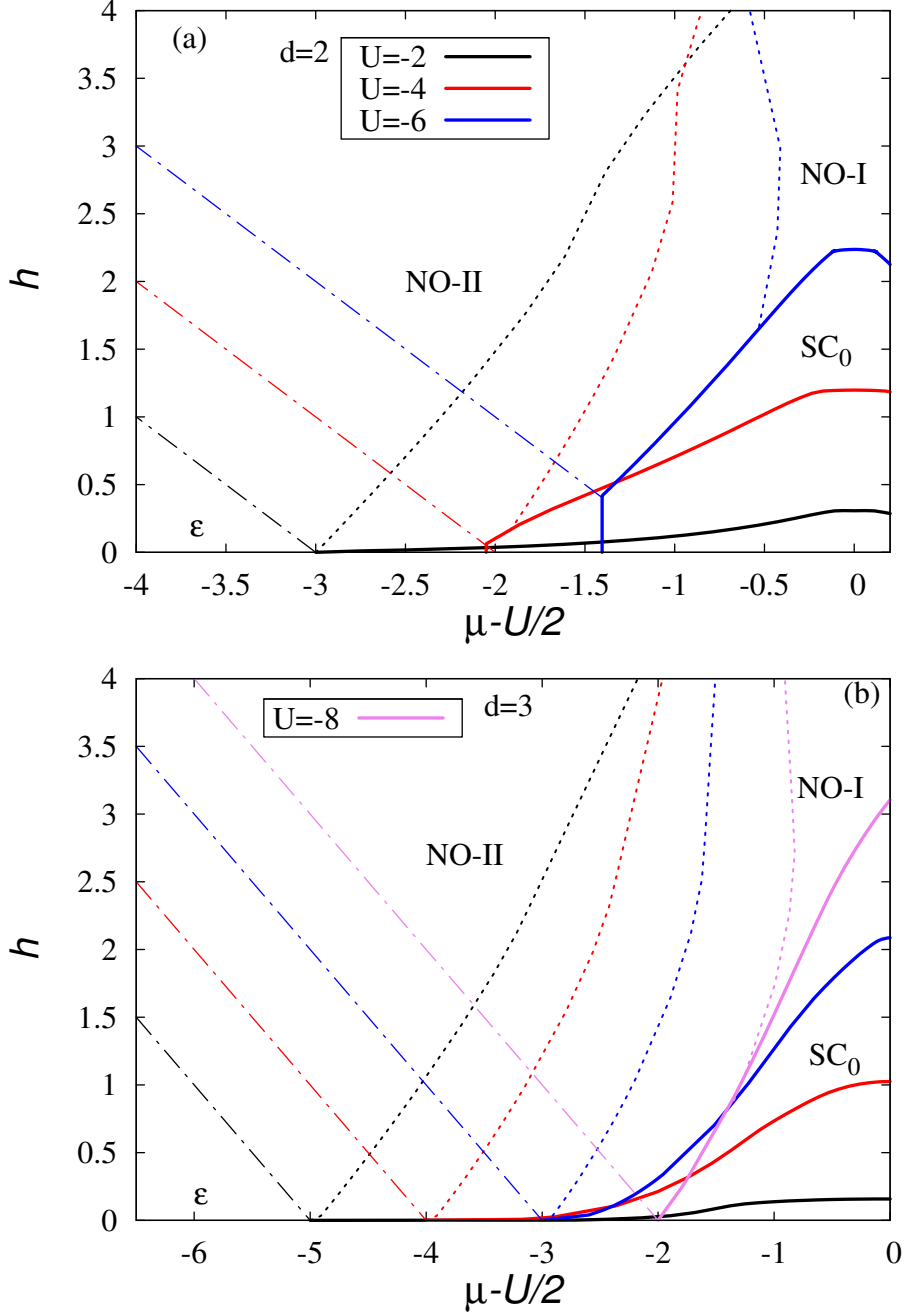


Figure 4.5: Critical magnetic field vs. the chemical potential for the first order SC_0 -NO transition, at $T = 0$, three different values of the attractive interaction; (a) square lattice, (b) simple cubic lattice. SC_0 – unpolarized superconducting state with $n_\uparrow = n_\downarrow$, NO-I – partially polarized ($P < 1$) and NO-II – fully polarized ($P = 1$) normal state, ϵ – empty state. Solid lines denote SC_0 -NO first order transition, dashed lines separate NO-I and NO-II states, borders between NO-II and empty states are shown with dash-dotted lines. If $|U|$ is higher than $|U_c|^{d=3}$, the behavior of the critical line in $d = 3$ becomes similar to that of $d = 2$ ($U/t = -8$).

dimensional case, because there exists a threshold value of $|U|$ for which a bound state is formed in the empty lattice. After the transition from SC_0 , the system is in the partially polarized normal state (NO-I), whose polarization is $P = (n_\uparrow - n_\downarrow)/(n_\uparrow + n_\downarrow) < 1$. With further increase in the magnetic field, the system goes smoothly to the fully polarized normal state (NO-II), for which $P = 1$ ($n_\downarrow = 0$). If the attraction is increased above the threshold for bound state formation in the empty lattice ($|U_c|^{d=3}/12t = 0.659$), a first order transition from SC_0 to NO-II takes place, for some values of the parameters (Fig. 4.5(b)). It should be emphasized that the magnetic field modifies the band edge, which is clearly visible in Fig. 4.5 (the thin dash-dotted lines). The first order transition lines at $T = 0$ were obtained numerically from the condition $\Omega_{T=0}^{SC} = \Omega_{T=0}^{NO}$ (where $\Omega_{T=0}^{NO}$ and $\Omega_{T=0}^{SC}$ denote the grand canonical potential of the normal ($\Delta = 0$, $P \neq 0$) and the superconducting ($\Delta \neq 0$, $P = 0$) state, respectively).

The situation is more complex for the two dimensional case (Fig. 4.5(a)). Since a critical interaction value for which a bound state is formed in the empty lattice does not exist, for any small value of the attraction, $\bar{\mu}$ can drop below the lower band edge. For $n \rightarrow 0$, $\bar{\mu} = -4t - \frac{1}{2}E_b$ (E_b – the binding energy in two-body problem). It is in agreement with a rigorous result of Randeria et al. [113, 114] that in the low density limit and $d = 2$, the presence of the bound state in the two-body problem is a necessary and sufficient condition for s -wave SC_0 to take place. Moreover, as opposed to the $d = 3$ case, for some values of the parameters, we find a first order transition directly from SC_0 to NO-II, even for weak and intermediate attractive interaction (Fig. 4.5(a)).

There are relevant differences between the phase diagrams obtained for fixed chemical potential and those for fixed electron concentration. Fig. 4.6 shows the dependence of the critical magnetic fields on the electron concentration, for three (four) different values of attraction, for $d = 2$ (a) and $d = 3$ (b). Here, due to the particle-hole symmetry, we only show the range of n from 0 to 1. In contrast to the fixed chemical potential case, if the number of particles is fixed and $n \neq 1$, one obtains two critical Zeeman fields (h_{c1} , h_{c2}) in the phase diagrams. The two critical field lines determine the phase separation region between SC_0 with the number of particles n_s and NO with the number of particles n_n . For the case of the square lattice and for higher values of the attractive interaction or smaller n , the transition from the PS region can be directly to NO-II. For the case of a simple cubic lattice, the situation is different, as long as $|U|$ is smaller than $|U_c|$ – the first order transition from PS to NO-I takes place in the whole range of the parameters and afterwards the system goes smoothly from NO-I to NO-II.

4.2 Finite temperatures

This section presents the results concerning the influence of the magnetic field on superfluidity at finite temperatures, based on the HF-BCS theory. For the $d = 2$ system at $h = 0$, the SC-NO transition is of the KT type. According to Eq. (3.11), the KT transition temperature is found from the intersection point of the straight line $\frac{2}{\pi}k_B T$ with

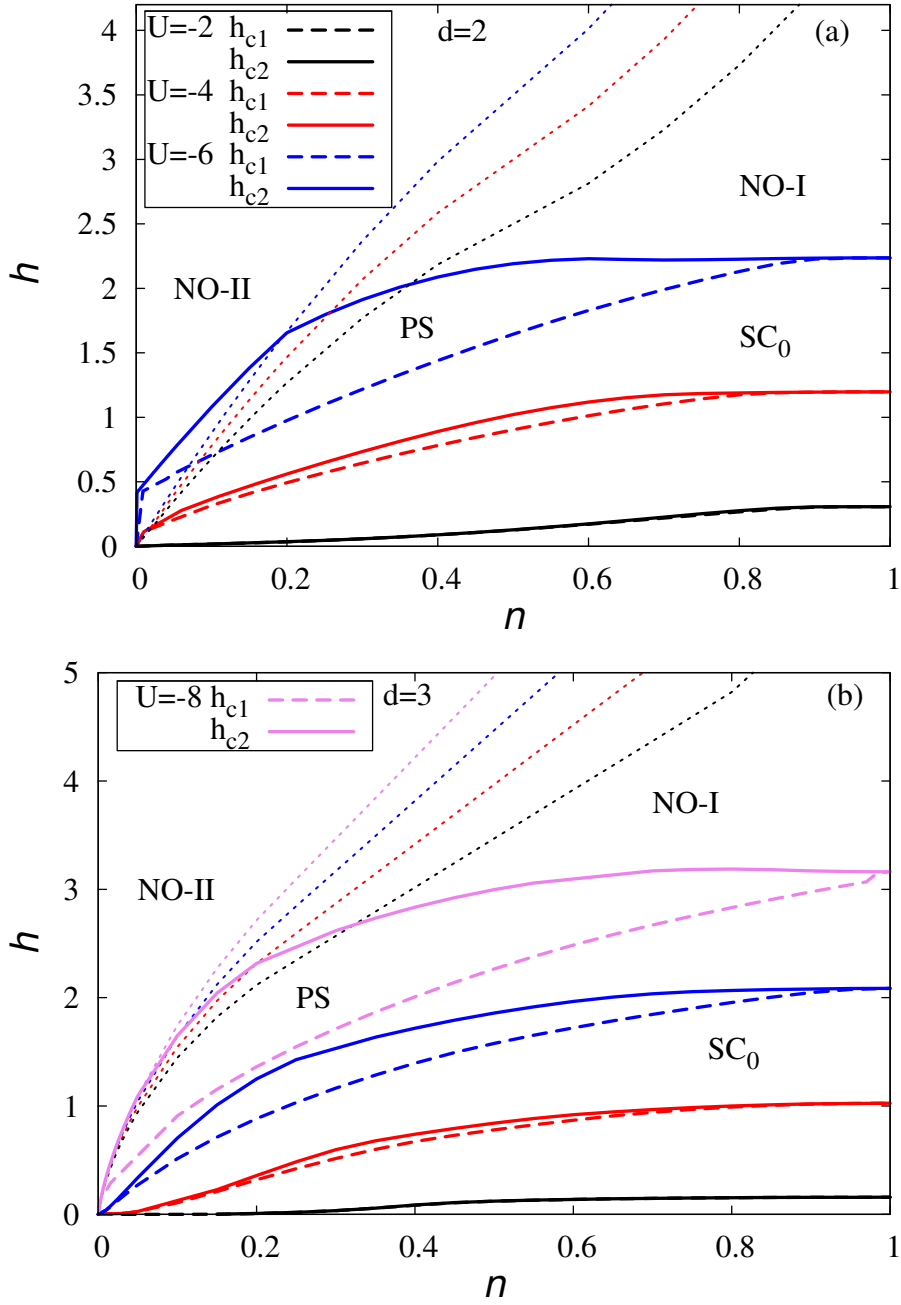


Figure 4.6: Critical magnetic field vs. electron concentration for the first order SC_0 -NO transition, at $T = 0$; (a) square lattice, (b) simple cubic lattice. PS – phase separation. Thick solid and dashed lines limit the region of PS, thin dashed lines border NO-I and NO-II states. Charge density wave (CDW) state, being degenerated with SC for $h = 0$, $n = 1$, is not shown.

the curve $\rho_s(T)$ ². Thus, we take into account phase fluctuations in our treatment, in 2D. We analyze the weak coupling regime for the $d = 2$ and $d = 3$ cases.

The results shown below for chosen values of the parameters U , n and μ , illustrate the typical behavior, but our analysis is general within the Hartree approximation. We start by investigating the stability of the gap solutions, at $T \neq 0$, for fixed $\mu \approx -1.358$ in $d = 2$.

Fig. 4.7 shows the dependence of the order parameter on magnetic field, for a few fixed values of temperature (a) and the order parameter vs. temperature, for a few fixed values of magnetic field (b), for a fixed μ , in $d = 2$. As mentioned above, at $T = 0$ only the solutions with $\Delta \neq 0$ and $P = 0$ are energetically favorable against NO, in the presence of the magnetic field. Hence, the BCS state is stable. The situation is more interesting for $T > 0$. For low magnetic fields, Δ vanishes continuously with increasing temperature. However, there arise two non-zero solutions for the order parameter, for $h = 0.23$ (Fig. 4.7(b)). The lower branch is unstable. We have also found very interesting behavior of the order parameter for fixed $h = 0.24$. In this case, Δ vanishes discontinuously at $T = 0.0225$ and there is a first order phase transition. The solutions with $\Delta \neq 0$ become energetically unfavorable, i.e. the upper branch is metastable and the lower branch is unstable for $T > T_c$. Moreover, the lower branch is also unstable for $T < T_c$, which is clearly visible in Fig. 4.7(c) and 4.7(e). If we investigate the behavior of the grand canonical potential vs. the order parameter, for fixed h and T , we find that at $h = 0.24$ and $T = 0.01$ (on the SC side) there is a maximum for the solution from the lower branch (i.e. it is unstable) and a global minimum for the solution from the upper branch (i.e. it is stable). For the same value of the magnetic field but for a higher value of temperature, $T = 0.03$ (which is on NO side), we still find a maximum for the solution from the lower branch, but for the solution from the upper branch there is a local minimum, indicating a metastable solution. Moreover, for $T \geq 0.06067$ the superconducting solution becomes favorable again (second order transition to SC state) and Δ vanishes continuously (second order phase transition to NO at $T = 0.0998$), which is shown in Fig. 4.7(d) and 4.7(f). Such behavior points out that for sufficiently high fields a reentrant transition takes place. Hence, an increase in temperature can induce superconductivity.

This interesting behavior at $T \neq 0$, for higher magnetic fields, is reflected by the temperature dependence of magnetization shown in Figs. 4.8(a) and 4.8(b). At $h = 0.23$, there is a second order transition to NO (lower branch). The upper branch is unstable. For a higher magnetic field ($h = 0.24$), the first order phase transition is revealed through a jump in magnetization. In the NO state, magnetization is continuous. After the second order transition to SC (reentrant transition), magnetization decreases abruptly. With increasing temperature, M increases and there is a second order transition to NO at $T = 0.0998$.

We also perform an analysis, similar to the above, for a simple cubic lattice, at fixed $\mu \approx -2.4439$ and $U = -4$.

At $T = 0$, in the weak coupling limit, only the solutions with $\Delta \neq 0$ and $P =$

²It should be added that we use expression for $\rho_s(T)$ derived in chapter 3.2. Thus, T_c is an upper bound on actual transition temperature.

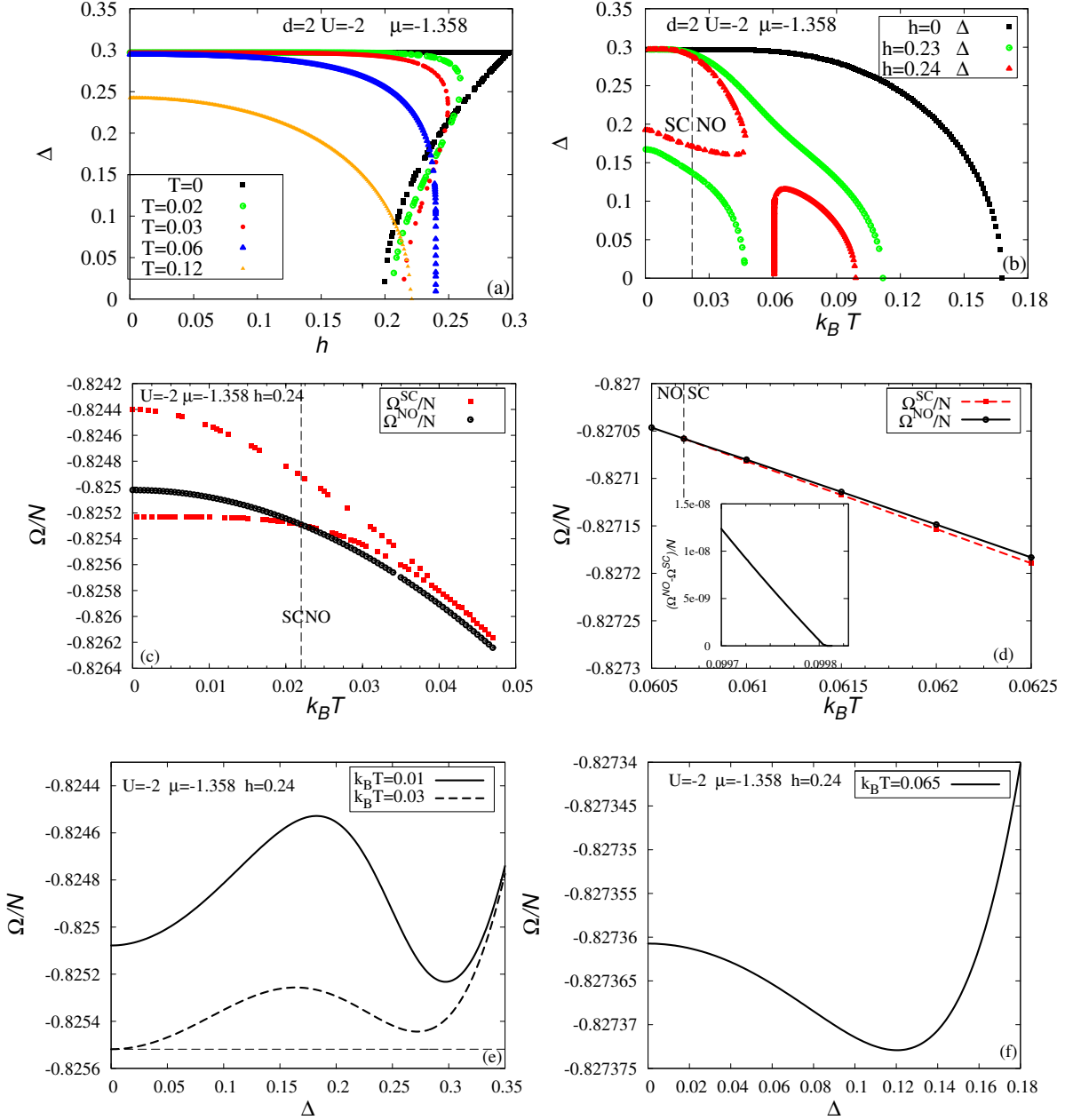


Figure 4.7: Dependence of the order parameter on the magnetic field (a) and temperature (b), $d = 2$, $U = -2$, for a fixed $\mu \approx -1.358$. In Fig (b), for $h = 0.23$ the lower branch is unstable. For $h = 0.24$ the vertical dashed line denotes the first order phase transition to the normal state and there are two second order transitions in the reentrant case (at $T = 0.06067$ and $T = 0.09891$). The grand canonical potential vs. temperature for $h = 0.24$: (c) the first order phase transition to the normal state, (d) the details of the reentrant transition: second order transition from NO to SC and from SC to NO (inset). The vertical dashed lines mark the H-F phase transition temperatures. The dependence of the grand canonical potential on the order parameter for $h = 0.24$, $T = 0.01$ (solid line) and $T = 0.03$ (dashed line) (e), and for $T = 0.065$ (f).

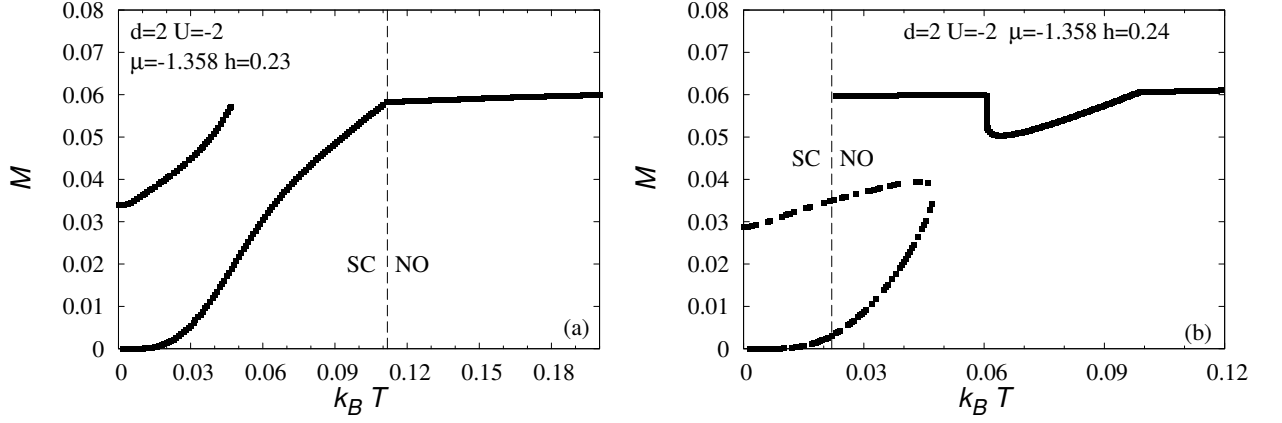


Figure 4.8: Magnetization vs. temperature, $d = 2$, $U = -2$, for a fixed $\mu \approx -1.358$. (a) $h = 0.23$, (b) $h = 0.24$.

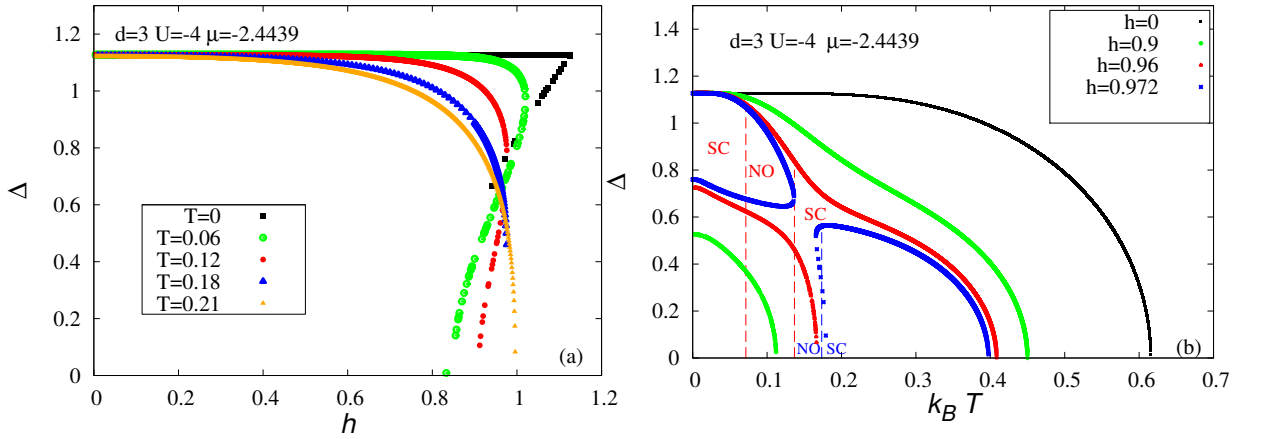


Figure 4.9: Dependence of the order parameter on the magnetic field (a) and temperature (b), $d = 3$, $U = -4$, for a fixed $\mu \approx -2.4439$. In Fig (b), for $h = 0.96$ the lower branch is unstable. For $h = 0.972$ the solutions from $T = 0$ to $T = 0.1362$ are unstable. The first order phase transition from the normal to the superconducting state (at $T = 0.1734$) and the second order transition from the superconducting to the normal state (at $T = 0.3975$) take place.

0 are favorable against NO, as in the 2D case. At $T > 0$, the dependencies of the order parameter on the magnetic field or temperature are also similar to those in the square lattice case. However, the sequences of the SC-NO or NO-SC transitions are more complex.

For low h , the order parameter tends to zero continuously, with increasing temperature. For higher magnetic fields, there is a change in the phase transition: from the second to the first order. There can arise two non-zero solutions for the order parameter (Fig.

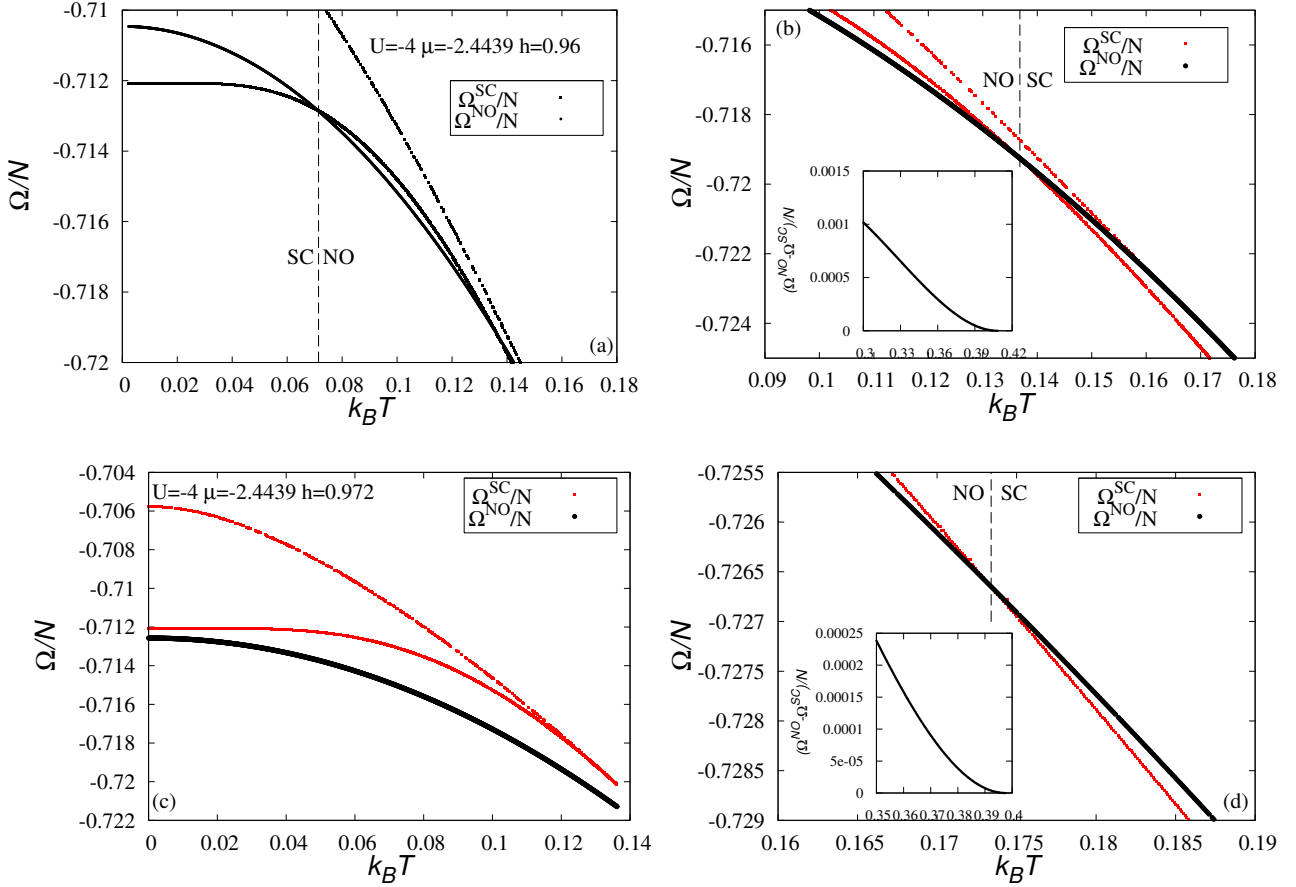


Figure 4.10: Grand canonical potential vs. temperature, $d = 3$, $U = -4$, for a fixed $\mu \approx -2.4439$, at $h = 0.96$: (a) the first order phase transition to the normal state, (b) the details of the reentrant transition: first order transition from NO to SC and second order transition from SC to NO (inset). The grand canonical potential vs. temperature for $h = 0.972$; (c) normal state is stable, (d) first order transition from NO to SC and second order transition from SC to NO (inset). The vertical dashed lines mark the phase transition temperatures.

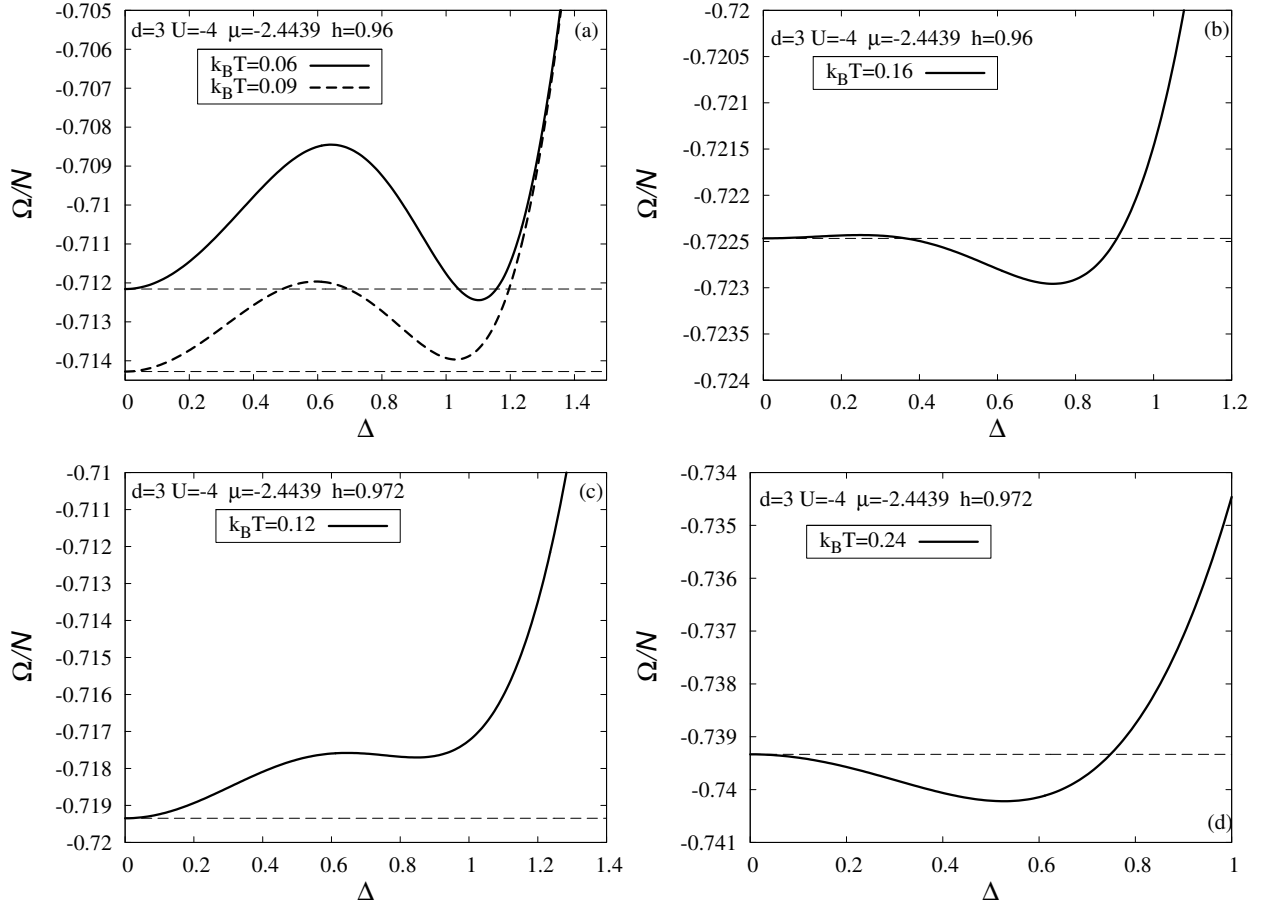


Figure 4.11: Dependence of the grand canonical potential on the order parameter, $d = 3$, $U = -4$, for a fixed $\mu \approx -2.4439$, at $h = 0.96$, $T = 0.06$ (solid line) $T = 0.09$ (dashed line) (a), $T = 0.16$ (b) and for $h = 0.972$, $T = 0.12$ (c), $T = 0.24$ (d).

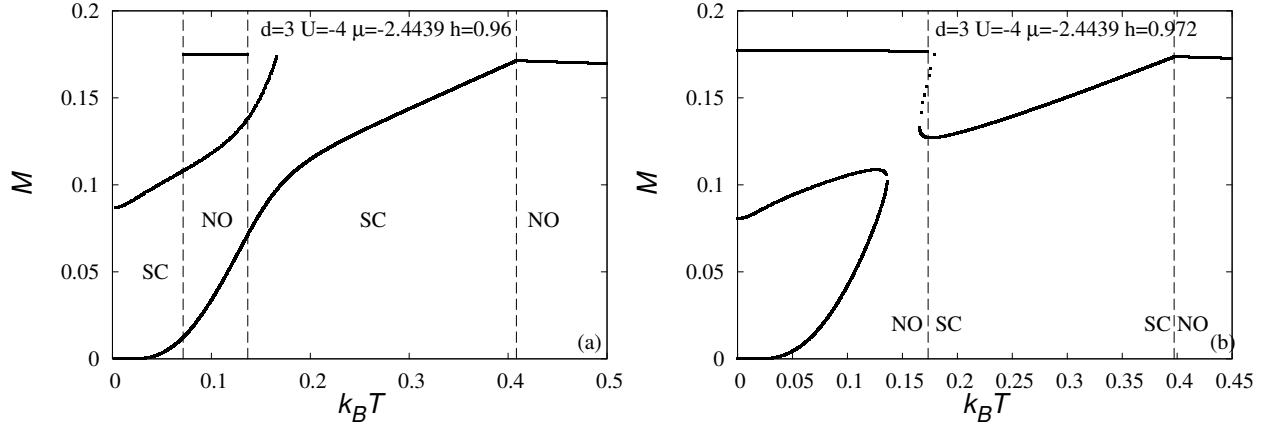


Figure 4.12: Magnetization vs. temperature for fixed $h = 0.96$ (a) and $h = 0.972$ (b); $d = 3$, $U = -4$, fixed $\mu \approx -2.4439$.

4.9(b)).

At $h = 0.9$, the upper branch is stable while the lower branch is thermodynamically unstable. At $h = 0.96$, the situation is more interesting. The lower branch is also unstable which is clearly visible in Figs. 4.10(a)-(b) and 4.11(a). There is a maximum of Ω for the solution from this branch. However, there is a global minimum for the solution from the upper branch. After the first order phase transition from SC to NO, at $T \approx 0.0714$, the solution from the upper branch becomes metastable (a local minimum at $T = 0.09$). At $T \approx 0.1368$, there is yet another first order transition from the NO to the SC state and up to $T \approx 0.42$ (the second order phase transition from SC to NO) the solutions from the upper branch are stable. Therefore, there is the following sequence of transitions in the system, for fixed $h = 0.96$: SC \rightarrow NO (1st order), NO \rightarrow SC (1st order) and SC \rightarrow NO (2nd order).

At $h = 0.972$, the solutions from $T = 0$ to $T = 0.1362$ are metastable (the upper branch – a local minimum) and unstable (the lower branch – a maximum) (Fig. 4.11(c)). The system is in the normal state. At $T \approx 0.1734$, the first order phase transition from the normal to the superconducting state takes place. Then, at $T \approx T_c = 0.3975$, the system goes to the normal state (2nd order transition).

Therefore, for sufficiently high magnetic fields a reentrant transition takes place, as in the 2D case. However, this transition is more complex in $d = 3$, which is also reflected in the behavior of spin magnetization (Fig. 4.12(a)-(b)).

4.2.1 The superfluid density

In this section, the properties of the superfluid stiffness – ρ_s , in the Zeeman magnetic field, will be discussed.

This physical quantity is important both because of a relation to the London penetration depth λ ($\rho_s \sim \lambda^{-2}$) [115] and its relevance in the Kosterlitz-Thouless temperature

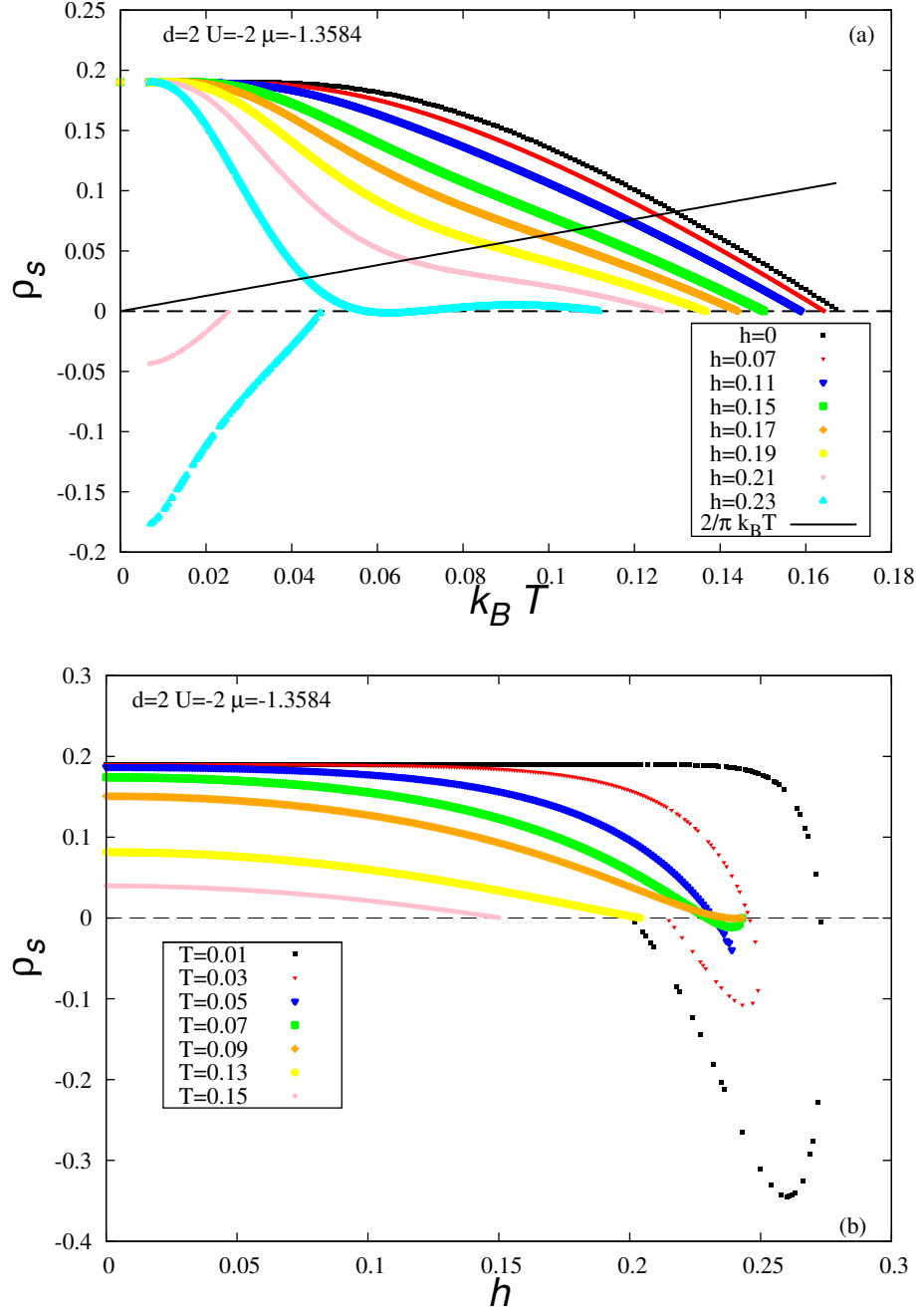


Figure 4.13: Superfluid density vs. temperature (a) and magnetic field (b) for the square lattice, $\mu \approx -1.358$, $U = -2$. The Kosterlitz-Thouless temperatures in 2D are found from the intersection point of the straight line $\frac{2}{\pi}k_B T$ with the curve $\rho_s(T)$.

determination procedure.

First, we solve the system of the self-consistent equations for the order parameter,

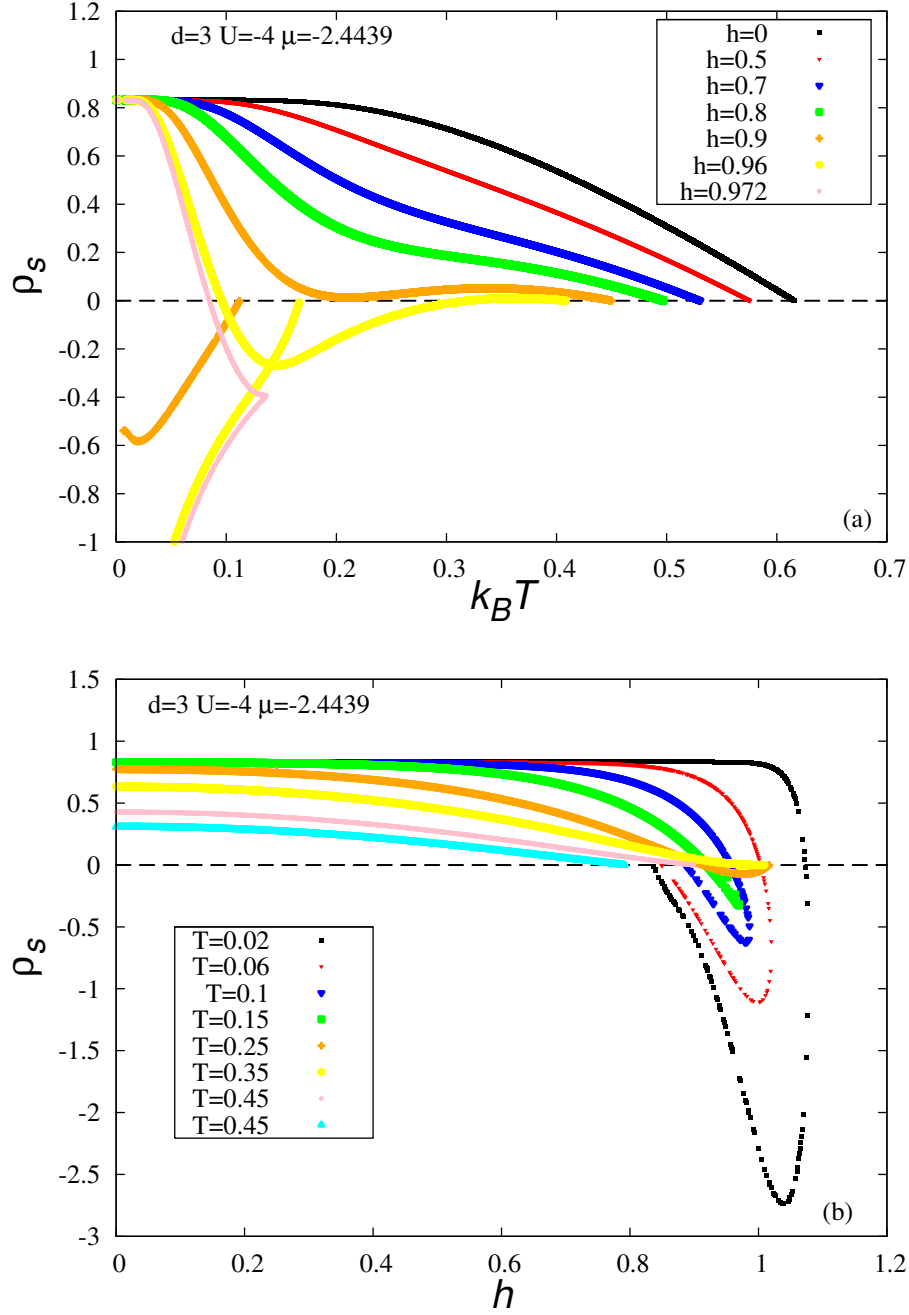


Figure 4.14: Superfluid density vs. temperature (a) and magnetic field (b) for the simple cubic lattice, $\mu \approx -2.4439$, $U = -4$.

chemical potential and magnetization, to determine ρ_s . For the s-wave pairing symmetry case, at $t^\uparrow = t^\downarrow$ and $h \neq 0$, we solve Eqs. (2.55), (4.4) and (4.5). We determine from these equations the values of Δ , $\bar{\mu}$, M and then we calculate the value of the superfluid

stiffness, from Eq. (3.35).

Let us consider the temperature dependencies of ρ_s . Figs. 4.13-4.14 show the superfluid density vs. magnetic field (a) and temperature (b), at fixed attractive interaction and a chemical potential, for $d = 2$ and $d = 3$, respectively.

The superfluid density is the highest in the ground state and falls to zero at the Hartree-Fock critical temperature. The decrease in ρ_s with the increasing temperature results from the paramagnetic part of the superfluid stiffness:

$$\rho_s^{para}(T) = \frac{1}{4N} \sum_{\vec{k}} \left\{ \left(\frac{\partial \epsilon_{\vec{k}}}{\partial k_x} \right)^2 \left[\frac{\partial f(E_{\vec{k}\uparrow})}{\partial E_{\vec{k}\uparrow}} + \frac{\partial f(E_{\vec{k}\downarrow})}{\partial E_{\vec{k}\downarrow}} \right] \right\}, \quad (4.9)$$

which increases with temperature and compensates the diamagnetic part of ρ_s :

$$\rho_s^{dia}(T) = \frac{1}{4N} \sum_k \left\{ \frac{\partial^2 \epsilon_{\vec{k}}}{\partial k_x^2} \left[1 - \frac{\bar{\epsilon}_{\vec{k}}}{2\omega_{\vec{k}}} \left(\tanh \left(\frac{\beta E_{\vec{k}\uparrow}}{2} \right) + \tanh \left(\frac{\beta E_{\vec{k}\downarrow}}{2} \right) \right) \right] \right\}. \quad (4.10)$$

If the excitations in the system have non-zero minimum energy at $h = 0$ (e.g. for the s-wave pairing symmetry), there is no significant decrease in $\rho_s(T)$ in low temperatures.

As mentioned above, there is a change in the character of the phase transition from the second to the first order with increasing magnetic field, which is also reflected in the ρ_s dependences. If the transition is of second order, the superfluid stiffness tends to zero continuously, at the mean-field transition point (in which the order parameter drops to zero). However, the situation is more complex for the first order phase transition. Then, there arise two non-zero solutions for the order parameter and also for the superfluid density. The lower branches are always energetically unstable. Therefore, $\rho_s < 0$ which means that these solutions are also dynamically unstable (see: Fig. 4.13(a), $h = 0.21$, $h = 0.23$ and Fig. 4.14(a), $h = 0.9$, $h = 0.96$, $h = 0.972$). However, one can find that ρ_s drops below zero for $h < h_c^{HF}$ ($h < h_c^{HF}$ – Hartree-Fock critical magnetic field) (see: Fig. 4.13(b), $T = 0.05$, $T = 0.07$, $T = 0.09$ and Fig. 4.14(b), $T = 0.25$, $T = 0.35$), afterwards increases to zero in the HF critical magnetic field. Therefore, there exists a region for which ρ_s is negative, despite the energetic stability. Then, the whole range of the reentrant transition, which is discussed above in details, turns out to be unstable, which is particularly important in the $d = 3$ case. This aspect of the reentrant transition will be analyzed in next section, which concerns the determination of the Hartree-Fock and Kosterlitz-Thouless critical temperature and also the phase diagrams construction.

4.2.2 Phase diagrams

In this subsection, we focus on the temperature phase diagrams for fixed chemical potential and electron concentration. We analyze the weak attraction case for $d = 2$ and $d = 3$.

One of the basic quantities characterizing the superconductor is the critical temperature (T_c). The theory of the second-order phase transitions was intensively studied by Landau in the 1930s. He found that a change in the symmetry of the system accompanies

each second-order phase transition. Therefore, Landau introduced a quantity called the order parameter to the theory. The order parameter is nonzero below T_c , but becomes zero above T_c , in the disordered state [116].

According to the Ginzburg-Landau theory [117], the order parameter ψ is zero above T_c of the superconductor, in the normal state and below T_c it is nonzero, in the superconducting phase. Then, one can write:

$$\psi = \begin{cases} 0 & \text{if } T > T_c \\ \psi(T) \neq 0 & \text{if } T < T_c \end{cases} \quad (4.11)$$

where ψ is a complex function.

Gor'kov showed that from the microscopic point of view, the order parameter ψ is related to the local value of the superconducting gap Δ [118].

The free energy F of the superconducting state shows a continuous dependence on ψ . As F is real and ψ is complex, the free energy can be dependent on $|\psi|$. Now, we can Taylor expand F in powers of $|\psi|$, because $\psi \rightarrow 0$ at the critical temperature. Therefore, the free energy density ($f \equiv F/V$) takes the form:

$$f_s(T) = f_n(T) + a(T)|\psi|^2 + \frac{1}{2}b(T)|\psi|^4 + \dots, \quad (4.12)$$

where $f_s(T)$ and $f_n(T)$ are the superconducting and normal free energy densities, respectively. $a(T)$, $b(T)$ – phenomenological parameters of the theory. Parameter $b(T)$ must be positive, so that the free energy density has a minimum. Above T_c , $a(T)$ is positive and the free energy density has one minimum at $\psi = 0$ and the system is in the normal state. However, if $a(T)$ decreases with decreasing temperature, the state of the system changes at $a(T) = 0$, i.e. for $T < T_c$ the free energy has a minimum at $\psi \neq 0$. Therefore, the temperature at $a(T) = 0$ can be identified as the critical temperature T_c .

As mentioned above, according to the BCS theory, it is the temperature at which the energy gap vanishes. We have to solve Eqs. (2.55)-(4.5) to determine T_c^{HF} . If $\Delta = 0$, the set of equations (2.55)-(4.5) for the s-wave pairing symmetry takes the form:

$$1 = -\frac{U}{N} \sum_{\vec{k}} \frac{1}{2(\epsilon_{\vec{k}} - \bar{\mu})} \left(\frac{1}{2} \tanh \left[\frac{\beta_c}{2} \left(\frac{UM}{2} + h + \epsilon_{\vec{k}} - \bar{\mu} \right) \right] + \frac{1}{2} \tanh \left[\frac{\beta_c}{2} \left(-\frac{UM}{2} - h - \epsilon_{\vec{k}} + \bar{\mu} \right) \right] \right), \quad (4.13)$$

$$n = 1 - \frac{1}{N} \sum_{\vec{k}} \frac{1}{4} \left(\tanh \left[\frac{\beta_c}{2} \left(\frac{UM}{2} + h + \epsilon_{\vec{k}} - \bar{\mu} \right) \right] - \tanh \left[\frac{\beta_c}{2} \left(-\frac{UM}{2} - h - \epsilon_{\vec{k}} + \bar{\mu} \right) \right] \right), \quad (4.14)$$

$$M = \frac{1}{2N} \sum_{\vec{k}} \left(\tanh \left[\frac{\beta_c}{2} \left(\frac{UM}{2} + h + \epsilon_{\vec{k}} - \bar{\mu} \right) \right] - \tanh \left[\frac{\beta_c}{2} \left(-\frac{UM}{2} - h - \epsilon_{\vec{k}} + \bar{\mu} \right) \right] \right). \quad (4.15)$$

It should be emphasized that the temperature in which the gap vanishes is closely related to the value of Δ in the ground state, i.e. the higher value of Δ at $T = 0$, the higher critical temperature can be expected.

The above method of the critical temperatures determination for the 2D superconductors can lead to an overestimate of T_c , because we neglect the fluctuation effects. However, the fluctuations play a crucial role in these systems. As mentioned above, the influence of the fluctuations can be included by the assumption that the phase transition from the superconducting to the normal state is the Kosterlitz-Thouless transition, with a characteristic jump in the superfluid stiffness $\frac{2}{\pi}$ at T_c . According to Eq. (3.11), the KT transition temperature is found from the intersection point of the straight line $\frac{2}{\pi}k_B T$ with the curve $\rho_s(T)$ in 2D (Fig. 4.13(a)).

The properties of the superfluid density which determines T_c^{KT} are described in the previous section. Now, we focus on the temperature phase diagrams for fixed chemical potential and electron concentration.

Fig. 4.15 shows $h - T$ phase diagrams, for the square lattice. Both the case of a fixed chemical potential with the Hartree term (a) and the case without the Hartree term (b) are presented. The chemical potential is chosen to yield $n \approx 0.75$ at $T = 0$ and $h = 0$. Similar results for a simple cubic lattice were obtained using the Hartree approximation (Fig. 4.15(c)). Fig. 4.16 shows $h - T$ phase diagrams for fixed $n = 0.75$ and $d = 2$. Thus, one can compare the fixed chemical potential and the fixed electron concentration cases in finite temperatures.

The temperature at which the amplitude of the order parameter reaches zero is that at which the Cooper pairs no longer exist. According to the BCS theory, this is the temperature of the pairs breaking and also the temperature of the second order transition from the superconducting to the normal state.

For a sufficiently low magnetic field, there is a KT transition from qSC($P \neq 0$) to NO through the region of incoherent pairs (so-called *pseudogap* region), below the HF critical temperature. With increasing magnetic field, the character of the qSC-NO transition changes from the second order to the first order. The curve below the first order transition line on the phase diagrams (the thin dashed line) is the extension of the HF second order transition line (metastable solutions). The dash-dotted line (above the first order transition line) constrains the range of occurrence of the FFLO state (the upper limit). Above this line, solutions with $\Delta \neq 0$ no longer exist. Moreover, one obtains the phase separation region in the $h - T$ diagram for the fixed $n \neq 1$, as opposed to the fixed μ case.

T_c^{KT} are much lower than T_c^{HF} . The range in which differences between the T_c^{KT} and T_c^{HF} temperatures occur can be read from the order parameter and ρ_s temperature dependences. As shown in the previous section, ρ_s reaches a maximum value in the ground

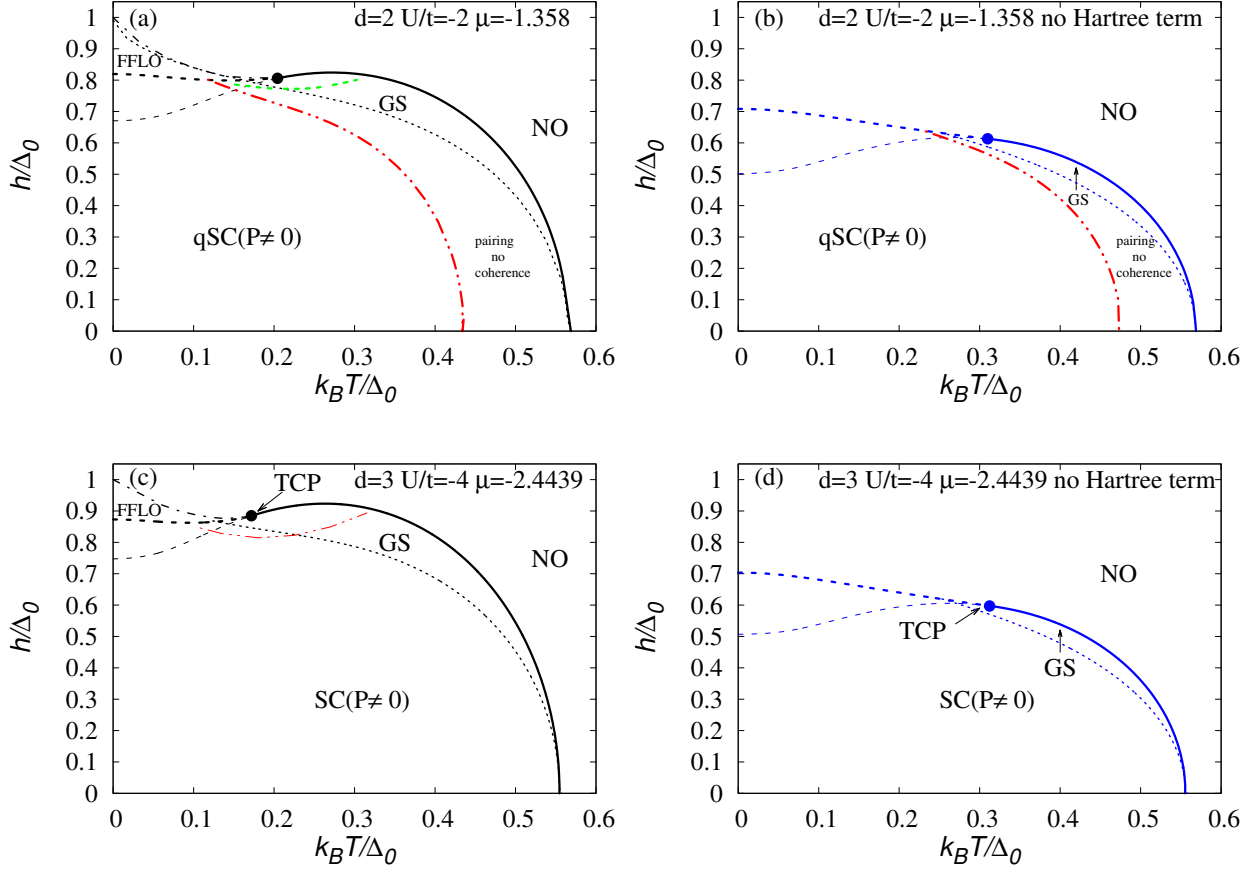


Figure 4.15: Temperature vs. magnetic field phase diagrams for $U = -2$ and fixed chemical potential $\mu \approx -1.358$. (a) diagram with Hartree term, (b) without Hartree term (blue color). (c) phase diagrams for $d = 3$, $U = 4$, $\mu \approx -2.4439$. The thick solid line is the second order phase transition line from pairing without coherence region to NO (Hartree approximation). The thin dashed line is an extension of the 2^{nd} order transition line (metastable solutions). The dashed-dotted line indicates the upper limit for the occurrence of the FFL0 state. The thick dashed-double dotted line (red color) is the Kosterlitz-Thouless transition line. The dashed green line limits the region with $\rho_s < 0$. The thick dotted line denotes the first order phase transition to NO, GS – gapless region. The chemical potential is chosen to yield $n \approx 0.75$ in the case of the Hartree term included, at $T = 0$ and $h = 0$. Δ_0 denotes the gap at $T = 0$ and $h = 0$.

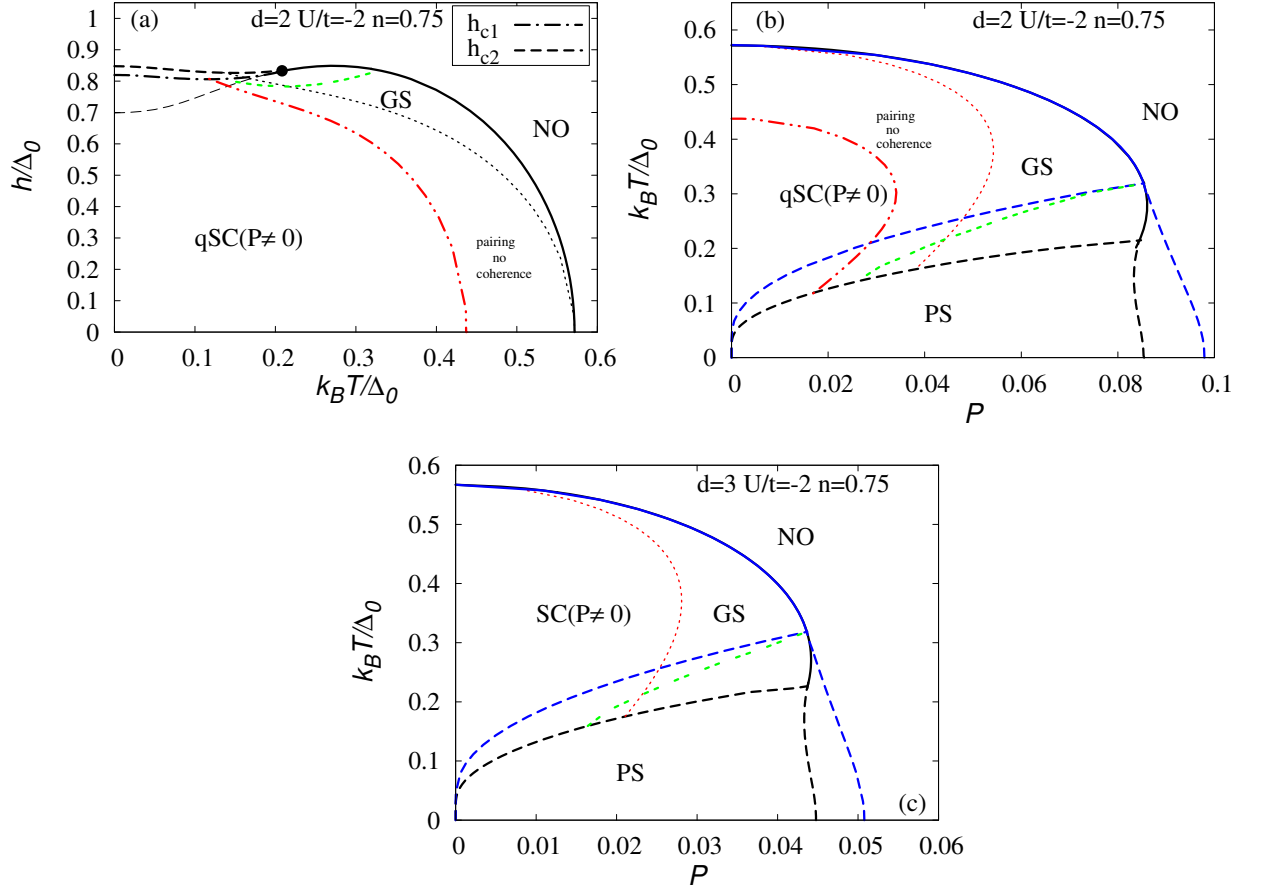


Figure 4.16: Temperature vs. magnetic field (a) and polarization (b) phase diagrams for square lattice, (c) T vs. P phase diagrams for simple cubic lattice; fixed $U = -2$ and $n = 0.75$. The thick dashed lines are the first order phase transition lines. The upper set of curves denotes the diagram without the Hartree term (blue color), red line limits the GS region. The dashed green line limits the region with $\rho_s < 0$. Δ_0 denotes the gap at $T = 0$ and $P = 0$.

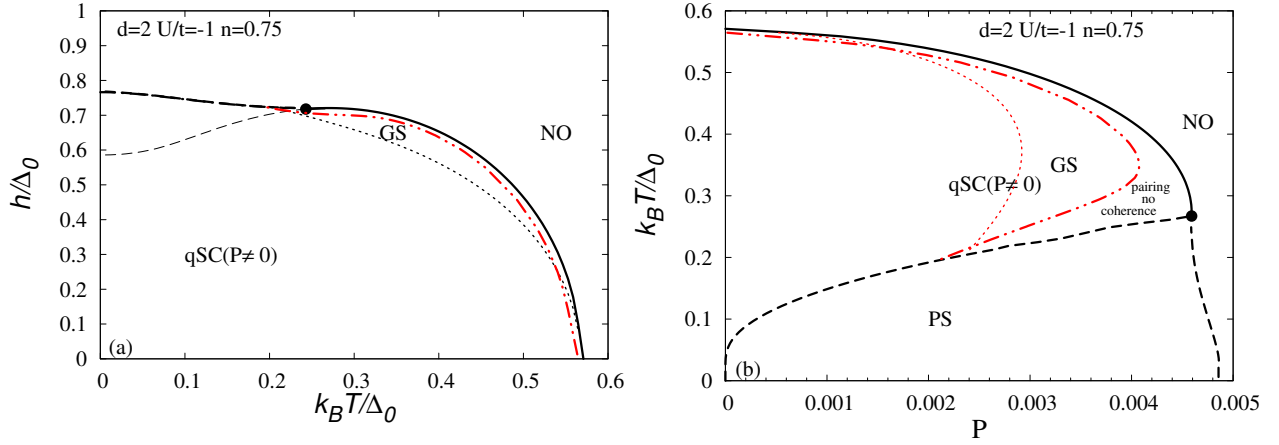


Figure 4.17: Temperature vs. magnetic field (a) and polarization (b) phase diagrams with the Hartree term, for the square lattice, fixed $U = -1$ and $n = 0.75$. The thick dashed-double dotted line (red color) is the Kosterlitz-Thouless transition line, thick dashed lines are the first order phase transition lines, GS – gapless region. Δ_0 denotes the gap at $T = 0$ and $P = 0$.

state and drops to zero at T_c^{HF} . The Kosterlitz-Thouless temperature is also limited by the value of the superfluid stiffness at $T = 0$ and, simultaneously, it must be lower than T_c^{HF} , which is proportional to the value of the order parameter in the ground state. Thus, comparing the values of Δ and ρ_s at $T = 0$, we can expect that whenever the order parameter is much smaller than the superfluid density, the quantity which limits T_c^{KT} is T_c^{HF} . The Kosterlitz-Thouless temperatures approach the Hartree-Fock temperatures in this region. If ρ_s is smaller than the order parameter, the value of T_c^{KT} can be estimated from the value of ρ_s at $T = 0$:

$$k_B T_c^{KT} \approx \frac{\pi}{2} \rho_s(T = 0). \quad (4.16)$$

The above dependence gives the upper limit for the temperatures in which the phase ordering appears. The smaller the value of ρ_s than the value of the order parameter, the larger the difference between the Kosterlitz-Thouless and Hartree-Fock temperatures. The order parameter increases with increasing attractive interaction, while the value of the superfluid stiffness decreases with increasing $|U|$ [106, 119]. Therefore, one can expect an increase in the differences between T_c^{KT} and T_c^{HF} . In turn, if the attraction decreases, the differences between T_c^{KT} and T_c^{HF} are smaller, which is clearly visible in Fig. 4.17 at fixed $n = 0.75$ and $U = -1$, with respect to Fig. 4.16 at $U = -2$.

An important aspect of the analysis is the influence of the Hartree term on the phase diagrams. Firstly, the presence of the Hartree term leads to the reentrant transition (RT), which is not observed in the phase diagrams without the Hartree term (blue color in Figs. 4.15(b), (d)). We also find the region in which $\rho_s < 0$ although $\Omega^{SC} < \Omega^{NO}$ (green double-dashed lines), in the phase diagrams with the Hartree term. If RT exists,

it becomes unstable because $\rho_s < 0$. However, the existence of RT does not influence the existence of the region with $\rho_s < 0$, i.e. even if there is no RT in the phase diagrams with the Hartree term, there is a region with $\rho_s < 0$ in the weak coupling limit. It is highly relevant especially for $d = 3$ (Fig. 4.16(c)), because it means that there exists an instability of the homogeneous superconducting state. This would suggest the existence of a stable FFLO state in the weak coupling regime. The Hartree term induces an increase in the Chandrasekhar-Clogston limit. It is worth mentioning that the Hartree term narrows the range of PS occurrence, which is clearly seen in $P - T$ diagrams (Fig. 4.16(b)-(c)).

Analyzing the spectrum of quasiparticle excitations, we also find a gapless region (GS), for $h > \Delta$ and at $T \neq 0$, i.e. the region, which has a gapless spectrum for the majority spin species (see: Appendix C).

Therefore, for fixed n one can distinguish the following states in $P - T$ diagrams. At $T \geq 0$ and $P = 0$ there is the unpolarized SC phase. At $T \neq 0$, $\Delta \neq 0$ and $P \neq 0$ (i.e. homogeneous superconductivity in the presence of the spin polarization), the system is also in SC (or in qSC in $d = 2$), but this region is narrowed (in diagrams with the Hartree term) through the area with $\rho_s < 0$. One can observe GS at sufficiently high values of the magnetic field. In the PS region, not only the polarizations, but also the particle densities in SC and NO are different. From a comparison of the two- and the three- dimensional cases, we find that the critical values of polarizations for the simple cubic lattice are lower than for the square lattice. Taking into account the phase fluctuations in $d = 2$, the region of incoherent pairs can be distinguished.

4.3 The influence of the pure d-wave pairing symmetry on the polarized superconducting phase stability

In this section, we briefly discuss the superfluid properties of the Extended Hubbard Model (2.15) with spin independent hopping integrals, in a magnetic field. We take into account only the pure d-wave pairing symmetry case. Then $W < 0$ and the equation for the order parameter takes the form:

$$\frac{4}{|W|} = \frac{1}{N} \sum_{\vec{k}} \frac{\eta_{\vec{k}}^2}{2\omega_{\vec{k}}} (1 - f(E_{\vec{k}\uparrow}) - f(E_{\vec{k}\downarrow})), \quad (4.17)$$

where: $\eta_{\vec{k}} = 2(\cos k_x - \cos k_y)$, $E_{\vec{k}\downarrow,\uparrow} = \pm h + \omega_{\vec{k}}$, $\omega_{\vec{k}} = \sqrt{\epsilon_{\vec{k}} + (\eta_{\vec{k}}\Delta_{\vec{k}})^2}$

Our motivation to study this kind of pairing symmetry is not only the interest in high-temperature superconductivity, but also the possibility of existence of new phases with non-trivial Cooper pairing mechanism in imbalanced Fermi gases [109].

One of the most important quantities related to superconductivity is the gap parameter. As well known, the BCS theory predicts the existence of an isotropic order parameter, which vanishes at the temperature of the superconductor-normal phase transition. However, intensive studies of the gap parameter for high- T_c superconductors indicate significant deviations from the predictions of the BCS theory. Accurate determination of

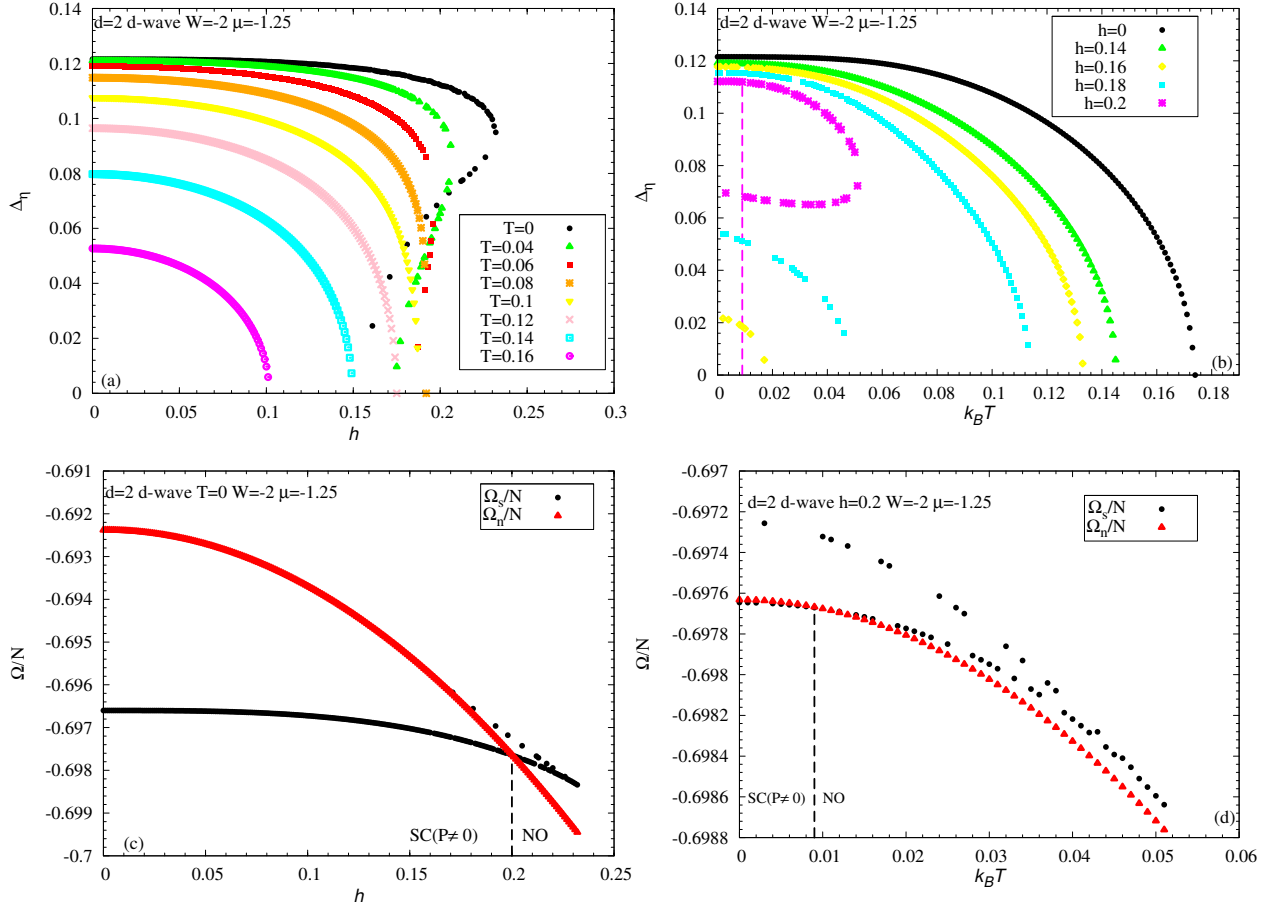


Figure 4.18: Dependence of Δ_η on the magnetic field (a) and temperature (b), $W/t = -2$, $U = 0$, for a fixed $\mu = -1.25$. In Fig. (b), for $h = 0.16$ and $h = 0.18$ the lower branches are unstable. For $h = 0.2$ the vertical dashed line denotes the first order phase transition from the magnetized superconducting state (SC($P \neq 0$)) to the normal state (NO). (c) The grand canonical potential (Ω) vs. h at $T = 0$ (first order phase transition); (d) Ω vs. T at $h = 0.2$.

the gap parameter encounters many difficulties. Most of the measurements show that its value in the ground state is much higher than the value of Δ in conventional superconductors [120]. The width of the gap is usually expressed in $k_B T$ units. For the superconductors to which the BCS theory applies, this ratio is around 3.5, while for the high- T_c superconductors it varies from 5 to 8, which corresponds to the energy gap value of around 50 meV. The symmetry of the energy gap can be determined from measurements of changes in its magnitude for different momentum directions $|\Delta_{\vec{k}}|$. Most studies indicate the $d_{x^2-y^2}$ pairing symmetry (with the energy gap $\Delta_{\vec{k}} = 2\Delta_\eta(\cos(k_x) - \cos(k_y))$) [121, 122, 123, 124, 125, 126].

The d-wave pairing symmetry is also very interesting from the point of view of the breached pair (BP) state (or Sarma phase) in imbalanced ultracold Fermi gases.

As in section 4.1, we start from the analysis of the influence of magnetic field on the order parameter characteristics.

If $h = 0$, in the case of the d-wave pairing symmetry, the energy gap vanishes for some values of the wave vector \vec{k} , i.e. along the lines $|k_x| = |k_y|$. Disappearance of the gap on the Fermi surface leads to the existence of zero energy quasiparticles. Therefore, it is justified to believe that the Sarma-type phases ($SC(P \neq 0)$) will be stable at $h \neq 0$, as opposed to the s-wave pairing symmetry case in 2D.

Fig. 4.18 shows the dependence of the order parameter amplitude (Δ_η) on magnetic field (a) and temperature (b), for $W = -2$, $\mu = -1.25$. As shown in Fig. 4.18(a), there are two different solutions for $\Delta_\eta \neq 0$, at $T = 0$, as in the s-wave pairing symmetry case. However, as opposed to the isotropic order parameter case (Fig. 4.1), the upper branch of the solutions of Δ_η is dependent on the magnetic field in the ground state. Therefore, a finite polarization occurs in the system, for an arbitrarily small value of the magnetic field, even at $T = 0$. This is explained by the creation of polarized excitations in the nodal points of the gap [127, 128]. Moreover, this branch is stable up to $h \approx 0.2$. At this point, the first order phase transition from the polarized superconducting to the normal state occurs. On the other hand, the lower branch, which also depends on h , is unstable at $T = 0$.

Obviously, the polarization increases with increasing temperature. Thus, the range of occurrence of the Sarma-type phase (the superconducting state with $P \neq 0$) increases.

As mentioned above, the d-wave pairing symmetry at $h = 0$ is gapless ($\Delta_{\vec{k}} = \Delta_\eta \eta_{\vec{k}} = 0$ at $|k_x| = |k_y|$) in four nodal points on the Fermi surface [129]. In the weak coupling limit, at $h = 0$, the nodal points are located at $\approx (\pm\frac{\pi}{2}, \pm\frac{\pi}{2})$. However, the gap (E_g) in the density of states is fixed by the location of the logarithmic singularities. The value of E_g is determined by the maximum value of the energy gap: $E_g = 2\Delta_{max}$, where $\Delta_{max} = 4\Delta_\eta$. An example of the density of states for the d-wave pairing symmetry, at $h = 0$ is shown in Fig. 4.19(a). At $h = 0$, the quasiparticle energies (Fig. 4.20(a)) for spin-up and spin-down are equal ($E_{\vec{k}\uparrow} = E_{\vec{k}\downarrow} \equiv E_{\vec{k}}$) and the quasiparticle spectrum function has one zero at the Fermi level. There is one (equal for both directions of spin) Fermi surface in the system. The momentum distribution function is a step function, as for the Fermi distribution in the ground state. The step change of $n_{\vec{k}}$ occurs in the nodal points on the diagonal of the Fermi surface.

The influence of the Zeeman magnetic field on the density of states, shown in Fig. 4.19(b), is analogous to that in the s-wave pairing symmetry case (see Fig. 4.3), i.e. $g_\uparrow(E)$ is shifted to the left and $g_\downarrow(E)$ to the right by the value of the magnetic field h . The corresponding quasiparticle energies are plotted in Fig. 4.20(b). The gap appears in the spectrum for the minority spin species and equals h , while the spectrum for the majority spin species is gapless. The occurrence of the gap in $E_{\vec{k}\downarrow}$ is caused by the existence of some minimum non-zero quasiparticle energy. The quasiparticle branch for the majority spin species ($E_{\vec{k}\uparrow}$) has two zeros, which indicates the occurrence of two Fermi surfaces in the system. This is confirmed in the plots of the momentum distribution along the diagonal $|k_x| = |k_y|$. If $h > 0$, there appears a region where $n_{\vec{k}\downarrow}$ has already vanished, while still $n_{\vec{k}\uparrow} = 1$, i.e. the Fermi momentum for the majority spin species is higher than

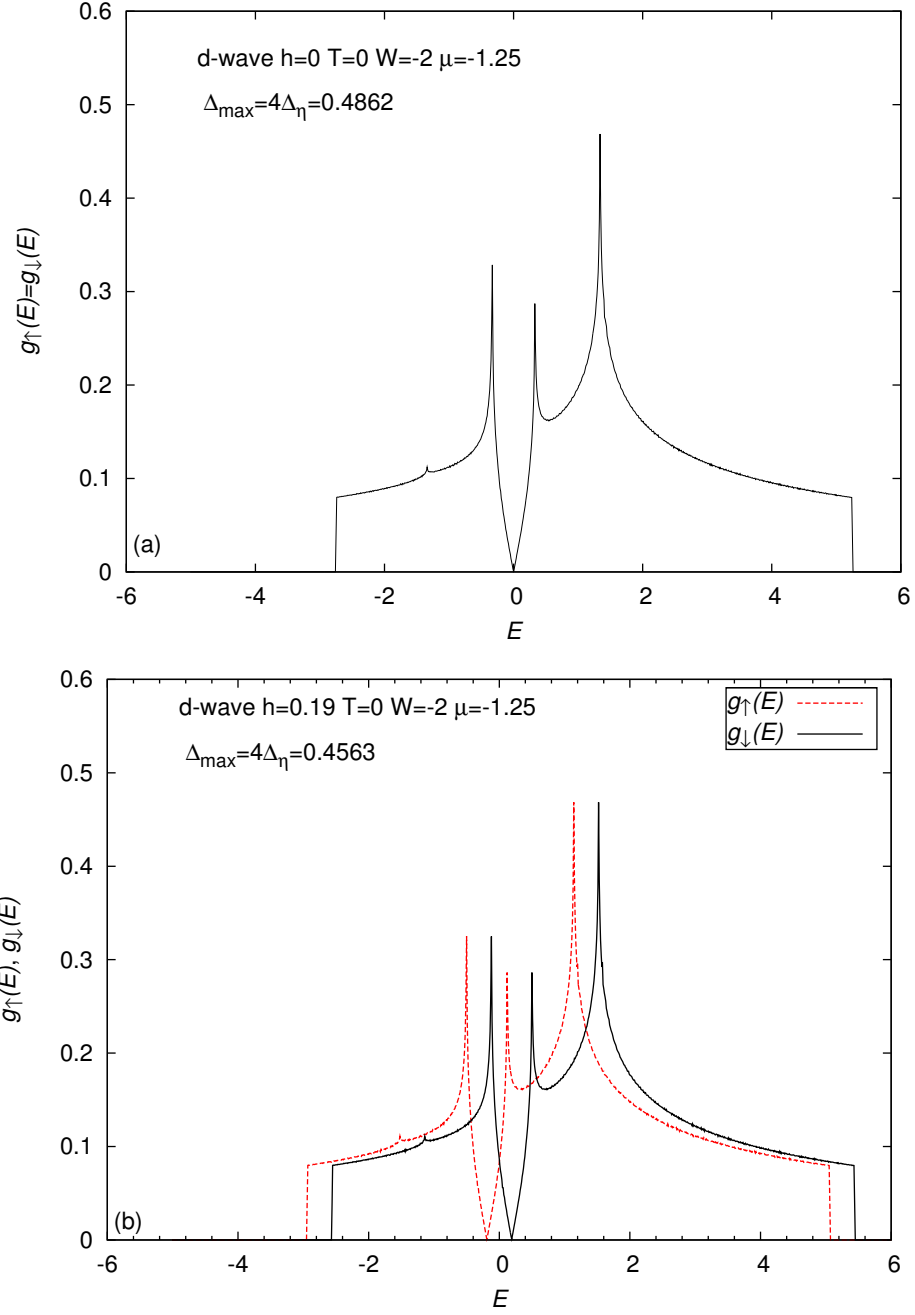


Figure 4.19: Density of states for $W = -2$, $U = 0$, $\mu = -1.25$, (a) $h = 0$ and (b) $h = 0.19$ at $T = 0$.

the one for the minority spin species.

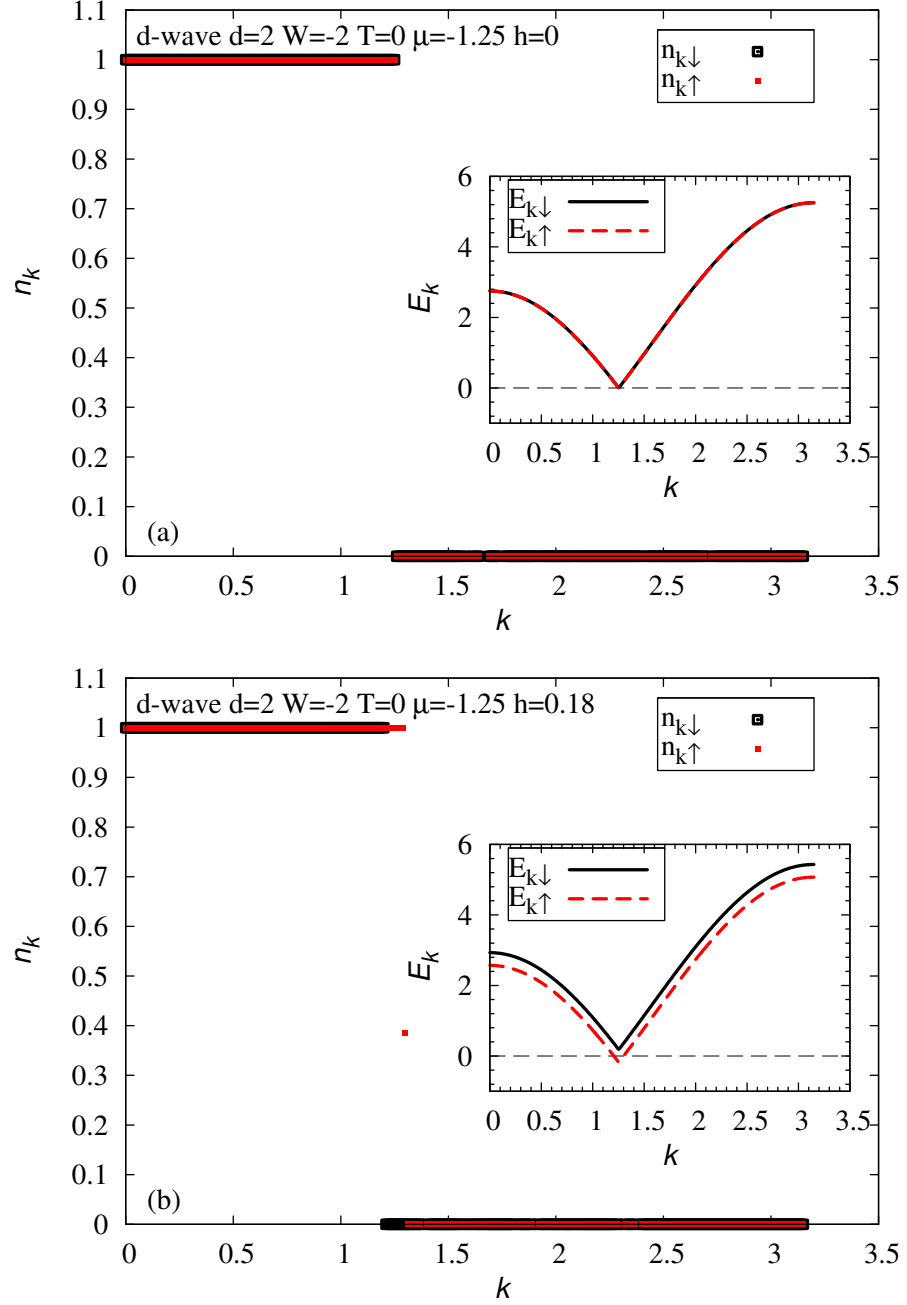


Figure 4.20: Plots of momentum occupation numbers $n_{\vec{k}\uparrow}$ (red points), $n_{\vec{k}\downarrow}$ (black points) vs. $k \equiv |k_x| = |k_y|$ and the corresponding quasiparticle spectra $E_{\vec{k}\uparrow}$, $E_{\vec{k}\downarrow}$ (inset) for $W = -2$, $\mu = -1.25$, $h = 0$ (a) and $h = 0.18$ (b).

Now, let us consider the ground state phase diagrams for the d-wave pairing symmetry

case, in the weak coupling regime. Both the fixed chemical potential and the fixed electron concentration case are analyzed. The influence of the Hartree term on the stability of the magnetized superfluid phases is not considered.

In the s-wave case and in the weak coupling regime, the SC_0 superconducting phase (with $P = 0$) is stable at $T = 0$. However, the analysis of the d-wave order parameter behavior, the density of states and the momentum distributions characteristics indicate the possibility of the occurrence of stable $SC(P \neq 0)$ phase at $T = 0$, even in the weak coupling regime, as opposed to the s-wave pairing symmetry case in 2D (Figs. 4.5(a), 4.6(a)). As shown above, for infinitesimally low value of the magnetic field, the $SC(P \neq 0)$ state is stable. Due to the vanishing of the gap at four nodal points on the Fermi surface, there is a spin-polarized normal state, at $h \neq 0$. Therefore, the $SC(P \neq 0)$ phase is the superfluid state of coexisting Cooper pairs and excess fermions, with the latter responsible for finite polarization (magnetization) and the gapless excitations characteristic for this state.

At higher values of the Zeeman magnetic field, $SC(P \neq 0)$ is destroyed by the paramagnetic effect or by population imbalance. Then, there is the first order phase transition from the polarized superconducting phase to the polarized normal state (Fig. 4.21(a)-(b)). The first order transition is manifested by the presence of the phase separation (PS) region in the phase diagrams at fixed n (see: Fig. 4.21(b)). The phase separation occurs between $SC(P \neq 0)$ with the number of particles n_s and NO with the number of particles n_n . It is worth mentioning that the d-wave superfluidity is stable around the half-filled band in the weak coupling limit and its range of occurrence widens with increasing attractive interaction.

Let us discuss the finite temperature phase diagrams. However, first let us analyze briefly the influence of the Zeeman magnetic field on the superfluid density characteristics. Fig. 4.22 shows the dependence of ρ_s on temperature (a) and magnetic field (b), for the d-wave pairing symmetry, $W = -2$ and $\mu = -1.25$. As mentioned before, the superfluid stiffness is the largest in the ground state and drops to zero at T_c^{HF} . The pairing symmetry plays the crucial role in the temperature dependences. For the d-wave pairing symmetry, at $h = 0$, ρ_s decreases linearly. This dependence is significantly different for the s-wave pairing symmetry case (Fig. 4.13(a)).

The magnetic field has a clear influence on the temperature characteristics of the superfluid stiffness. The example dependences, for some chosen values of h , are presented in Fig. 4.22(a). One can see that the differences in the shapes of the plots for s-wave and d-wave pairing symmetries decrease at $h \neq 0$. The linearity of the plot vanishes for the d-wave pairing symmetry, in the presence of the magnetic field.

As mentioned above, the quasiparticle energy can be zero, for the d-wave pairing symmetry. It takes place when $\Delta_{\vec{k}} = 0$ on the Fermi surface (nodal points). The existence of the zero-energy excitations can increase the value of ρ_s^{para} significantly, because of the presence of the derivatives in Eq. (4.9). In this case, one observes a sudden decrease of ρ_s and the temperature dependence has a linear character. However, if $h \neq 0$, the excitations in the system have some minimum non-zero energy for the minority spin species ($E_{\vec{k}\downarrow}$) and there is no significant decrease of $\rho_s(T)$ at low temperatures.

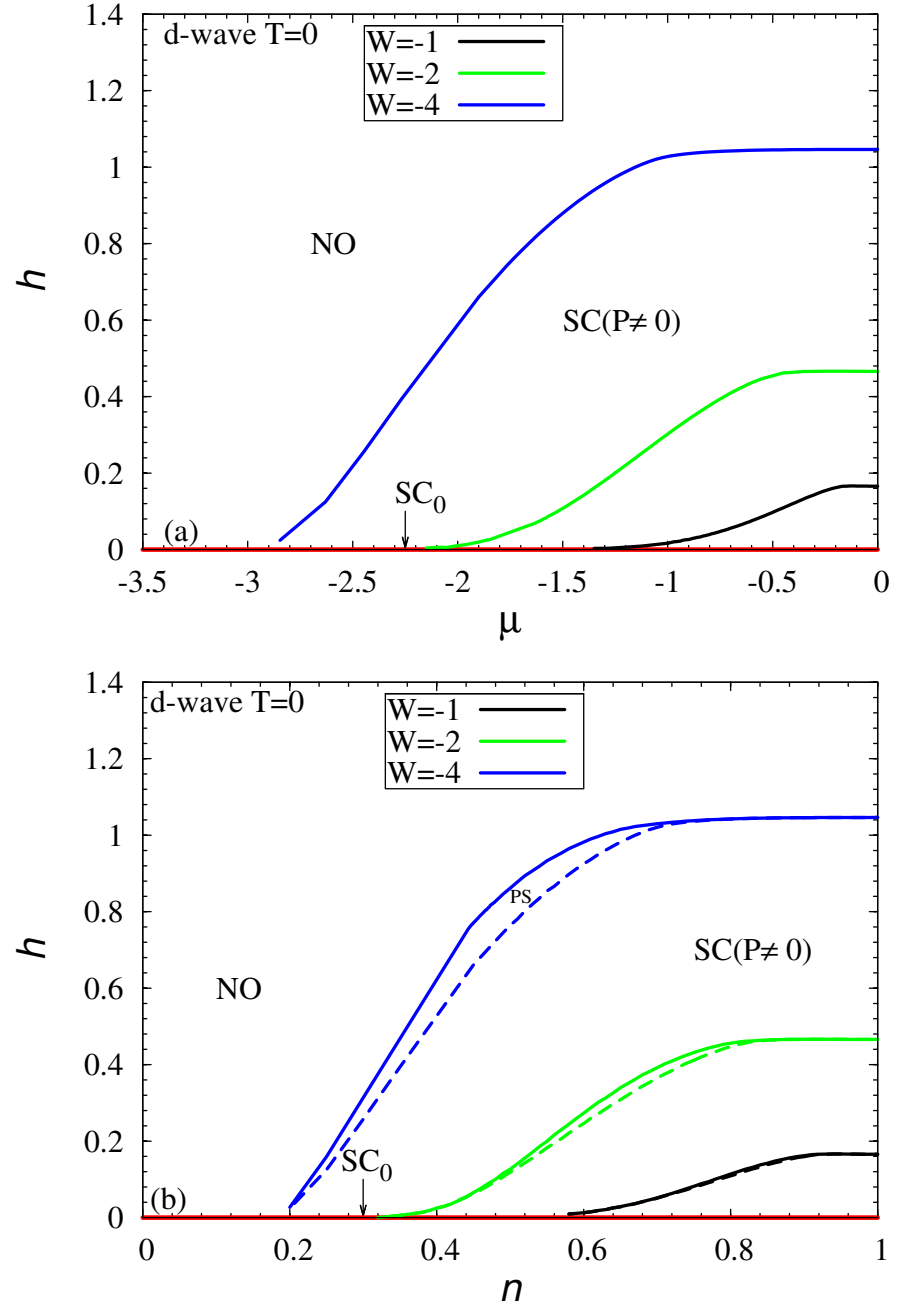


Figure 4.21: Critical magnetic field vs. chemical potential (a) and electron concentration (b) for the first order SC($P \neq 0$)-NO transition, at $T = 0$; three different values of the attractive interaction.

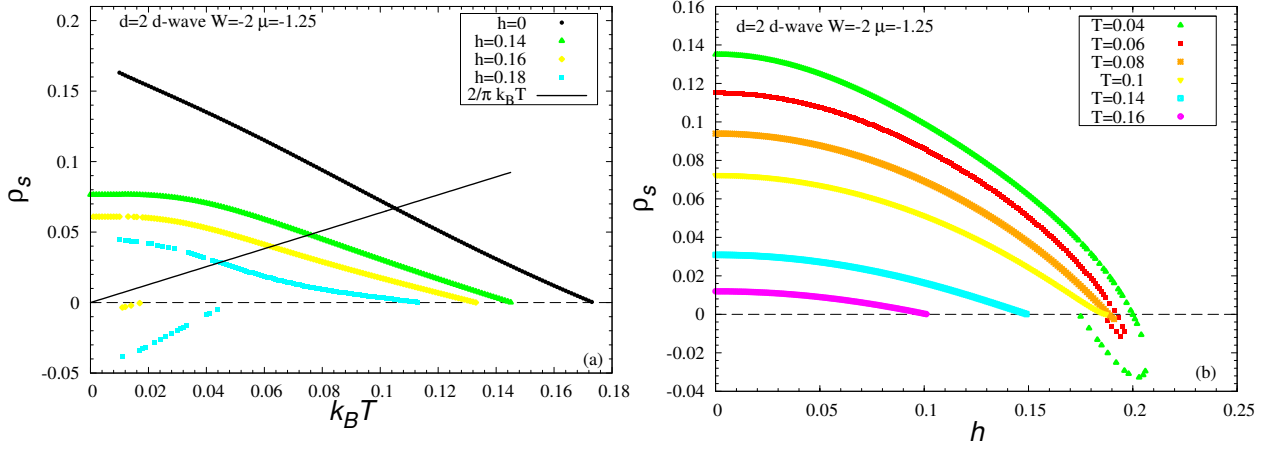


Figure 4.22: Superfluid density vs. temperature (a) and magnetic field (b) for 2D d-wave pairing symmetry, $\mu = -1.25$, $W = -2$, $U = 0$. The Kosterlitz-Thouless temperatures in 2D are found from the intersection point of the straight line $\frac{2}{\pi}k_B T$ with the curve $\rho_s(T)$.

As mentioned in the introduction to this thesis, the impact of the Zeeman coupling between the spins of the electrons and the applied magnetic field on superconductivity has been being analyzed for many years [53, 55, 56, 70, 130]. One of the well-known results concerning this influence is the existence of the *so-called* Chandrasekhar-Clogston limit. In the weak coupling regime, for the s-wave pairing symmetry case, at $T = 0$, the superconductivity is destroyed through the paramagnetic effect and the first order phase transition to the normal state at a universal value of the critical magnetic field $h_c = \Delta_0/\sqrt{2} \approx 0.707\Delta_0$, where Δ_0 is, as usual, the gap at $T = 0$ and $h = 0$. In turn, this universal value of the magnetic field in which the superconducting state is destroyed in the ground state, for the d-wave pairing symmetry case is: $h_c^{d-wave} = 0.56\Delta_{max}$ [128], where $\Delta_{max} = 4\Delta_\eta$ at $T = 0$ and $h = 0$.

Fig. 4.23 shows the temperature vs. magnetic field ($T - h$) and polarization ($T - P$) phase diagrams for $W = -2$ and three values of the chemical potential. These fixed values of μ correspond to lower values of n than $n = 1$, therefore the d-wave Chandrasekhar-Clogston limit is not reached. However, our results for $\mu = 0$ ($n = 1$) agree with the ones from the paper [128], i.e. indeed $h_c^{d-wave} = 0.56\Delta_{max}$ for this case.

We take into account the phase fluctuations in $d = 2$ within the KT scenario, as in the s-wave pairing symmetry case (Figs.: 4.15(a)-(b), 4.16(a)-(b), 4.17). In such way, we can estimate the phase coherence temperatures, in addition to the MF temperatures. The solid lines (2^{nd} order transition lines) and the PS region are obtained within the MF approximation. The curves below the first order phase transition lines on the phase diagrams (the thin dotted lines) are merely extensions of the 2^{nd} order transition lines below tricritical points. The thick dash-double dotted lines denote the KT transition. The system is a quasi superconductor (qSC) below T_c^{KT} . Between T_c^{KT} and T_c^{HF} pairs still exist, but without a long-range phase coherence (the pseudogap behavior). The KT temperatures are much smaller than T_c^{HF} . It can be seen particularly clearly for fixed

$\mu = -0.5$ or $n = 0.75$ (Fig. 4.24) and $W = -2$ cases – the difference between T_c^{KT} and T_c^{HF} amounts to nearly 50%. However, this difference decreases with decreasing μ (decreasing n) and decreasing attraction (in the weak coupling limit). Both for fixed μ and fixed n , a finite temperature second order phase transition takes place from the pairing without coherence region to the normal state at sufficiently low values of the magnetic field. With increasing h , the character of the transition between the pairing without coherence region and the normal state changes from the second to the first order, which is manifested by the existence of the MF tricritical point on the phase diagrams. In this MF TCP, the state of incoherent pairs, the normal phase and the phase separation region (in the case of fixed n) coexist. Therefore, the topology of the $(T - h)$ diagrams is the same as in the s-wave case.

However, qualitative differences between the s-wave and d-wave pairing symmetries are clearly visible in $(P - T)$ phase diagrams. At $T \geq 0$ and $P = 0$, there is the unpolarized superconducting phase, both for the s-wave and the d-wave pairing symmetry case. At $T = 0$, there is only the PS region, for the whole range of polarizations, i.e. $P > 0$, for the isotropic order parameter case. In turn, in the d-wave pairing symmetry case, there is the spin-polarized superconducting phase ($SC(P \neq 0)$) at $T = 0$, up to some critical value of the polarization, for which the first order phase transition to the normal state takes place. In the PS region, not only the polarizations, but also the particle densities in SC and NO are different. At $T = 0$ and for the s-wave pairing symmetry, this separation region is between the non-polarized superconducting phase and the normal state, while in the d-wave pairing symmetry it is between $SC(P \neq 0)$ and NO. At $T \neq 0$, $\Delta \neq 0$ and $P \neq 0$, the system is also in the polarized qSC phase (i.e. homogeneous superconductivity in the presence of the spin polarization) in the s-wave pairing symmetry case up to T_c^{KT} . The KT phase is restricted to the weak coupling region and low values of P , as in the d-wave pairing symmetry case. Increasing polarization favors the phase of incoherent pairs. As shown in Fig. 4.23(b), the range of occurrence of qSC in the presence of P widens in the weak coupling regime with increasing n (increasing μ). In the s-wave pairing symmetry case, one can distinguish the gapless region at sufficiently high values of the magnetic field and temperature. As mentioned before, the d-wave pairing symmetry at $h = 0$ is gapless ($\Delta_{\vec{k}} = \Delta_{\eta\vec{k}} = 0$ at $|k_x| = |k_y|$) in four nodal points on the Fermi surface. Therefore, a natural consequence of this is the occurrence of the gapless region also for infinitesimally low values of h , even at $T = 0$.

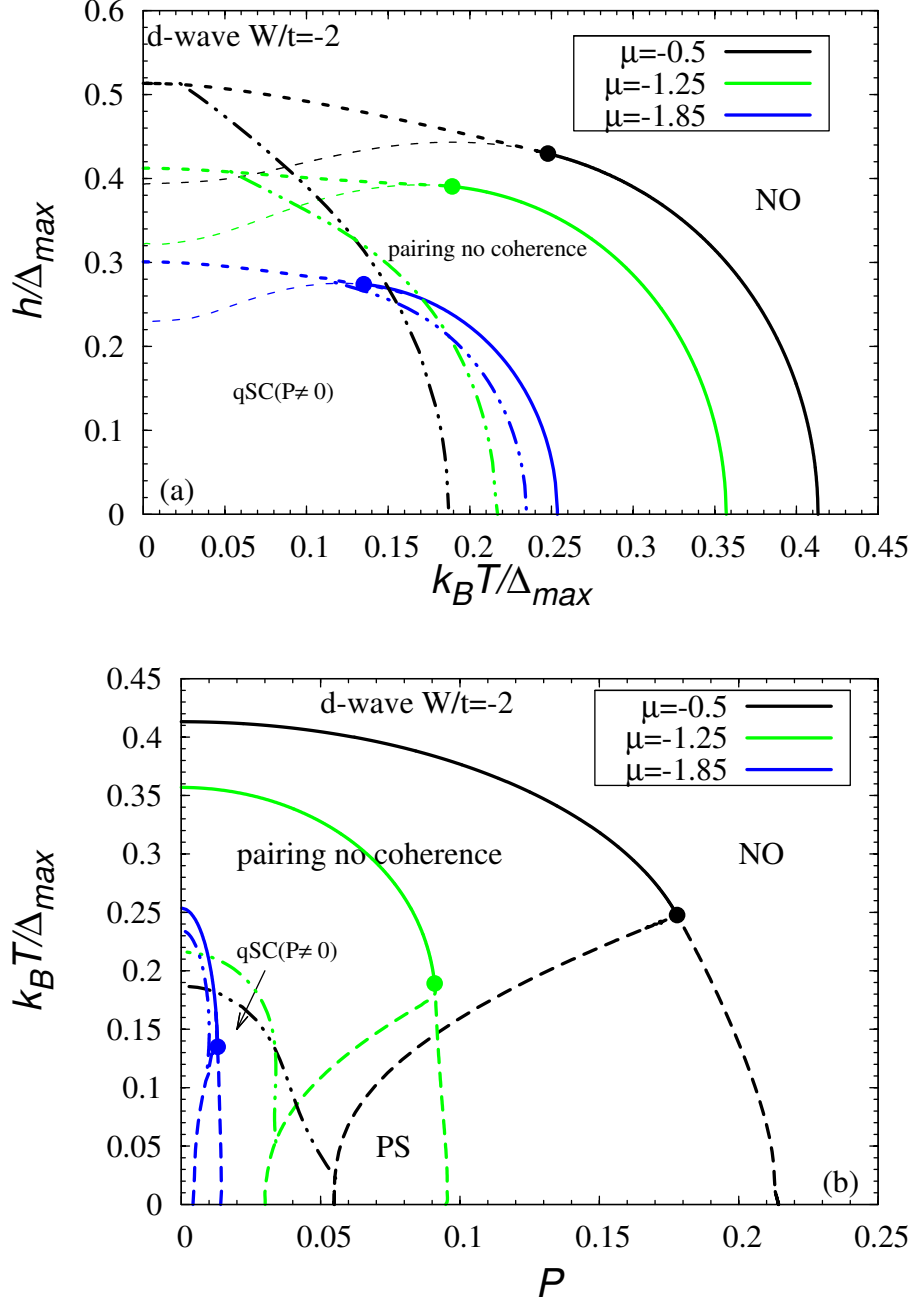


Figure 4.23: Temperature vs. magnetic field (a) and polarization (b) phase diagrams for $W = -2$, $U = 0$, three values of μ ; SC_0 – non-polarized superconducting state ($P = 0$), $SC(P \neq 0)$ – 2D superconductor in the presence of polarization, NO – partially-polarized normal state. The thick solid line is the second order phase transition line from the pairing without coherence region to NO . The thin dashed line is an extension of the 2^{nd} order transition line (metastable solutions). The thick dashed-double dotted line is the Kosterlitz-Thouless transition line. The thick dotted line denotes the first order phase transition to NO . $\Delta_{max} = 4\Delta_\eta$ denotes the gap at $T = 0$ and $h = 0$.

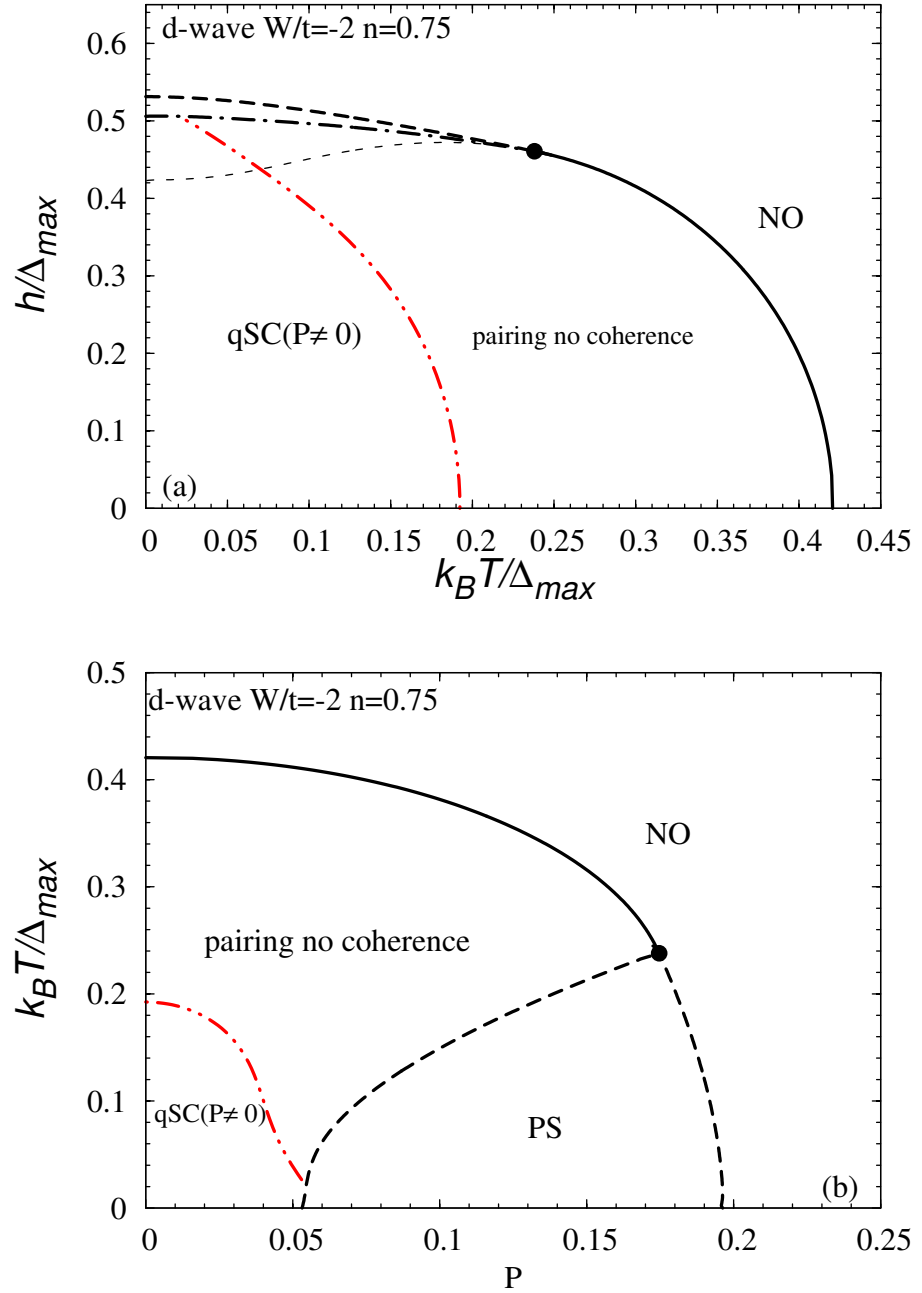


Figure 4.24: Temperature vs. magnetic field (a) and polarization (b) phase diagrams for $W = -2$, $U = 0$, $n = 0.75$; SC_0 – non-polarized superconducting state ($P = 0$), $SC(P \neq 0)$ – 2D superconductor in the presence of polarization, NO – partially-polarized normal state. The thick solid line is the second order phase transition line from the pairing without coherence region to NO. The thin dashed line is an extension of the 2^{nd} order transition line (metastable solutions). The thick dashed-double dotted line is the Kosterlitz-Thouless transition line. The thick dotted line denotes the first order phase transition to NO. $\Delta_{max} = 4\Delta_\eta$ denotes the gap at $T = 0$ and $h = 0$.

Chapter 5

The BCS-BEC crossover at $T = 0$ in the spin-polarized Attractive Hubbard Model with spin independent hopping integrals

In this chapter, we analyze the influence of magnetic field on the BCS-LP (BEC) crossover at $T = 0$, for $d = 2$ (square lattice) and $d = 3$ (simple cubic lattice), within the spin-polarized AHM. Development of experimental techniques in cold atomic Fermi gases with tunable attractive interactions (through Feshbach resonance) has allowed the study of the BCS-BEC crossover and the properties of exotic states in these systems.

In the strong coupling limit of AHM the tightly bound local pairs of fermions behave as hard-core bosons (see also Chapter 6 and 7) and can exhibit a superfluid state similar to that of $^4\text{He II}$ [27]. The evolution from the weak attraction (BCS-like) limit to that of the strong attraction (LP) takes place when the interaction is increased or the electron concentration is decreased at moderate fixed attraction. According to the Leggett criterion [21], the Bose regime begins when the modified chemical potential $\bar{\mu}$ drops below the lower band edge (the limiting value is $\bar{\mu}/t = -4$ and $\bar{\mu}/t = -6$, at $h = 0$, for $d = 2$ and $d = 3$, respectively).

For spin independent hopping integrals ($t^\uparrow = t^\downarrow$, $r = 1$), at $T = 0$ we find no magnetized superconducting phase in the strong attraction limit in the two dimensional case – PS is energetically favorable. However, for strong attraction and in the dilute limit we show that the existence of the homogeneous magnetized superconducting phase (SC_M) is possible for 3D case. The SC_M phase is a specific superfluid state, being a coherent mixture of LP's (hard-core bosons) and excess of spin-up fermions. We also briefly discuss the influence of different lattice geometries (or densities of states) on the stability of the SC_M phase. Some of our results have been published in Refs. [131, 132].

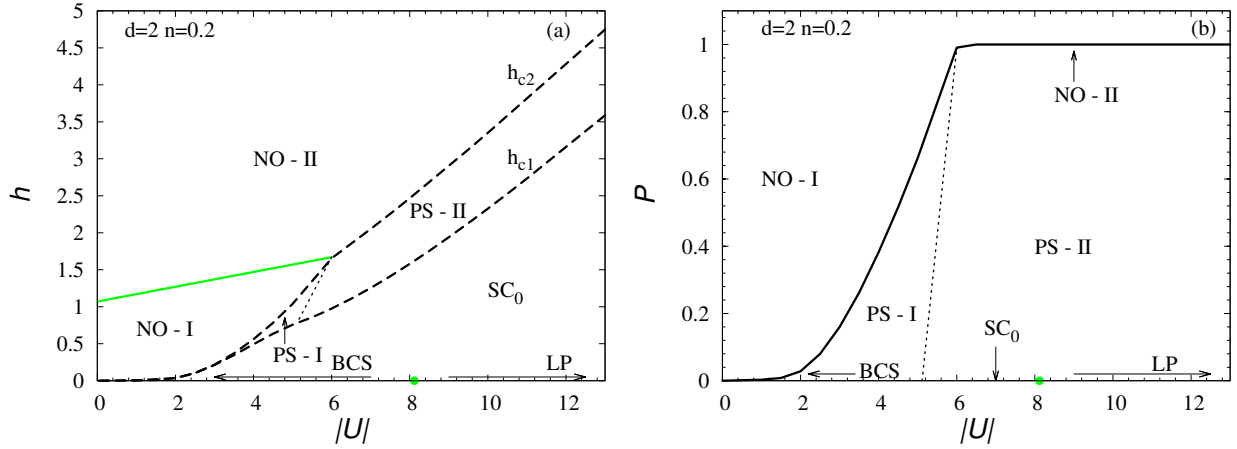


Figure 5.1: Magnetic field vs. on-site attraction (a) and polarization (b) phase diagrams, at $T = 0$ and fixed $n = 0.2$, for the square lattice. SC_0 – unpolarized superconducting state with $n_\uparrow = n_\downarrow$, LP – tightly bound local pairs. Green solid line separates partially polarized (NO-I) and fully polarized (NO-II) normal states. PS-I ($SC_0 + \text{NO-I}$) – partially polarized phase separation, PS-II ($SC_0 + \text{NO-II}$) – fully polarized phase separation, h_{c1} , h_{c2} – critical fields defining the PS region. The green point in (a)-(b) shows the BCS-LP crossover point ($U/t \approx -8.12$).

5.1 2D square lattice

From the point of view of the BCS-LP crossover, construction of the phase diagrams which describe the evolution of the system with increasing attraction is very important.

Here, we present the results of calculations for rather low electron concentrations and arbitrary values of on-site attraction $|U|$, for the case of $d = 2$. The particle concentration is fixed at $n = 0.2$ (Fig. 5.1). For fixed n , the 1st order SC-NO transition line in the $(\mu - h)$ plane is replaced by the PS region bounded by two critical Zeeman fields h_{c1} and h_{c2} . We find an unmagnetized SC_0 phase in the strong attraction limit. With increasing magnetic field, PS is energetically favored i.e. even in the strong attraction limit, the Sarma or breached (BP-1) phase is unstable. Superconductivity is destroyed by pair breaking in the weak coupling regime. On the other hand, in the strong coupling regime, the transition from the superconducting to the normal state goes in addition through phase separation ($SC_0 \rightarrow \text{PS-II} \rightarrow \text{NO-II}$).

In the limiting case of $n = 0$, one can perform an exact analysis. In this case, the BCS equation can be reduced to the Schrödinger equation for a single pair, where the chemical potential plays the role of the pair binding energy E_b . In the lattice fermion model, for the case of s -wave pairing, the two-particle binding energy is given by [27]:

$$\frac{2D}{U} = -\frac{1}{N} \sum_{\vec{k}} \frac{1}{\left(\frac{E_b}{2D} + 1\right) - \frac{\gamma_{\vec{k}}}{z}}, \quad (5.1)$$

where: $D = zt$, $z = 2d$ is the coordination number, $\gamma_{\vec{k}} = 2\Theta_{\vec{k}}$.

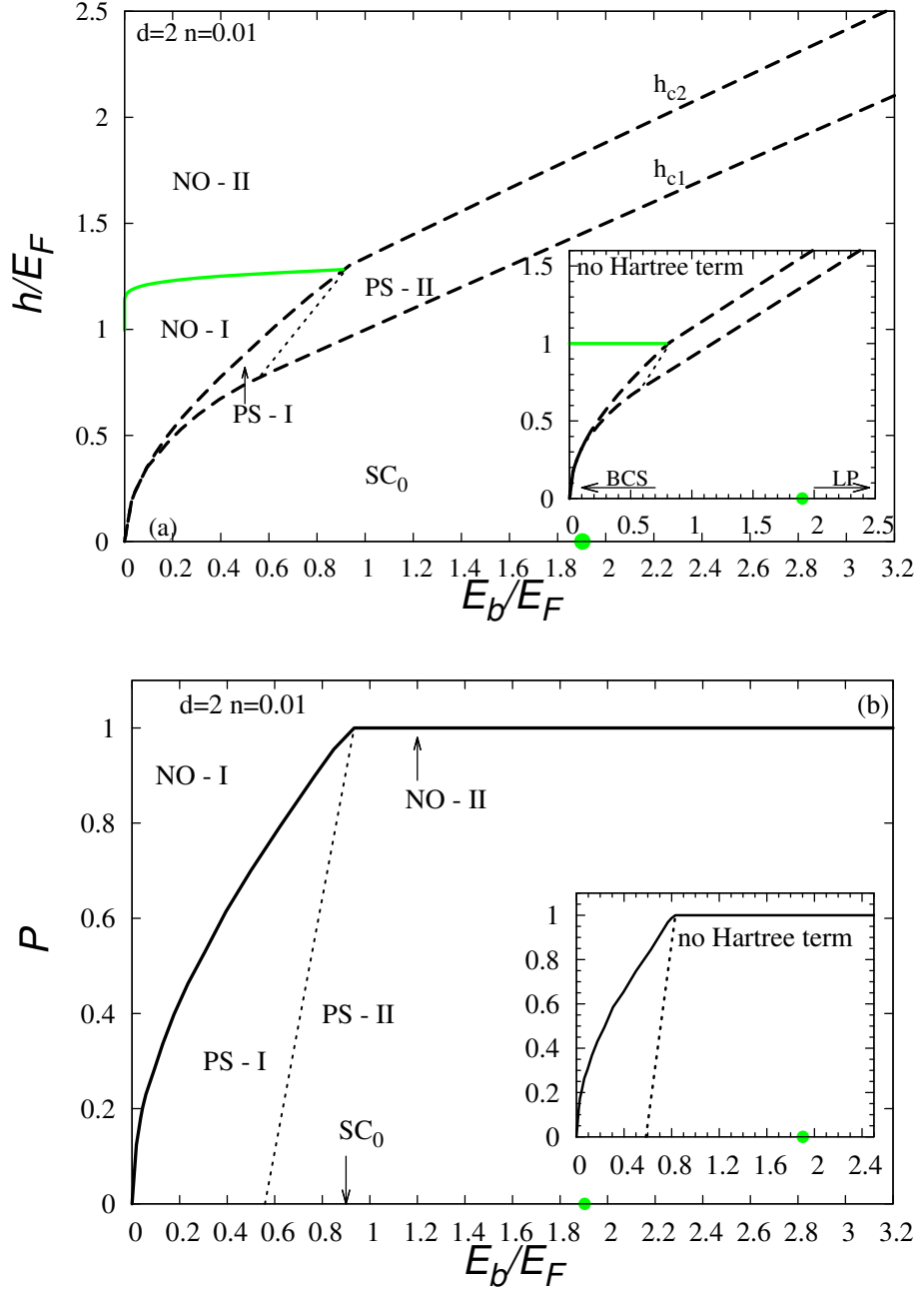


Figure 5.2: h/E_F vs. binding energy (a) and polarization (b) phase diagrams both with and without the Hartree term (inset), at $T = 0$ and fixed $n = 0.01$ for $d = 2$. SC_0 – unpolarized superconducting state with $n_\uparrow = n_\downarrow$, LP – tightly bound local pairs. Green solid line separates partially polarized (NO-I) and fully polarized (NO-II) normal states. PS-I (SC_0 +NO-I) – partially polarized phase separation, PS-II (SC_0 +NO-II) – fully polarized phase separation, h_{c1} , h_{c2} – critical fields defining the PS region. The green point in (a)-(b) shows the BCS-LP crossover point ($U/t = -4.01959$). Labels of states in the insets are the same as in the main figures.

Since in $d = 2$ the two-body bound state is formed for any attraction (if $h = 0$), one can replace the pairing potential $|U|$ by E_b . This is of interest as far as a comparison with the continuum model of a dilute gas of fermions is concerned.

A mapping of the phase diagrams (Fig. 5.1(a) and 5.1(b)) was also performed, using E_b in units of the lattice Fermi energy E_F (calculated from: $n = \frac{2}{N} \sum_{\vec{k}} \Theta(\mu - \epsilon_{\vec{k}} + \epsilon_0)$), instead of $|U|$ and the results for lower n are shown in Fig. 5.2(a)-(b). In the dilute limit, the lattice effects are smaller and the lattice model gives results similar to those of the model in continuum. To show this, we fix the electron concentration to $n = 0.01$. In this case, one finds the same phases as in Fig. 5.1(a) and 5.1(b). The phase diagrams without the Hartree term have also been constructed and shown in the inset of Fig. 5.2(a)-(b). Let us point out that these diagrams are in good agreement with the results for the continuum fermion model in $d = 2$ [133]. However, if we consider the continuum model, the chemical potential changes its sign exactly at $E_b = 2E_F$, which indicates the point of the BCS-BEC crossover. Our analysis gives a smaller ratio E_b/E_F . The differences are attributed to lattice effects, because the electron concentration is relatively small, but still non-zero. On the other hand, our results do not agree with the analysis in Ref. [134], according to which the BP-2 state is stable at $r = 1$ in $d = 2$. However, we have examined the stability of all phases very thoroughly.

If one takes corrections beyond mean-field (MF) into account, the existence of the spin imbalanced superfluid mixture of bosonic molecules and Fermi atoms can not be excluded in the BEC limit [135]. We should also add that the deep BEC side is better described by a Boson-Fermion mixture of hard-core bosons and spin-up fermions.

5.2 3D simple cubic lattice

We also investigate the BCS-BEC crossover diagrams in the presence of a Zeeman magnetic field in 3D for a simple cubic lattice. The diagrams in $(h, |U|)$ and $(P, |U|)$ planes are displayed in Figs. 5.3(a) and 5.3(b) for $n = 0.2$. These diagrams are typical for $d = 3$ and a relatively low n , with possible FFLO state on the BCS side. A similar behavior persists for higher n .

However, for strong attraction and in the dilute limit, the homogeneous magnetized superconducting phase occurs. In general, the solutions of this type (Sarma-type with $\Delta(h)$) appear when $h > \Delta$ (on the BCS side) or when $h > E_g/2$, where $E_g = 2\sqrt{(\bar{\mu} - \epsilon_0)^2 + |\Delta|^2}$ (on the BEC side) (see: Appendix C). As shown above, the SC_M phase is unstable in the weak coupling regime, but can be stable in the strong coupling LP limit ($E_b \gg \Delta$). Consequently, the quasiparticle branches in that regime are given by:

$$E_{\vec{k}\downarrow} = \epsilon_{\vec{k}} - \mu_{\downarrow} + g(\vec{k}) \approx \epsilon_{\vec{k}} - \epsilon_0 + \frac{1}{2}E_b + g(\vec{k}), \quad (5.2)$$

$$E_{\vec{k}\uparrow} = \epsilon_{\vec{k}} - \mu_{\uparrow} + g(\vec{k}), \quad (5.3)$$

where: $g(\vec{k}) = \frac{|\Delta|^2}{2(\epsilon_{\vec{k}} - \epsilon_0) + E_b}$ is a self-energy correction for fermions due to the interaction

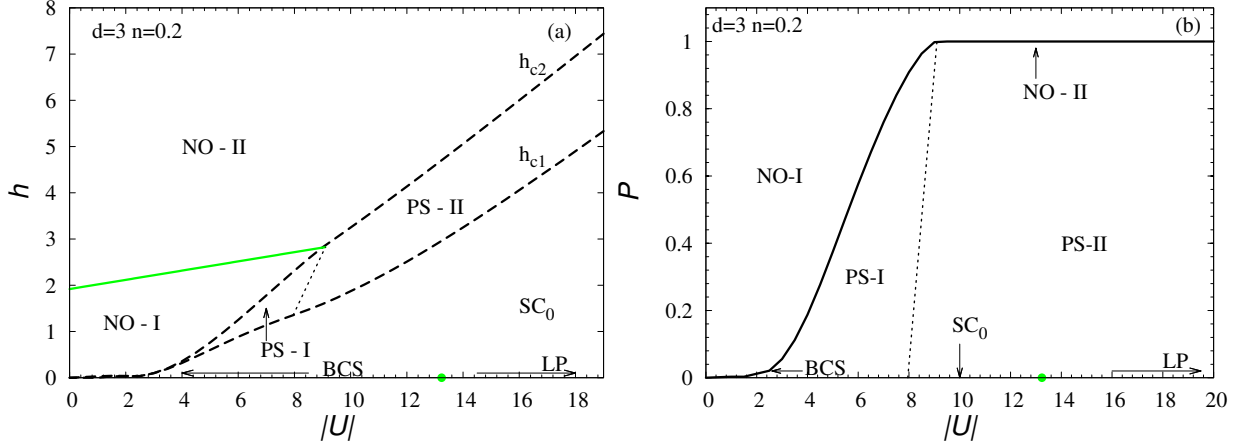


Figure 5.3: Magnetic field vs. on-site attraction (a) and polarization (b) phase diagrams, at $T = 0$ and fixed $n = 0.2$, for the simple cubic lattice. SC_0 – unpolarized superconducting state with $n_{\uparrow} = n_{\downarrow}$, LP – tightly bound local pairs. Green solid line separates partially polarized (NO-I) and fully polarized (NO-II) normal states. PS-I ($SC_0 + NO-I$) – partially polarized phase separation, PS-II ($SC_0 + NO-II$) – fully polarized phase separation, h_{c1} , h_{c2} – critical fields defining the PS region. The green point in (a)-(b) shows the BCS-BEC crossover point.

with the Bose condensate of LP, $\mu_{\sigma} = \bar{\mu} + \sigma(\frac{UM}{2} + h)$. E_b is the LP binding energy calculated from Eq. (5.1).

Deep in the BEC limit, unpaired spin down fermions do not exist. Hence, the SC_M phase is a specific superfluid state, which is a coherent mixture of LP's and an excess of spin-up fermions.

Let us start our analysis from the phase diagrams at fixed μ_m and h (Fig. 5.4). We define $\mu_m = \mu - \epsilon_0 + \frac{1}{2}E_b$ as one half of the pair chemical potential (molecular potential). The structure of these diagrams is different from the ones illustrated in Fig. 4.5(b), where one can distinguish only first order phase transition from pure SC_0 to the NO phase. Here, we observe also the continuous phase transition from SC_0 to SC_M with decreasing chemical potential and increasing magnetic field. The transition from SC_M to NO can be either of the first or second order. The character of this transition changes with decreasing μ . Hence, we also find the tricritical point in these diagrams (blue point). Therefore, we can distinguish the following sequences of transitions: $SC_0 \rightarrow NO$ or $SC_0 \rightarrow SC_M \rightarrow NO$. In fact $SC_0 \rightarrow SC_M$ is a topological quantum phase transition (Lifshitz type) (see: Appendix C). There is a cusp in the order parameter and polarization vs. magnetic field plots (for fixed n , for μ vs. h as well), which is clearly visible in Fig. 5.5. After transition to the SC_M phase, the polarization increases up to its maximum value and there is the 2nd order transition to the fully polarized normal state. There is also a change in the electronic structure. In the SC_0 phase there is no Fermi surface (FS), but in the SC_M state there is one FS for excess fermions. One can notice that the presence of the Hartree term restricts the range of occurrence of the SC_M phase, except for a very dilute limit (it

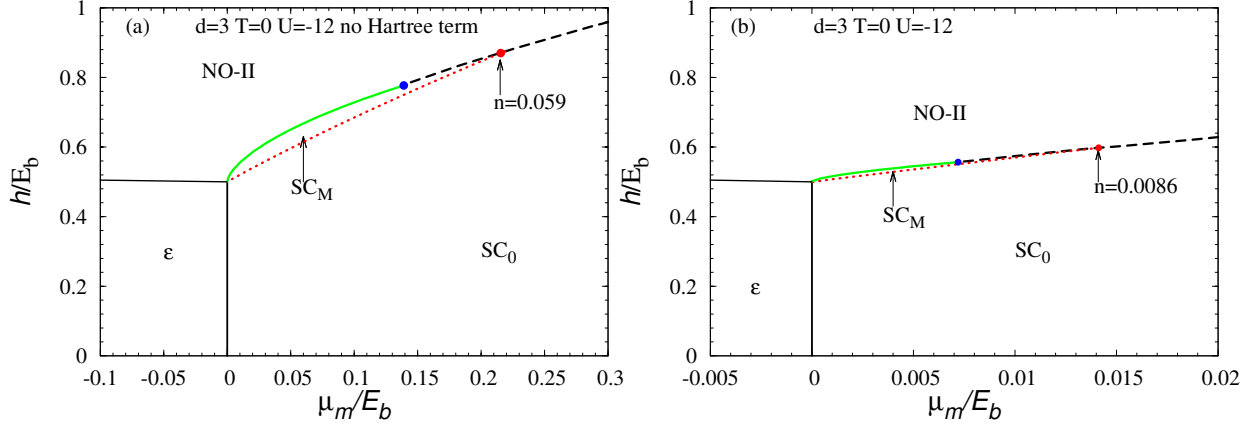


Figure 5.4: Critical magnetic field vs. chemical potential for $d = 3$, $U = -12$ on LP side. Diagram without (a) and with (b) Hartree term. SC_0 – unpolarized SC state with $n_\uparrow = n_\downarrow$, SC_M – magnetized SC state, NO-II – fully polarized normal state, ϵ – empty state, μ_m – half of the pair chemical potential defined as: $\mu - \epsilon_0 + \frac{1}{2}E_b$, where $\epsilon_0 = -6t$, E_b is the binding energy for two fermions in an empty lattice. Red point – $h_c^{SC_M}$ (quantum critical point (QCP)), blue point – tricritical point. The dotted red and the solid green lines are continuous transition lines.

will be discussed later).

Fig. 5.6 shows the critical magnetic fields vs. attractive interaction, for fixed $n = 0.01$ (a) and h vs. n for fixed $U = -12$ (b), without the Hartree term. In a very weak coupling limit (Fig. 5.6(a)) superconductivity is destroyed by the pair breaking. However, there exists a critical value of $|U_c|^{SC_M}$ (red point in the diagrams), above which the SC_M state becomes stable. As shown in Fig. 5.6(a), for $|U| < |U_c|^{SC_M}$ the transition from SC_0 to NO takes place, as previously, through PS-I or PS-II. However, the transition from SC_M to NO can be accomplished in two ways: (i) through PS-III ($SC_M + NO-II$) or (ii) through the second order phase transition (for higher $|U|$). Hence, TCPs are found in the $(h - |U|)$ and $(h - n)$ diagrams. As mentioned above, magnetized superconducting state is stable in the deep LP limit (for high $|U|$ and very low n (see Fig. 5.6(b))).

The diagrams with and without the Hartree term for a sc lattice in a very dilute limit are in good agreement with the ones for the continuum model of a dilute gas of fermions, plotted in terms of lattice E_F (calculated from: $n = \frac{2}{N} \sum_{\vec{k}} \Theta(\mu - \epsilon_{\vec{k}} + \epsilon_0)$) and $k_F a_s$ [67, 81, 82, 136] (where a_s is the scattering length between fermions for a two-body problem in vacuum). The scattering length is related to the contact interaction potential g via the Lippmann-Schwinger equation: $m/(4\pi a_s) = 1/g + 1/V \sum_{\vec{k}} 1/2\epsilon_{\vec{k}}$. On the lattice: $m = 1/2t$. We take $g = U$. Then, $E_F = k_F^2 t$ ($a = 1$, $\hbar = 1$), from Eq. (5.1) $1/|U_c| = \frac{1}{N} \sum_{\vec{k}} \frac{1}{2(\epsilon_{\vec{k}} - \epsilon_0)}$ and after short calculations we have: $1/k_F a_s = \left(\frac{1}{|U_c|^{d=3}} - \frac{1}{|U|} \right) \frac{8\pi}{\sqrt{E_F}}$.

Fig. 5.7 shows the critical magnetic field (a) and polarization (b) vs. $1/k_F a_s = \left(\frac{1}{|U_c|^{d=3}} - \frac{1}{|U|} \right) \frac{8\pi}{\sqrt{E_F}}$, where $|U_c|^{d=3}/12 = 0.659$, for $n = 0.001$, with the Hartree term. In

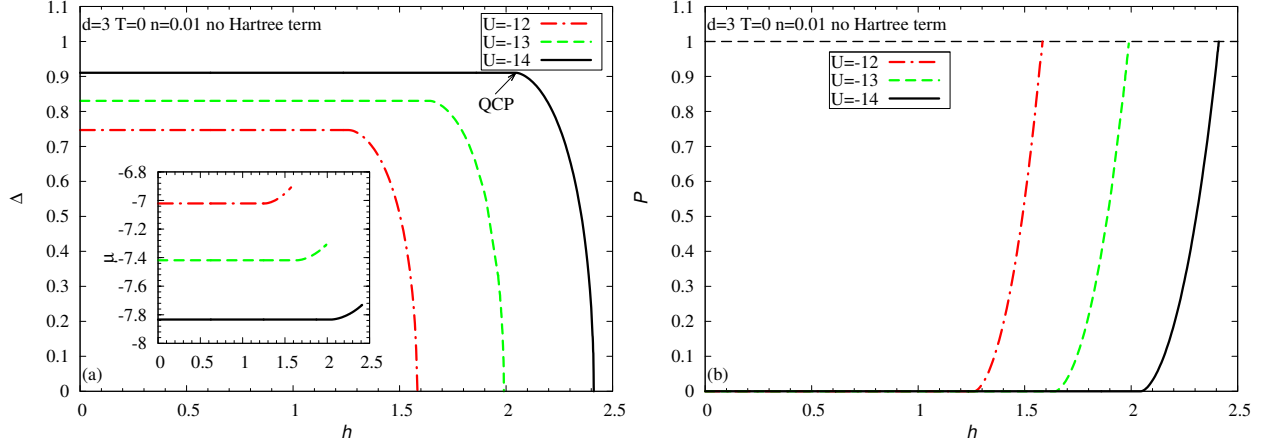


Figure 5.5: Dependence of the order parameter (a), chemical potential (inset) and the polarization (b) on the magnetic field for $d = 3$, at $T = 0$, fixed $n = 0.01$ and three values of the attraction. The arrow points the quantum critical point (QCP).

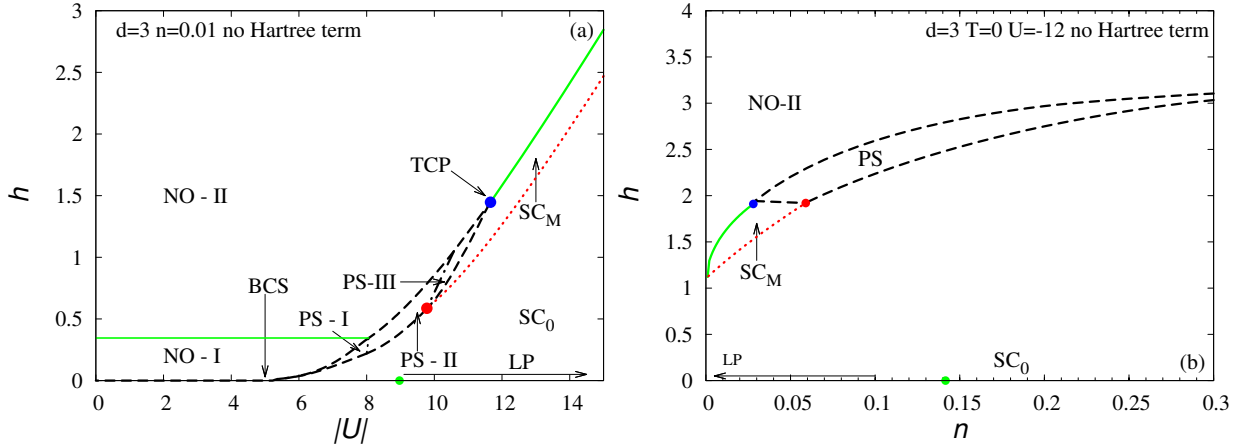


Figure 5.6: Critical magnetic field vs. $|U|$ for fixed $n = 0.01$ (a) and electron concentration for fixed $U = -12$ (b) phase diagrams, $T = 0$, $d = 3$. SC_0 – unpolarized superconducting state, SC_M – magnetized superfluid phase, LP – tightly bound local pairs. Green solid line separates partially polarized (NO-I) and fully polarized (NO-II) normal states. PS-I (SC_0 +NO-I) – partially polarized phase separation, PS-II (SC_0 +NO-II) – fully polarized phase separation, PS-III – SC_M +NO-II. Red point – quantum critical point, blue point – tricritical point. The green point in (a)-(b) shows the BCS-BEC crossover point.

the strong coupling limit at $P = 0$, the system is in the SC_0 phase. For arbitrarily low values of polarization, the SC_M state becomes stable (as opposed to the $n = 0.2$ case (Fig. 5.3(b))). When polarization increases, local pairs are broken and at $P = 1$ there is the second order phase transition to the fully-polarized normal state. With decreasing attractive interaction, the system goes through phase separation to the NO state. One can perform comparison with the case of the model in continuum within mean-field analysis

[81] and also quantum Monte Carlo (QMC) method [136]. The tricritical point (blue point) on the ground state phase diagram ($h/E_F - 1/k_F a_s$) (Fig. 5.7) is located at $h/E_F \approx 6.854$ and $1/k_F a_s \approx 2.41$. Similar to the case of the model in continuum – $h/E_F \approx 6.876$, $1/k_F a_s \approx 2.368$. In turn, the values in the QMC method are: $1/k_F a_s \approx 2.142$ with $P = 1$. Moreover, there is also phase separation between magnetized superfluid and partially-polarized phases as opposed to the mean-field case.

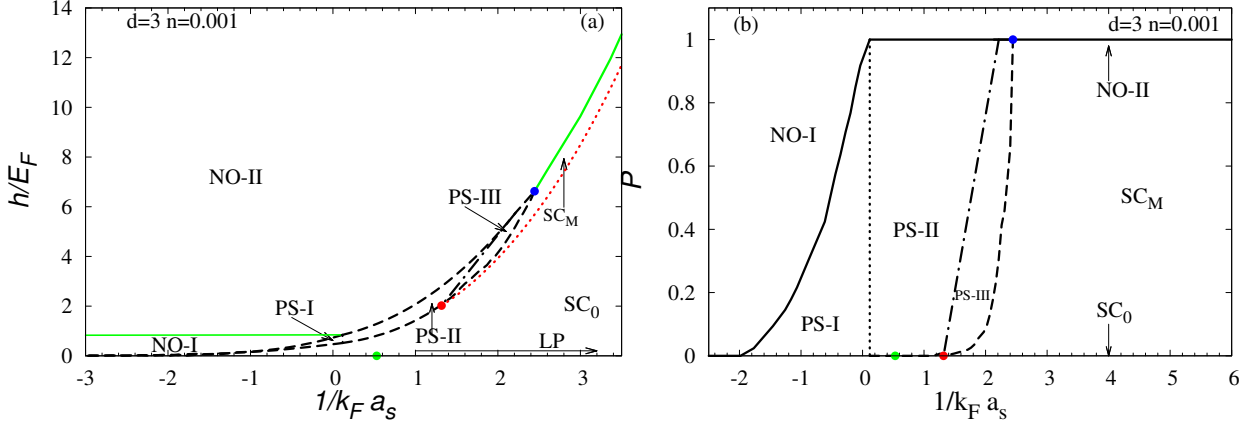


Figure 5.7: h/E_F (a) and polarization (b) vs. $1/k_F a_s = \left(\frac{1}{|U_c|^{d=3}} - \frac{1}{|U|} \right) \frac{8\pi}{\sqrt{E_F}}$, where $|U_c|^{d=3}/12t = 0.659$, for the sc lattice. SC_M – magnetized superconducting state, PS-III – ($SC_M + NO-II$). Red point – $h_c^{SC_M}$, blue point – tricritical point. The dotted red and the solid green lines are continuous transition lines. The diagrams are with the Hartree term.

Here we discuss in detail the BCS-BEC crossover for the simple cubic lattice without the Hartree term. Fig. 5.8 shows $(P-|U|)$ phase diagrams for four fixed values of the particle concentration. The diagram for $n = 0.001$ with the Hartree term (Fig. 5.7(b)) has already been discussed. When we plot Fig. 5.8(a) in terms of E_F and $k_F a_s$, we can compare the case with and without the Hartree term in a very dilute limit. The results are the same, both qualitatively and quantitatively. However, if the number of particles increases, the range of occurrence of SC_M narrows. At $n = 0.03$, for $|U| < 30$, the diagram looks very similar to the diagram for $n = 0.001$. However, if the polarization and the attractive interaction increase, the character of the transition changes from second to first order and a second tricritical point appears. In the very strong coupling limit, at $P \neq 0$, phase separation is energetically more stable than the SC_M phase. For higher values of n (see Fig. 5.8(c) and 5.8(d)) the range of SC_M is still decreasing and the system goes through phase separation to the NO state for the whole range of parameter values. The tricritical point does not exist. Thus, there are qualitative differences between the results for the spin polarized attractive Hubbard model and for the continuum model of a dilute gas of fermions.

A very important quantity from the point of view of the BCS-BEC crossover is the coherence length ξ . The suggestions to study this quantity in this context follow from the

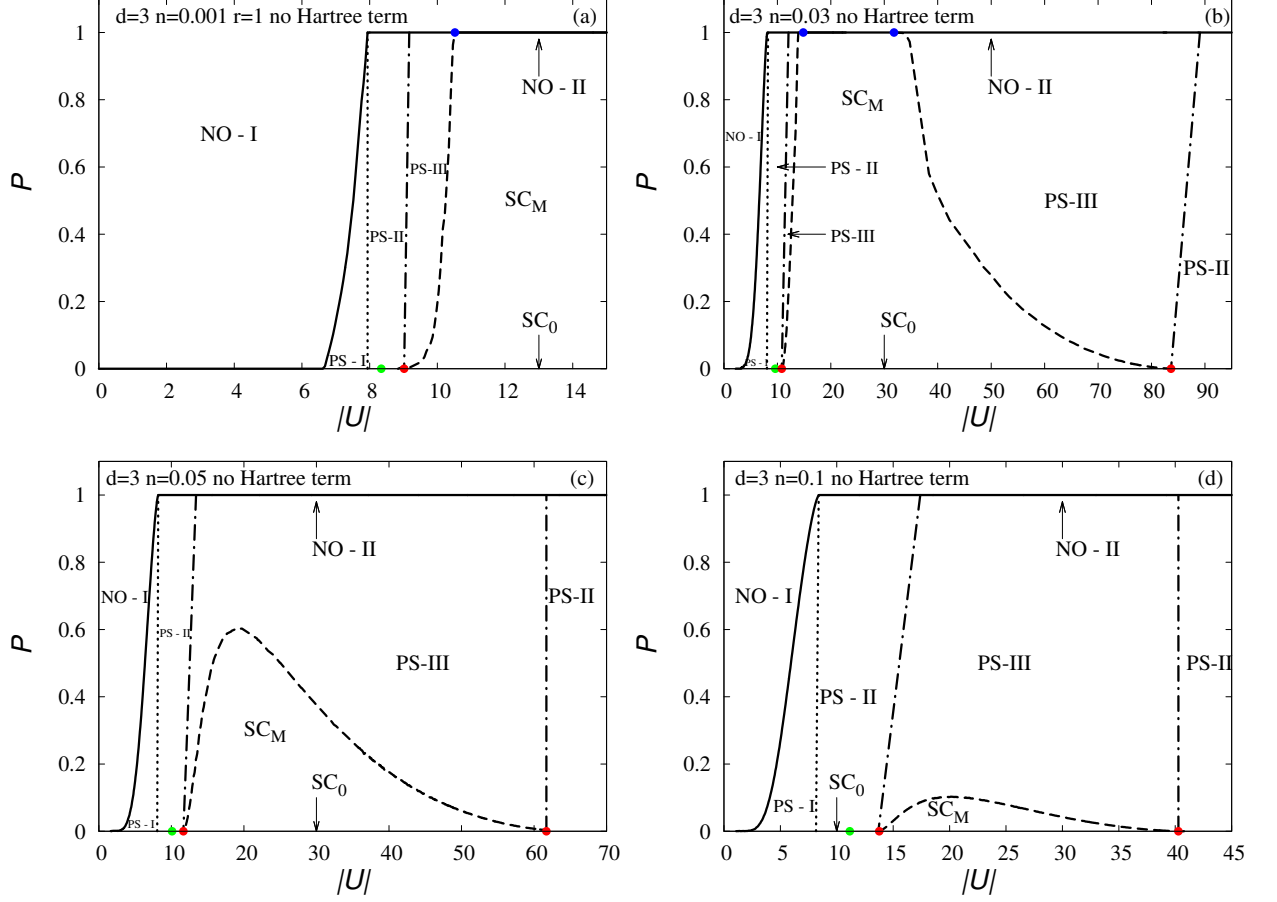


Figure 5.8: Polarization vs. on-site attraction phase diagrams, at $T = 0$ and fixed $n = 0.001$ (a), $n = 0.03$ (b), $n = 0.05$ (c), $n = 0.1$ (d), for the simple cubic lattice. SC_0 – unpolarized superconducting state with $n_\uparrow = n_\downarrow$, SC_M – magnetized superconducting state, PS-I (SC_0 +NO-I) – partially polarized phase separation, PS-II (SC_0 +NO-II) – fully polarized phase separation, PS-III (SC_M +NO-II). Green point shows the BCS-BEC crossover point, blue point – tricritical point, red point – $|U|_c^{SC_M}$. The diagrams are without the Hartree term.

observations of the properties of exotic superconductors. In agreement with the Uemura's plot [20], the unconventional superconductors have a considerably shorter coherence length ($\sim 20 - 50 \text{ \AA}$) than the conventional superconductors ($\xi \sim 10^3 - 10^4 \text{ \AA}$). The coherence length ξ can be defined through the pair correlation function with opposite spins [87, 137, 138]:

$$g(\vec{r}) = \frac{1}{n^2} |\langle \Phi | \Psi_\uparrow^\dagger(\vec{r}) \Psi_\downarrow^\dagger(0) | \Phi \rangle|^2, \quad (5.4)$$

(where: $\Psi_\sigma(\vec{r})$ – fermionic field operator) in such a way that:

$$\xi^2 = \frac{\int d\vec{r} g(\vec{r}) \vec{r}^2}{\int d\vec{r} g(\vec{r})} = \frac{\sum_k |\nabla_k \phi_k|^2}{\sum_k |\phi_k|^2}, \quad (5.5)$$

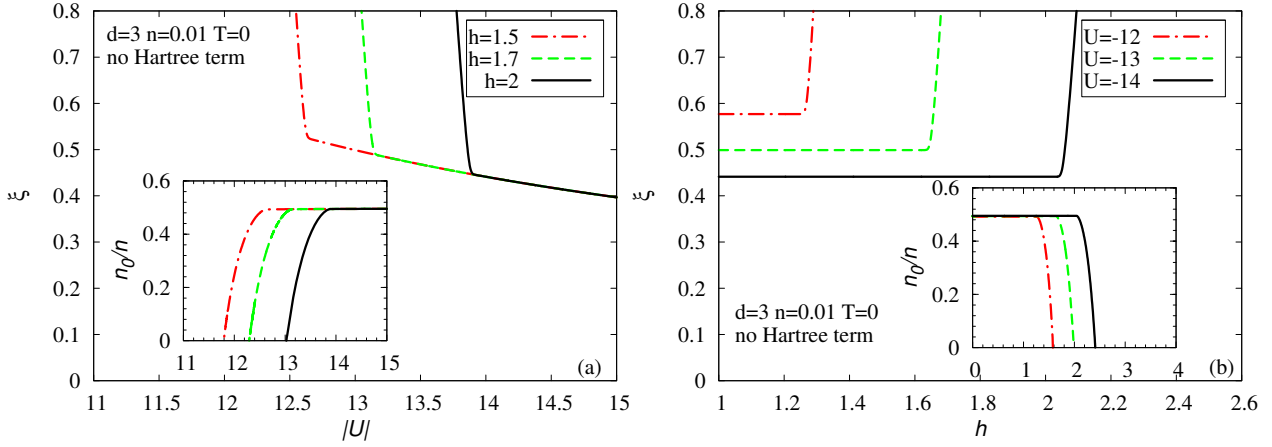


Figure 5.9: Dependence of the coherence length ξ (in units of the lattice constant) on h (a) and $|U|$ (b). ξ is computed for finite but small T ($T = 5 \times 10^{-3}$). Fraction of pairs in condensate n_0/n vs. h (inset (a)) and $|U|$ (inset (b)); $d = 3$, $n = 0.01$.

where $\phi_{\vec{k}}$ is the pair wave function in the BCS ground state. For finite temperatures we use Eq. (5.5) with $\phi_{\vec{k}} \rightarrow \mathcal{F}_{\vec{k}} = u_{\vec{k}}^* \nu_{\vec{k}} [1 - f(E_{\vec{k}\uparrow}) - f(E_{\vec{k}\downarrow})] = \Delta / (E_{\vec{k}\uparrow} + E_{\vec{k}\downarrow}) [1 - f(E_{\vec{k}\uparrow}) - f(E_{\vec{k}\downarrow})]$ which is the pair wave function at finite T and $E_{\vec{k}\uparrow, \downarrow}$ are given by Eq. (4.3). In the ground state, the pair wave function is: $\phi_{\vec{k}} = u_{\vec{k}}^* \nu_{\vec{k}} = \Delta / (E_{\vec{k}\uparrow} + E_{\vec{k}\downarrow})$ if $E_{\vec{k}\uparrow} > 0$.

The condensate density is given:

$$n_0 = \frac{1}{N} \sum_{\vec{k}} |\mathcal{F}_{\vec{k}}|^2 = \frac{1}{N} \sum_{\vec{k}} \frac{|\Delta|^2}{(E_{\vec{k}\uparrow} + E_{\vec{k}\downarrow})^2} [1 - f(E_{\vec{k}\uparrow}) - f(E_{\vec{k}\downarrow})]^2 \quad (5.6)$$

and is in general temperature dependent. The fraction of pairs in the condensate can be expressed by the formula:

$$\frac{n_0}{n} = \frac{1}{N} \sum_{\vec{k}} \frac{|\mathcal{F}_{\vec{k}}|^2}{n}, \quad (5.7)$$

where n is the particle concentration.

Fig. 5.9 shows the dependence of the coherence length ξ (in units of the lattice constant) and the fraction of condensed particles on the magnetic field and attractive interaction, for $d = 3$ and $n = 0.01$. In the strong coupling limit, the pair size is smaller than the lattice constant. Only tightly bound local pairs exist in the system (SC_0 phase) and the coherence length does not depend on the magnetic field. The transition from SC_0 to SC_M (see Fig. 5.6(a)) is manifested through sharp increase in ξ , because the Pauli Exclusion Principle prohibits the bound pairs and the excess of spin-up fermions to occupy the same lattice site. This behaviour of ξ seems to be characteristic for a topological transition to gapless superfluid state. The SC_M phase can be considered as a miscible mixture of tightly bound pairs (composite bosons) and excess of spin-up fermions. The interaction between bosons and unpaired fermions is repulsive. If $n_p = n_{\downarrow}$ is number of pairs then $n_F = n_{\uparrow} - n_{\downarrow}$ is number of unpaired fermions such that $n = 2n_p + n_F$ is

constant. This interpretation is consistent with the fact that the chemical potential (see Fig. 5.5) is below the band bottom indicating the bosonic regime [136].

The character of the magnetized superfluid phase is also reflected in the features of the fraction of condensed particles. The maximum value of the ratio n_0/n is 0.5, because if all particles in the system form pairs and condense, their concentration is twice lower than the initial electron concentration. If the system is in the SC_0 state (in the strong coupling regime), n_0/n does not depend on the magnetic field and takes the largest possible value. The fraction of condensed pairs decreases rapidly after the transition to SC_M and equals zero in the NO state. There is a cusp in the n_0/n vs. magnetic field and $|U|$ plots, at the point of $SC_0 \rightarrow SC_M$ transition.

Now, we also discuss the density of states features in the strong coupling regime, paying special attention to changes in the quasiparticle spectrum in the SC_M phase.

The density of states in the superconducting ground state is determined from Eq. (4.7).

Fig. 5.10 shows the density of states plot for the simple cubic lattice, $n = 0.01$, $U = -12$ (LP region). There exists an energy gap at $h = 0$, both in the weak and strong coupling regime. The gap in the density of states is fixed by the location of the logarithmic singularities. However, in the BCS and LP limits the gap width is determined in a different way. As mentioned above, for the s-wave pairing symmetry case, the energy gap width in the density of states equals $E_g = 2\Delta$, in the BCS regime. However, since $\bar{\mu}$ lies below the bottom of the band in the LP regime, the behavior of the quasiparticle energies changes and the energy gap width in the density of states equals $E_g = 2\sqrt{(\epsilon_0 - \bar{\mu})^2 + |\Delta|^2}$.

In the presence of a magnetic field, the densities of states are shifted by h to the left ($g_\uparrow(E)$) and to the right ($g_\downarrow(E)$). For $h = 0.6$ (Fig. 5.10(b)), the gapped regions $g_\uparrow(E) = 0$ and $g_\downarrow(E) = 0$ still overlap and the total density of states $g(E)$ has a gap. However, for magnetic fields higher than $E_g/2 = \sqrt{(\epsilon_0 - \bar{\mu})^2 + |\Delta|^2}$ (Fig. 5.10(c), for this case $h = 1.35$, while $E_g/2 \approx 1.23$), i.e. after the transition to the SC_M state (see Fig. 5.6(a)), the energy gap does not exist in the total density of states $g(E)$. This also implies that the quasiparticle energy $E_{\vec{k}\uparrow}$ becomes gapless. Hence, the SC_M state is characterized by a gapless spectrum for the majority spin species when $h > E_g/2$.

5.3 The influence of different lattice geometries (densities of states) on the stability of the magnetized superfluid phase

In this section, we briefly discuss the influence of different lattice geometries on the stability of the SC_M phase. In the previous section, we have analyzed the impact of the Zeeman magnetic field on the BCS-BEC crossover at $T = 0$ for $d = 3$ simple cubic lattice (sc) and shown that the existence of the SC_M phase is possible for the sc lattice case and for spin independent hopping integrals.

Here, we construct the BCS-BEC crossover phase diagrams at $T = 0$, for the body-centered cubic (BCC) and face-centered cubic (FCC) lattices. As mentioned above, the

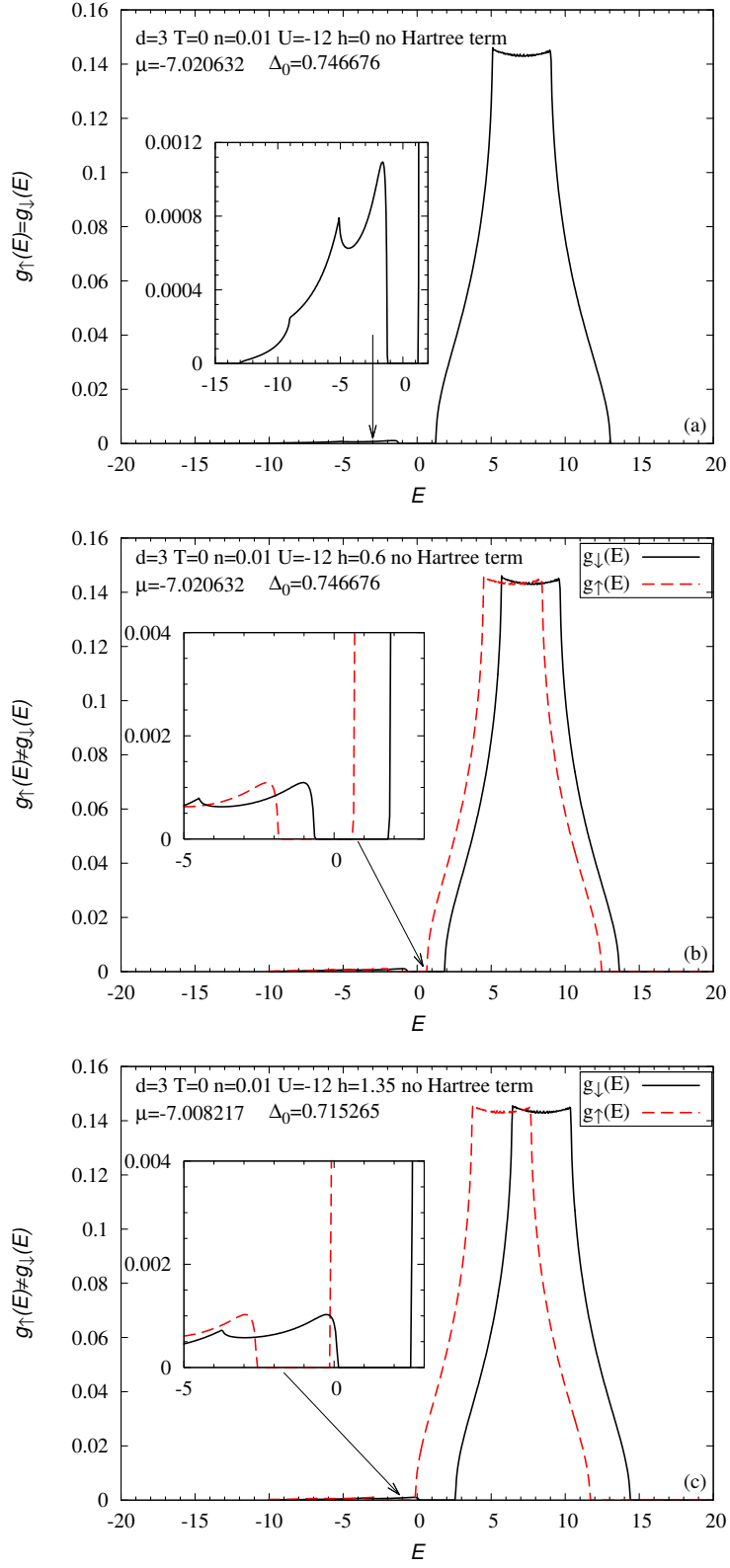


Figure 5.10: Density of states for $d = 3$, $n = 0.01$, $U = -12$, $h = 0$ and two different values of the magnetic field.

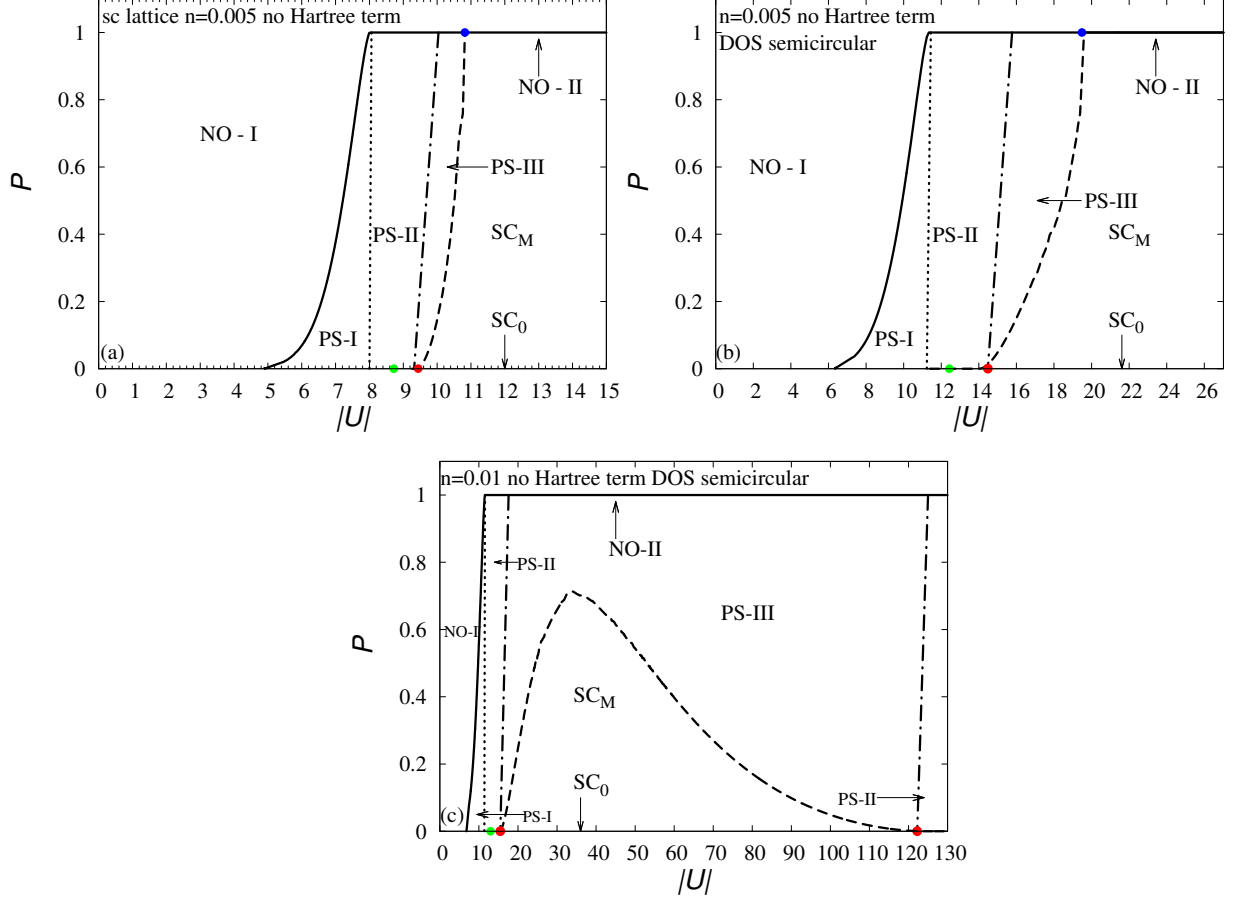


Figure 5.11: Polarization vs. $|U|$ ground state phase diagrams for (a) sc lattice $n = 0.005$, (b) semicircular DOS $n = 0.005$, (c) semicircular DOS $n = 0.01$. SC_0 – unpolarized superconducting state, SC_M – magnetized superconducting state, PS-I (SC_0 +NO-I) – partially polarized phase separation, PS-II (SC_0 +NO-II) – fully polarized phase separation, PS-III (SC_M +NO-II). Green point – BCS-BEC crossover point, blue point – tricritical point, red point – $|U|_c^{SC_M}$. The diagrams are constructed in units of t .

results contained in this thesis have been obtained by numerical calculations. However, the sums over the first Brillouin zone were performed with the use of the density of states, whenever possible. The formulas for the density of states are presented in Appendix E. We also use the semicircular (s-circ) DOS [139] in our calculations, which can be realized as the Bethe lattice (tree lattice in infinite dimensions) or as an approximate DOS in $d = 3$ but without Van Hove's singularities.

Obviously, the Hubbard model is a lattice model and is expected to give similar results as its continuum counterpart (universal behavior) only in the dilute limit, when both $n \rightarrow 0$ and $a \rightarrow 0$ (a – lattice constant). Therefore, the specifics of the lattice are relevant, at every finite n . Hence, the range of occurrence of the SC_M phase can be

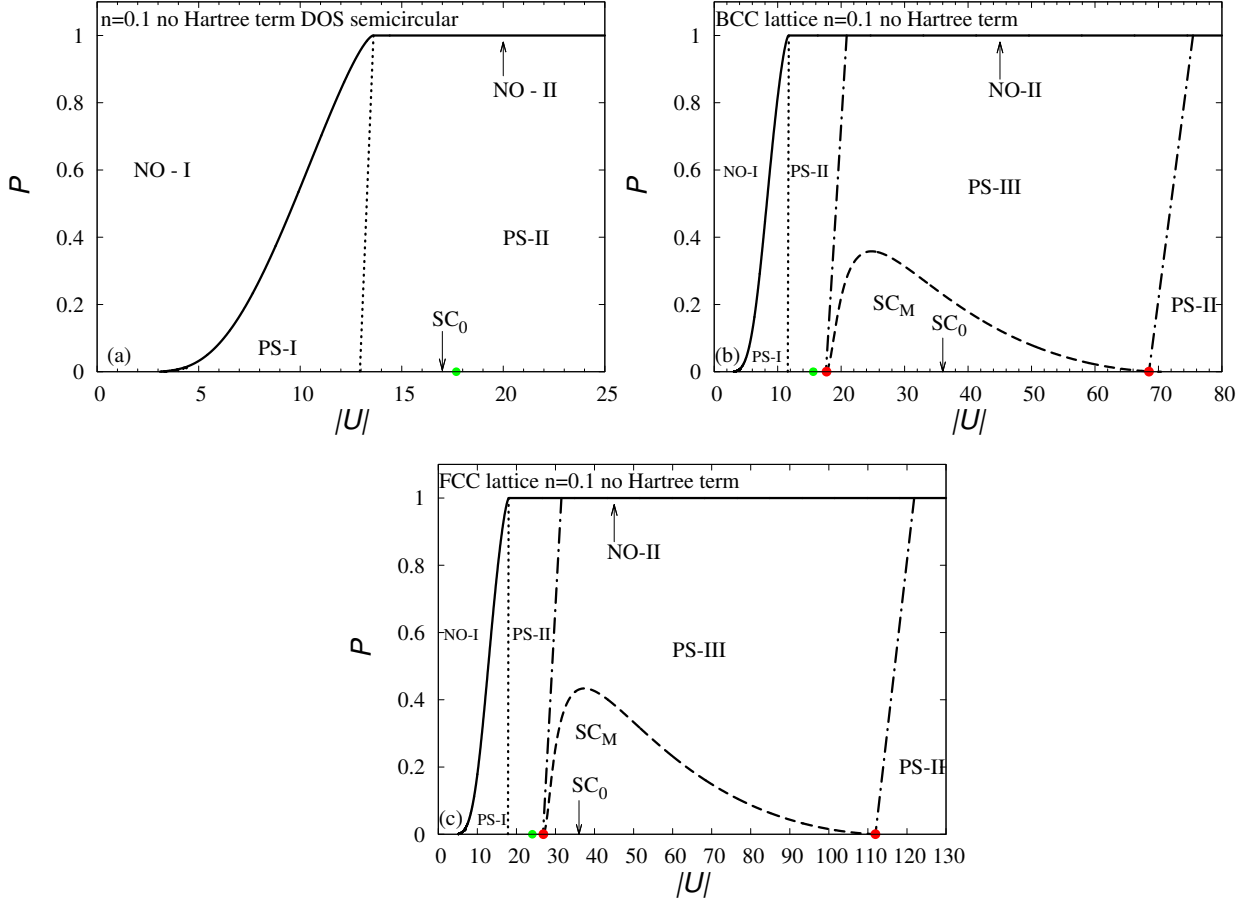


Figure 5.12: Polarization vs. $|U|$ ground state phase diagrams, at fixed $n = 0.1$, for (a) semicircular DOS, (b) BCC lattice, (c) FCC lattice. SC_0 – unpolarized superconducting state, SC_M – magnetized superconducting state, PS-I (SC_0 +NO-I) – partially polarized phase separation, PS-II (SC_0 +NO-II) – fully polarized phase separation, PS-III (SC_M +NO-II). Green point – BCS-BEC crossover point, blue point – tricritical point, red point – $|U|_c^{SC_M}$.

essentially different for different lattice geometries.

Now, we briefly discuss the ground state phase diagrams for different types of lattices.

As mentioned above, the critical value of attraction for bound state formation in the empty lattice equals $|U_c|^{sc}/12t = 0.659$, for sc. In turn, for the semicircular DOS one finds $|U_c|^{s-circ} \approx 10.80732$ [139]. Therefore, one can expect that there are some quantitative differences in the phase diagrams between the sc and semicircular DOS, even at low electron concentration.

Fig. 5.11(a)-(b) shows the $(P-|U|)$ diagrams at fixed $n = 0.005$, for the sc and semicircular DOS. The topology of these diagrams is the same. There is the SC_0 state for low values of attraction. With increasing polarization, there is the 1st order transition to the

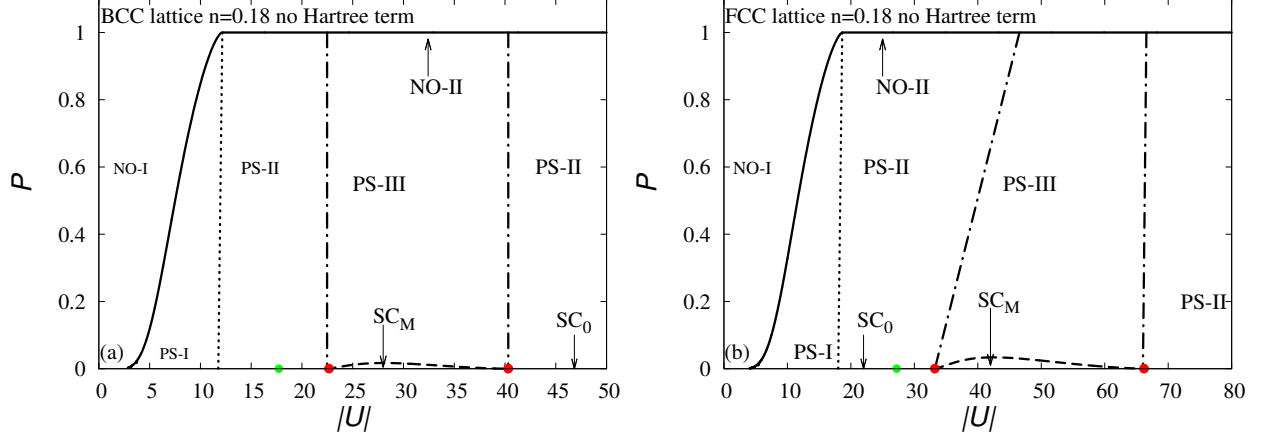


Figure 5.13: Polarization vs. $|U|$ ground state phase diagrams, at fixed $n = 0.18$, for (a) BCC lattice, (b) FCC lattice. SC_0 – unpolarized superconducting state, SC_M – magnetized superconducting state, PS-I (SC_0 +NO-I) – partially polarized phase separation, PS-II (SC_0 +NO-II) – fully polarized phase separation, PS-III (SC_M +NO-II). Green point – the BCS-BEC crossover point, blue point – tricritical point, red point – $|U|_c^{SC_M}$.

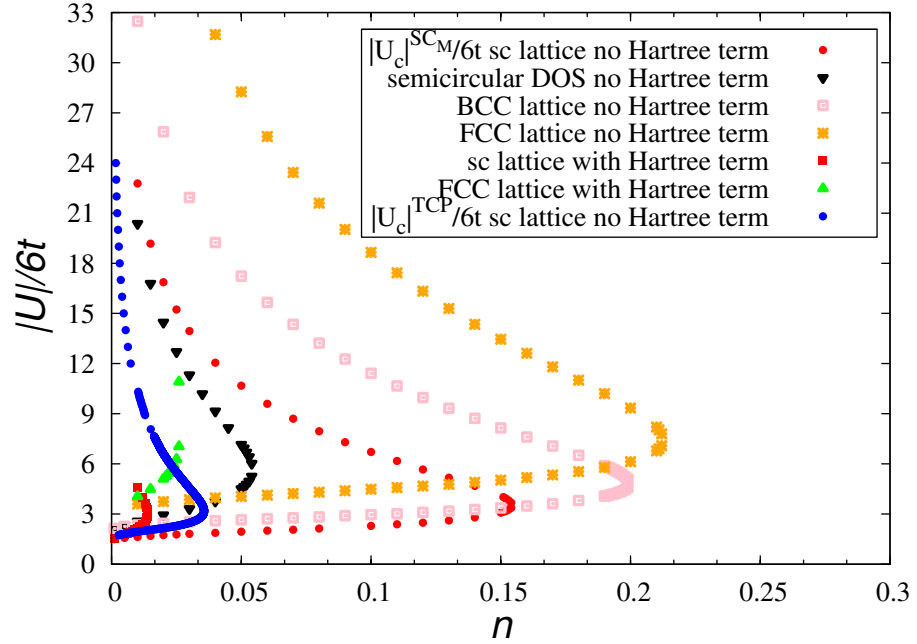


Figure 5.14: Critical values of the attraction, for which the SC_M state arises stable and tricritical points at $T = 0$ vs. electron concentration. $h_c^{SC_M} = \sqrt{(\bar{\mu} - \epsilon_0)^2 + |\Delta|^2}$, where $\Delta = \Delta(h = 0)$.

normal phase, through the PS-I or PS-II regions. If $|U|$ increases, the SC_M state appears

in the phase diagrams, both for the sc and semicircular DOS. However, the SC_M phase moves towards higher $|U|$ values, in the semicircular DOS case. Therefore, the location of TCP is also different in this case. Moreover, the PS-III region is larger for the s-circ DOS than for the sc lattice. Obviously, the range of occurrence of the SC_M state decreases with increasing electron concentration (Fig. 5.11(c)).

We have performed a similar comparative analysis for different types of lattices, at fixed $n = 0.1$ (Fig. 5.12). In the s-circ DOS case, with increasing polarization, PS is energetically favored, i.e. even on the LP side, SC_M is unstable. The situation is different in the sc case. As shown in section 5.2 (Fig. 5.8(d)), SC_M is stable for fixed $n = 0.1$, but the range of SC_M is decreasing and the system goes through phase separation to the NO state for the whole range of parameter values. The tricritical point does not exist. One can observe a similar behavior for the BCC and FCC lattices. However, the range of occurrence of SC_M is much larger than in the other cases (s-circ and sc DOS). While, for the sc lattice, a critical value of n above which the SC_M state becomes unstable equals $n \approx 0.154$ (for semicircular DOS this value is even smaller), one can find the SC_M phase in the diagrams for FCC and BCC lattices case, even at fixed $n = 0.18$ (Fig. 5.13).

We have also performed an analysis of the evolution of the critical values of the attraction, for which the SC_M state becomes stable for different types of lattices and of the tricritical points (blue circle points, without the Hartree term in the sc lattice case) with increasing n (Fig. 5.14). The occurrence of the SC_M phase depends on lattice structure. As shown in this chapter, SC_M is unstable for $d = 2$, but it can be realized for $d = 3$ lattices.

We have also investigated the influence of the Hartree term on the SC_M phase stability.

In the very dilute limit, there is only one value of $|U_c|^{SC_M}$ and it is the same for the case with and without the Hartree term, for all types of lattices. For each value of $n < n_c$ (n_c defined below), there are two critical values of the attraction for which the SC_M state becomes stable (except for the very dilute limit, where there is only the lower critical value, i.e. the upper critical value becomes infinite). The system is in the SC_M phase between the lower and upper critical points in this plot. However, with increasing particle concentration, the range of stability of SC_M is smaller and there exists a critical value of n (n_c) above which the SC_M state becomes unstable. For the semicircular DOS case, without the Hartree term, this value is the lowest and equals $n_c \approx 0.054$, while for the sc lattice $n_c = 0.154$, for the BCC lattice $n_c \approx 0.199$ and the highest for the FCC lattice $n_c \approx 0.212$. Additionally, as opposed to the results for the continuum model of a dilute gas of fermions, there are always two values of $|U_c|^{SC_M}$, for higher values of n . We have also found the range of n , for which the transition from SC_M to NO is of the first order, even for a very strong attraction.

The presence of the Hartree term restricts the range of occurrence of the SC_M phase, which is clearly visible in Fig. 5.14 (red square points for the sc lattice and green triangular points for the FCC lattice). A critical value of n above which the SC_M state becomes unstable equals $n \approx 0.0145$ (the sc lattice) and $n \approx 0.026$ (the FCC lattice). The Hartree term, usually promoting ferromagnetism in the Stoner model ($U > 0$), here ($U < 0$), strongly competes with superconductivity. Thus, such a term restricts the SC_M state to

lower densities. However, as we will show in the following chapters, the mass imbalance can change this behavior even for $d = 2$ due to spin polarization stemming from the kinetic energy term.

Chapter 6

The BCS-BEC crossover at finite temperatures in the spin-polarized AHM with spin independent hopping integrals

In this chapter, we extend the BCS-BEC crossover analysis to finite temperatures by taking into account phase fluctuations in $d = 2$ within the Kosterlitz-Thouless scenario and pairing fluctuations in $d = 3$ (self-consistent T-matrix scheme). The T-matrix scheme goes beyond the standard mean-field, since it includes the effects of non-condensed pairs with $\vec{q} \neq 0$ and allows a description of the BEC regime of the crossover. In general, the method works in the low density regime. The crossover diagrams include the pseudogap state. Some of our results have been published in Ref. [132].

6.1 2D square lattice. The Kosterlitz-Thouless scenario

Here, the results concerning the influence of a magnetic field on superfluidity at finite temperatures are presented.

One should emphasize that phase transitions in quantum systems are dependent on the dimensionality of these systems. Two-dimensional Fermi systems exhibit features which are not observed in the three-dimensional case. According to the Mermin-Wagner theorem, the long-range order does not exist in one- and two-dimensional lattice spin systems, at non-zero temperatures, if the system has a continuous symmetry group (e.g. the Heisenberg model or the XY model).

As mentioned above, for $d = 2$ AHM at $h = 0$, the SC-NO transition is of the Kosterlitz-Thouless type, i.e. below T_c^{KT} the system has a quasi-long-range (algebraic) order which is characterized by a power law decay of the order parameter correlation function and non-zero superfluid stiffness. According to Eq. (3.11), the KT transition temperature is found from the intersection point of the straight line $\frac{2}{\pi}k_B T$ with the curve

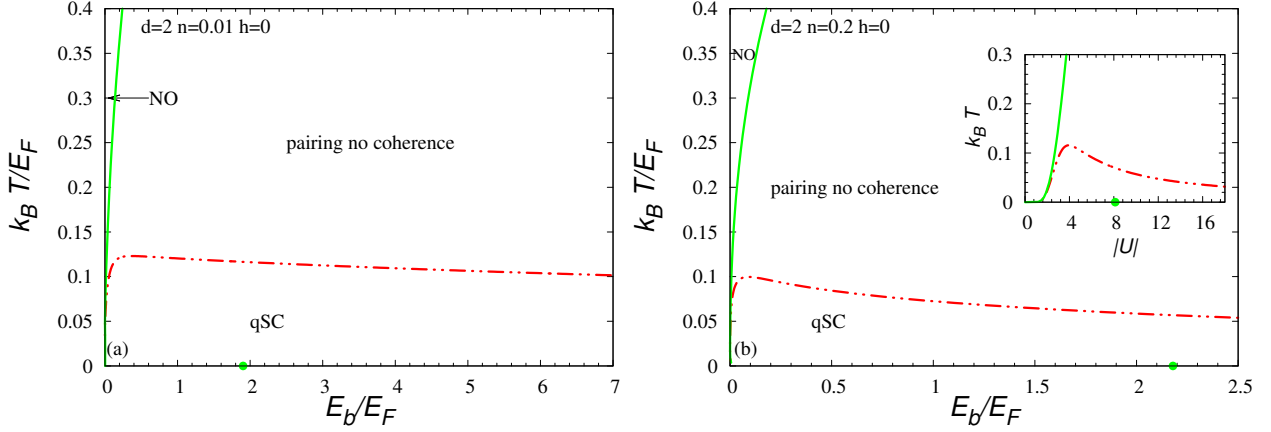


Figure 6.1: Temperature vs. binding energy phase diagrams in units of the lattice Fermi energy at $h = 0$, (a) $n = 0.01$, (b) $n = 0.2$ and T vs. $|U|$ phase diagram (inset of (b)). Thick dashed-double dotted line (red color) is the KT transition line, thick solid line denotes transition from pairing without coherence region to NO within the Hartree approximation. qSC – superconductor (algebraic order). The green point in (a)-(b) shows the BCS-LP crossover point at $T = 0$.

$\rho_s(T)$. In such a way, we can estimate the phase coherence temperatures and extend the analysis of the crossover from the weak to strong coupling to finite T [87]. The results obtained for the Kosterlitz-Thouless temperatures give upper bounds on actual transition temperatures.

First, we analyze the influence of increasing attractive interaction on the critical temperatures at $h = 0$. Fig. 6.1 shows the temperature vs. binding energy phase diagrams in units of the lattice Fermi energy E_F at $h = 0$ and low values of the electron concentration. The temperatures T_c^{KT} (dashed-double dotted line (red color) in the diagram) are generally much smaller than T_c^{HF} (solid line (green color) in the diagram) but on reducing the attraction, in the absence of magnetic field, the difference between T_c^{KT} and T_c^{HF} decreases.

In the weak coupling regime, in which the value of the order parameter is low in comparison with the value of the superfluid stiffness, T_c^{KT} is limited by the temperature determined in the Hartree-Fock approximation. However, with increasing attraction, the order parameter increases, the value of the superfluid density decreases and the quantity which limits the KT temperatures is $\rho_s(T = 0)$. In the strong coupling regime, T_c^{KT} are very well approximated by the value of $\frac{\pi}{2}\rho(0)$. This means that despite the unlimited increase in T_c^{HF} with increasing $|U|$ (E_b), T_c^{KT} , after the increase to the maximum value for the optimal value of the interaction, begin to decrease and are limited by the finite value of $\rho_s(0)$ [106, 107, 119, 141, 142]. Similar behavior of the Kosterlitz-Thouless critical temperatures (i.e. an increase followed by a decrease) was also observed for the s-extended- and d-wave pairing symmetry cases, within the Extended Hubbard Model [87].

Here, we perform an analysis of the influence of a Zeeman magnetic field on the BCS-

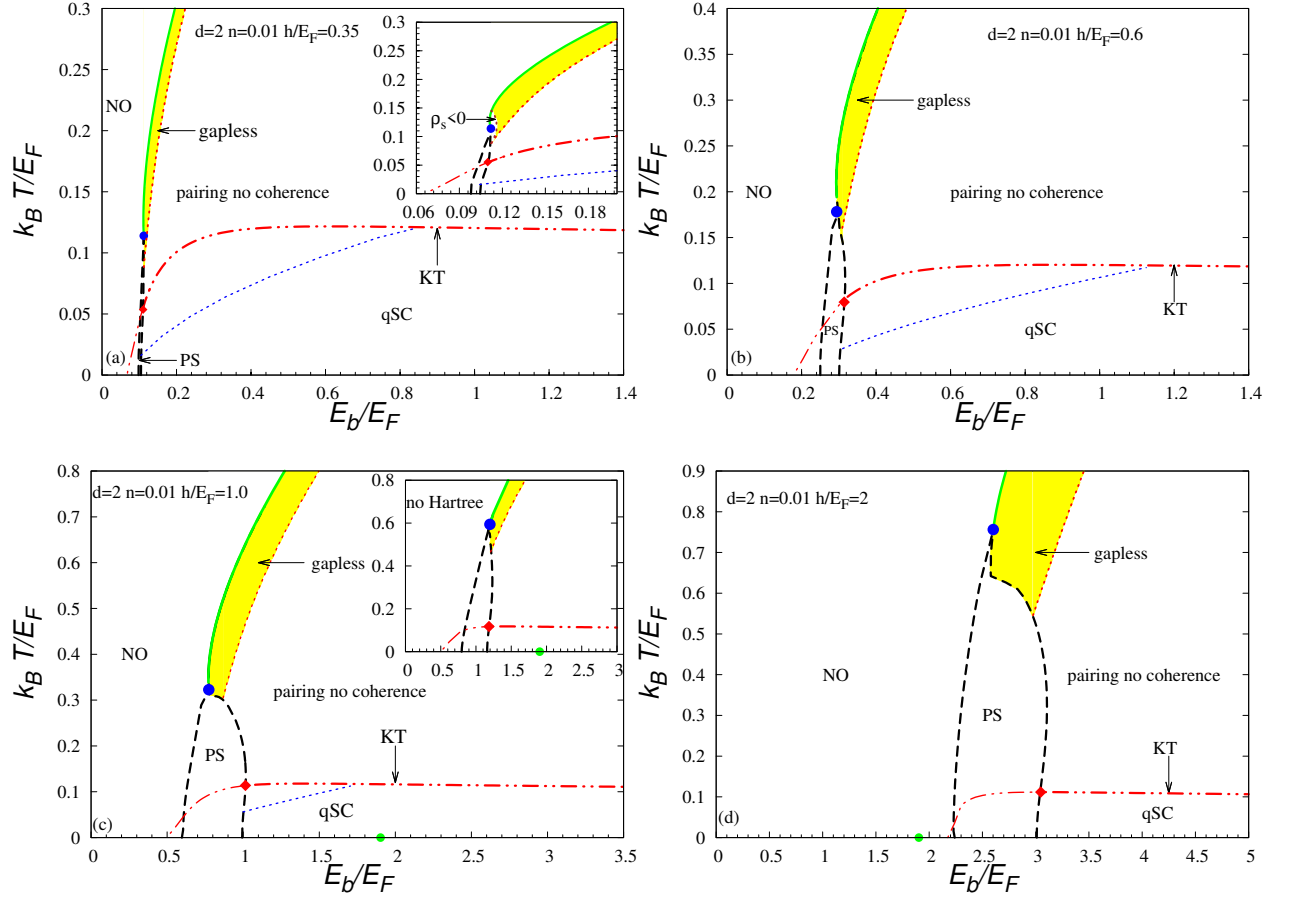


Figure 6.2: Temperature vs. binding energy phase diagrams in units of the lattice Fermi energy at (a) $h/E_F = 0.35$ (inset – details of the region around TCP), (b) $h/E_F = 0.6$, (c) $h/E_F = 1$ (inset – diagram without the Hartree term) and (d) $h/E_F = 2$. Thick dash-double dotted line (red color) is the KT transition line. Thin dash-double dotted line is the KT transition line to the metastable superfluid state. Thick solid line denotes transition from pairing without coherence region to NO within the Hartree approximation, with distinguished gapless region (yellow color). *qSC* – 2D quasi superconductor, PS – phase separation. Below thin dotted line (blue color) – $P < 10^{-4}$ (i.e. zero polarization within numerical precision). The green point in (c)-(d) shows the BCS-LP crossover point at $T = 0$; blue point is the MF TCP point.

BEC crossover phase diagrams. Fig. 6.2 shows $(T - E_b)$ phase diagrams in units of the Fermi energy, for fixed values of the magnetic field: (a) $h/E_F = 0.35$ (on the BCS side), (b) $h/E_F = 0.6$, (c) $h/E_F = 1$ (in the intermediate couplings) and (d) $h/E_F = 2$ (on the LP side). The solid lines (2^{nd} order transition lines) and PS regions are obtained within the Hartree approximation. The thick dash-double dotted line (red color) denotes the KT transition determined from Eqs. (3.35), (3.11).

The system is a quasi superconductor (qSC) below T_c^{KT} . Polarization can be induced

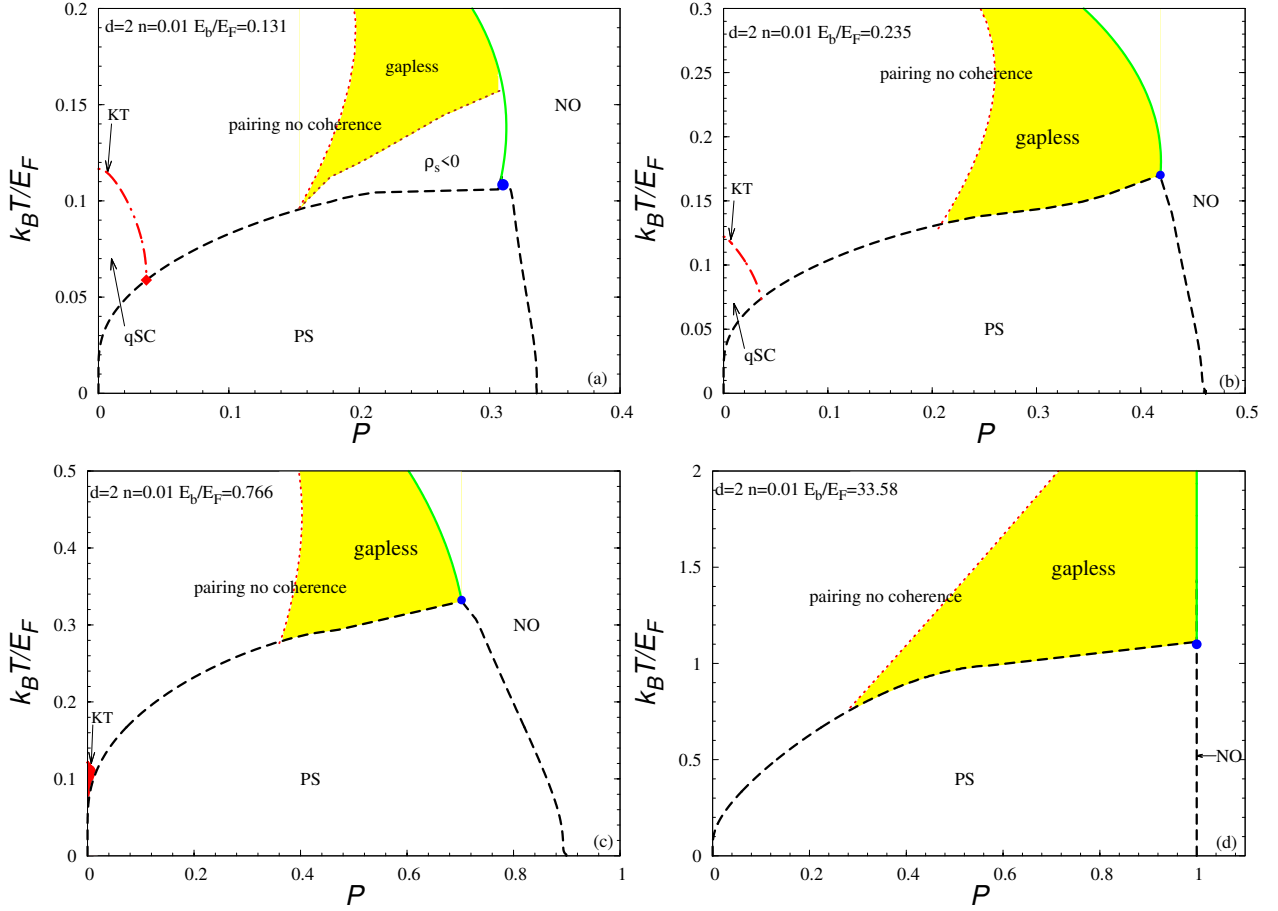


Figure 6.3: Temperature vs. polarization at (a) $E_b / E_F = 0.131$ ($U = -2.8$), (b) $E_b / E_F = 0.235$ ($U = -3$), (c) $E_b / E_F = 0.766$ ($U = -3.5$) and (d) $E_b / E_F = 33.58$ ($U = -8$). Thick dashed-double dotted line (red color) is the KT transition line. Thick solid line denotes transition from pairing without coherence region to NO within the Hartree approximation, with distinguished gapless region (yellow color). qSC – 2D quasi superconductor, PS – phase separation, blue point is the MF TCP point.

by thermal excitations of quasiparticles. Above T_c^{KT} , but below T_c^{HF} (pair breaking temperature), pairs exist but without a long-range phase coherence. In this region a pseudogap behavior is observed. $T_{pair} \sim T_c^{HF}$ can be interpreted as the temperature at which the amplitude of the order parameter takes a finite value, but short-range phase correlations are negligible (superconducting correlation length is of the order of the lattice spacing). It corresponds to the occurrence of incoherent pairs, either Cooper pairs in the weak coupling or LP's in the strong coupling regime. With lowering the temperature, these fluctuating pairs develop short-range phase correlations. Near but above T_c^{KT} , the phase correlation length increases and becomes much longer than the lattice spacing. At T_c^{KT} , the phase transition occurs and the system becomes superconducting. Superconducting long-range order sets in at $T = 0$.

As mentioned above, the temperatures T_c^{KT} are generally lower than T_c^{HF} , but on reducing the attraction, in the absence of magnetic field, the difference between T_c^{KT} and T_c^{HF} decreases in the weak coupling limit. At $h = 0$ and $E_b \ll 1$, $T_c^{HF} \neq 0$ and $T_c^{KT} \neq 0$. When the magnetic field increases, $T_c^{HF} = 0$, below some value of the binding energy. This critical E_b increases with h . In the strict BCS-MFA diagram the tricritical point (TCP) exists at finite magnetic fields. In this mean-field TCP, the SC MF phase, the NO state and PS coexist. There is also “TCP” on the KT curve in which three states meet: the qSC phase, the state of incoherent pairs and PS. The PS range widens with increasing h and the distance between the TCP MF and KT “TCP” is longer. As shown in Fig. 6.3, the effect of finite P on the KT superfluid state is strong. If $t^\uparrow = t^\downarrow$, the KT phase is restricted to the weak coupling region and low values of P , which is clearly visible in Fig. 6.4. The phase diagrams are plotted in $(T - E_b)$ variables in units of the Fermi energy, for fixed values of population imbalance $P = 0.02$ (a) and $P = 0.1$ (b). One can observe that the region of the KT phase existence is rather narrow, even at very low $P = 0.02$ and is essentially restricted to weak couplings. Moreover, the qSC state is not gapless. For higher value of $P = 0.1$, even in the weak coupling limit, the qSC state disappears. One can distinguish the gapless region in the weak coupling limit, but only within the state of incoherent pairs.

With increasing attractive interaction, the range of occurrence of the KT phase becomes narrower in the intermediate couplings region (Fig. 6.3(b)-(c)) and disappears on the LP side (Fig. 6.3 (d)), in favor of the phase separation region. Therefore, the qSC state is highly reduced with increasing attractive interaction even for low population imbalance. Increasing polarization favors the phase of incoherent pairs. The range of occurrence of qSC in the presence of P widens in the weak coupling regime with increasing n .

As shown before, in the analysis of the quasiparticle excitation spectrum, we also find a gapless region (yellow color in diagrams), for $h > \Delta$ (the BCS side) and for $h > E_g/2$, where $E_g = 2\sqrt{(\bar{\mu} - \epsilon_0)^2 + |\Delta|^2}$ (on the LP side). If $t^\uparrow = t^\downarrow$, this gapless region can only be realized at $T > 0$ and has excess fermions with two FS in the weak coupling limit. In Figs. 6.2 and 6.3, the gapless region is distinguished within the state of incoherent pairs, i.e. is non-superfluid. In the strong coupling regime, the temperature can induce the spin-polarized gapless region (in the state of incoherent pairs) with one FS. This is in contrast to the 3D case, where the BP-1 phase can be stable even without mass imbalance at $T = 0$ and low n [131]. In the strong coupling limit, T_c^{KT} does not depend on magnetic field and approximately approaches $k_B T_c^{KT}/E_F \approx \frac{t}{2|U|}(1 - \frac{n}{2})$ for $|U| \gg t$, $E_F = 2\pi t n$, in contrast to the continuum model which yields in that limit $k_B T_c^{KT}/E_F = \frac{1}{8}$ [140]. For $k_B T \ll |U|$, there exist only LPs not broken by the magnetic field and the system is equivalent to that of a hard-core Bose gas on a lattice. The thin dash-double dotted line in Fig. 6.2 inside the NO state marks the region where Ω has two minima (below the curve): lower at $\Delta = 0$ and higher at $\Delta \neq 0$. It means that there can exist a metastable superconducting state.

As discussed in chapter 4, an important aspect of the analysis is the influence of the Hartree term on the phase diagrams. First, the presence of the Hartree term leads to

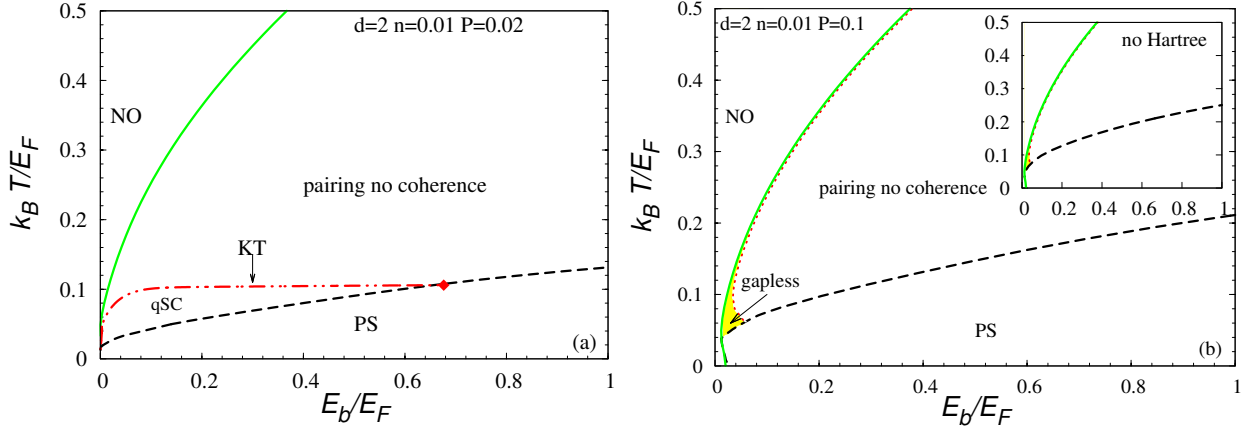


Figure 6.4: Temperature vs. binding energy phase diagrams in units of the lattice Fermi energy at (a) $P = 0.02$, (b) $P = 0.1$ (inset – diagram without the Hartree term). Thick dashed-double dotted line (red color) is the KT transition line. Thick solid line denotes transition from pairing without coherence region to NO within the Hartree approximation, with distinguished gapless region (yellow color) in Fig. (b). *qSC* – 2D quasi superconductor, PS – phase separation.

the reentrant transition (RT) in the weak coupling limit (Figs. 6.2(a) and 6.3(a)), which is not observed in the phase diagrams without the Hartree term. We also find a region around MF TCP in which formally $\rho_s < 0$, although $\Omega^{SC} < \Omega^{NO}$ (Figs. 6.2(a) inset and 6.3(a)), in the phase diagram on the BCS side with the Hartree term. If RT exists, it becomes dynamically unstable because $\rho_s < 0$. In addition, the Hartree term causes an increase in the Chandrasekhar-Clogston limit [52, 110, 111].

6.2 3D simple cubic lattice. T-matrix approach

6.2.1 Formalism

In this section, we discuss the T-matrix approach. As mentioned earlier, the most interesting and promising ideas assume that the properties of High- T_c superconductors (and also other unconventional superconductors) place them between two regimes: BCS and BEC. To extend the analysis of the crossover from weak to strong coupling to finite temperatures in 3D, it is necessary to take into account the pairing fluctuations effects. For intermediate couplings, the normal state can have a pseudo-gap (PG) in the single particle energy spectrum. It is connected with the presence of preformed fermionic pairs in the normal state. These pairs are formed at the temperature T_p , which is much higher than T_c at which the long-range phase coherence occurs and a phase transition to the superconducting state takes place. T_c corresponds to the condensation of pairs with $\vec{q} = 0$ and the pairs with finite center-of-mass momentum ($\vec{q} \neq 0$) remain as excitations. In the BCS limit, pairs form and condense at the same temperature. For many years, many different

approaches have been developed to extend the BCS-BEC crossover to finite temperatures – most of them concern different T-matrix schemes in which one considers coupled equations between particles (with the propagator G) and pairs (with the propagator $T(q)$, hence the name T-matrix).

As mentioned before, Eagles [144] and Leggett [21] discussed the BCS-BEC crossover concept in the ground state; Eagles for superconductors with low carrier concentration while Leggett in the context of p-wave pairing symmetry in ^3He . Leggett suggested that the system evolves continuously from BCS to BEC with increasing attractive interaction. Furthermore, Robaszkiewicz, Micnas and Chao analyzed the evolution from BCS to LP limit within the extended attractive Hubbard model [23, 24, 27]. In 1985 Nozieres and Schmitt-Rink (NSR) [22] extended Leggett's analysis to calculate the critical temperature. A very important point of their work was the introduction of the self-energy in the scattering T-matrix. They used the so-called $(G_0G_0)G_0$ scheme, where, in general, the symbols in parentheses denote the type of Green functions that enter the equation for the pairing susceptibility ($\chi(q) = \sum_k G_0(k)G_0(q-k)$, see below for notation and further details) and the latter symbol stands for the type of Green function in the self-energy equation ($\Sigma(k) = \sum_q T(q)G_0(q-k)$). Here, G_0 is the bare (non-interacting) fermionic Green function. As a consequence, in this approach, the self-energy is not included in the gap equation, hence it is not completely self-consistent.

The BCS-BEC crossover concept has been adapted to explain some different features of HTC superconductors by Micnas [27, 145] Uemura [20] and Randeria [28]. Many works of the Levin's group [146, 147, 148] on the BCS-BEC crossover are based on the s-wave pairing symmetry in the 3D helium.

Many theoretical approaches to derivation of the formula for the transition temperature in the presence of the pseudo-gap are based on Kadanoff and Martin (KM) works [149]. This scheme was also extended by Patton [150] to analyze superconducting fluctuations in a dirty low dimensional superconductor near the critical temperature. The KM scheme relies on the reformulation of the BCS theory within Green functions formalism (Green function equations of motion or the correlation functions) and it is very similar to the Thouless formalism [151]. This is the so-called $(GG)G_0$ scheme, where G denotes the dressed (interacting or full) Green function. One can also determine the equations for T_c within the $(GG)G_0$ scheme, which is discussed in detail below.

We start from the consideration of the single component model of fermions:

$$\mathcal{H} = \sum_{\vec{k}\sigma} \bar{\epsilon}_{\vec{k}} c_{\vec{k}\sigma}^\dagger c_{\vec{k}\sigma} + \frac{1}{N} \sum_{\vec{k}, \vec{k}', \vec{q}} U_{\vec{k}, \vec{k}'} c_{\vec{k}+\vec{q}/2, \uparrow}^\dagger c_{-\vec{k}+\vec{q}/2, \downarrow}^\dagger c_{-\vec{k}'+\vec{q}/2, \downarrow} c_{\vec{k}'+\vec{q}/2, \uparrow}, \quad (6.1)$$

where: $U_{\vec{k}, \vec{k}'} = g\phi_{\vec{k}}\phi_{\vec{k}'}$ – separable attractive potential, $\phi_{\vec{k}}$ – specifies the pairing symmetry, $\bar{\epsilon}_{\vec{k}} = \epsilon_{\vec{k}} - \mu$. In the Attractive Hubbard Model on the simple cubic lattice: $g = U$, $\phi_{\vec{k}} = 1$ and $\epsilon_{\vec{k}} = -2t(\cos(k_x) + \cos(k_y) + \cos(k_z)) + 6t$, the momentum summation is restricted to the first Brillouin zone.

The formalism that we will employ makes use of the one- and two-particle Green functions, i.e. expectation values of time-ordered products of creation and annihilation

operators. The equation for the one-particle Green function is used in the exact form, while the formulas for the two-particle Green functions are approximate, following KM. The corresponding two-particle correlation functions can be conveniently expressed in terms of a T-matrix (which can be shown to play the role of a pair propagator, see below) and one-particle Green functions. For a detailed derivation of the relevant equations satisfied by the Green functions, self-energies, pairing susceptibilities and the T-matrix in real and reciprocal space, we refer the Reader to Appendix D. After Fourier transforming to momentum space, one obtains the self-consistent equations in the normal state:

$$T^{-1}(q) = g^{-1} + \sum_k G(k)G_0(q-k)\phi_{\vec{k}-\vec{q}/2}^2 \quad (6.2)$$

is the T-matrix in separable channels,

$$\Sigma(k) = \sum_q T(q)G_0(q-k)\phi_{\vec{k}-\vec{q}/2}^2 \quad (6.3)$$

is the self-energy equation. The full Green function satisfies the Dyson equation:

$$G^{-1}(k) = G_0^{-1}(k) - \Sigma(k), \quad (6.4)$$

where: $G_0^{-1}(k) = i\omega_n - \bar{\epsilon}_{\vec{k}}$ - free fermionic Green function, $\beta = 1/k_B T$.

Here, we introduce the following notation: $k = (\vec{k}, i\omega_n)$, $q = (\vec{q}, i\nu_n)$, $\sum_k = \frac{1}{\beta N} \sum_{\vec{k}, \omega_n}$, $\sum_q = \frac{1}{\beta N} \sum_{\vec{q}, \nu_n}$, $\omega_n = \frac{2\pi}{\beta}(n + \frac{1}{2})$, $\nu_n = \frac{2\pi}{\beta}n$ - odd, even Matsubara frequencies, respectively, n - integer.

The pairing susceptibility equation takes the form:

$$\chi(q) = \sum_k G(k)G_0(q-k)\phi_{\vec{k}-\vec{q}/2}^2. \quad (6.5)$$

Eq. (6.2) can be written as:

$$T^{-1}(q) = g^{-1} + \chi(q). \quad (6.6)$$

For high temperatures, the T-matrix is finite for all values of q . When the temperature is lowered, metastable or long-lived pairs appear. At the superconducting (superfluid) transition temperature, the T-matrix becomes divergent for $q = 0$ (the Thouless criterion), i.e.:

$$g^{-1} + \chi(\vec{0}, 0, T_c) = 0. \quad (6.7)$$

If we assume slow fluctuations of the pairing field close to T_c , i.e. the term with $q \approx 0$ is dominant, then the fermionic self-energy can be approximated in the following way:

$$\Sigma(k) = \sum_q T(q)G_0(q-k)\phi_{\vec{k}-\vec{q}/2}^2 \approx G_0(-k)\phi_{\vec{k}}^2 \sum_q T(q) = \frac{\Delta_{pg}^2 \phi_{\vec{k}}^2}{i\omega_n + \bar{\epsilon}_{-\vec{k}}}. \quad (6.8)$$

where: Δ_{pg}^2 is the pseudogap parameter:

$$\Delta_{pg}^2 \equiv - \sum_q T(q) = - \frac{1}{\pi N} \sum_{\vec{q} \neq 0} \int_{-\infty}^{\infty} \text{Im } T(\vec{q}, \Omega) b(\Omega) d\Omega, \quad (6.9)$$

where $b(\Omega) = 1/(\exp(\beta\Omega) - 1)$ is the Bose function.

From the Dyson equation 6.4:

$$G^{-1}(k) = i\omega_n - \bar{\epsilon}_{\vec{k}} - \frac{\Delta_{pg}^2 \phi_{\vec{k}}^2}{i\omega_n + \bar{\epsilon}_{\vec{k}}}. \quad (6.10)$$

Therefore, the full fermionic Green function reads:

$$G(k) = \frac{i\omega_n + \bar{\epsilon}_{\vec{k}}}{(i\omega_n)^2 - (\bar{\epsilon}_{\vec{k}}^2 + \Delta_{pg}^2 \phi_{\vec{k}}^2)} \quad (6.11)$$

and it has poles in $\pm E_{\vec{k}} = \sqrt{\bar{\epsilon}_{\vec{k}}^2 + \Delta_{pg}^2 \phi_{\vec{k}}^2}$. This form of the Green function is analogous to the one in the standard BCS theory.

Using (6.11) we can evaluate the pairing susceptibility (6.5). Summing over Matsubara frequencies, one obtains:

$$\chi(q) = - \frac{1}{N} \sum_{\vec{k}} \left[\frac{f(E_{\vec{k}}) + f(\bar{\epsilon}_{\vec{q}-\vec{k}}) - 1}{\bar{\epsilon}_{\vec{q}-\vec{k}} + E_{\vec{k}} - i\nu_n} u_{\vec{k}}^2 + \frac{f(\bar{\epsilon}_{\vec{q}-\vec{k}}) - f(E_{\vec{k}})}{\bar{\epsilon}_{\vec{q}-\vec{k}} - E_{\vec{k}} - i\nu_n} v_{\vec{k}}^2 \right] \phi_{\vec{k}-\vec{q}/2}^2, \quad (6.12)$$

where, as usual: $u_{\vec{k}}^2 + v_{\vec{k}}^2 = 1$, $u_{\vec{k}}^2 = \frac{1}{2}(1 + \bar{\epsilon}_{\vec{k}}/E_{\vec{k}})$, $f(\omega) = 1/(\exp(\beta\omega) + 1)$ is the Fermi function.

The equation for the number of particles is:

$$n = \frac{2}{\beta N} \sum_{\vec{k}, \omega_n} e^{i\eta\omega_n} G(k). \quad (6.13)$$

where: $\eta = 0^+$.

Performing summation over Matsubara frequencies, the above equation takes the form:

$$n = \frac{1}{N} \sum_{\vec{k}} \left[1 - \frac{\bar{\epsilon}_{\vec{k}}}{E_{\vec{k}}} \tanh(\beta_c E_{\vec{k}}/2) \right]. \quad (6.14)$$

From the Thouless criterion (Eq. (6.7)) with the use of Eq. (6.12) we get:

$$1 = |g| \frac{1}{N} \sum_{\vec{k}} \phi_{\vec{k}}^2 \frac{\tanh(\beta_c E_{\vec{k}}/2)}{2E_{\vec{k}}}. \quad (6.15)$$

To calculate the pseudogap parameter in the neighborhood of the transition region, it is sufficient to approximate the imaginary part of the T-matrix by the value at small Ω

and $|\vec{q}|$. Performing analitical continuation ($i\nu_n \rightarrow \Omega + i\eta$), the real and imaginary parts of the inverse of the T-matrix can be written as:

$$\text{Re } T^{-1}(\vec{q}, \Omega) \approx A'_0(\Omega - \Omega_{\vec{q}}), \quad (6.16)$$

$$\text{Im } T^{-1}(\vec{q}, \Omega) \approx A''_0\Omega, \quad (6.17)$$

where $\Omega_{\vec{q}}$ – fermion pairs energy dispersion and the parameters A'_0 , A''_0 are approximately constant and close to T_c their ratio $\varepsilon \equiv A''_0/A'_0 \ll 1$.

Writing:

$$T^{-1}(\vec{q}, \Omega) = \text{Re } T^{-1}(\vec{q}, \Omega) + i \text{Im } T^{-1}(\vec{q}, \Omega), \quad (6.18)$$

one has:

$$T(\vec{q}, \Omega) = \frac{1}{\text{Re } T^{-1}(\vec{q}, \Omega) + i \text{Im } T^{-1}(\vec{q}, \Omega)} = \frac{\text{Re } T^{-1}(\vec{q}, \Omega) - i \text{Im } T^{-1}(\vec{q}, \Omega)}{(\text{Re } T^{-1}(\vec{q}, \Omega))^2 + (\text{Im } T^{-1}(\vec{q}, \Omega))^2}. \quad (6.19)$$

Hence:

$$\text{Im } T(\vec{q}, \Omega) = -\frac{\text{Im } T^{-1}(\vec{q}, \Omega)}{(\text{Re } T^{-1}(\vec{q}, \Omega))^2 + (\text{Im } T^{-1}(\vec{q}, \Omega))^2}. \quad (6.20)$$

Using now Eqs. (6.16)-(6.17), one obtains:

$$\text{Im } T(\vec{q}, \Omega) \approx -\frac{A''_0\Omega}{A_0'^2(\Omega - \Omega_{\vec{q}})^2 + A_0''^2\Omega^2} = -\frac{1}{A'_0\Omega} \frac{\varepsilon}{(1 - \Omega_{\vec{q}}/\Omega)^2 + \varepsilon^2}. \quad (6.21)$$

In this formula, one can recognize the Poisson kernel $\eta_\varepsilon(x) = \frac{1}{\pi} \frac{\varepsilon}{x^2 + \varepsilon^2}$, which in the limit of $\varepsilon \rightarrow 0$ becomes the Dirac delta function. Finally:

$$\text{Im } T(\vec{q}, \Omega) \approx -\frac{\pi}{A'_0} \delta(\Omega - \Omega_{\vec{q}}). \quad (6.22)$$

This can be rewritten, using the Weierstrass theorem, as:

$$T(\vec{q}, \Omega) \approx \frac{A_0'^{-1}}{\Omega - \Omega_{\vec{q}} + i\varepsilon\Omega}, \quad (6.23)$$

which has the natural interpretation of the pair propagator.

The pair dispersion is determined from Eqs. (6.16) and (6.12), and is given by:

$$\begin{aligned} \Omega_{\vec{q}} &= \frac{1}{A'_0} \left\{ \frac{1}{N} \sum_{\vec{k}} \left[\frac{f(E_{\vec{k}}) + f(\bar{\varepsilon}_{\vec{q}-\vec{k}}) - 1}{\bar{\varepsilon}_{\vec{q}-\vec{k}} + E_{\vec{k}}} u_{\vec{k}}^2 + \frac{f(\bar{\varepsilon}_{\vec{q}-\vec{k}}) - f(E_{\vec{k}})}{\bar{\varepsilon}_{\vec{q}-\vec{k}} - E_{\vec{k}}} v_{\vec{k}}^2 \right] \phi_{\vec{k}-\vec{q}/2}^2 \right. \\ &\quad \left. + \frac{1 - 2f(E_{\vec{k}})}{2E_{\vec{k}}} \phi_{\vec{k}}^2 \right\}, \end{aligned} \quad (6.24)$$

where:

$$A'_0 = \frac{1}{2\Delta_{pg}^2} \left[n - 2\frac{1}{N} \sum_{\vec{k}} f(\bar{\varepsilon}_{\vec{k}}) \right].$$

For small $|\vec{q}|$, $\Omega_{\vec{q}}$ is quadratic in \vec{q} :

$$\Omega_{\vec{q}} \approx \frac{\vec{q}^2}{2M^*}, \quad (6.25)$$

where M^* is the effective pair mass, which can be determined from the expansion of $\Omega_{\vec{q}}$.

Finally, the pseudogap parameter equation (6.9) can be written in terms of the Bose function:

$$\Delta_{pg}^2 = \frac{1}{A'_0} \frac{1}{N} \sum_{\vec{q} \neq 0} b(\Omega_{\vec{q}}). \quad (6.26)$$

To summarize, we gather here all equations for the superconducting transition temperature:

$$1 = |g| \frac{1}{N} \sum_{\vec{k}} \phi_{\vec{k}}^2 \frac{\tanh(\beta_c E_{\vec{k}}/2)}{2E_{\vec{k}}}, \quad (6.27)$$

$$n = \frac{1}{N} \sum_{\vec{k}} \left[1 - \frac{\bar{\epsilon}_{\vec{k}}}{E_{\vec{k}}} \tanh(\beta_c E_{\vec{k}}/2) \right], \quad (6.28)$$

$$\Delta_{pg}^2 = \frac{1}{A'_0} \frac{1}{N} \sum_{\vec{q} \neq 0} b(\Omega_{\vec{q}}), \quad (6.29)$$

where $\Omega_{\vec{q}}$ and A'_0 are given by Eqs. (6.24) and (6.25), respectively.

The form of the first two Eqs. (6.27)-(6.28) is analogous to the standard BCS theory (but without the Hartree term), with the gap parameter replaced by the pseudogap parameter. The third Eq. (6.29) gives the pseudogap parameter in terms of the Bose function. These equations are solved self-consistently for a given band structure and filling and together they determine T_c .

The above scheme is the so-called $(GG_0)G_0$ scheme, i.e. the pair susceptibility is expressed by GG_0 and the self-energy is expressed by G_0 .

6.2.1.1 $(GG)G_0$ scheme

Now, we briefly discuss the $(GG)G_0$ scheme [152].

The starting point is to use the self-consistent T-matrix equations for the normal state, i.e. for $T(q)$, $\Sigma(k)$ and $G(k)$, as given by Eqs. (6.2)-(6.4), where all the Green functions are fully dressed. We introduce the pseudogap parameter in the fermionic Green function as above, in the calculations of T_c from the T-matrix equations. However, the Green

functions in the pairing susceptibility are fully dressed (G). Therefore, one gets:

$$\begin{aligned}
\chi(q) &= \sum_k G(k)G(q-k)\phi_{k-q/2}^2 = \frac{1}{N} \sum_{\vec{k}} \frac{1}{\beta} \sum_{\omega_n} G(\vec{k}, i\omega_n) G(\vec{q}-\vec{k}, i\nu_n - i\omega_n) \phi_{k-q/2}^2 = \\
&= \frac{1}{N} \sum_{\vec{k}} \left(\frac{v_{\vec{k}}^2 v_{\vec{q}-\vec{k}}^2}{i\nu_n + E_{\vec{k}} + E_{\vec{q}-\vec{k}}} - \frac{u_{\vec{k}}^2 u_{\vec{q}-\vec{k}}^2}{i\nu_n - E_{\vec{k}} - E_{\vec{q}-\vec{k}}} \right) [1 - f(E_{\vec{k}}) - f(E_{\vec{q}-\vec{k}})] \phi_{k-q/2}^2 \\
&+ \frac{1}{N} \sum_{\vec{k}} \left(\frac{u_{\vec{k}}^2 v_{\vec{q}-\vec{k}}^2}{i\nu_n + E_{\vec{q}-\vec{k}} - E_{\vec{k}}} - \frac{u_{\vec{q}-\vec{k}}^2 v_{\vec{k}}^2}{i\nu_n - E_{\vec{q}-\vec{k}} + E_{\vec{k}}} \right) [f(E_{\vec{k}}) - f(E_{\vec{q}-\vec{k}})] \phi_{k-q/2}^2. \quad (6.30)
\end{aligned}$$

Formally, the pseudogap and the number equations keep the same form as in the $(GG_0)G_0$ scheme. We use again the small Ω , $|\vec{q}|$ expansion of the T-matrix in the evaluation of the pseudogap, i.e. we take at T_c : $T(\vec{q}, \Omega) = \frac{Z^{-1}}{\Omega - \Omega_{\vec{q}}}$, where Z is specified below. This scheme has also been recently considered by T. Ozawa and G. Baym [153]. The Thouless criterion is:

$$1 + g\chi(\vec{0}, 0, T_c) = 0. \quad (6.31)$$

Therefore, the equations for T_c in the $(GG)G_0$ scheme take the final form:

$$\frac{1}{|g|} = \frac{1}{N} \sum_{\vec{k}} \phi_{\vec{k}}^2 \left[\frac{1}{2} \left(1 + \frac{\bar{\epsilon}_{\vec{k}}^2}{E_{\vec{k}}^2} \right) \frac{\tanh(\beta_c E_{\vec{k}}/2)}{2E_{\vec{k}}} - \frac{\Delta_{pg}^2}{2E_{\vec{k}}^2} f'(E_{\vec{k}}) \right], \quad (6.32)$$

$$n = \frac{1}{N} \sum_{\vec{k}} \left[1 - \frac{\bar{\epsilon}_{\vec{k}}}{E_{\vec{k}}} \tanh(\beta_c E_{\vec{k}}/2) \right], \quad (6.33)$$

$$\Delta_{pg}^2 = \frac{1}{Z} \frac{1}{N} \sum_{\vec{q} \neq 0} b(\Omega_{\vec{q}}), \quad (6.34)$$

where:

$$\begin{aligned}
\Omega_{\vec{q}} &= \frac{1}{Z} \left\{ \frac{1}{N} \sum_{\vec{k}} \left[\left(\frac{u_{\vec{k}}^2 u_{\vec{q}-\vec{k}}^2 + v_{\vec{k}}^2 v_{\vec{q}-\vec{k}}^2}{E_{\vec{k}} + E_{\vec{q}-\vec{k}}} \right) [f(E_{\vec{k}}) + f(E_{\vec{q}-\vec{k}}) - 1] \phi_{k-q/2}^2 \right. \right. \\
&+ \left. \left(\frac{u_{\vec{k}}^2 v_{\vec{q}-\vec{k}}^2 + u_{\vec{q}-\vec{k}}^2 v_{\vec{k}}^2}{E_{\vec{q}-\vec{k}} - E_{\vec{k}}} \right) [f(E_{\vec{q}-\vec{k}}) - f(E_{\vec{k}})] \right] \phi_{k-q/2}^2 + \chi(\vec{0}, 0) \right\}, \quad (6.35)
\end{aligned}$$

$$Z = \frac{1}{N} \sum_{\vec{k}} \left[\frac{\bar{\epsilon}_{\vec{k}}}{2E_{\vec{k}}^2} \left(\frac{1 - 2f(E_{\vec{k}})}{2E_{\vec{k}}} + f'(E_{\vec{k}}) \right) \right], \quad (6.36)$$

where: $f' = \partial f(\omega)/\partial \omega$ - derivative of the Fermi function.

The pair dispersion for small $|\vec{q}|$ is taken as previously: $\Omega_{\vec{q}} = q^2/2M^*$, where M^* is the effective pair mass.

Comparing $(GG_0)G_0$ and $(GG)G_0$ T-matrix schemes we see the differences in the first equation for T_c and also in the pair dispersion. For a small pseudogap parameter, Eq. (6.32) goes over to Eq. (6.15). The numerical solutions for T_c in both schemes are discussed later.

6.2.1.2 Hubbard model with $U < 0$ in a magnetic field – $(GG_0)G_0$ scheme

Now, we discuss the generalization of the T_c equations in non-zero Zeeman magnetic field case, for the 3D simple cubic lattice and the s-wave pairing symmetry case. For more details, we refer the Reader to Appendix D.3. In particular, we discuss there the nature of the approximation involved.

Let us introduce the symmetrized pairing susceptibility [154]:

$$\chi(q) = \frac{1}{2} [\chi_{\uparrow\downarrow}(q) + \chi_{\downarrow\uparrow}(q)], \quad (6.37)$$

where:

$$\chi_{\uparrow\downarrow}(q) = \sum_k G_{0\uparrow}(q-k)G_{\downarrow}(k), \quad (6.38)$$

$$\chi_{\downarrow\uparrow}(q) = \sum_k G_{0\downarrow}(q-k)G_{\uparrow}(k), \quad (6.39)$$

$$G_{0\sigma}^{-1}(k) = i\omega_n - \bar{\epsilon}_{\vec{k}} - \sigma h. \quad (6.40)$$

The full Green functions for fermions with spin σ are given by the Dyson equation:

$$G_{\sigma}^{-1}(k) = G_{0\sigma}^{-1}(k) - \Sigma_{\sigma}(k), \quad (6.41)$$

In the pairing approximation:

$$\Sigma_{\sigma}(k) = \sum_q T(q)G_{0\bar{\sigma}}(q-k) \approx -\Delta_{pg}^2 G_{0\sigma}(k), \quad (6.42)$$

where: $\bar{\sigma} = -\sigma$. Therefore:

$$G_{\uparrow,\downarrow}(k) = \frac{u_{\vec{k}}^2}{i\omega_n \pm h - E_{\vec{k}}} + \frac{v_{\vec{k}}^2}{i\omega_n \pm h + E_{\vec{k}}}, \quad (6.43)$$

where, as usual: $E_{\vec{k}} = \sqrt{\bar{\epsilon}_{\vec{k}}^2 + \Delta_{pg}^2}$, $u_{\vec{k}}^2 = \frac{1}{2}(1 + \frac{\bar{\epsilon}_{\vec{k}}}{E_{\vec{k}}})$, $u_{\vec{k}}^2 + v_{\vec{k}}^2 = 1$.

The pseudogap parameter is determined as previously:

$$\Delta_{pg}^2 = - \sum_q T(q) = -\frac{1}{\pi N} \sum_{\vec{q} \neq 0} \int_{-\infty}^{\infty} \text{Im} T(\vec{q}, \Omega) b(\Omega) d\Omega \quad (6.44)$$

and

$$T^{-1}(q) = 1/g + \chi(q). \quad (6.45)$$

The pairing susceptibility is obtained after performing summation over the Matsubara frequencies in Eqs. (6.37)-(6.39):

$$\chi(q) = -\frac{1}{N} \sum_{\vec{k}} \left[\frac{\bar{f}(E_{\vec{k}}) + \bar{f}(\bar{\epsilon}_{\vec{q}-\vec{k}}) - 1}{\bar{\epsilon}_{\vec{q}-\vec{k}} + E_{\vec{k}} - i\nu_n} u_{\vec{k}}^2 + \frac{\bar{f}(\bar{\epsilon}_{\vec{q}-\vec{k}}) - \bar{f}(E_{\vec{k}})}{\bar{\epsilon}_{\vec{q}-\vec{k}} - E_{\vec{k}} - i\nu_n} v_{\vec{k}}^2 \right], \quad (6.46)$$

where:

$$\bar{f}(x) = \frac{1}{2} [f(x+h) + f(x-h)] \quad (6.47)$$

is the symmetrized Fermi function.

Finally, the equations for T_c in the presence of the Zeeman magnetic field take the form:

$$0 = 1 + U\chi(0) = 1 + U \frac{1}{N} \sum_{\vec{k}} \frac{1 - 2\bar{f}(E_{\vec{k}})}{2E_{\vec{k}}}, \quad (6.48)$$

$$n = 2 \frac{1}{N} \sum_{\vec{k}} \left[v_k^2 + \frac{\bar{\epsilon}_{\vec{k}}}{E_{\vec{k}}} \bar{f}(E_{\vec{k}}) \right], \quad (6.49)$$

$$Pn = \frac{1}{N} \sum_{\vec{k}} [f(E_{\vec{k}} - h) - f(E_{\vec{k}} + h)], \quad (6.50)$$

$$\Delta_{pg}^2 = \frac{1}{A_0} \frac{1}{N} \sum_{\vec{q} \neq 0} b(\Omega_{\vec{q}}), \quad (6.51)$$

where: $P = (n_{\uparrow} - n_{\downarrow})/n$ - spin polarization, $f(x) = 1/[\exp(\beta x) + 1]$ and $b(x) = 1/[\exp(\beta x) - 1]$ are Fermi and Bose functions, respectively. Eqs. (6.48)-(6.50) have the form of the BCS equations (without the Hartree term), with the gap parameter replaced by the pseudogap parameter.

The pairing susceptibility $\chi(\vec{q}, \Omega)$ and the pair dispersion $\Omega_{\vec{q}}$ are given as previously, but the Fermi function $f(x)$ is replaced by the symmetrized one $\bar{f}(x)$:

$$\begin{aligned} \Omega_{\vec{q}} = & \frac{1}{A_0'} \left\{ \frac{1}{N} \sum_{\vec{k}} \left[\frac{\bar{f}(E_{\vec{k}}) + \bar{f}(\bar{\epsilon}_{\vec{q}-\vec{k}}) - 1}{\bar{\epsilon}_{\vec{q}-\vec{k}} + E_{\vec{k}}} u_k^2 + \frac{\bar{f}(\bar{\epsilon}_{\vec{q}-\vec{k}}) - \bar{f}(E_{\vec{k}})}{\bar{\epsilon}_{\vec{q}-\vec{k}} - E_{\vec{k}}} v_k^2 \right] \right. \\ & \left. + \frac{1 - 2\bar{f}(E_{\vec{k}})}{2E_{\vec{k}}} \right\}, \end{aligned} \quad (6.52)$$

$$A_0' = \frac{1}{2\Delta_{pg}^2} \left[n - 2 \frac{1}{N} \sum_{\vec{k}} \bar{f}(\bar{\epsilon}_{\vec{k}}) \right]. \quad (6.53)$$

For small $|\vec{q}|$, $\Omega_{\vec{q}}$ is quadratic in \vec{q} :

$$\Omega_{\vec{q}} \approx \frac{\vec{q}^2}{2M^*}, \quad (6.54)$$

where M^* is the effective pair mass, which can be determined from the expansion of $\Omega_{\vec{q}}$:

$$\begin{aligned} \frac{1}{M^*} = & \frac{1}{A_0'} \frac{1}{\Delta_{pg}^2} \sum_{\vec{k}} \left[\frac{1}{2} \left[(1 - 2\bar{f}(\bar{\epsilon}_{\vec{k}})) - \frac{\bar{\epsilon}_{\vec{k}}}{E_{\vec{k}}} (1 - 2\bar{f}(E_{\vec{k}})) \right] (2t \cos k_x) - \right. \\ & \left. \left\{ 2\bar{f}'(\bar{\epsilon}_{\vec{k}}) + \frac{E_{\vec{k}}}{\Delta_{pg}^2} \left[\left(1 + \frac{\bar{\epsilon}_{\vec{k}}^2}{E_{\vec{k}}^2} \right) (1 - 2\bar{f}(E_{\vec{k}})) - 2 \frac{\bar{\epsilon}_{\vec{k}}}{E_{\vec{k}}} (1 - 2\bar{f}(\bar{\epsilon}_{\vec{k}})) \right] \right\} (2t \sin k_x)^2 \right], \end{aligned} \quad (6.55)$$

where $\bar{f}'(x)$ is the derivative of $\bar{f}(x)$.

Eq. (6.51) gives the pseudogap parameter in terms of the Bose function.

Next, we explicitly sum over the vectors $\vec{q} \neq 0$ in Eq. (6.51). We replace the sum over \vec{q} with an integral over spherical coordinates. Therefore:

$$\frac{1}{N} \sum_{\vec{q} \neq 0} b(\Omega_{\vec{q}}) = \frac{1}{(2\pi)^3} \int_0^{2\pi} \int_0^\pi \int_0^\Lambda q^2 dq \frac{1}{e^{\beta_c \Omega_{\vec{q}}} - 1}, \quad (6.56)$$

where: Λ – the sphere radius. To evaluate this integral, we extend the integration range to infinity. We also write the expression $(e^x - 1)^{-1}$ as the geometric series. Then:

$$\frac{1}{N} \sum_{\vec{q} \neq 0} b(\Omega_{\vec{q}}) = \frac{1}{2\pi^2} \int_0^\infty dq q^2 \sum_{l=1}^\infty e^{-l\beta_c \Omega_{\vec{q}}} = \frac{1}{2\pi^2} \sum_{l=1}^\infty \int_0^\infty dq q^2 e^{-\frac{l\beta_c q^2}{2M^*}}. \quad (6.57)$$

After changing the variables $l\beta_c q^2 = x^2$, we get:

$$\frac{1}{N} \sum_{\vec{q} \neq 0} b(\Omega_{\vec{q}}) = \frac{1}{2\pi^2} \sum_{l=1}^\infty \left(\frac{\beta_c l}{2M^*} \right)^{-3/2} \int_0^\infty dx x^2 e^{-x^2} = \frac{1}{2\pi^2} \sum_{l=1}^\infty \frac{1}{l^{3/2}} \int_0^\infty dx x^2 e^{-x^2}. \quad (6.58)$$

Using: $\sum_{l=1}^\infty \frac{1}{l^{3/2}} \equiv \zeta(3/2)$ – the Riemann zeta function and $\int_0^\infty dx x^2 e^{-x^2} = \sqrt{\pi}/4$ (a Gaussian integral), we get:

$$\frac{1}{N} \sum_{\vec{q} \neq 0} b(\Omega_{\vec{q}}) = \frac{1}{8} \zeta(3/2) \left(\frac{2M^*}{\pi\beta_c} \right)^{3/2}. \quad (6.59)$$

Thus, finally the equation for the pseudogap parameter (Eq. (6.51)) takes the form:

$$\Delta_{pg}^2 = \frac{1}{A'_0} \frac{1}{8} \zeta(3/2) \left(\frac{2M^*}{\pi\beta_c} \right)^{3/2}. \quad (6.60)$$

To determine T_c , this equation together with Eqs. (6.48)-(6.50) are solved numerically.

6.2.2 Numerical results

In this section we present the numerical results concerning the BCS-BEC crossover in non-zero temperatures. In the following analysis, we consider the 3D case for AHM in the Zeeman magnetic field, extending the results of section 5.2 on the BCS-BEC crossover in the ground state. The transition temperature from the superconducting state to the pseudogap region (PG) is determined from Eqs. (6.48)-(6.50), together with Eq. (6.60), within the $(GG_0)G_0$ scheme for $h \neq 0$.

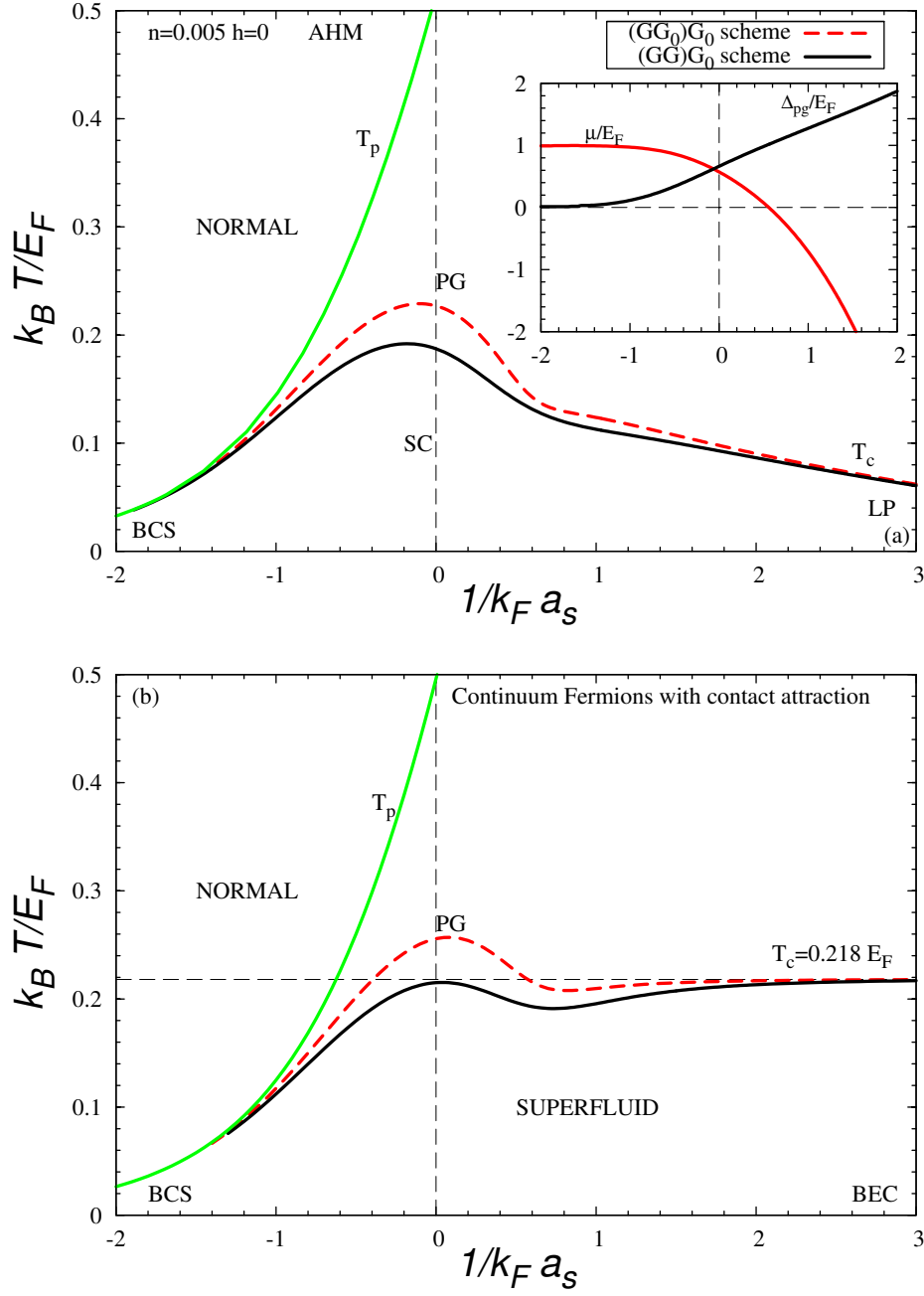


Figure 6.5: (a) $k_B T / E_F$ (E_F – lattice Fermi energy) vs. $1/k_F a_s$ phase diagram of the AHM at fixed $n = 0.005$ for the sc lattice. (b) the analogous diagram for the 3D continuum model with contact attraction; $h = 0$. The red dashed line – T_c determined within $(GG_0)G_0$ scheme, the black solid line – T_c determined within $(GG)G_0$ scheme, the green solid line – T_c determined within MF approximation (denoted as T_p). Inset shows μ/E_F and Δ_{pg}/E_F vs. $1/k_F a_s$ at T_c .

6.2.2.1 $h = 0$ case

Here, we start from a brief discussion of the BCS-BEC crossover at $h = 0$. Within this analysis, we perform a comparison of the results obtained from the $(GG_0)G_0$ and $(GG)G_0$ scheme.

Fig. 6.5 shows typical temperature phase diagrams, illustrating the changes in the 3D system which evolves from the weak to strong coupling limit [152]. We analyze the BCS-BEC crossover diagrams at non-zero temperatures within both AHM (Fig. 6.5(a)) and the continuum model of a dilute gas of fermions (Fig. 6.5(b)). In the first case, the fixed particle concentration is very low ($n = 0.005$), i.e. the system is very diluted. These two diagrams are plotted in terms of E_F and $k_F a_s$ (where a_s is the scattering length between fermions for a two-body problem). In the continuum model with the Hamiltonian:

$$H = \sum_{\vec{k}\sigma} \xi_{\vec{k}} c_{\vec{k}\sigma}^\dagger c_{\vec{k}\sigma} + \frac{g}{V} \sum_{\vec{k}\vec{k}'\vec{q}} c_{\vec{k}\uparrow}^\dagger c_{\vec{k}+\vec{q}\uparrow} c_{\vec{k}'\downarrow}^\dagger c_{\vec{k}'-\vec{q}\downarrow}, \quad (6.61)$$

where: $\xi_{\vec{k}} = \epsilon_{\vec{k}} - \mu = \frac{k^2}{2m} - \mu$, the scattering length is related to the contact interaction potential g via the Lippmann-Schwinger equation: $m/(4\pi a_s) = 1/g + 1/V \sum_{\vec{k}} 1/2\epsilon_{\vec{k}}$. For comparison, we remind here also the definition of $1/k_F a_s$ in the lattice model case: $1/k_F a_s = \left(\frac{1}{|U_c|^{d=3}} - \frac{1}{|U|} \right) \frac{8\pi}{\sqrt{E_F}}$ ($|U|$ and E_F are in units of t), where $|U_c|^{d=3}/12 = 0.659$ and E_F is the lattice Fermi energy. Maximum T_c is around the unitarity point ($1/k_F a_s = 0$). The minimum in T_c plots corresponds to the change of sign of the chemical potential (beginning of the bosonic regime).

As discussed above, in the weak coupling limit, the fermionic pairs form and condense at the same temperature T_c . In the BCS theory, the gap (Δ_{sc}) decreases with increasing temperature and drops to zero at T_c . When the attractive interaction increases, the pseudogap (Δ_{pg}) appears in the excitation spectrum, which is non-zero also above T_c . The pseudogap parameter behavior in the critical temperature is shown in Fig. 6.5(a) (inset). In the BCS limit, $\Delta_{pg} \rightarrow 0$, while it becomes non-zero for the intermediate and strong couplings. In the pseudogap region (below T_p and above T_c) there are long-lived, incoherent pair excitations (i.e. non-condensed pairs with $\vec{q} \neq 0$). The range of occurrence of PG widens with increasing attraction. Therefore, the temperature of the pair condensation is much lower than the temperature of the pairs creation – T_p in the strong coupling limit.

One can also observe changes in the chemical potential behavior when the system evolves from the weakly interacting fermionic pairs to the strong coupling local pairs 6.5(a) (inset). In the BCS limit, $\mu = E_F$ and there is a Fermi surface in the system. With increasing attractive interaction, μ drops below zero, the Fermi surface disappears and the system becomes bosonic in the strong coupling limit.

In Fig. 6.5, T_c is determined within the $(GG_0)G_0$ and the $(GG)G_0$ scheme. First, let us consider a continuum model of a gas of fermions in 3D. In this case, $T_c = \frac{8e^{-2\gamma}}{\pi} E_F e^{\frac{-\pi}{2k_F a_s}}$, where $\gamma = 1.78$ in the BCS limit, while in the BEC limit $T_c/E_F = 0.218$. The latter comes from the formula for the temperature of BEC for a gas of molecules with mass

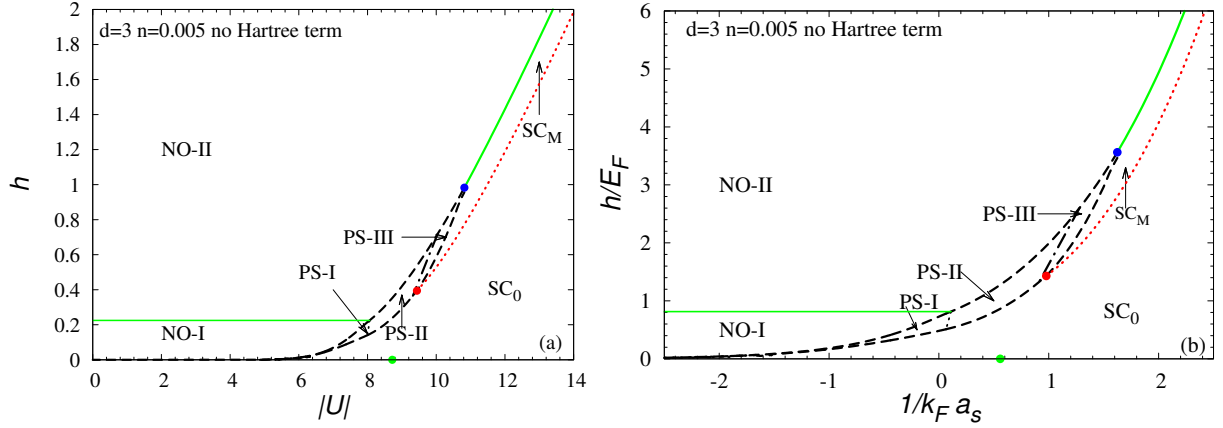


Figure 6.6: h vs. $|U|$ ground state phase diagram of spin polarized AHM (a) and critical magnetic field in units of the lattice Fermi energy E_F vs. $1/k_F a_s$ (b), sc lattice, $n = 0.005$. SC_0 – unpolarized superconducting state, SC_M – magnetized superconducting state, PS-I ($SC_0 + NO-I$) – partially polarized phase separation, PS-II ($SC_0 + NO-II$) – fully polarized phase separation, PS-III – ($SC_M + NO-II$). Red point – $h_c^{SC_M}$, blue point – tricritical point. The dotted red and the solid green lines are the second order transition lines.

$2m_F$. The calculations within the $(GG_0)G_0$ and the $(GG)G_0$ schemes give very similar results in these two extreme limits. However, there are differences in the unitarity regime ($1/k_F a_s = 0$), i.e. the critical temperature determined within the $(GG_0)G_0$ scheme equals: $T_c/E_F = 0.256$, while T_c calculations within the $(GG)G_0$ scheme give: $T_c/E_F = 0.215$. For comparison, the value of T_c obtained from the QMC method for the model of continuum fermions with contact attraction in the unitarity regime varies from $T_c/E_F = 0.15$ [155] to $T_c/E_F = 0.18$ [156]. Therefore, the results obtained from the $(GG)G_0$ scheme are more consistent with the QMC studies (than the ones from the $(GG_0)G_0$ scheme).

A comparison of the above results (Fig. 6.5(b)) with those obtained within the Attractive Hubbard model (Fig. 6.5(a)) is quite interesting. As shown in Fig. 6.5(a), the value of T_c in the BCS limit does not change significantly in comparison to the continuum model case. However, there are large differences between the results obtained within AHM and those obtained within the 3D continuum model in the BEC limit. The value of T_c which is determined within the model on the lattice is much lower than $T_c/E_F = 0.218$. As we know, for the AHM, in the LP limit, the effective mass of the hard-core bosons is $m_B = U/4t^2$ and increases with $|U|$ and it is reflected by the results of the T-matrix calculations. At the unitarity, the results for AHM ($n = 0.005$) are as follows: $T_c/E_F = 0.227$ in the $(GG_0)G_0$ scheme and $T_c/E_F = 0.187$ in the $(GG)G_0$ scheme.

6.2.2.2 $h \neq 0$ case

Fig. 6.6 shows the critical magnetic field vs. $|U|$ (a) and vs. $-1/k_F a_s$ (b), for $n = 0.005$, at $T = 0$. These diagrams are only shown so that we could refer to them in our further

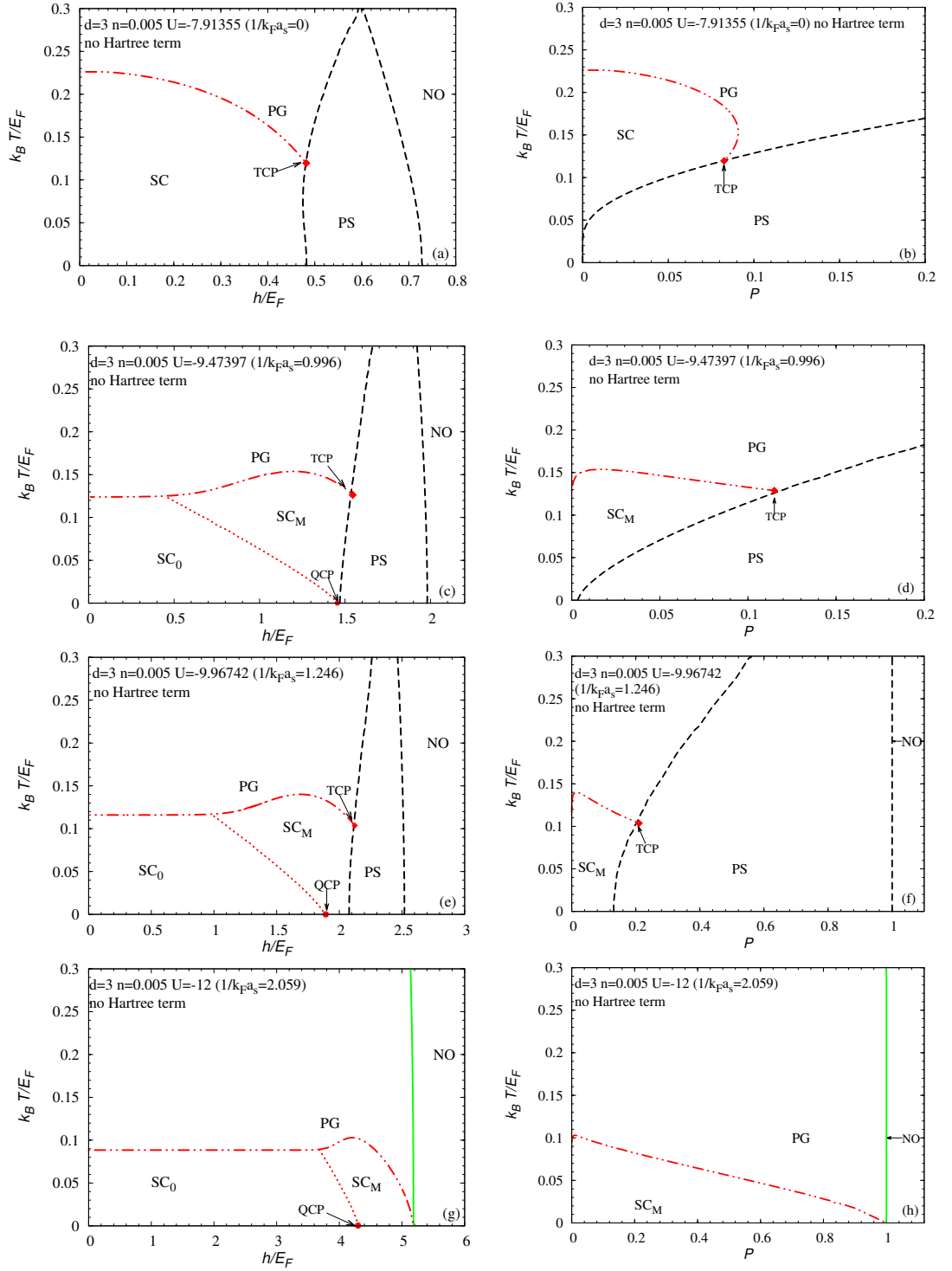


Figure 6.7: T vs. h and T vs. P phase diagrams of spin polarized AHM in units of the lattice Fermi energy, at fixed $n = 0.005$ for the sc lattice. (a), (b) – unitarity limit, (c), (d), (e), (f), (g), (h) – on the LP side. Dashed-double dotted red line – T_c determined from the $(GG_0)G_0$ scheme, SC_M – magnetized superconducting state, PG – pseudogap, TCP – tricritical point, QCP – quantum critical point (Lifshitz-type).

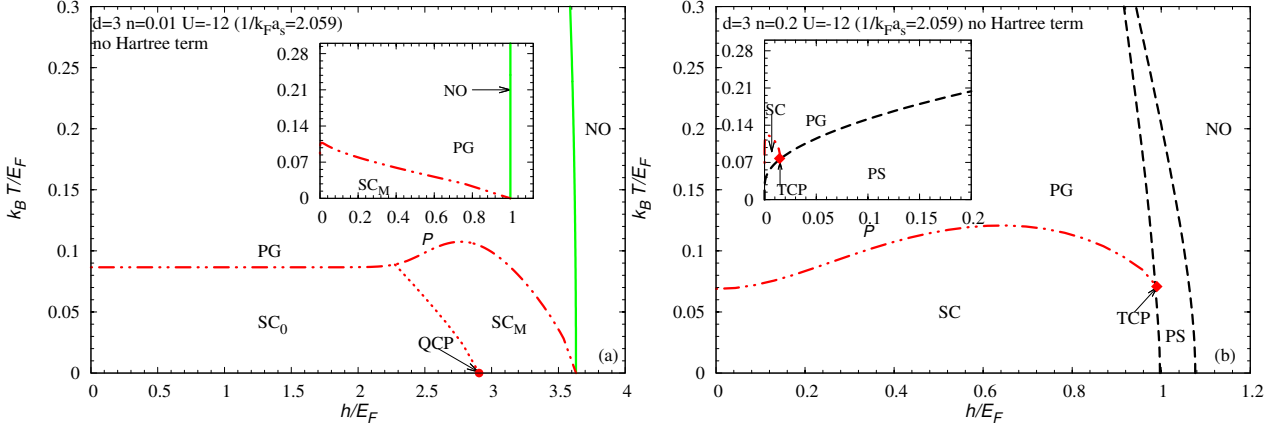


Figure 6.8: T vs. h and T vs. P (insets) phase diagrams of spin polarized AHM in units of the lattice Fermi energy, at fixed $n = 0.01$ (a) and $n = 0.2$ (b) for the sc lattice, $U = -12$. Dashed-double dotted red line – T_c determined from the $(GG_0)G_0$ scheme, SC_M – magnetized superconducting state, PG – pseudogap, TCP – tricritical point, QCP – quantum critical point (Lifshitz-type).

considerations, when the zero-temperature results are extended to finite temperatures. The topology of the diagrams 6.6 is the same as that in Fig. 5.7. Therefore, we do not discuss Fig. 6.6 in detail.

Now, the results concerning the influence of the magnetic field on superconductivity in 3D at finite temperatures are presented. As mentioned above, T_c is determined within the $(GG_0)G_0$ scheme [160].

Fig. 6.7 shows temperature vs. magnetic field and T vs. P phase diagrams¹ in units of the Fermi energy, at fixed $n = 0.005$ and four values of $|U|$ ($1/k_F a_s$). The PS regions are obtained within the Hartree approximation. The thick dash-double dotted line (red color) denotes the T_c curve. In other words, above this curve (above T_c but below T_p (T_c^{MF}) – not shown in the figures) there are long lived incoherent pairs with $\vec{q} \neq 0$ (PG region) in the system. At T_c these pairs condense and below the T_c curve the system is superconducting with zero-momentum coherent pairs. It should be noted that the pair breaking temperature is much higher than the superconducting critical temperature. This difference between T_p and T_c increases with increasing attractive interaction. The evolution of TCP which is presented in Fig. 6.7 shows that the tricritical point at $T \neq 0$ tends to TCP at $T = 0$.

In the unitarity regime (Fig. 6.7(a)-(b)), one can distinguish four states in the phase diagrams. There is the SC state at sufficiently low temperatures. The system goes from SC to the normal state across the PS region with increasing magnetic field. When temperature increases, one observes a transition to the PG region. As shown in Fig. 6.7(b), the effect of finite polarization on the superconducting state is not so strong as

¹Note that in the context of imbalanced two-component Fermi gases on optical lattices, magnetic field translates to chemical potential difference, while polarization to population imbalance.

in the 2D case in which the KT superfluid phase is restricted only to the weak coupling region and low values of P (see: Fig. 6.3).

One should mention that our results are different from those obtained by the Levin's group results concerning the unitarity regime, for the continuum model of two component Fermi gas with population imbalance [157]. Considering the phase diagram T vs. P , according to their predictions, the superfluid phase is stable at low temperatures and low polarizations, whereas from our calculations we find the phase separation region (e.g. around $P = 0.01$, according to [157] (Fig. 7), the SF phase is stable down to $T/T_F \approx 0.03$, while as follows from our calculations the SC phase is stable only down to $T/T_F \approx 0.065$). This difference can stem from two possible reasons. First, our model is the lattice model with a very low ($n = 0.005$), but still finite electron concentration. Second, the methods of analysis of the superfluid phase stability are different. The Levin's group has applied the stability condition which involves the calculation of $\partial^2\Omega/\partial\Delta^2$, where Ω is the thermodynamic potential and Δ – fermionic excitation gap. Then, they impose the requirement that the quantity $\partial^2\Omega/\partial\Delta^2$ has to be non-negative, i.e. $\partial^2\Omega/\partial\Delta^2 \geq 0$. However, this stability condition does not take into account the possibility of a first order transition and the existence of phase separation regions in the system. Therefore, our approach seems to be more appropriate and the condition that $\partial^2\Omega/\partial\Delta^2 \geq 0$ can be considered to be the lower bound for the stability of the superfluid phase.

The situation is different in the strong coupling case (Fig. 6.7(c)-(h)). The most important feature is the occurrence of the stable spin polarized superfluid phase. Because of the occurrence of the magnetized superconducting state at $T = 0$ for higher attractive interactions in 3D (see: Fig.6.6), this phase can persist to non-zero temperatures. For sufficiently high value of $|U|$, below T_c , the spin polarized superfluid state with gapless spectrum and one FS can be stable. The appearance of the SC_M phase in the diagrams is manifested by the existence of QCP at $T = 0$. The transition from the non-polarized superconducting state SC_0 to the SC_M phase is of the Lifshitz type. With increasing attractive interaction, the range of occurrence of SC_M widens, even up to $P = 1$ (Fig. 6.7(h)). An increase in the temperature causes an increase in the polarization and, as a consequence, the widening of the range of the SC_M phase. The character of the transition from the SC_M to the NO state changes with increasing $|U|$. For $|U| = 12$ this transition is of the second order. Therefore, it is possible to observe the polarized superfluid state even at finite temperatures in the strong coupling regime in 3D, as opposed to the 2D case in which this phase is unstable.

However, the SC_M state is stable for rather low electron concentrations, at $T \neq 0$. It is clearly visible in Fig. 6.8. For $|U| = 12$ and $n = 0.01$ the SC_M phase is stable. However, for higher value of the electron concentration ($n = 0.2$) the SC phase is restricted to low polarizations. Moreover, this phase is not gapless for higher n . Here, one should emphasize, that the SC phase and the SC_M state are formally different phases.

The evolution of the T_c curve with increasing attractive interaction or electron concentration is also very interesting. Fig. 6.9 shows T_c determined from the $(GG_0)G_0$ scheme vs. h for three values of n at $U = -12$ (a) and at fixed $n = 0.005$ for six values of $|U|$. For low values of the electron concentration and high values of attraction (Fig. 6.9(b)),

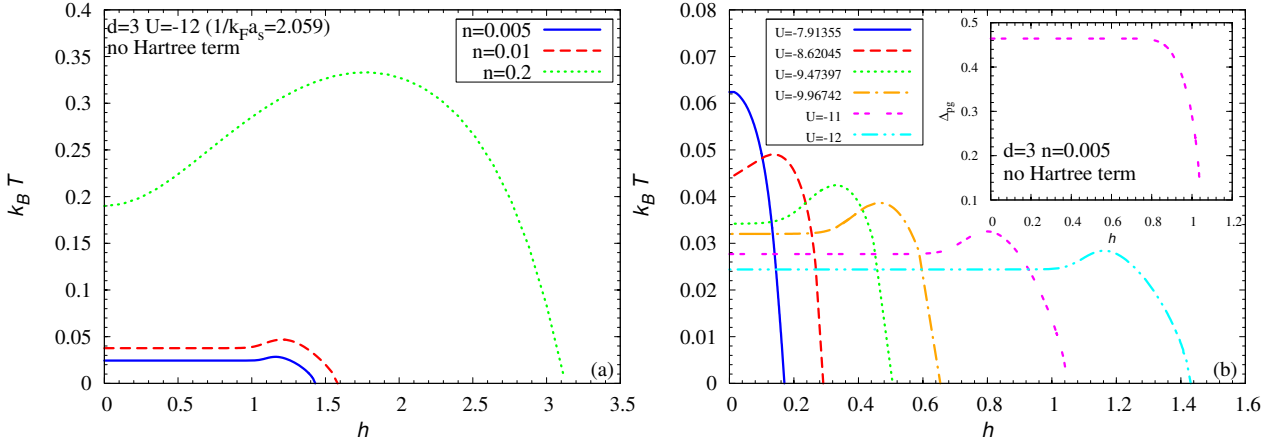


Figure 6.9: T_c determined from the $(GG_0)G_0$ scheme vs. h for three values of n at $U = -12$ (a) and at fixed $n = 0.005$ for six values of $|U|$ (b). Inset of (b) shows the behavior of Δ_{pg} vs. h for fixed $n = 0.005$ and $U = -11$.

the critical temperature and the pseudogap parameter do not depend on the magnetic field for a wide range of values of h . The system is in the SC_0 phase. When non-zero polarization appears, the critical temperature increases and after reaching some maximum, it starts to decrease. Moreover, in this non-zero polarization region, an increase in h leads to a decrease in the pseudogap parameter, which tends to zero (as does the critical temperature) for some critical value of the magnetic field.

When the electron concentration is increased (Fig. 6.9(a)), the range of values of h for which the critical temperature does not depend on h shrinks and disappears for large enough n , similarly as for lower values of attraction (Fig. 6.9(b)).

Chapter 7

The influence of spin dependent hopping integrals (mass imbalance) on the BCS-BEC crossover

Two-component Fermi systems with different fermion masses in optical lattices [143] are characterized by a new parameter, i.e. the ratio of the spin dependent hopping integrals ($t^\uparrow/t^\downarrow \equiv r$, where $t^\uparrow \neq t^\downarrow$), which enables the appearance of various exotic states in these systems. The case of spin dependent masses is also studied in papers of Spalek group in the context of unconventional superconducting materials including the heavy fermion systems [161].

In this chapter, we examine the influence of spin dependent hopping integrals on the stability of the SC_M phase. We study the evolution from the weak coupling (BCS-like limit) to the strong coupling limit of tightly bound local pairs with increasing attraction, within the attractive Hubbard model in a magnetic field with spin-dependent hopping integrals, for square and simple cubic lattices. The broken symmetry Hartree approximation, as well as the strong coupling expansion are used. In the 2D case, we also apply the KT scenario to determine the phase coherence temperatures.

Some theoretical studies of Fermi condensates in systems with spin and mass imbalances have shown that the BP state can have excess fermions with two FS's (BP-2 or interior gap state) [73, 75, 79, 80]. According to some investigations, the interior gap state [73] is always unstable even for large mass ratio r and PS is favored [81, 82]. Therefore, the problem of stability of the BP-2 state is still open.

At strong attraction, the SC_M phase occurs in three-dimensional imbalanced Fermi gases [67, 81, 82], as well as in the spin-polarized attractive Hubbard model in the dilute limit (for $h \neq 0$, $r = 1$ [131] and $r \neq 1$ [158]). As noted in the previous chapter, this homogeneous magnetized superfluid state consisting of a coherent mixture of LP's (hard-core bosons) and excess spin-up fermions (Bose-Fermi mixture) can only have one Fermi surface (BP-1).

We also show that if $r \neq 1$, the SC_M phase can be realized in $d = 2$ for the intermediate and strong coupling regimes, as opposed to the $r = 1$ case. In other words, the

simultaneous presence of mass and population imbalance can stabilize the BP-1 phase in 2D, on the BEC side of the crossover. We determine the critical value of n above which SC and the charge density wave ordered (CO) state can form the PS state at $h = 0$ and $r \neq 1$. We find that the BP-2 state is unstable in the whole range of parameters, in the $d = 2$ one-band spin-polarized AHM. Nevertheless, one can suppose that the Liu-Wilczek (BP-2) phase can be realized within the two-band model.

Some of our results have been published in Refs. [132, 159].

In this chapter, we study the superfluid phases in the AHM in a magnetic field with spin-dependent hopping. The Hamiltonian (2.15) is reduced to the form [132, 159]:

$$H = \sum_{ij\sigma} (t_{ij}^\sigma - \mu\delta_{ij}) c_{i\sigma}^\dagger c_{j\sigma} + U \sum_i n_{i\uparrow} n_{i\downarrow} - h \sum_i (n_{i\uparrow} - n_{i\downarrow}), \quad (7.1)$$

where: t_{ij}^σ – hopping integrals, $\sigma = \uparrow, \downarrow$.

7.1 The large- U limits

In this section, we use the canonical transformation method of the Schrieffer-Wolff type [162] to map the Hamiltonian (7.1) ($h = 0$, $r \neq 1$) onto the pseudo-spin model in the large- $|U|$ limits [23, 27, 163].

The canonical transformation method allows us to isolate the interactions that dominate the dynamics of the system. Strongly correlated Hubbard models have been investigated for many years. The large-positive- U (LPU) limit was used to explain some aspects of antiferromagnetism and superconductivity [164]. Harris and Lange [165] have carried out the calculations for the Hubbard model with the use this transformation. Then, Chao, Spalek and Oleś have proposed an iterative method for the derivation of an appropriate transformation for higher orders of perturbation theory [166]. This scheme has been improved by McDonald, Girvin and Yoshioka [167]. The canonical transformation method has also been used in Refs.: [168, 169, 170]. The large-negative- U limit has also been widely discussed in literature [23, 27, 171, 172, 173].

Here, we briefly introduce the concept of the canonical transformation. Let us consider the Hamiltonian:

$$H = H_0 + H_I, \quad (7.2)$$

where: H_0 – unperturbed part, H_I – perturbation.

Now, we define the canonical transformation as:

$$\tilde{H} = e^S H e^{-S}, \quad (7.3)$$

where: $S^\dagger = -S$ – anti-Hermitian operator.

The Hamiltonian (7.3) can be expanded:

$$\tilde{H} = H + [S, H] + \frac{1}{2}[S, [S, H]] + \dots, \quad (7.4)$$

We decompose the Hamiltonian (7.1) ($h = 0$) into:

$$H_1 = \sum_{ij\sigma} t_{ij}^\sigma (c_{i\sigma}^\dagger (1 - n_{i\bar{\sigma}}) c_{j\sigma} (1 - n_{j\bar{\sigma}}) + c_{i\sigma}^\dagger n_{i\bar{\sigma}} c_{j\sigma} n_{j\bar{\sigma}}), \quad (7.5)$$

$$H_{mix} = \sum_{ij\sigma} t_{ij}^\sigma (c_{i\sigma}^\dagger (1 - n_{i\bar{\sigma}}) n_{j\bar{\sigma}} + c_{i\sigma}^\dagger n_{i\bar{\sigma}} c_{j\sigma} (1 - n_{j\bar{\sigma}})), \quad (7.6)$$

$$H_U = U \sum_i n_{i\uparrow} n_{i\downarrow}. \quad (7.7)$$

where: $\bar{\sigma} = -\sigma$. Therefore, the Hamiltonian (7.2) can be rewritten as: $H = H_U + H_1 + H_{mix}$, where $H_0 = H_U + H_1$ and $H_I = H_{mix}$. In this way:

$$\tilde{H} = H_U + H_1 + H_{mix} + [S, H_U] + [S, H_1] + [S, H_{mix}] + \frac{1}{2}[S, [S, H]] + \dots \quad (7.8)$$

By means of the canonical transformation, the perturbation ($H_I = H_{mix}$) can be eliminated to first order. Therefore, we demand that the generator S satisfies the condition: $H_{mix} + [S, H_U] = 0$. Then, the Hamiltonian (7.8) takes the form:

$$\tilde{H} = H_U + H_1 + [S, H_1] + \frac{1}{2}[S, H_{mix}] + \dots \quad (7.9)$$

In the lowest order, the Hamiltonian (7.9) is well approximated by:

$$\tilde{H}' = H_U + H_1 + \frac{1}{2}[S, H_{mix}] + \dots \quad (7.10)$$

Let us introduce the Hubbard operators. We have the following four local basis states in the Hubbard model [83]:

$$\begin{aligned} |0\rangle_j & \text{site } j \text{ is empty} \\ |+\rangle_j = c_{j\uparrow}^\dagger |0\rangle_j & \text{site } j \text{ is occupied by an } \uparrow \text{-electron} \\ |-\rangle_j = c_{j\downarrow}^\dagger |0\rangle_j & \text{site } j \text{ is occupied by an } \downarrow \text{-electron} \\ |2\rangle_j = c_{j\uparrow}^\dagger c_{j\downarrow}^\dagger |0\rangle_j & \text{site } j \text{ is doubly occupied.} \end{aligned} \quad (7.11)$$

The corresponding local projectors take the form:

$$\hat{P}_{j0} = |0\rangle_j \langle 0| = (1 - n_{j\uparrow})(1 - n_{j\downarrow}), \quad (7.12)$$

$$\hat{P}_{j+} = |+\rangle_j \langle +| = n_{j\uparrow}(1 - n_{j\downarrow}), \quad (7.13)$$

$$\hat{P}_{j-} = |-\rangle_j \langle -| = n_{j\downarrow}(1 - n_{j\uparrow}), \quad (7.14)$$

$$\hat{P}_{j2} = |2\rangle_j \langle 2| = n_{j\uparrow} n_{j\downarrow}, \quad (7.15)$$

and satisfy:

$$\hat{P}_{j0} + \hat{P}_{j+} + \hat{P}_{j-} + \hat{P}_{j2} = \hat{1}, \quad (7.16)$$

where: $\hat{1}$ – the unit operator.

Now, we can define the Hubbard operator as:

$$X_j^{ba} = |b\rangle_j \langle a|. \quad (7.17)$$

One can notice that the projection operators (7.12)-(7.15) are the diagonal Hubbard operators: $\hat{P}_{ja} = |a\rangle \langle a| = X_j^{aa}$, e.g. $X_j^{22} = n_{j\uparrow} n_{j\downarrow}$. In turn, an example of the off-diagonal Hubbard operator takes the form:

$$X_j^{\sigma 0} = c_{j\sigma}^\dagger (1 - n_{j\bar{\sigma}}), \quad (7.18)$$

or:

$$X_j^{20} = \eta(\sigma) c_{j\sigma}^\dagger c_{j\bar{\sigma}}^\dagger, \quad (7.19)$$

where the sign factor:

$$\eta(\sigma) = \begin{cases} +1 & \text{if } \sigma = \uparrow (+) \\ -1 & \text{if } \sigma = \downarrow (-) \end{cases} \quad (7.20)$$

The products of the Hubbard operator are given by:

$$X_j^{cf} X_j^{ba} = \delta_{bf} X_j^{cb} X_j^{ba} = \delta_{bf} X_j^{ca}. \quad (7.21)$$

The Hubbard operators description is an alternative approach to the standard creation and annihilation operators picture.

Let us consider the $c_{j\uparrow}^\dagger$ operator to understand the correspondences between these two descriptions. As is well known, $c_{j\uparrow}^\dagger$ operator acting on an empty state gives $|+\rangle$ or, acting on an $|-\rangle$, gives a doubly occupied state $|2\rangle$. Then, one can write:

$$c_{j\uparrow}^\dagger = X_j^{+0} + X_j^{2-} \quad (7.22)$$

and similarly $c_{j\downarrow}^\dagger$:

$$c_{j\downarrow}^\dagger = X_j^{-0} - X_j^{2+}. \quad (7.23)$$

Now, one can write (7.22) and (7.23) in a compact form:

$$c_{j\sigma}^\dagger = X_j^{\sigma 0} + \eta(\sigma) X_j^{2\bar{\sigma}}, \quad (7.24)$$

It is worth mentioning that the Hubbard operators obey the following commutation relations:

$$[X_i^{ba}, X_j^{dc}]_{\pm} = \delta_{ij} (\delta_{ad} X_i^{bc} \pm \delta_{bc} X_i^{da}), \quad (7.25)$$

where:

$$\begin{aligned} + & \text{ if both operators are fermionic type,} \\ - & \text{ if at least one of them is bosonic type.} \end{aligned} \quad (7.26)$$

Now, parts of the Hamiltonian (7.1) ((7.5)-(7.7)) can be rewritten in terms of the Hubbard operators:

$$H_1 = \sum_{ij\sigma} t_{ij}^\sigma \left(X_i^{\sigma 0} X_j^{0\sigma} + X_i^{2\bar{\sigma}} X_j^{\bar{\sigma} 2} \right), \quad (7.27)$$

$$H_{mix} = \sum_{ij\sigma} \eta(\sigma) t_{ij}^\sigma \left(X_i^{\sigma 0} X_j^{\bar{\sigma} 2} + X_i^{2\bar{\sigma}} X_j^{0\sigma} \right), \quad (7.28)$$

$$H_U = U \sum_i X_i^{22}. \quad (7.29)$$

The generator S of the canonical transformation is given by:

$$S = \frac{1}{2i} \left(\int_0^\infty (H_{mix}(t) - H_{mix}(-t)) e^{-\epsilon t} dt \right) \Big|_{\epsilon \rightarrow 0}, \quad (7.30)$$

where:

$$H_{mix}(t) = A e^{-iUt} + B e^{iUt}, \quad (7.31)$$

$$A = \sum_{ij\sigma} \eta(\sigma) t_{ij}^\sigma X_i^{\sigma 0} X_j^{\bar{\sigma} 2}, \quad B = \sum_{ij\sigma} \eta(\sigma) t_{ij}^\sigma X_i^{2\bar{\sigma}} X_j^{0\sigma}.$$

Substituting Eq. (7.31) into Eq. (7.30) we get:

$$S = -\frac{1}{U} (A - B). \quad (7.32)$$

Now, let us calculate the expression:

$$\bar{\bar{H}} \equiv \frac{1}{2} [S, H_{mix}] = -\frac{1}{2U} [A - B, A + B] = -\frac{1}{2U} ([A, B] - [B, A]) = -\frac{1}{U} [A, B], \quad (7.33)$$

where:

$$[A, B] = \sum_{ij\sigma} \sum_{kl\sigma'} \eta(\sigma) \eta(\sigma') t_{ij}^\sigma t_{kl}^{\sigma'} [X_i^{\sigma 0} X_j^{\bar{\sigma} 2}, X_k^{2\bar{\sigma}'} X_l^{0\sigma'}], \quad (7.34)$$

$t_{ij}^\sigma = t_{ji}^\sigma$. We take into account the terms for which $i = k, j = l$ or $i = l, k = j$ and omit the three-site terms. In this way, we get two commutators:

$$[X_i^{\sigma 0} X_j^{\bar{\sigma} 2}, X_i^{2\bar{\sigma}'} X_j^{0\sigma'}] \quad \text{or} \quad [X_i^{\sigma 0} X_j^{\bar{\sigma} 2}, X_j^{2\bar{\sigma}'} X_i^{0\sigma'}]. \quad (7.35)$$

After the simple calculations, first of them equals:

$$[X_i^{\sigma 0} X_j^{\bar{\sigma} 2}, X_i^{2\bar{\sigma}'} X_j^{0\sigma'}] = \delta_{\sigma'\bar{\sigma}} X_i^{20} X_j^{02}, \quad (7.36)$$

and the second:

$$[X_i^{\sigma 0} X_j^{\bar{\sigma} 2}, X_j^{2\bar{\sigma}'} X_i^{0\sigma'}] = X_i^{\sigma\sigma'} X_j^{\bar{\sigma}\bar{\sigma}'} - \delta_{\sigma\sigma'} X_i^{00} X_j^{22}. \quad (7.37)$$

Substituting Eqs. (7.36), (7.37) into Eq. (7.33) we get:

$$\bar{\bar{H}} = \frac{1}{U} \sum_{ij\sigma} t_{ij}^\sigma t_{ij}^{\bar{\sigma}} X_i^{\sigma\bar{\sigma}} X_j^{\bar{\sigma}\sigma} - \frac{1}{U} \sum_{ij\sigma} (t_{ij}^\sigma)^2 (X_i^{\sigma\sigma} X_j^{\bar{\sigma}\bar{\sigma}} - X_i^{00} X_j^{22}) + \frac{1}{U} \sum_{ij\sigma} t_{ij}^\sigma t_{ij}^{\bar{\sigma}} X_i^{20} X_j^{02}. \quad (7.38)$$

The effective Hamiltonian can be written as:

$$H_{eff} = H_U + H_1 + \bar{\bar{H}}. \quad (7.39)$$

Let us introduce the spin operators:

$$\begin{aligned} S_i^+ &= c_{i\uparrow}^\dagger c_{i\downarrow} = X_i^{+-}, \\ S_i^- &= c_{i\downarrow}^\dagger c_{i\uparrow} = X_i^{-+}, \\ S_i^z &= \frac{1}{2}(n_{i\uparrow} - n_{i\downarrow}) = X_i^{++} - X_i^{--}. \end{aligned} \quad (7.40)$$

The effective Hamiltonian (7.39) for large U takes the form:

$$\begin{aligned} H_{eff} &= (U + K_0) \sum_i X_i^{22} + \sum_{ij\sigma} t_{ij}^\sigma (X_i^{\sigma 0} X_j^{0\sigma} + X_i^{2\bar{\sigma}} X_j^{\bar{\sigma} 2}) + \\ &+ \frac{1}{2} \sum_{ij} J_{ij} (S_i^+ S_j^- + S_i^- S_j^+) + \sum_{ij} K_{ij} (S_i^z S_j^z - \frac{1}{4} n_i n_j) + \\ &+ \sum_{ij} J_{ij} X_i^{20} X_j^{02}. \end{aligned} \quad (7.41)$$

where: $K_0 = \sum_j K_{ij}$, $K_{ij} = \frac{(t_{ij}^\uparrow)^2 + (t_{ij}^\downarrow)^2}{U}$, $J_{ij} = 2 \frac{t_{ij}^\uparrow t_{ij}^\downarrow}{U}$.

If we take into account large positive U ($U > 0$), the double occupancies have to be projected out. Therefore, in a limited space: $X_i^{22} = X_i^{2\sigma} = X_i^{20} = 0$. In this way, the effective Hamiltonian for the large positive U case and $n = 1$, $r \neq 1$ takes the form:

$$H_{eff}^{Heisenberg} = \sum_{ij} J_{ij} (S_i^x S_j^x + S_i^y S_j^y) + \sum_{ij} K_{ij} (S_i^z S_j^z - \frac{1}{4}), \quad (7.42)$$

where: $S_i^x = \frac{1}{2}(S_i^+ + S_i^-)$, $S_i^y = \frac{1}{2i}(S_i^+ - S_i^-)$. The above Hamiltonian (7.42) is the anisotropic spin-1/2 Heisenberg model.

In turn, if $r = 1$ and $n \leq 1$ the Hamiltonian (7.41) is reduced to the t-J model:

$$H_{eff}^{t-J} = \sum_{ij\sigma} t_{ij} (1 - n_{i\bar{\sigma}}) c_{i\sigma}^\dagger c_{j\sigma} (1 - n_{j\bar{\sigma}}) + \sum_{ij} J_{ij} (\vec{S}_i \cdot \vec{S}_j - \frac{1}{4} n_i n_j), \quad (7.43)$$

operating in the lower Hubbard subband. It is worth mentioning that we neglected 3-site terms.

Finally, in the most general case ($n \leq 1$) the Hamiltonian (7.41) for the large positive U case takes the form:

$$\begin{aligned} H_{eff}^{U>0} &= \sum_{ij\sigma} t_{ij}^\sigma (1 - n_{i\bar{\sigma}}) c_{i\sigma}^\dagger c_{j\sigma} (1 - n_{j\bar{\sigma}}) + \sum_{ij} J_{ij} (S_i^x S_j^x + S_i^y S_j^y) \\ &+ \sum_{ij} K_{ij} (S_i^z S_j^z - \frac{1}{4} n_i n_j), \end{aligned} \quad (7.44)$$

which is the generalized (anisotropic) t-J model.

In the large-negative- U limit ($|U| \gg t^\uparrow, t^\downarrow$) and without spin imbalance, the effective Hamiltonian operates in the subspace of states without single occupancies. Hence, one should impose an appropriate constraint:

$$n_{i\uparrow} - n_{i\downarrow} = 0. \quad (7.45)$$

Therefore, $X_i^{\sigma 0} = X_i^{2\sigma} = X_i^{+-} = S_i^z = 0$. Then, the effective Hamiltonian (7.41) takes the form:

$$H_{eff}^{U<0} = -\frac{1}{2} \sum'_{i,j} J_{ij}(\rho_i^+ \rho_j^- + h.c.) + \sum'_{i,j} K_{ij} \rho_i^z \rho_j^z - \tilde{\mu} \sum_i (2\rho_i^z + 1) - \frac{N}{4} K_0, \quad (7.46)$$

and: $n = \frac{1}{N} \sum_i \langle 2\rho_i^z + 1 \rangle$, $\tilde{\mu} = \mu + \frac{|U|}{2}$, $K_0 = \sum_j K_{ij}$, $J_{ij} = 2 \frac{t_{ij}^\uparrow t_{ij}^\downarrow}{|U|} = 4 \frac{t^2}{|U|} \frac{2r}{(r+1)^2}$, $K_{ij} = 2 \frac{(t_{ij}^\uparrow)^2 + (t_{ij}^\downarrow)^2}{2|U|} = 4 \frac{t^2}{|U|} \frac{1+r^2}{(1+r)^2}$. The pseudo-spin operators are: $\rho_i^+ = X_i^{20} = c_{i\uparrow}^\dagger c_{i\downarrow}^\dagger$, $\rho_i^- = X_i^{02} = c_{i\downarrow} c_{i\uparrow}$, $\rho_i^z = X_i^{22} - \frac{1}{2} = \frac{1}{2}(n_\uparrow + n_\downarrow - 1)$, primed sum excludes terms with $i = j$. The Hamiltonian (7.46) is of the form of the anisotropic pseudospin Heisenberg model in a magnetic field (chemical potential). The pseudo-spin operators satisfy the commutation rules of $s = \frac{1}{2}$ operators, i.e.:

$$[\rho_i^+, \rho_j^-] = 2\rho_i^z \delta_{ij}, \quad (7.47)$$

$$[\rho_i^\pm, \rho_j^z] = \mp \rho_i^\pm \delta_{ij}, \quad (7.48)$$

$$(\rho_i^+)^2 = (\rho_i^-)^2 = 0. \quad (7.49)$$

After the transformation to the bosonic operators: $\rho_i^+ = b_i^\dagger$, $\rho_i^- = b_i$, $\rho_i^z = -\frac{1}{2} + b_i^\dagger b_i$, the Hamiltonian (7.46) takes the form:

$$H = -\frac{1}{2} \sum'_{i,j} J_{ij}(b_i^\dagger b_j + h.c.) + \sum'_{i,j} K_{ij} n_i n_j - \tilde{\mu} \sum_i n_i. \quad (7.50)$$

The above Hamiltonian describes a system of hard-core bosons on a lattice with the commutation relations [27, 174, 175]: $[b_i, b_j^\dagger] = (1 - 2n_i) \delta_{ij}$, $b_i^\dagger b_i + b_i b_i^\dagger = 1$, where $n_i = b_i^\dagger b_i$, $\tilde{\mu} = 2\mu + |U| + K_0$ - chemical potential for bosons.

With the mass imbalance, it is possible that the charge (density wave) ordered (CO) state can develop for any particle concentration. The SC to CO transition is of first order at $h = 0$, $t^\uparrow \neq t^\downarrow$ and $n \neq 1$. The critical n (n_c) (within the mean field approximation) above which superconductivity can coexist with commensurate CO is given by [27, 177]:

$$|n_c - 1| = \sqrt{\frac{K_0 - J_0}{K_0 + J_0}}. \quad (7.51)$$

Substituting expressions for J and K , one obtains:

$$n_c = 1 \pm \left| \frac{r - 1}{r + 1} \right|. \quad (7.52)$$

SC/CO is in fact the region of phase separation of the SC domain and CO domain (with $n = 1$).

Fig. 7.1 shows n above which SC can coexist with commensurate CO. If $r = 1$, the SC and CO phases are degenerate at $n = 1$. When the hopping imbalance increases, the CO phase becomes energetically favorable and in the limit of infinite r (the Falicov-Kimball model [178]) only the CO state is possible at half filling. However, away from half filling

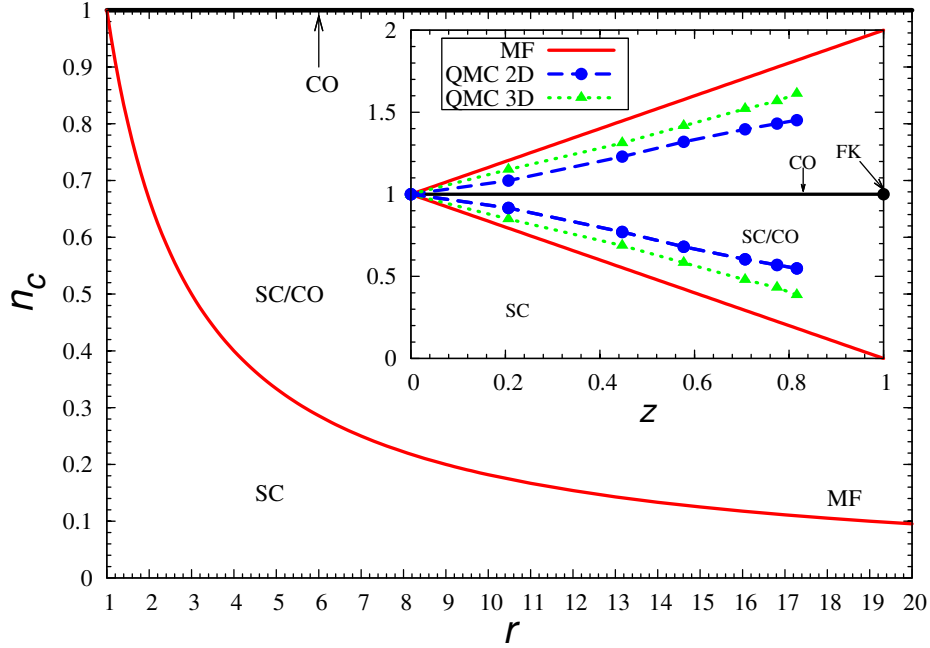


Figure 7.1: The critical n (n_c) (within the mean field (MF) approximation – red solid line) above which superconductivity can coexist with commensurate CO for different values of r . Inset – n_c vs. $z = \left| \frac{r-1}{r+1} \right|$ above which superconductivity can coexist with commensurate CO. The results from the Quantum Monte Carlo (QMC) method for the anisotropic Heisenberg model (Yunoki [176]) are also shown – blue circles (2D) and green triangles (3D). The blue dashed and the green dotted lines are a guide to the eye. FK – Falicov-Kimball model limit.

the quantum fluctuations can extend the region of stability of the SC phase at $T = 0$ and enhance n_c [174, 175, 176]. This is clearly visible in Fig. 7.1 (inset), showing the results of QMC simulations (blue circles and green triangles), in comparison to MF (red solid line).

7.2 AAHM on 2D square lattice

In this section, we investigate the influence of hopping imbalance on the evolution from the weak to strong coupling limit of tightly bound local pairs with increasing attraction for $d = 2$. We focus on the analysis of stability of the SC_M phase in the crossover diagrams in the ground state. Most of the phase diagrams of the hopping asymmetric AHM (AAHM) of are constructed without the Hartree term. We do not study CO stability, because we fix $n < n_c$ and consider mostly low electron concentrations in our analysis. We also extend our analysis to finite temperatures. We apply the KT scenario to determine the phase coherence temperatures.

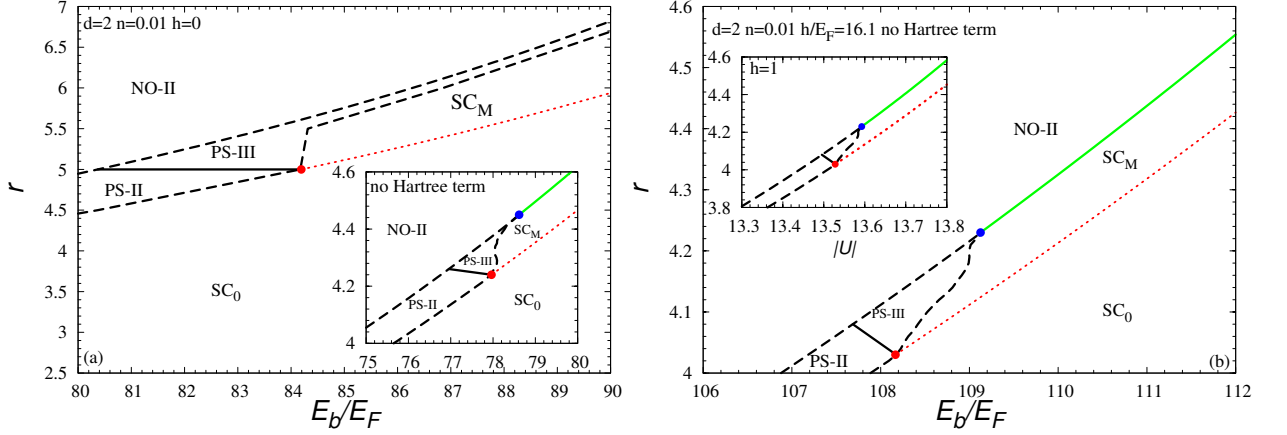


Figure 7.2: Ground state phase diagrams of AAHM for the $d = 2$ square lattice: mass imbalance vs. E_b/E_F (where E_F is the lattice Fermi energy of unpolarized, non-interacting fermions with hopping t , E_b is the binding energy for two fermions in an empty lattice with hopping t ($t = (t^\uparrow + t^\downarrow)/2$)) for $n = 0.01$, (a) $h = 0$ with and without Hartree term (inset), (b) $h/E_F = 16.1$ (inset – r vs. $|U|$, $h = 1$). SC_M – magnetized superconducting state, NO-I – partially polarized normal state, NO-II – fully polarized normal state, PS-I – ($SC_0 + \text{NO-I}$), PS-II – ($SC_0 + \text{NO-II}$), PS-III – ($SC_M + \text{NO-II}$). Red points – $h_c^{SC_M}$, blue points – tricritical points, green points – the BCS-LP crossover points in the SC_0 phase ($r = 1$). The dotted red and the solid green lines are continuous transition lines.

7.2.1 Ground state phase diagrams

The BCS-LP crossover diagrams in the presence of a Zeeman magnetic field for $r \neq 1$ exhibit a novel behavior. As opposed to the $r = 1$ case, for strong attraction, SC_M occurs at $T = 0$. For $r > 1$, the solutions of this type (Sarma-type with $\Delta(h)$) appear when $h > (\frac{r-1}{r+1})\bar{\mu} + 2\Delta\frac{\sqrt{r}}{r+1}$ (on the BCS side) or when $h > \sqrt{(\bar{\mu} - \epsilon_0)^2 + |\Delta|^2} - D\frac{r-1}{r+1}$ (on the LP side). The SC_M phase is unstable in the weak coupling regime at $T = 0$, but can be stable in the intermediate and strong coupling LP limit. As mentioned before, deep in the LP limit, unpaired spin down fermions do not exist. Hence, the SC_M phase is the superfluid state of coexisting LP's (hard-core bosons) and single-species fermions, with the latter responsible for finite polarization (magnetization) and the gapless excitations characteristic of this state of Bose-Fermi mixture. Note also that the SC_0 solutions are such as for particles with the effective hopping integral $t = (t^\uparrow + t^\downarrow)/2$ or, equivalently, for the effective particle mass of $2/m = 1/m^\uparrow + 1/m^\downarrow$.

The structure of the ground state diagrams in Fig. 7.2 is different from that shown in Fig. 5.2 (Chapter 5), where one has only a first order phase transition from pure SC_0 to the NO phase in the $(\mu - h)$ plane. In addition, there are critical values of $|U|$ ($|U_c|^{SC_M} - \text{QCP}$, red points in the diagrams), for which the SC_M state becomes stable, instead of PS. However, one should mention that there is a critical value of r , for which SC_M is stable, as opposed to the 3D case, in which the magnetized superconducting phase can be stable

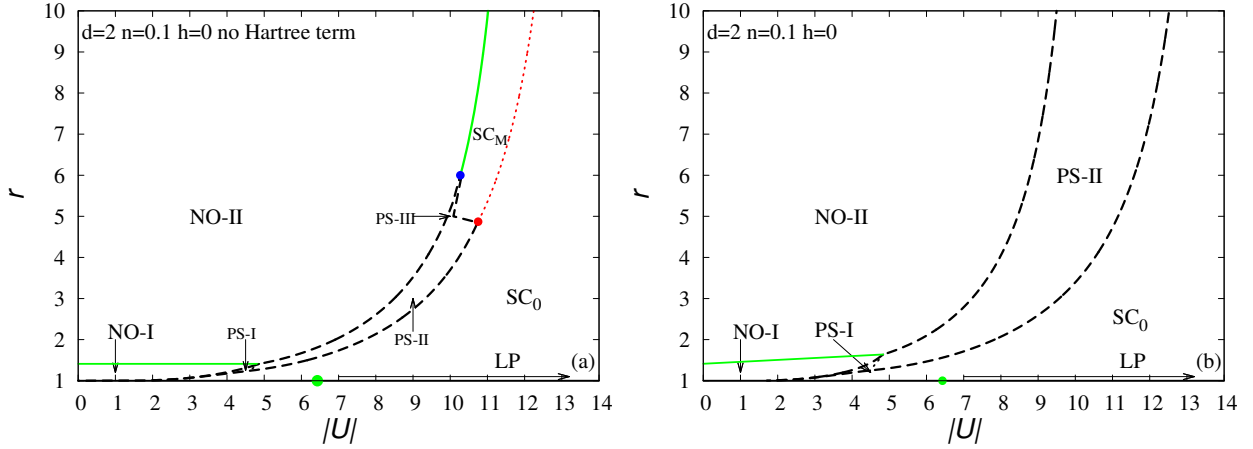


Figure 7.3: Ground state phase diagrams of AAHM r vs. $|U|$ for $n = 0.1$, $h = 0$ (a) without the Hartree term, (b) with Hartree term. SC_0 – unpolarized SC state, SC_M – magnetized SC state, NO-I (NO-II) – partially (fully) polarized normal states. PS-I (SC_0 +NO-I) – partially polarized phase separation, PS-II (SC_0 +NO-II) – fully polarized phase separation, PS-III – (SC_M +NO-II). Red point – $|U|^{SC_M}$ (quantum critical point), blue point – tricritical point, green point – the BCS-BEC crossover point in the SC_0 phase ($t = 1$).

even at $r = 1$.

Fig. 7.2 shows the ground state ($r - E_b/E_F$) phase diagrams for fixed $n = 0.01$, (a) $h = 0$, (b) $h/E_F \approx 16.1$. If $h = 0$, the SC_M state does not appear (is not stable) up to $r_c \approx 5$ in the diagram with the Hartree term and also up to $r_c \approx 4.2$ in the diagram without the Hartree term. In turn, if $h \neq 0$ (Fig. 7.2(b), diagram without the Hartree term), the QCP point moves towards smaller values of r (for $h/E_F \approx 16.1$, $r_c \approx 4$). However, in this case, the SC_M state is stable for higher values of attraction.

The influence of the Hartree term on the stability of the SC_M state is reflected in Fig. 7.3, which shows the ($r - |U|$) ground state phase diagrams for fixed $n = 0.1$, both without (a) and with (b) the Hartree term. If the Hartree term is not included in the construction of the diagram (Fig. 7.3(a)), we have the following sequences of transitions with increasing $|U|$: NO-II \rightarrow $SC_M \rightarrow$ SC_0 (for higher values of r , up from $r_c \approx 4.87$) or NO-II (NO-I) \rightarrow PS \rightarrow SC_0 (for lower values of r). In the diagram with the Hartree term (Fig. 7.3(b)), the SC_M state is not stable even at $r = 10$. Therefore, the presence of this term restricts the range of occurrence of SC_M , except for a dilute limit. Moreover, this term widens the range of occurrence of the PS region, compared to the case without the Hartree term. It is worth mentioning that the value of $|U|/t$ for which $\bar{\mu}$ reaches the lower band edge does not depend on the mass imbalance in the SC_0 state.

The diagrams ($h - |U|$) for higher filling ($n = 0.2$) and fixed r are presented in Fig. 7.4. For higher n , the region of SC_M is narrowing. The SC_M state is unstable even at $r = 5$, in the diagram without the Hartree term (Fig. 7.4(a)). SC_M occurs in the phase diagrams for higher values of r (Fig. 7.4(b)-(c)). The transition from SC_M to NO-II can

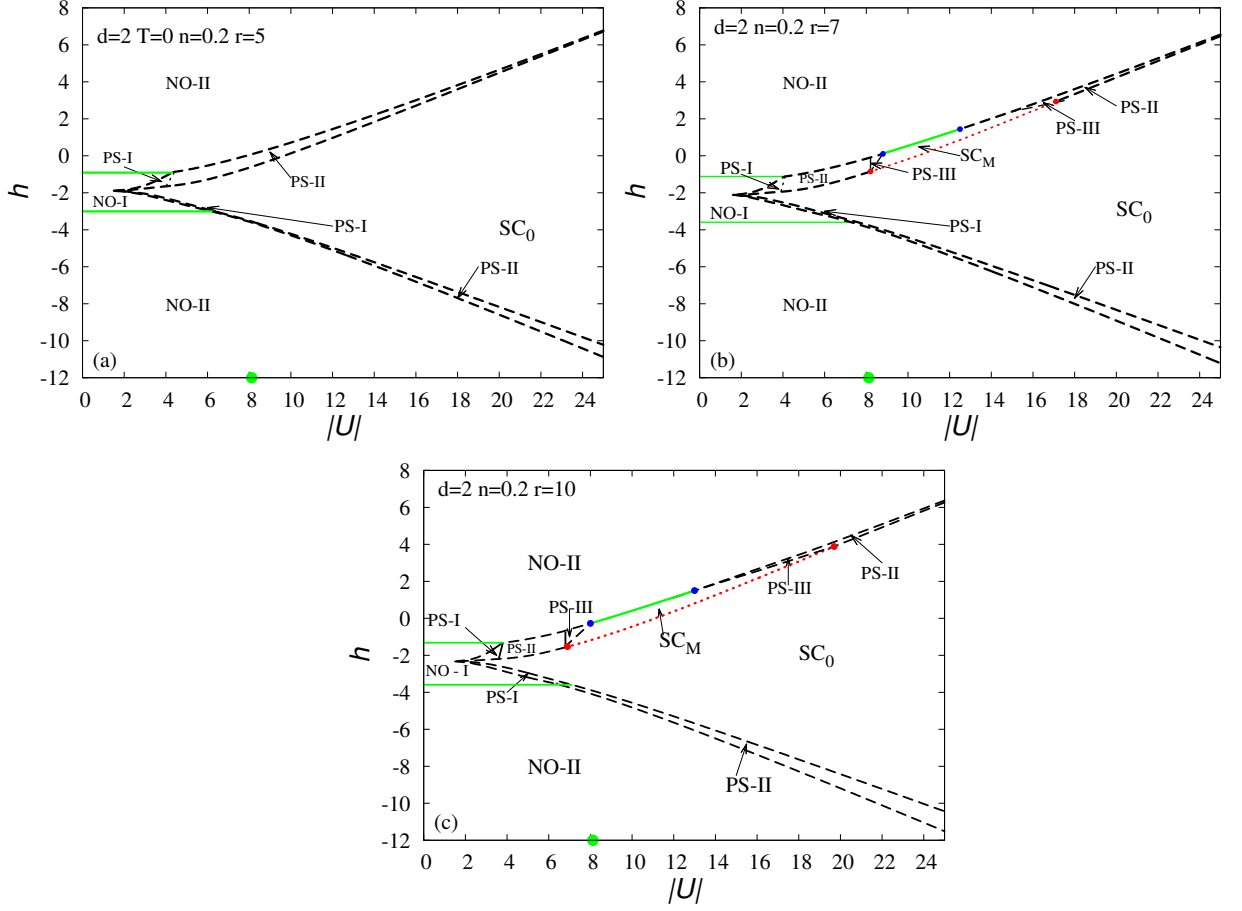


Figure 7.4: Magnetic field vs. attractive interaction phase diagrams of AAHM for three values of r : (a) $r = 5$, (b) $r = 7$, $r = 10$ and $n = 0.2$, without Hartree term. SC_M – magnetized superconducting state, NO-I – partially polarized normal state, NO-II – fully polarized normal state, PS-I – (SC_0 +NO-I), PS-II – (SC_0 +NO-II), PS-III – (SC_M +NO-II). Red points – $h_c^{SC_M}$, blue points – tricritical points, green points – the BCS-LP crossover points in the SC_0 phase ($r = 1$). The dotted red and the solid green lines are continuous transition lines ($t = 1$).

be accomplished in two ways: through PS-III (SC_M +NO-II) or through a 2^{nd} order phase transition. The character of this transition changes with increasing $|U|$. In the very strong coupling limit, PS is more stable than the SC_M phase. Hence, we also find two TCP in these diagrams. The distance between these two critical points changes with increasing r . For fixed $r = 7$, TCPs are located at $|U| \approx 8.8$ and $|U| \approx 12.5$, while for $r = 10$ at $|U| \approx 8$ and $|U| \approx 13$. However, in the very dilute limit ($n \rightarrow 0$) there is only one TCP in the $(h - |U|)$ diagram.

The BP-2 phase in $d = 2$ is unstable, even for large mass ratio. If $r \neq 1$, the symmetry with respect to $h = 0$ is broken. However, this symmetry is restored upon replacement

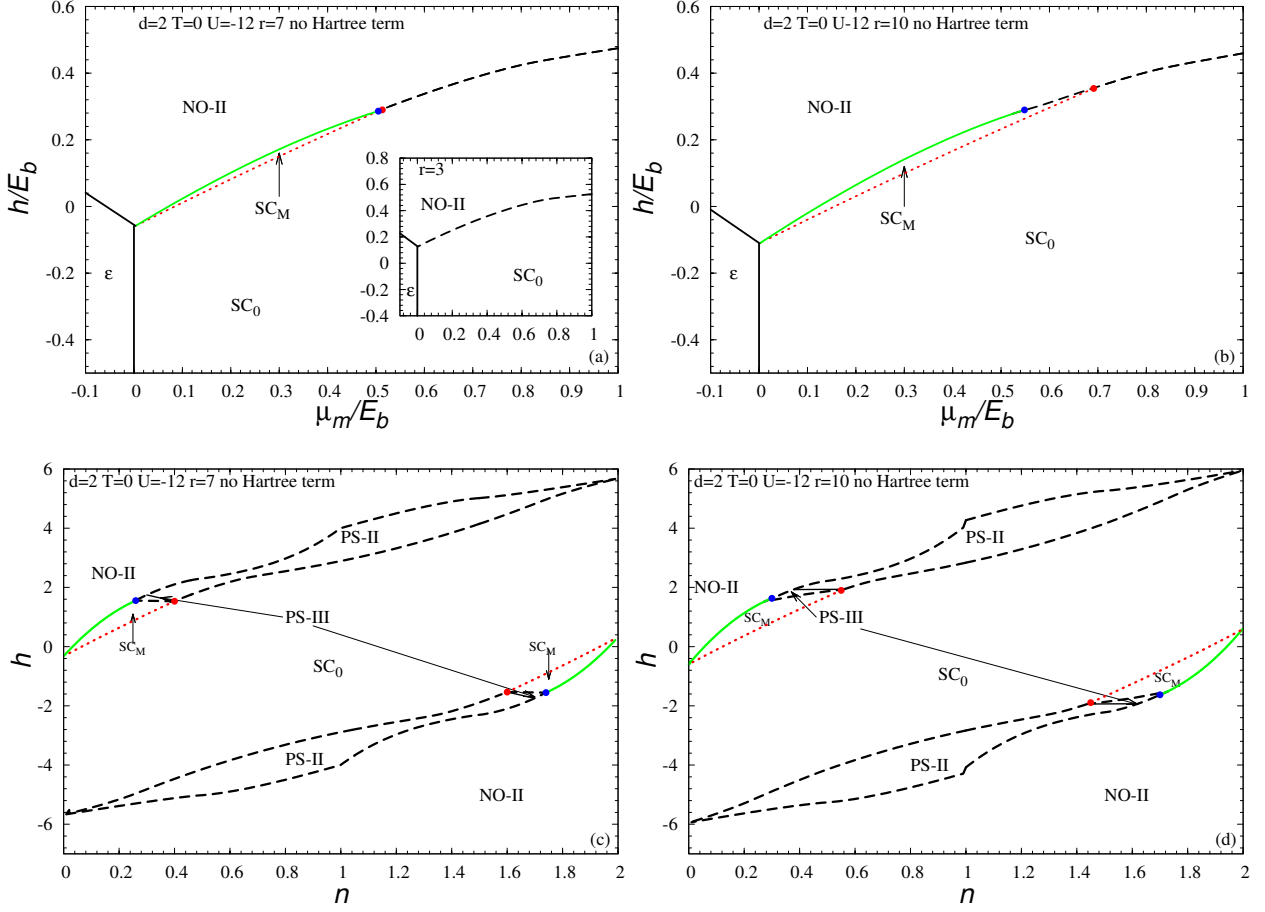


Figure 7.5: Critical magnetic field vs. chemical potential diagrams of AAHM for $d = 2$ at fixed $U = -12$ (a) $r = 7$ ($r = 3$ – inset), (b) $r = 10$. (c), (d) h vs. n phase diagrams. SC_0 – unpolarized SC state, SC_M – magnetized SC state, NO-II – fully polarized normal state, ε – empty state, μ_m – half of the pair chemical potential defined as: $\mu_m = \mu - \epsilon_0 + \frac{1}{2}E_b$, where $\epsilon_0 = -4t$, E_b is the binding energy for two fermions in an empty lattice with hopping t . Red point – $h_c^{SC_M}$, blue point – tricritical point. These points are close to each other for $r = 7$. The dotted red and the solid green lines are continuous transition lines. The dashed black line is the 1st order transition line. The possible region of existence of the commensurate CO phase is not shown in these diagrams – for the relevant values of parameters, see Fig. 7.1.

$$r \rightarrow r^{-1}.$$

Fig. 7.5 shows the phase diagrams at a fixed molecular potential μ_m and h (a)-(b), on the LP side and h vs. n (c)-(d). As usual, we define $\mu_m = \mu - \epsilon_0 + \frac{1}{2}E_b$ as one half of the pair chemical potential. In Fig. 7.5(a) (inset) there is only the first order phase transition from pure SC_0 to the NO phase (with increasing h) at fixed $r = 3$. However, for higher values of the hopping ratio ($r = 7$, $r = 10$), we observe also a continuous phase transition from SC_0 to SC_M , with decreasing chemical potential and increasing magnetic

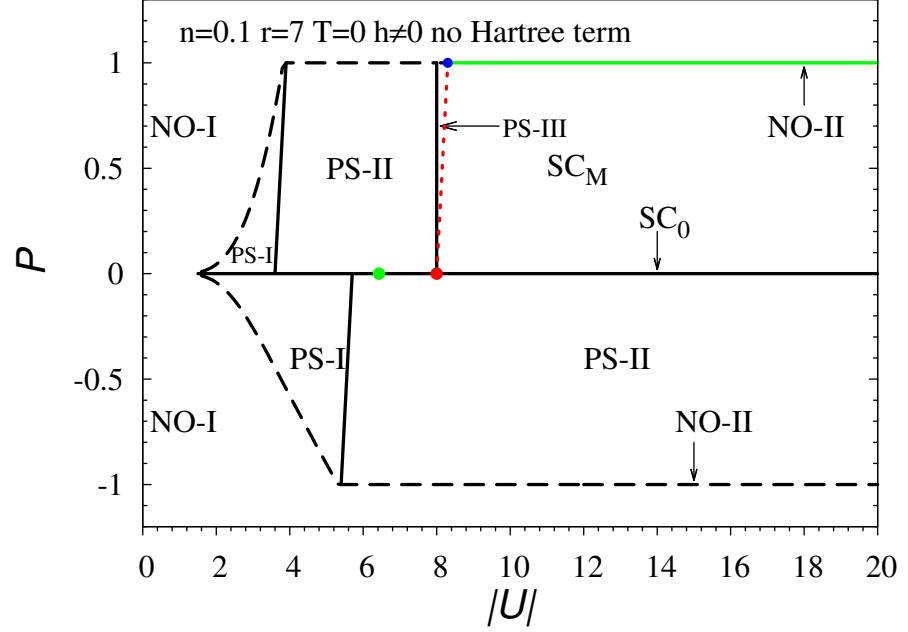


Figure 7.6: Polarization vs. on-site attraction ground state phase diagram of AAHM at fixed $n = 0.1$ and $r = 7$, for the square lattice. SC_0 – unpolarized SC state with $n_\uparrow = n_\downarrow$, SC_M – magnetized SC state, NO-I (NO-II) – partially (fully) polarized normal states. PS-I (SC_0 +NO-I) – partially polarized phase separation, PS-II (SC_0 +NO-II) – fully polarized phase separation, PS-III – (SC_M +NO-II). Red point – $|U|_c^{SC_M}$ (quantum critical point), blue point – tricritical point, green point – the BCS-BEC crossover point in the SC_0 phase.

field. This fact confirms the earlier observations that there exists a critical value of r above which the SC_M state is stable in the 2D case. The character of the transition from the superconducting to the normal phase changes with decreasing μ . Hence, we also find TCP in the diagrams (blue point), at which the second order transition from SC_M to NO-II terminates. The tricritical and quantum critical points are close to each other for $r = 7$. However, for higher values of r (Fig. 7.5(b)), the distance between these points increases. This increase is due to the fact that the SC_M phase becomes stable for higher values of μ_m , which corresponds to higher values of n (Fig. 7.5(d)). As shown in Figs. 7.5(c)-(d), the results for the fixed chemical potential have been mapped onto the case of fixed n . This implies the PS region occurrence in the $h - n$ plane. These diagrams are good examples of the $(h, n) \rightarrow (-h, 2 - n)$ symmetry, i.e. a combined particle-hole symmetry and the symmetry with respect to a change in the direction of the magnetic field. We emphasize again that we have not considered the commensurate CO phase in these diagrams. This phase can occur above some critical value n_c which depends on the hopping imbalance – for more details about the relevant region of parameters, see Fig. 7.1.

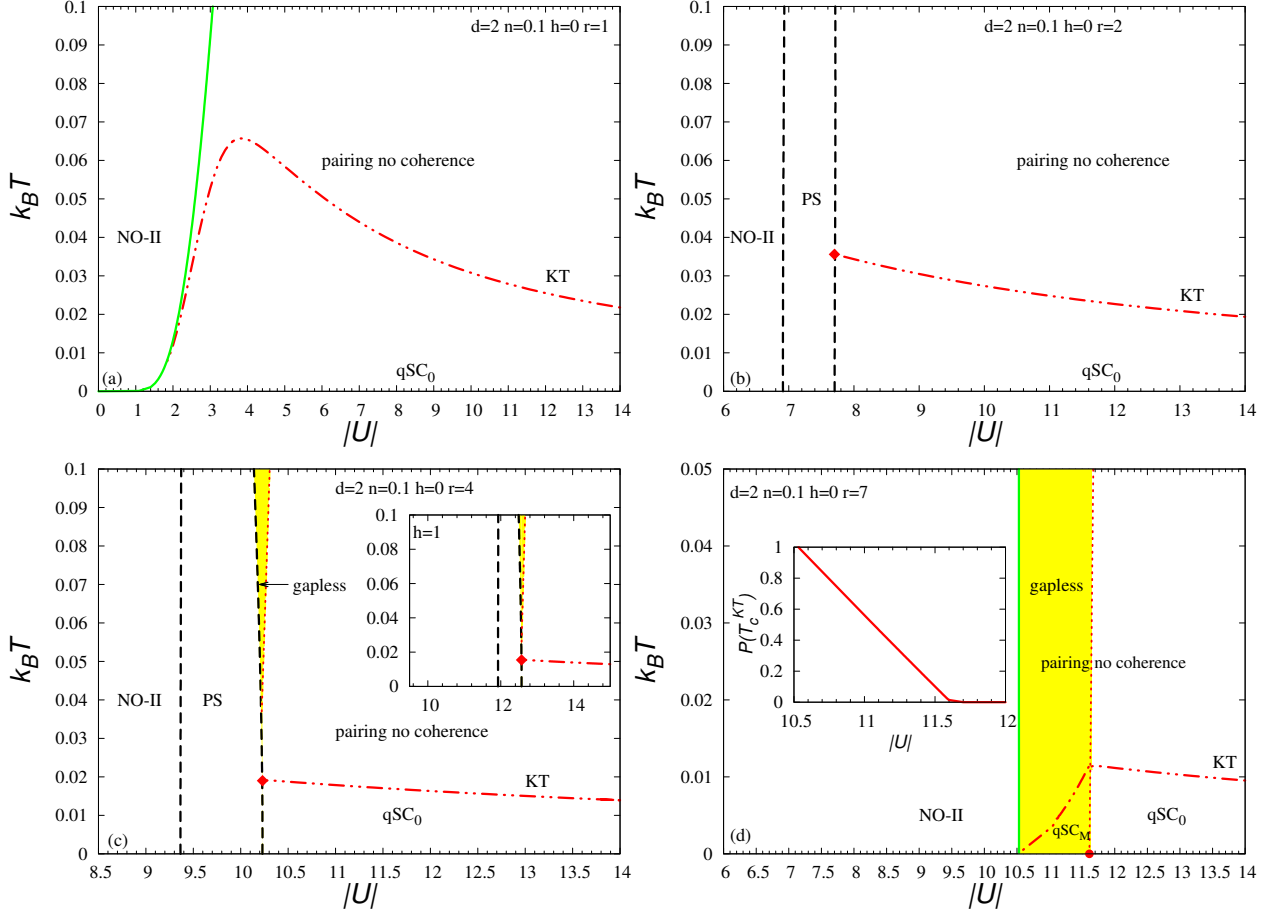


Figure 7.7: Temperature vs. $|U|$ phase diagrams of AAHM, at fixed $n = 0.1$, $h = 0$ for the square lattice. (a) $r = 1$, (b) $r = 2$, (c) $r = 4$ (inset – $h = 1$) (d) $r = 7$ (inset – $P(T_c^{KT})$ vs. $|U|$). The thick dashed-double dotted line (red color) is the KT transition line. Thick solid line denotes transition from pairing without coherence region to NO-II within the BCS approximation, dotted line (red color) is continuous transition line from qSC₀ to qSC_M state at $T = 0$ or from qSC₀ to the gapless region (yellow color) at $T \neq 0$. PS – phase separation, qSC₀ – 2D qSC without polarization, qSC_M – 2D qSC in the presence of polarization (a spin polarized KT superfluid). Red point at $T = 0$ (see Fig. (d)) – QCP for Lifshitz transition.

7.2.2 Finite temperature phase diagrams

Because of the occurrence of the SC_M state at $T = 0$ for higher r , one can expect that this phase persists to non-zero temperatures.

In Fig. 7.6, we present the $P - |U|$ ground state diagram for low electron concentration $n = 0.1$ and fixed r , at $h \neq 0$. This diagram is only shown so that we could refer to it in our further considerations, when the zero-temperature results are extended to finite temperatures. As mentioned above, in the 2D system at $r = 1$, for $h \neq 0$, the SC_M phase

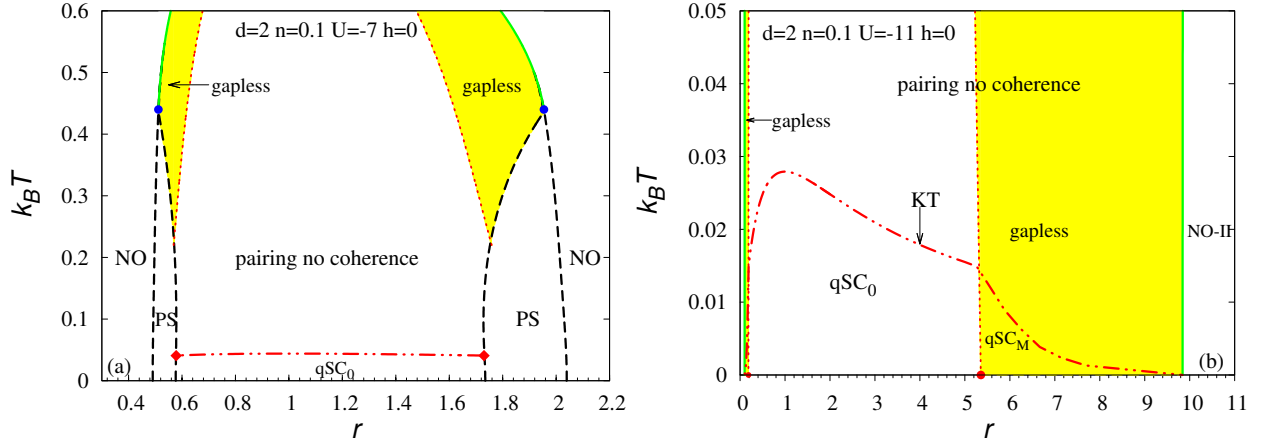


Figure 7.8: Temperature vs. r phase diagrams of AAHM, at fixed $n = 0.1$, $h = 0$ for the square lattice. (a) $U = -7$, (b) $U = -11$. The thick dashed-double dotted line (red color) is the KT transition line. Dotted line (red color) is continuous transition line from qSC_0 to qSC_M state at $T = 0$ or from qSC_0 to the gapless region (yellow color) at $T \neq 0$. PS – phase separation, qSC_0 – 2D qSC without polarization, qSC_M – 2D qSC in the presence of polarization (a spin polarized KT superfluid). Red point at $T = 0$ (see Fig. (b)) – QCP for Lifshitz transition.

is unstable even in the strong coupling limit and phase separation is favorable. This is in opposition to the 3D case in a Zeeman magnetic field in which for $r = 1$ the SC_M phase occurs for strong attraction and in the dilute limit. However, as shown in Sec. 7.2.1, for $r \neq 1$ SC_M in $d = 2$ can be stable. There is a critical value of $|U_c|^{SC_M}$ (red point in the diagram), for which the SC_M state becomes stable, instead of PS. The transition from SC_M to NO can be accomplished in two ways for fixed n : through PS-III ($SC_M + NO-II$) or through the second order phase transition for higher $|U|$. The change in the character of this transition is manifested through TCP. For so chosen parameters ($n = 0.1$, $r = 7$), the magnetized superconducting state is stable only on the BEC side (see Fig. 7.6, $P > 0$), but as shown in Sec. 7.2.1, SC_M can also be stable in the intermediate couplings (for higher values of r , e.g. $r = 10$). If $r \neq 1$, the symmetry with respect to $h = 0$ is broken. Hence, the diagram is not symmetric with respect to $P = 0$ and for $P < 0$ the PS is favorable instead of SC_M in the LP limit (Fig. 7.6). The presented phase diagram has been constructed without the Hartree term.

Here, we perform a detailed analysis of the BCS-LP crossover phase diagrams for finite temperatures and show that if $r \neq 1$, the appearance of a new phase is possible at $T \neq 0$.

Fig. 7.7 shows $(T - |U|)$ phase diagrams for $h = 0$, $n = 0.1$ and four fixed values of r : (a) $r = 1$, (b) $r = 2$, (c) $r = 4$ and (d) $r = 7$. As usual, the solid lines (2^{nd} order transition lines) and the PS regions are obtained within the BCS approximation, while the thick dash-double dotted line (red color) denotes the KT transition determined from Eqs. (3.11) and (3.26). As mentioned before, the temperatures T_c^{KT} are much smaller than T_c^{HF} . However, as shown in Fig. 7.7(a) ($h = 0$, $r = 1$), the difference between T_c^{KT}

and T_c^{HF} decreases with decreasing attractive interaction and in the weak coupling limit these temperatures are comparable. The KT temperature increases with increasing $|U|$, reaches its maximum for some value of $|U|$ and then decreases. At $h = 0$ and $r = 1$, both T_c^{HF} as T_c^{KT} are nonzero, for very low values of $|U|$. However, $r \neq 1$ gives a similar effect to $h \neq 0$, i.e. $T_c^{HF} = 0$, below a definite value of attractive interaction. This critical $|U|$ increases with r , which is clearly visible in Fig. 7.7(b)-(d). Moreover, if additionally $h \neq 0$, one can see (Fig. 7.7(c) – inset) that $T_c^{HF} = 0$ moves towards larger $|U|$ (e.g. if $h = 0$, $r = 4 - |U_c| \approx 9.4$ and if $h = 1$, $r = 4 - |U_c| \approx -11.9$).

Because of the occurrence of the magnetized superconducting state at $T = 0$ for higher r , this phase persists to non-zero temperatures (as shown in Fig. 7.7(d), $r = 7$). However, if SC_M is unstable at $T = 0$ (compare with Fig. 7.3(a)) for lower r (Fig. 7.7(b)-(c)), the gapless region can still occur at some temperatures (with one FS in the strong coupling). Moreover, the combination of $r \neq 1$ and $h \neq 0$ causes a decrease in temperature at which this gapless region occurs (compare: Fig. 7.7(c) and its inset). It is worth mentioning that there is a gapless region in the diagram for fixed $r = 2$, but at definitely higher temperatures.

The system is a quasi superconductor below T_c^{KT} . Apart from the unpolarized qSC_0 state, qSC_M occurs, which can be termed a *spin polarized KT superfluid* (Fig. 7.7(d)). Above T_c^{KT} , we have an extended region of incoherent pairs which is bounded from above by the pair breaking temperature. In the strong coupling limit, T_c^{KT} does not depend on magnetic field, but it depends on mass imbalance and its upper bound takes the form:

$$k_B T_c^{KT} = 2\pi \frac{r}{(1+r)^2} \frac{t^2}{|U|} n(2-n), \quad (7.53)$$

for $r > 0$. In that limit only LP's exist and the system is equivalent to that of hard-core Bose gas on a lattice, described by the Hamiltonian (7.46).

In Fig. 7.8 we present the $(T - |U|)$ phase diagrams for $n = 0.1$ and fixed $|U|$, at $h = 0$ to illustrate, among others, the symmetry $(h, r) \rightarrow (-h, 1/r)$. At $T = 0$, for $U = -7$ (Fig. 7.8(a)) the transition from the superconducting to the normal state goes through PS both for $r > 1$ and $r < 1$. The phase separation region is limited by two critical values of r : for $r > 1 - r_{c1}^{r>1} \approx 1.735$, $r_{c2}^{r>1} \approx 2.0392$, while for $r < 1 - r_{c1}^{r<1} \approx 0.576$, $r_{c2}^{r<1} \approx 0.49$. As can be easily seen, $r_{c1}^{r>1} \rightarrow 1/r_{c1}^{r<1}$ and $r_{c2}^{r>1} \rightarrow 1/r_{c2}^{r<1}$. At low temperatures, the system is a quasi superconductor without polarization up to T_c^{KT} . There exist only local pairs. For higher temperatures (above T_c^{KT} and below T_c^{HF}) there is a region of pairs without the phase coherence. Obviously, we can distinguish two gapless regions both for $r > 1$ and $r < 1$. Two MF TCP, which terminate the second order transition are located at the same value of temperature because of the $r \rightarrow 1/r$ symmetry.

For higher attractive interaction ($U = -11$), because of the existence of the SC_M phase at $T = 0$ (see: Fig. 7.6), this state is continued to finite temperatures. The transition from the KT superfluid to the normal state is of the second order for $r > 1$ and $r < 1$. The critical values $r_c^{r>1}$ (for $t^\uparrow > t^\downarrow$) and $r_c^{r<1}$ (for $t^\uparrow < t^\downarrow$) for which SC_M becomes stable (gapless region – yellow color in the diagrams) and for which the 2^{nd} order transition to the NO phase takes place are related by $r_c^{r<1} = 1/r_c^{r>1}$, which is another confirmation of

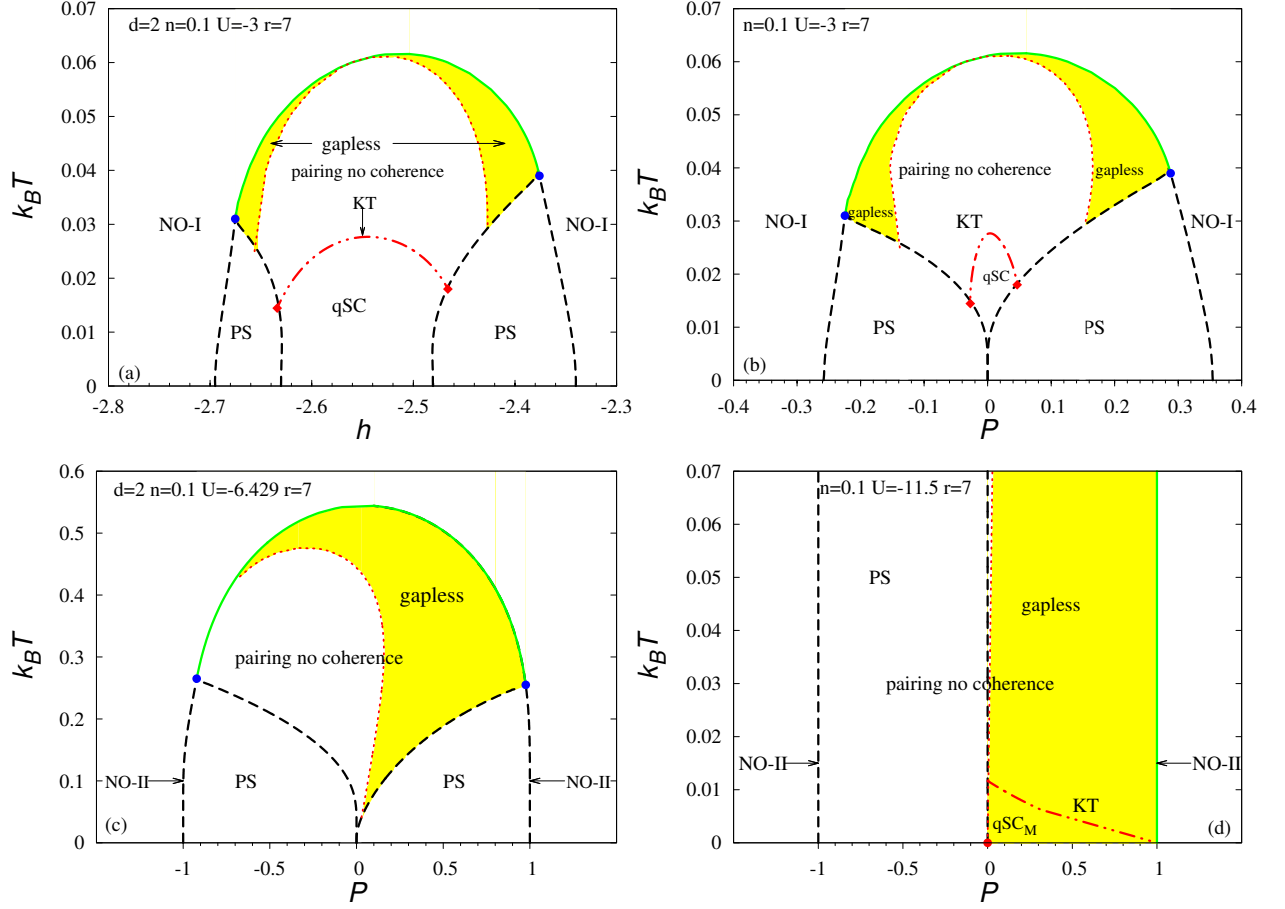


Figure 7.9: Temperature vs. magnetic field (a) and polarization (b)-(d) phase diagrams of AAHM without the Hartree term, at fixed $n = 0.1$, $r = 7$, for the square lattice. (a)-(b) $U = -3$, (c) $U = -6.429$, (d) $U = -11.5$. The thick dashed-double dotted line in (red color) is the KT transition line. Thick solid line denotes transition from pairing without coherence region to NO within the BCS approximation. Above the dotted line (red color) – gapless (yellow color) – the region which has a gapless spectrum for the majority spin species. qSC – 2D KT superconductor, SC_M – gapless KT SC with one FS in the presence of polarization (a spin polarized KT superfluid). Red point at $T = 0$ (see Fig. (d)) – QCP for Lifshitz transition.

the $r \rightarrow 1/r$ symmetry at $h = 0$. As in the $U = -7$ case, for lower temperatures, below T_c^{KT} there are only local pairs and the system is equivalent to that of hard-core Bose gas on a lattice. The maximum value of T_c^{KT} is located at $r = 1$ and decreases with increasing and decreasing r . The transition from qSC_0 to qSC_M is manifested by a cusp on the KT critical temperature line, both for $r > 1$ and $r < 1$. The region of the SC_M occurrence at $T = 0$ is between $r \approx 5.356$ (red point in Fig. 7.8(b)) and $r \approx 9.842$ for $r > 1$. Because of the $r \rightarrow 1/r$ symmetry this region is visually much narrower for $r < 1$.

Fig. 7.9 shows $T - h$ and $T - P$ phase diagrams for $n = 0.1$, $r = 7$, at $h \neq 0$ and

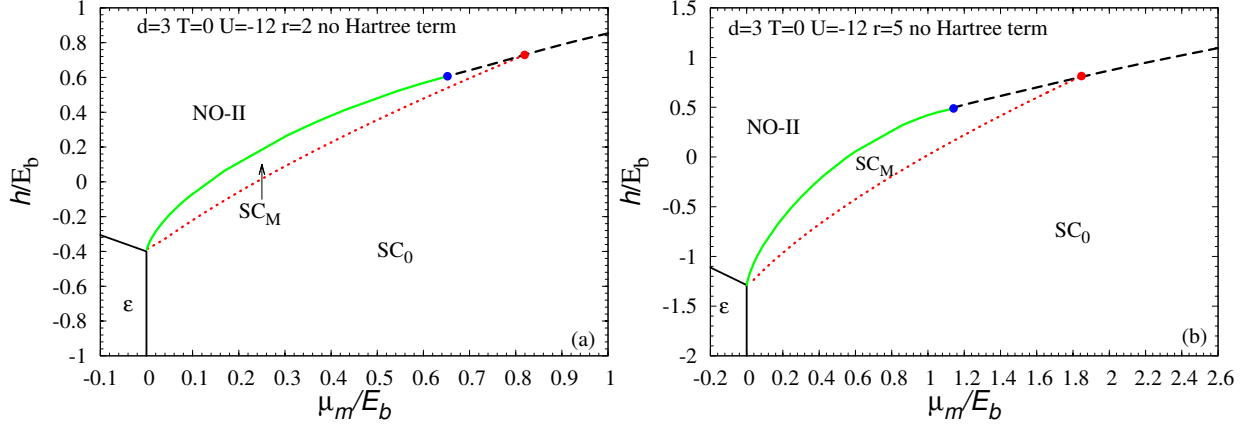


Figure 7.10: Critical magnetic field vs. chemical potential for $d = 3$, $U = -12$ on LP side, (a) $r = 2$ and (b) $r = 5$. SC_0 – unpolarized SC state with $n_\uparrow = n_\downarrow$, SC_M – magnetized SC state, NO-II – fully polarized normal state, ε – empty state, μ_m – half of the pair chemical potential defined as: $\mu - \epsilon_0 + \frac{1}{2}E_b$, where $\epsilon_0 = -6t$, E_b is the binding energy for two fermions in an empty lattice with hopping t . Red point – $h_c^{SC_M}$ (quantum critical point (QCP)), blue point – tricritical point. The dotted red and the solid green lines are continuous transition lines.

three values of attraction – moderately weak ($U = -3$, $E_b/E_F = 0.024$), intermediate ($U = -6.429$ – critical value of U at which the chemical potential drops below the lower band edge) and strong ($U = -11.5$) coupling. These diagrams have also been constructed within the mean field approximation (the solid lines (2^{nd} order transition lines), PS and gapless regions), but the phase coherence temperatures have been obtained as usual within the KT scenario (thick dash-double dotted line (red color)). In our approach the qSC phase is characterized by a non-zero gap ($\Delta \neq 0$) and non-zero superfluid stiffness ($\rho_s \neq 0$). In the weak coupling regime, the KT superconductor exists at low $|P|$ and low T (Fig. 7.9(a)-(b)). Despite the fact that $r \neq 1$, the SC phase is restricted to low $|P|$, while for larger $|P|$ the PS region is favored. There is also the nonsuperfluid region (pairs without coherence), formally defined by $\Delta \neq 0$, $\rho_s = 0$. As mentioned above, in this region one observes a pseudogap behavior. Therefore, the region of incoherent pairs is different from the normal phase. In the $T - P$ diagrams (see: Fig. 7.9(b)-(c)), one finds MF TCPs at which the thermal transition changes from the second to the first order. We also show the gapless area within the state of pairing without coherence. This gapless region is above the KT coherence temperatures in the weak coupling limit.

In the intermediate coupling (Fig. 7.9), below T_c^{KT} the SC state is strongly reduced to very low $|P|$. At the BCS-LP crossover point a polarized SC does not exist even for $r \neq 1$.

The situation is radically different in the spin asymmetric hopping and strong coupling case (Fig. 7.9(d)). As mentioned above, for sufficiently high value of r , below T_c^{KT} , the spin polarized KT superfluid state with gapless spectrum and one FS can be stable for

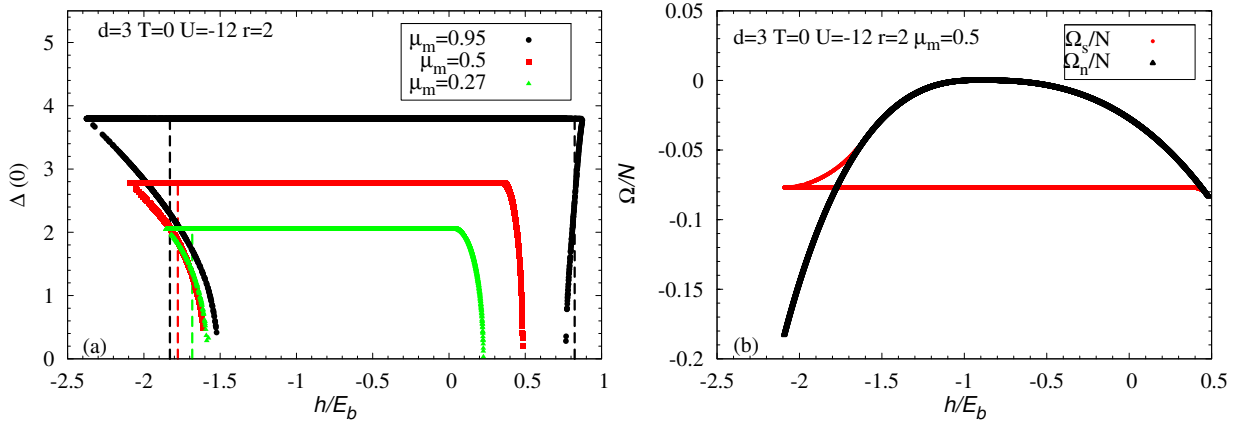


Figure 7.11: Dependence of the order parameter (a) and the grand canonical potential (b) on the magnetic field in the units of the binding energy E_b at $T = 0$, $d = 3$, $U = -12$, $r = 2$, for three values of $\mu_m = \mu - \epsilon_0 + \frac{1}{2}E_b$. The vertical dashed lines mark the Hartree-Fock phase transition magnetic field – the first order phase transition to the normal state at $T = 0$.

all $P > 0$. If $P < 0$, there is the PS region at low T .

We notice however that the polarized KT superfluid is restricted to low temperatures $T_c^{KT}/E_F \sim 0.02$ for this value of n . For lower n T_c^{KT}/E_F will be higher and upper limit is set by the value for continuum case.

7.3 AAHM on 3D simple cubic lattice

In chapter 5, among other things, we analyzed the BCS-BEC crossover ground state phase diagrams in the presence of the Zeeman magnetic field in 3D for a simple cubic lattice. For strong attraction and in the dilute limit, the homogeneous magnetized superconducting phase and the tricritical point were found in the $(h - \mu)$ and $(h - n)$ diagrams. In this section, we briefly study the hopping asymmetric AHM (i.e. $t^\uparrow \neq t^\downarrow$) and show that the introduction of a mismatch between the hopping integrals causes an extension of the range of occurrence of the SC_M phase in the 3D case. The importance of the Hartree term in the broken symmetry Hartree-Fock approximation is also indicated.

We start our analysis from a comparison of three ground state phase diagrams of AHM at fixed μ_m and h , for $r = 1$ (Fig. 5.4), $r = 2$ (Fig. 7.10(a)) and $r = 5$ (Fig. 7.10(b)). As usual, we define $\mu_m = \mu - \epsilon_0 + \frac{1}{2}E_b$ as one half of the pair chemical potential (molecular potential). As mentioned above, many experiments have indicated that in the density profiles of trapped Fermi mixtures with population (mass) imbalance, there is an unpolarized superfluid core in the center of the trap and a polarized normal state surrounding this core, in the BCS and unitarity regimes. These experimental observations are in good agreement with our earlier analysis (see: chapter 4) according to which there is non-polarized ($n_\uparrow = n_\downarrow$) superfluid phase for higher μ and polarized ($n_\uparrow \neq n_\downarrow$) normal

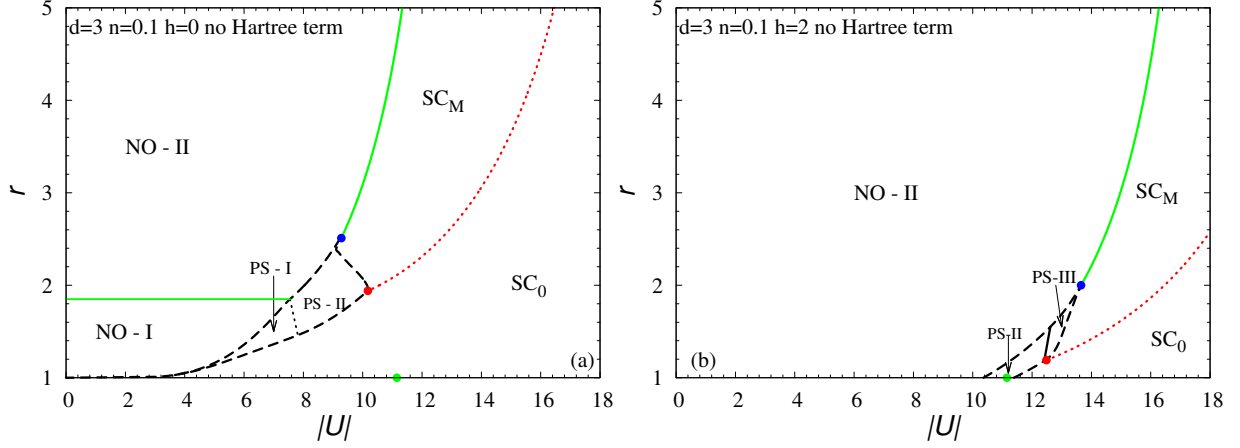


Figure 7.12: Ground state phase diagrams r vs. $|U|$ for $d = 3$, $n = 0.1$, (a) $h = 0$ (b) $h = 2$. SC₀ – unpolarized SC state, SC_M – magnetized SC state, NO-I (NO-II) – partially (fully) polarized normal states. PS-I (SC₀+NO-I) – partially polarized phase separation, PS-II (SC₀+NO-II) – fully polarized phase separation, PS-III – (SC_M+NO-II). Red point – $|U|_c^{SC_M}$ (quantum critical point), blue point – tricritical point, green point – the BCS-BEC crossover point in the SC₀ phase.

state for lower μ at fixed h and attractive interaction (see: Fig. 4.5(b)). On the BEC side, in contrast to the BCS limit, there can appear a shell of the SC_M phase (with a finite polarization and a gapless spectrum) between the SC₀ and the NO phases, as shown in Figs. 5.4, 7.10(a) and 7.10(b). The structure of the above diagrams has been discussed in detail in chapter 5 for the $r = 1$ case. The topology of the diagrams in Fig. 7.10 for $r \neq 1$ and 5.4 for $r = 1$ is the same. We still observe the first order phase transition from the SC₀ to the NO phase or the continuous transition from SC₀ to SC_M and then first or second order to the normal state. However, there are quantitative differences. While for the $r = 1$ case, the SC_M phase appears only in the dilute limit (in particular in the diagrams with the Hartree term), e.g. at $U = -12$ a critical value of n (n_c) below which the SC_M state becomes stable equals around 0.059 (without the Hartree term case) or $n_c \approx 0.0086$ (with the Hartree term included), for $r = 2$ $n_c \approx 0.238$ and for $r = 5$ $n_c \approx 0.56$. Hence, TCP moves towards higher values of μ (n). There are also differences in the phase diagrams around the empty state, due to the $h \rightarrow -h$ symmetry breaking for $r \neq 1$. For $r = 1$, $\mu_m/E_b = 0$ for $h/E_b = 0.5$, while for $r \neq 1$ the ratio h/E_b which gives $\mu_m/E_b = 0$ moves toward negative values with increasing r . Moreover, as one can see in Fig. 7.11 which shows the order parameter vs. magnetic field in the units of the binding energy at $T = 0$, the transition from the SC₀ to the NO phase is always of the first order for $h < 0$ and negative values of $\mu = \mu_m + \epsilon_0 - \frac{1}{2}E_b$ (left part of Fig. 7.11). In turn, as mentioned above, the transition from SC₀ to NO can take place in two ways in the $h - n$ plane for $h > 0$: through phase separation (for higher μ_m , e.g. $\mu_m = 0.95$ in Fig. 7.11, which corresponds to $n \approx 0.279$) or through the SC_M state (for lower μ_m , e.g. $\mu_m = 0.5$, $\mu_m = 0.27$ in Fig. 7.11, which corresponds to $n \approx 0.142$ and $n \approx 0.0756$, respectively.).

Fig. 7.12 shows $(r - |U|)$ phase diagrams for fixed $n = 0.1$, $h = 0$ and $h = 2$. Here, we consider a rather low value of n , but still not the very dilute case. Hence, there is the critical value of $r \neq 1$ for which the SC_M is stable both for $h = 0$ as for $h = 2$, while the magnetized superfluid state can be stable even for $r = 1$ in the 3D case. The structure of the diagram 7.12(a) is very similar to that from section 7.2.1 (Fig. 7.3(a)), for the 2D case. However, r_c is much lower in the simple cubic lattice case than in the square lattice case. Moreover, the SC_M state is stable in the intermediate region for 3D as opposed to the 2D case for which this phase is stable only in the strong coupling limit, for so chosen parameters. Next, if $h \neq 0$ (Fig. 7.12(b)), the SC_M phase moves towards higher values of attractive interactions. However, the critical value r_c is lower than in the case without the Zeeman magnetic field. The presence of h breaks the $r \rightarrow 1/r$ symmetry. Moreover, there is neither PS-I, nor the partially polarized normal state in the phase diagram at finite h , even for $r = 1$.

It is interesting that the combination of $h \neq 0$ and higher values of r widens the range of occurrence of the SC_M phase and the PS-III region disappears in the crossover phase diagrams, which is clearly visible in Fig. 7.13. If $r = 2$, the SC_M is stable but limited by the two critical values of the attractive interaction: $|U|_c^{SC_M} \approx 10.08$ and $|U|_c^{SC_M} \approx 64.86$. There is only the first order phase transition from SC_M to the fully polarized normal state, through PS-III. For higher hopping asymmetry of r (Fig. 7.13(b)-(d)), the region of SC_M stability is much larger. As mentioned above, the region in which the SC_M phase and the NO-II state separate spatially (PS-III) is unstable with regard to the pure spatially homogeneous magnetized superfluid. Therefore, there is the second order phase transition from the SC_M to the NO-II phase in the whole range of SC_M occurrence. The Lifshitz type quantum critical point (red color) moves towards lower $|U|$, with increasing r and even for relatively low hopping imbalance ($r = 5$), the SC_M phase is stable in the intermediate couplings region. However, the position of the tricritical point does not move with increasing r , starting from some definite value of $r \approx 5$. Moreover, it is worth mentioning that the BP-II phase is unstable in the whole range of parameters in 3D, as well as in the 2D case. To confirm this hypothesis, let us analyze in detail the behavior of the superconducting solutions for different fixed parameters. For this purpose, we show in Fig. 7.14 the plots of the momentum occupation numbers vs. $k \equiv k_x = k_y = k_z$ and the corresponding quasiparticle spectra $E_{\vec{k}\uparrow}$, $E_{\vec{k}\downarrow}$ for fixed $r = 5$, $n = 0.1$ and different values of h and $|U|$. For $U = -12$ and $h = -3.5$, the system is in the unpolarized superconducting state on the LP side. Therefore, there is no Fermi surface and both of the quasiparticle branches are gapped, as shown in Fig. 7.14(a). For higher values of magnetic field, on the LP side, there is a continuous transition from the SC_0 to the SC_M state. There is one Fermi surface which comes from the excess of spin-up fermions in the SC_M phase with the gapless spectrum (Fig. 7.14(b)-(c)). These unpaired fermions occupy the region around momentum $k = 0$.

We also analyze a superconducting solution from the phase separation region, for an intermediate value of coupling (Fig. 7.14(d)). A solution of this type (interior gap superfluidity or the BP-II phase) was analyzed in [73]. We show that the occurrence of such a solution is possible, but it is energetically unstable. As mentioned above, the BP-II

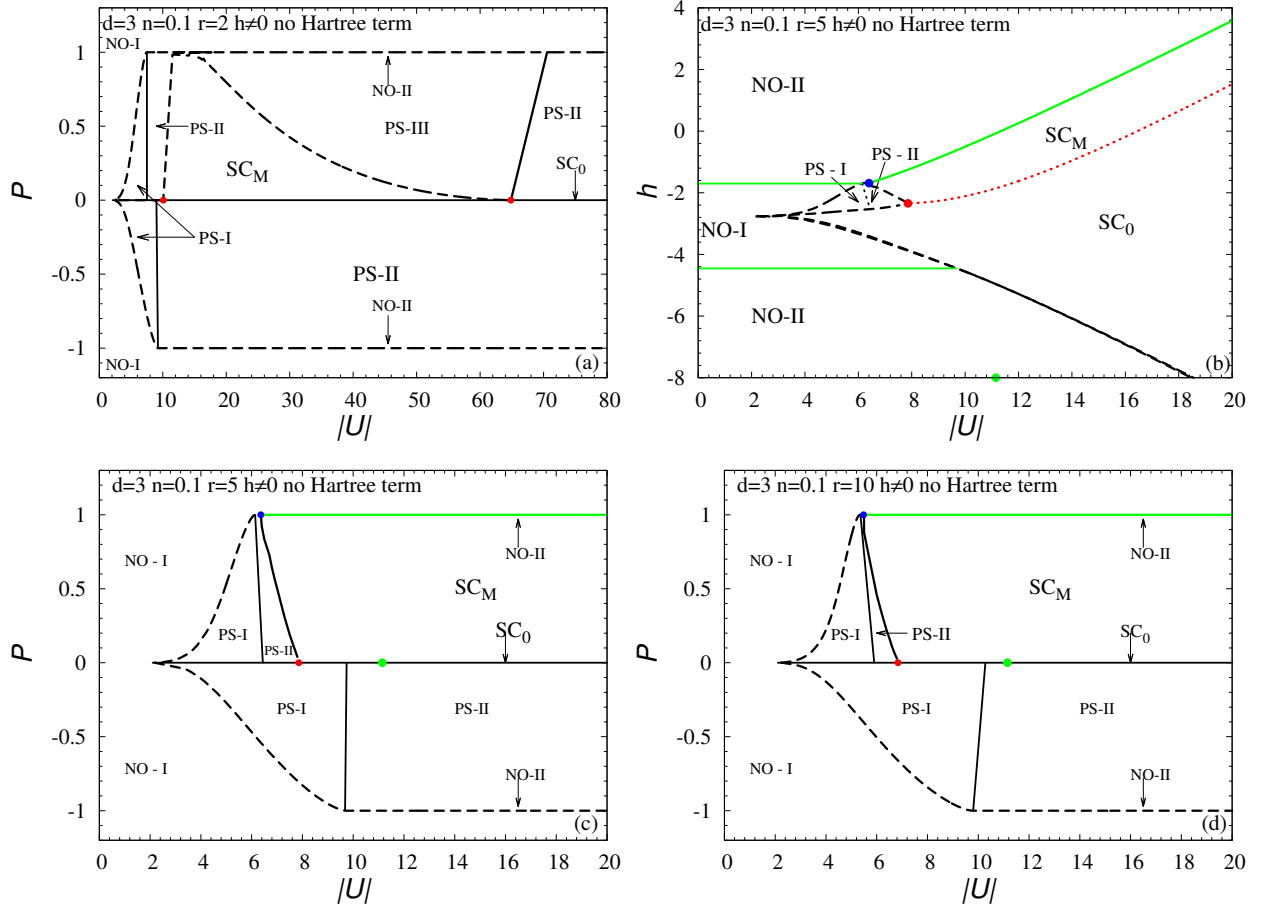


Figure 7.13: Polarization vs. $|U|$ ground state phase diagrams of spin polarized AHM, at fixed $n = 0.1$, for (a) $r = 2$, (b), (c) $r = 5$, (d) $r = 10$. SC_0 – unpolarized superconducting state, SC_M – magnetized superconducting state, PS-I (SC_0 +NO-I) – partially polarized phase separation, PS-II (SC_0 +NO-II) – fully polarized phase separation, PS-III (SC_M +NO-II). Green point – the BCS-BEC crossover point, blue point – tricritical point, red point – $|U|_c^{SC_M}$.

state can have excess of fermions with two FS's at $T = 0$ and a gapless spectrum for the majority spin species. For $r = t^\uparrow/t^\downarrow = 5$, the heavier fermions are the ones with spin-down, but the majority spin species are the spin-up fermions. As shown in Fig. 7.14(d), the unpaired fermions occupy the state around the Fermi momentum, in contrast to the BP-I case. The energy spectrum for the lighter fermions (the majority spin species) is gapless (Fig. 7.14(d) – inset). There are two zeros in the plot of $E_{\vec{k}\uparrow}$.

Another important aspect of this section is the influence of hopping imbalance on the SC_M phase stability in the presence of the Hartree term. As discussed in Chapter 5, the occurrence of the BP-I phase depends on the lattice structure, i.e. if $r = 1$, SC_M is unstable for $d = 2$ but it can be realized for $d = 3$ lattices. However, in the AHM, the very existence of the BP-I phase is restricted to low fillings. The Hartree term, usually

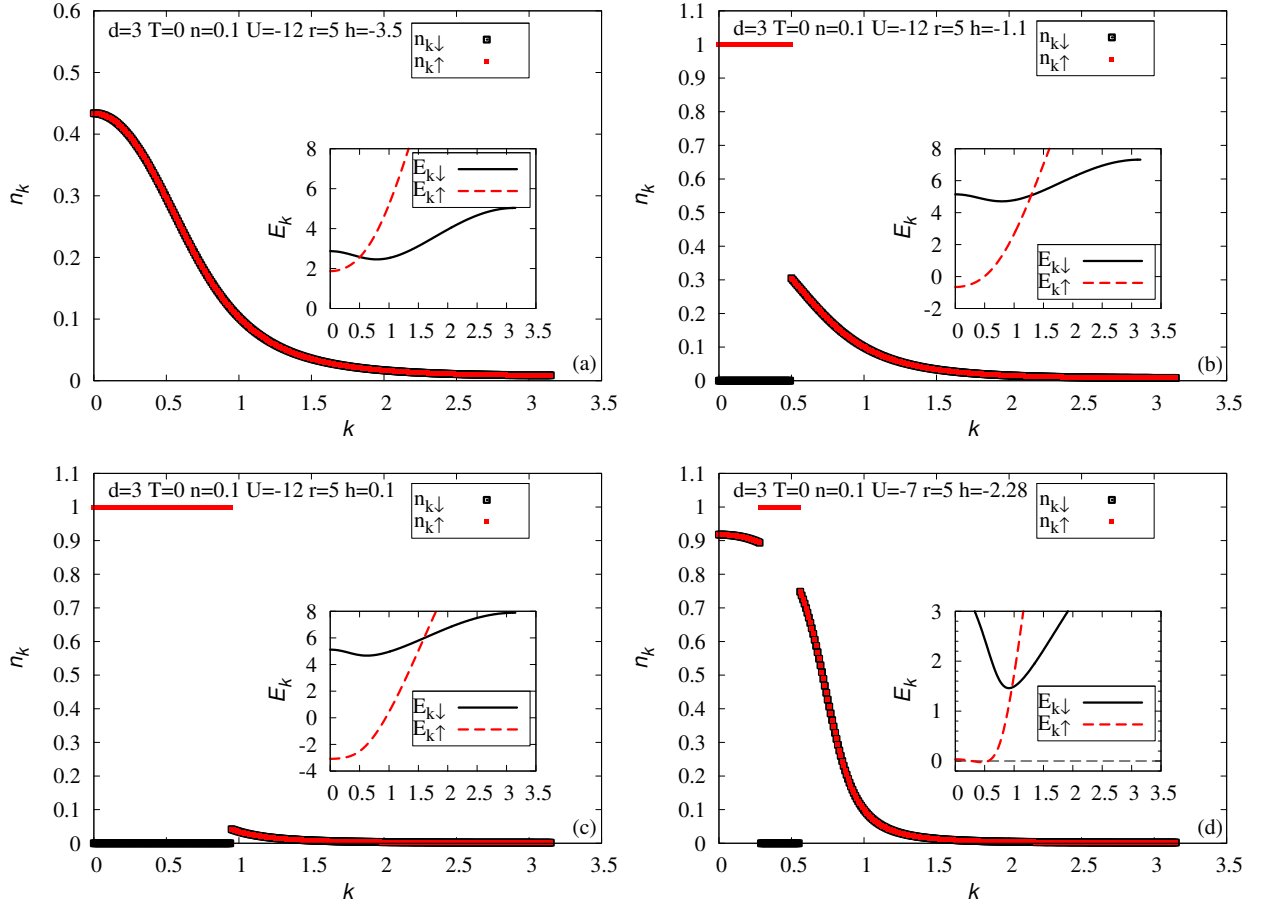


Figure 7.14: Plots of momentum occupation numbers $n_{\vec{k}\uparrow}$ (red points), $n_{\vec{k}\downarrow}$ (black points) vs. $k \equiv k_x = k_y = k_z$ and the corresponding quasiparticle spectra $E_{\vec{k}\uparrow}$, $E_{\vec{k}\downarrow}$ (inset) for $d = 3$, $n = 0.1$, $r = 5$, $U = -12$. (a) $h = -3.5$ – on the LP side, SC_0 phase; (b) $h = -1.1$ – on the LP side, SC_M phase; (c) $h = 0.1$ – strongly correlated superconductor, SC_M phase; (d) $U = -7$, $h = -2.28$ – unstable SC_M phase (PS region).

promoting ferromagnetism in the Stoner model ($U > 0$), here ($U < 0$) strongly competes with superconductivity. Thus, such term restricts the SC_M state to lower densities as shown in Figs. 5.14 and also 7.15. If $r = 1$, the critical value of n above which the SC_M state becomes unstable equals $n \approx 0.0145$ for the simple cubic lattice case. However, the mass imbalance can change this behavior because of spin polarization stemming from the kinetic energy term. In this way, SC_M can be realized for the intermediate and strong coupling regimes for higher values of n , even in the presence of the Hartree term. Then, the hopping imbalance increases a critical value of n above which the SC_M state becomes unstable and for $r = 2$ $n \approx 0.07$, as shown in Fig. 7.15. For each value of n , there are two critical values of the attraction for which the SC_M state becomes stable (except for the very dilute limit, where there is only the lower critical value, i.e. the upper critical value becomes infinite). The system is in the SC_M phase between the lower and upper critical

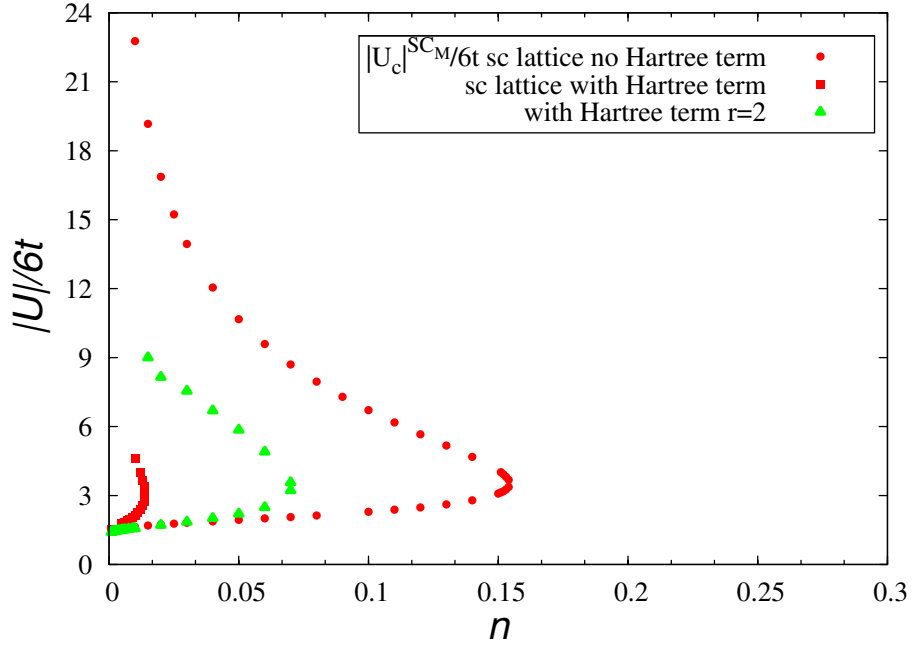


Figure 7.15: Critical values of the attraction for which the SC_M state becomes stable at $T = 0$ vs. electron concentration. A comparison of two cases: $r = 1$ vs. $r = 2$ with and without the Hartree term. $h_c^{SC_M} = \sqrt{(\bar{\mu} - \epsilon_0)^2 + |\Delta|^2} - D \frac{r-1}{r+1}$, where $\Delta = \Delta(h = 0)$.

points in this plot.

Conclusions and prospects

The main aim of this thesis was to investigate the influence of the Zeeman magnetic field on superconducting properties and the BCS-BEC crossover in the systems with local fermion pairing. An extensive analysis of the superconducting properties of the spin polarized Hubbard model, with on-site attractive interaction $|U|$ (s-wave pairing symmetry), both for the square (2D) and the simple cubic (3D) lattices, has been performed. We have also studied the stability of the superfluid phases with the pure d-wave pairing symmetry in 2D, within the extended Hubbard model with nearest neighbor attractive interaction $|W|$ in the presence of a Zeeman magnetic field. In addition, we have analyzed in detail the phase diagrams and BCS-BEC crossover for the case of spin dependent hopping integrals ($t^\uparrow \neq t^\downarrow$) within the spin polarized attractive Hubbard model, both for the 2D and 3D.

The main results

- We have investigated the influence of the Zeeman magnetic field on the superfluid characteristics of the attractive Hubbard model, both in the weak coupling ($|U| < 2zt$, where z – the number of nearest neighbors) and in the strong coupling limit ($|U| \gg t$). The ground state phase diagrams have been obtained in the cases of a fixed chemical potential (μ) and a fixed electron concentration, within the Hartree-Fock approximation. This method includes the spin-dependent Hartree term and can be called a BCS-Stoner approach. If the number of particles is fixed and $n \neq 1$, one obtains two critical Zeeman magnetic fields, which limit the phase separation of the superconducting (SC) and the normal (NO) states. Superconductivity is destroyed by the pair breaking in a very weak coupling regime. On the other hand, in the intermediate or strong coupling regimes and $d = 2$, the transition from the unpolarized ($P = 0$) superconducting (SC_0) to the spin polarized normal state (NO-I/NO-II – partially ($P \neq 0$)/fully ($P = 1$) polarized NO states) goes in addition through phase separation. Therefore, for the 2D square lattice and spin independent hopping integrals ($t^\uparrow = t^\downarrow$), we find no stable homogeneous polarized superfluid state for the strong attraction and obtain that for two-component Fermi system on a 2D lattice with population imbalance, the phase separation is energetically favorable for a fixed particle concentration, even on the LP (BEC) side. The ground state phase diagrams in the $(h - |U|)$ and $(P - |U|)$ planes which have been constructed without the Hartree term in the $d = 2$ and $d = 3$ case for low electron concentration, agree

well with those obtained in the framework of the continuum model of a dilute gas of fermions in $d = 2$ and $d = 3$.

- We have also investigated the ground state BCS-BEC crossover diagrams in the presence of the Zeeman magnetic field in 3D, for the simple cubic lattice. As opposed to the $d = 2$ case, for strong attraction and in the dilute limit, a homogeneous magnetized superconducting phase (SC_M (or breached pairing (BP))) has been found in the phase diagrams. The SC_M phase is a specific superfluid state consisting of a coherent mixture of LP's (hard-core bosons) and excess spin-up fermions (Bose-Fermi mixture). This state can only have one Fermi surface (FS), hence can be called BP-1. Therefore, the occurrence of the BP-1 phase depends on the lattice structure, i.e. if $t^\uparrow = t^\downarrow$, SC_M is unstable for $d = 2$ but it can be realized for $d = 3$ lattices. We have also found a topological quantum phase transition (Lifshitz type) from the unpolarized superfluid phase to SC_M and tricritical points in the ground state phase diagrams. Analysis of the influence of the Hartree term on the BCS-BEC crossover diagrams in a magnetic field shows that the presence of such a term restricts the range of occurrence of the SC_M phase. The critical electron concentration (n_c) above which the SC_M state becomes unstable against the phase separation region has been estimated (with the Hartree term $n_c = 0.0145$, without the Hartree term $n_c = 0.154$). The Hartree term, usually promoting ferromagnetism in the Stoner model ($U > 0$), here ($U < 0$) strongly competes with superconductivity. We have analyzed the influence of different lattice geometries on the stability of the SC_M phase. The body-centered cubic (BCC) and face-centered cubic (FCC) lattices have been taken into account. We have also constructed the BCS-BEC crossover phase diagrams at $T = 0$ with the use of the semicircular density of states, which can be realized as the Bethe lattice. For the latter, in the case without the Hartree term, n_c is the lowest and equals $n_c \approx 0.054$, while for the BCC lattice $n_c \approx 0.199$ and the highest for the FCC lattice $n_c \approx 0.212$.
- The finite temperature phase diagrams of AHM with magnetic field have been obtained (both at fixed μ and fixed n) for 2D and 3D, including an analysis of the role of the Hartree term. In $d = 2$ ($h = 0$), the transition from the superconducting to the normal phase is of the Kosterlitz-Thouless (KT) type from the topologically ordered to the non-ordered state. Below the critical temperature T_c^{KT} , such topological ordering is manifested by the existence of tightly bound vortex-antivortex pairs, which are broken by thermal fluctuations when temperature increases above T_c^{KT} . The phase transition is characterized by a universal jump of the superfluid density (ρ_s) at T_c^{KT} . In this way, we have partly included the effects of phase fluctuations at $h \neq 0$ in our calculations and we have estimated the KT critical temperatures.
- The $(T - h)$ and $(T - P)$ phase diagrams have been obtained for the 2D and 3D Hubbard model with $U < 0$ in the Zeeman magnetic field, in the weak coupling regime. In the weak coupling regime and for fixed n , the following states have been found in 2D: the quasi-superconducting state qSC (below T_c^{KT}), region of

pairs without the phase coherence (bounded by the Hartree temperature), the spin polarized region with a gapless spectrum for the majority spin species, the PS region and the normal state. We have also found an energetically stable region with $\rho_s < 0$, both for the $d = 2$ and the $d = 3$ case, in the diagrams with the Hartree term. It suggests the existence of a stable FFLO state in $d = 3$, in the weak coupling limit. As far as the role of the Hartree term is concerned, we have found that the Hartree term leads to an increase in the Chandrasekhar-Clogston limit.

- We have investigated the influence of the Zeeman magnetic field on the superfluid characteristics of the extended Hubbard model with $W < 0$ and $t^\uparrow = t^\downarrow$. We have analyzed the pure d-wave pairing symmetry case. At $T = 0$, in the presence of the magnetic field, the ground state is the spatially homogeneous spin-polarized superfluid state, which has a gapless spectrum for the majority spin species and two FS (BP-2), for weak attraction, as opposed to the s-wave pairing symmetry case in 2D. We have also extended our analysis to finite temperatures in $d = 2$ by invoking the KT scenario. At finite temperatures, in the weak coupling regime and for fixed μ , the following states have been found in the 2D system: at $h = 0$ – the SC_0 phase; at $T = 0$, $h \neq 0$ – polarized superfluid state with a gapless spectrum for the majority spin species; at $T > 0$ – qSC($P \neq 0$) (below T_c^{KT}); region of pairs without coherence (below the Hartree temperature); the PS region and NO. PS terminates at the mean-field tricritical point, in $(T - P)$ phase diagrams.
- We have also studied in detail the mass imbalance case in the spin polarized attractive Hubbard model with spin dependent hopping integrals ($t^\uparrow \neq t^\downarrow$, $t^\uparrow/t^\downarrow \equiv r$). The BCS-LP crossover diagrams in the presence of the Zeeman magnetic field for $d = 2$ and $t^\uparrow \neq t^\downarrow$ exhibit a novel behavior. As opposed to the $t^\uparrow = t^\downarrow$ case, for strong attraction, SC_M occurs at $T = 0$. In general, the solutions of these type (Sarma-type with $\Delta(h)$) appear (for $r > 1$) when $h > (\frac{r-1}{r+1})\bar{\mu} + 2\Delta\frac{\sqrt{r}}{r+1}$ (on the BCS side) or when $h > \sqrt{(\bar{\mu} - \epsilon_0)^2 + |\Delta|^2} - D\frac{r-1}{r+1}$ (on the LP side). If $r \neq 1$, the SC_M phase (or BP-2 phase) is unstable in the weak coupling regime at $T = 0$, but BP-1 can be stable in the strong coupling LP limit, both for $d = 2$ and $d = 3$. The influence of the Hartree term on the SC_M state stability has been investigated in the hopping asymmetric case. If $t^\uparrow \neq t^\downarrow$ (see above) such a term restricts the SC_M state to lower densities. However, the mass imbalance can change this behavior even for $d = 2$ due to spin polarization stemming from the kinetic energy term.
- We have used the strong coupling expansion to map AAHM onto the pseudospin model and determine the critical value of particle concentration above which the SC phase can coexist with charge ordering (CO) at $h = 0$ and $r \neq 1$. SC/CO is a region of the phase separation with domain of SC and domain of CO (with $n = 1$).
- We have also extended the analysis of the crossover to finite temperatures in $d = 2$ by invoking the KT scenario. The KT transition temperatures are much lower than those determined in the BCS scheme. Moreover, spin polarization has a strong

destroying influence on the KT superfluid state at $r = 1$ and allows this phase in the weak coupling regime, in agreement with the results for the continuum case. In the strong coupling limit, T_c^{KT} does not depend on magnetic field (below h_{c1}), but it depends on mass imbalance and its upper bound takes the form: $k_B T_c^{KT} = 2\pi \frac{r}{(1+r)^2} \frac{t^2}{|U|} n(2-n)$ ($r > 0$). For $k_B T \ll |U|$, only unbroken LP's exist, which can form unpolarized qSC below T_c^{KT} or remain phase disordered. The system is equivalent to that of a hard-core Bose gas on a lattice. If $r \neq 1$ in $d = 2$, a spin polarized KT superfluid state can be stable even in the intermediate and strong coupling region.

- The BCS-BEC crossover has also been studied at finite temperatures in the spin polarized Hubbard model with $U < 0$ ($t^\uparrow = t^\downarrow$), for $d = 3$, going beyond the standard mean field approximation. The critical temperatures of the superconducting transition have been determined within the self-consistent T-matrix approach. We have performed a comparison of the results obtained from the $(GG_0)G_0$ and $(GG)G_0$ schemes, both for the 3D continuum model with contact attraction and the AHM at fixed low electron concentration. At finite temperatures, at $h = 0$, the following states have been found in the 3D system: the SC/SF phase (below T_c), the pseudogap region (above the temperature of the pair condensation T_c and below the temperature of the pair formation T_p) and normal state (above T_p). In the pseudogap region there are long-lived, incoherent pair excitations. The calculations within the $(GG_0)G_0$ and the $(GG)G_0$ schemes give in a dilute limit very similar results in the two extreme limits: BCS and BEC (LP). However, the critical temperature at the unitarity, determined within the $(GG_0)G_0$ scheme is higher than that obtained within the $(GG)G_0$ scheme, which is more consistent with the Quantum Monte Carlo results. We have shown that there are large differences between the results obtained within AHM and those obtained within the 3D continuum model in the BEC limit. The reason is that in the LP limit for AHM, the effective mass of the hard-core bosons increases with $|U|$ and this behavior is reflected in the results of the T-matrix calculations.
- We have also obtained the temperature BCS-BEC crossover phase diagrams for $d = 3$, at $h \neq 0$. The critical temperature of the superconducting transition has been determined within the $(GG_0)G_0$ T-matrix scheme in the presence of the Zeeman magnetic field. The interesting result is that a spin polarized superfluid state with a gapless region for the majority spin species can be stable in the strong coupling regime, as opposed to the 2D system for $r = 1$.

Prospects

Let us finish by pointing to possible directions of extending the work presented in this thesis:

- In this work, we have restricted the analysis to the s-wave and d-wave pairing only with $\vec{q} = 0$. We have also used the strong coupling expansion to determine the critical value of particle concentration above which the SC phase can coexist with charge ordering (CO) at $h = 0$ and $r \neq 1$. However, an investigation of the competition between the superconducting phases, CDW diagonal ordering and unconventional spin density wave (SDW) [179], in particular within the spin polarized Hubbard model, would be an interesting extension.
- We have not considered non-homogeneous states such as FFLO, which are possible in weak to intermediate attraction range, although much more susceptible to phase fluctuations at finite T in a 2D system [59, 180].
- In this thesis, we have shown that the BP-2 state is unstable in the ground state in the whole range of parameters, within one-band spin polarized AHM, both on $d = 2$ square lattice and $d = 3$ simple cubic lattice. Such a phase can be stable in d-wave pairing symmetry case. One can suppose that the Liu-Wilczek phase can be realized in s-wave case, in two-band model.
- Continuation of our study of the AAHM by strong coupling expansion method would be of interest. In particular, this concerns a description of the low density limit in terms of the (hard-core) bosons and fermions mixture.
- Investigation of the influence of a Zeeman magnetic field on the superfluid properties of the model of a mixture of mutually interacting bound electron pairs and itinerant fermions (boson-fermion model) [27, 181, 182, 183] is an important extension of the analysis presented in this work. The boson-fermion (BF) model can be applied to the high- T_c superconductivity and to description of the superfluidity in ultracold gases near the Feshbach resonance. Our preliminary study indicated that in a certain limit of parameters and for the dilute case the properties of the BF model in Zeeman field closely follow those of the spin polarized attractive Hubbard model [185].
- In this thesis, the impact of the Zeeman magnetic field on superfluidity has been investigated. Taking into consideration the orbital pair breaking mechanism [184] would also make an important extension of the analysis presented in this work.

Streszczenie w języku polskim pracy doktorskiej pt. *Wpływ pola magnetycznego na własności nadprzewodzące i przejście BCS-BEC w układach z lokalnym parowaniem fermionów*

Niekonwencjonalne nadprzewodnictwo z nietrywialnym mechanizmem parowania w układach silnie skorelowanych elektronów oraz spinowo spolaryzowana nadciekłość (w kontekście ultrazimnych atomowych gazów fermionowych) są obecnie intensywnie badane oraz szeroko dyskutowane w wiodącej literaturze światowej. Stanowią one jedne z najbardziej aktualnych kierunków badań w zakresie fizyki ciała stałego i ultrazimnych gazów kwantowych. Ogromny postęp technik eksperymentalnych w ultrazimnych gazach fermionowych z dostrajalnym oddziaływaniem przyciągającym (poprzez rezonanse Feshbacha) pozwala badać własności różnych egzotycznych stanów materii realizowanych w tych układach, w tym fizykę przejścia BCS-BEC. Realizowane są także eksperymenty, w których gazy fermionowe (lub bozonowe) umieszcza się na sieciach optycznych. Zarówno głębokość periodycznego potencjału pułapkującego jak i geometria mogą być w pełni kontrolowane. Dzięki temu można badać układy silnie skorelowane o różnej geometrii sieci. Gazy atomowe z dostrajalnym oddziaływaniem na sieciach optycznych umożliwiają nowe eksperymentalne realizacje modeli Hubbarda.

Własności układu fermionów w ekstremalnych granicach BCS oraz BEC są bardzo różne, zwłaszcza w stanie normalnym.

Reżim BCS charakteryzuje się tym, że:

- pary tworzą się i kondensują w tej samej temperaturze (T_c),
- parowanie zachodzi w przestrzeni odwrotnej, a w tworzeniu par Coopera uczestniczy tylko niewielka liczba elektronów o energiach bliskich energii Fermiego,
- oddziaływanie pomiędzy fermionami ($|U|$) jest słabe,

- rozmiar par w kondensacie jest znacznie większy niż średnia odległość pomiędzy nimi (stąd silne przekrywanie),
- szczelina energetyczna maleje monotonicznie ze wzrostem T i zanika w T_c ,
- temperatura krytyczna oraz termodynamika określone są wzbudzeniami jednocząstkowymi – rozerwanymi parami Coopera, z eksponencjalnie małą szczeliną,
- powyżej temperatury krytycznej stan normalny opisywany jest teorią cieczy Fermiego.

Z kolei granica BEC (lub par lokalnych) charakteryzuje się tym, że:

- tworzenie się par następuje w temperaturze T_p , znacznie wyższej od temperatury krytycznej, w której pojawia się dalekozasięgowa koherencja fazowa i przejście do stanu nadprzewodzącego,
- parowanie zachodzi w przestrzeni rzeczywistej i sparowane są wszystkie elektrony,
- oddziaływanie pomiędzy fermionami jest silne,
- pary są znacznie mniejsze niż średnia odległość pomiędzy nimi,
- energia wiązania par jest proporcjonalna do $|U|$, pary istnieją powyżej T_c , aż do T_p ,
- temperatura krytyczna oraz termodynamika są określone przez mody kolektywne,
- stan normalny jest opisywany cieczą Bosego silnie związanych i nieskorelowanych fazowo par (w zakresie $T_c < T < T_p$).

Dla pośrednich sprzężeń stan normalny może wykazywać pseudo-szczelinę (ang. *pseudo-gap*) i odchylenia od standardowej teorii Landaua cieczy Fermiego.

Efekty przejścia BCS-BEC są bardzo wyraźnie widoczne w zachowaniu potencjału chemicznego μ w temperaturze $T = 0$. W granicy słabego sprzężenia $\mu = E_F$ (E_F – energia Fermiego) i obowiązuje standardowa teoria BCS. Jednak przy odpowiednio silnym sprzężeniu potencjał chemiczny zaczyna maleć, aż w końcu spada do zera i staje się ujemny w granicy BEC. Punkt $\mu = 0$ można uznać za punkt przejścia BCS-BEC, ale ponieważ w jego okolicach zachowanie układu nie przypomina ani granicy BCS, ani BEC, więc możemy mówić o całym obszarze przejścia, a nie tylko jednym punkcie. Gdy $\mu > 0$, to w układzie występuje powierzchnia Fermiego i mamy do czynienia z kondensatem par Coopera, natomiast gdy μ staje się ujemne, powierzchnia Fermiego znika i mówimy o kondensacie bozonowym par.

W 2003 roku trzy grupy eksperymentalne zaobserwowały kondensację par atomów fermionowych w regionie przejścia BCS-BEC. Grupa M. Grimma z Uniwersytetu w Innsbrucku oraz W. Ketterlego z MIT zastosowała atomy ^6Li . Grupa D. S. Jin z Los Angeles schłodziła pułapowany gaz atomów ^{40}K do odpowiednio niskich temperatur rzędu

$5 \cdot 10^{-8} \text{K}$. Następnie, poprzez rezonans Feshbacha, kontrolowano oddziaływanie międzyatomowe. Na podstawie pomiarów, przy użyciu spektroskopii radiowej wykazano pojawienie się przerwy energetycznej, rok później ostatecznie potwierdzono istnienie fazy nadciekłej obecnością wirów.

Kolejne prace grup eksperymentalnych z MIT oraz z Uniwersytetu Rice w roku 2005 zapoczątkowały badania kwantowych gazów fermionowych (^6Li), o różnej liczbie fermionów ze „spinem w górę” (\uparrow) oraz „w dół” (\downarrow) (ang. *systems with population imbalance*). W trójwymiarowym układzie atomów profile gęstości obserwowane w eksperymentach pokazują niespolaryzowany nadciekły rdzeń w centrum pułapki harmoniczej oraz otaczający go gaz atomów w stanie normalnym. W tym układzie istnieje również rejon separacji fazowej pomiędzy niespolaryzowanym stanem nadciekłym i spolaryzowanym stanem normalnym.

Możliwość realizacji takich silnie skorelowanych układów fermionowych w laboratorium stanowi motywację zarówno dla grup teoretycznych jak i eksperymentalnych do prowadzenia badań nad fizyką przejścia BCS-BEC. Umożliwiło to także badanie wpływu Zeemanowskiego pola magnetycznego na własności nadciekłe.

Obecność pola magnetycznego Zeemana (h) powoduje rozszczepienie powierzchni Fermiego na dwie, odpowiadające cząstkom ze spinem w górę i w dół. Przejściu z fazy nadprzewodzącej do spinowo spolaryzowanego stanu normalnego towarzyszy skok parametru porządku i mamy wówczas do czynienia z przejściem pierwszego rodzaju, zachodzącym dla uniwersalnej wartości krytycznego pola magnetycznego $h_c = \Delta_0/\sqrt{2}$ (granica Clogstona-Chandrasekhara), gdzie Δ_0 jest przerwą energetyczną w $T = 0$ oraz $h = 0$. W granicy słabego sprzężenia, przy znacznej nierównowadze cząstek, mogą istnieć stany, charakteryzujące się nietrywialnym mechanizmem parowania. Jednym z nich jest stan FFLO (Fulde-Ferrell i Larkin-Ovchinnikov), w którym pary Coopera w kondensacie mają niezerowy pęd całkowity. Istnieją uzasadnione przypuszczenia, że stan FFLO może realizować się w nadprzewodnikach ciężkofermionowych. Jednak ze względu na niszczący wpływ efektu orbitalnego na nadprzewodnictwo, zaobserwowanie tego stanu jest niezwykle trudne w związkach nadprzewodzących. Istnieje jednak szansa na realizację eksperymentalną fazy FFLO w ultrazimnych gazach fermionowych z dostrajalnym oddziaływaniem przyciągającym.

Innym możliwym rodzajem parowania i koherencji fazowej jest jednorodny przestrzennie spinowo spolaryzowany stan nadciekły z parami o zerowym pędzie całkowitym (w literaturze określany jako *breached pairing* (BP) lub faza Sarmy), charakteryzujący się bezszczelinowym widmem dla większościowego kierunku spinu.

Głównym celem pracy doktorskiej było zbadanie wpływu pola magnetycznego Zeemana na własności nadprzewodzące i przejście BCS-BEC w układach z lokalnym parowaniem fermionów. Przeprowadzono kompletną analizę własności nadprzewodzących spinowo spolaryzowanego modelu Hubbarda z jednowęzłowym oddziaływaniem przyciągającym (symetria parowania typu s) w przypadku 2D (sieć kwadratowa) oraz 3D (sieć prosta kubiczna). Zbadano także wpływ symetrii parowania typu d na stabilność faz nadciekłych w 2D w rozszerzonym modelu Hubbarda z oddziaływaniem międzywęzłowym $|W|$, w obecności pola magnetycznego. Rozważyliśmy też szczegółowo nadprzewodnictwo w układach

ze spinowo zależnymi całkami przeskoku ($t^\uparrow \neq t^\downarrow$) w ramach spinowo spolaryzowanego modelu Hubbarda w 2D i 3D.

Główne rezultaty pracy są następujące.

- Zbadano wpływ pola magnetycznego na własności nadciekłe modelu Hubbarda z przyciąganiem na węźle, zarówno w granicy słabego ($|U| < 2zt$, gdzie z – liczba sąsiadów, t – całka przeskoku), jak i silnego sprzężenia ($|U| \gg t$). W ramach przybliżenia pola średniego (BCS-Stoner) otrzymano diagramy fazowe stanu podstawowego w przypadku ustalonego potencjału chemicznego oraz ustalonej liczby cząstek. W tym drugim przypadku, dla koncentracji elektronów (n) różnej od 1, otrzymano na diagramach fazowych dwa krytyczne pola Zeemana, które wyznaczają obszar separacji fazowej pomiędzy fazą nadprzewodzącą (SC) i stanem normalnym (NO). W granicy słabego sprzężenia, nadprzewodnictwo jest niszczone poprzez rozrywanie par. Z drugiej strony, w granicy silnego sprzężenia oraz w reżimie przejścia w 2D, przejście od niespolaryzowanego ($P = 0$) nadprzewodnictwa (SC_0) do spinowo spolaryzowanego stanu normalnego (NO-I/NO-II – częściowo ($P \neq 0$)/całkowicie ($P = 1$) spolaryzowane stany NO) następuje poprzez obszar separacji fazowej. Stąd, w przypadku 2D sieci kwadratowej i spinowo niezależnych całek przeskoku ($t^\uparrow = t^\downarrow$), nie istnieje stabilny energetycznie spolaryzowany stan nadciekły w przypadku silnego przyciągania, lecz korzystne energetycznie jest utworzenie obszaru separacji fazowej (przy ustalonej liczbie cząstek) nawet po stronie LP (BEC). Skonstruowane bez członu Hartree diagramy fazowe w płaszczyznach $(h - |U|)$ i $(P - |U|)$, przy niskich koncentracjach elektronów w 2D i 3D bardzo dobrze zgadzają się z rezultatami dla modelu rozrzedzonego gazu fermionów w continuum.
- Zbadane zostały także diagramy fazowe stanu podstawowego przejścia BCS-BEC w obecności pola magnetycznego Zeemana dla 3D sieci prostej kubicznej. W przeciwieństwie do przypadku 2D, dla silnego przyciągania i w granicy niskiej koncentracji elektronów, realizuje się jednorodny spinowo spolaryzowany stan nadciekły (SC_M (ang. *breached pairing* (BP))). Jest to specyficzny stan nadciekły będący koherentną mieszaniną silnie związanych par lokalnych (bozonów z twardym rdzeniem) oraz nadwyżką fermionów ze spinem w górę. Taki stan może posiadać tylko jedną powierzchnię Fermiego (FS), stąd nazywany jest BP-1. Występowanie stanu BP-1 zależy od wymiaru i geometrii sieci, tzn. dla $t^\uparrow = t^\downarrow$, faza SC_M jest niestabilna dla 2D, ale występuje w przypadku sieci 3D. W układzie zaobserwowano także topologiczne kwantowe przejście fazowe typu Lifshitz, od niespolaryzowanej fazy nadciekłej do stanu SC_M i wyznaczono na diagramach fazowych punkty trójkrytyczne. Przeanalizowano także wpływ członu Hartree na diagramy opisujące przejście BCS-BEC w polu magnetycznym i pokazano, że obecność tego członu bardzo ogranicza zakres występowania fazy SC_M . Oszacowano krytyczną koncentrację nośników, powyżej której spinowo spolaryzowany stan nadciekły staje się niestabilny względem separacji fazowej (z uwzględnieniem członu Hartree $n = 0.0145$, bez członu Hartree $n = 0.154$). Człon Hartree, który zwykle faworyzuje ferromagnetyzm w modelu Stonera ($U > 0$), w rozważanym przypadku ($U < 0$) silnie współzawodniczy z

nadprzewodnictwem. Przeanalizowano również wpływ różnych geometrii sieci na stabilność fazy SC_M (sieć przestrzennie centrowana (BCC) oraz powierzchniowo centrowana (FCC)). Skonstruowano również diagramy fazowe przejścia BCS-BEC w $T = 0$ używając półkolistej (ang. *semicircular*) gęstości stanów, która może być zrealizowana jako tzw. sieć Bethego. Dla tej ostatniej, w przypadku bez członu Hartree, n_c jest najniższa i wynosi $n_c \approx 0.054$, podczas gdy dla sieci BCC $n_c \approx 0.199$, a dla sieci FCC jest najwyższa $n_c \approx 0.212$.

- Otrzymano temperaturowe diagramy fazowe (zarówno przy ustalonym μ , jak i n) dla 2D i 3D, zarówno z członem Hartree, jak i bez niego. W $d = 2$ ($h = 0$) przejście ze stanu nadprzewodzącego do normalnego jest typu Kosterlitz-Thoulessa (KT) ze stanu topologicznie uporządkowanego do stanu nieuporządkowanego. Poniżej temperatury krytycznej takie uporządkowanie manifestuje się istnieniem ściśle związanych par wir-antywir, które są rozrywane przez fluktuacje termiczne, gdy temperatura wzrasta powyżej temperatury krytycznej. Przejście fazowe objawia się uniwersalnym skokiem gęstości składowej nadciekłej (ρ_s) w temperaturze T_c^{KT} . Uwzględniono częściowo w obliczeniach fluktuacje fazowe dla $h \neq 0$ i oszacowano temperaturę T_c^{KT} .
- Skonstruowano diagramy temperaturowe (w płaszczyźnie $(T - h)$ and $(T - P)$) dla modelu Hubbarda z $U < 0$ w polu magnetycznym w granicy słabego sprzężenia na sieci dwu- i trójwymiarowej. W zakresie słabego przyciągania, w 2D znaleziono następujące stany przy ustalonym n : stan kwazi-nadprzewodzący qSC (poniżej temperatury T_c^{KT}), obszar par bez koherencji fazowej (poniżej temperatury Hartree-Focka), spinowo spolaryzowany obszar z bezszczelinowym widmem dla cząstek ze spinem w górę, region separacji fazowej oraz stan normalny. Zaobserwowano również występowanie energetycznie stabilnego obszaru diagramów fazowych z formalnie ujemną gęstością składowej nadciekłej ($\rho_s < 0$) w 2D i 3D, na diagramach z członem Hartree. Sugeruje to istnienie stabilnego stanu FFLO w 3D w granicy słabego sprzężenia. Uwzględnienie członu Hartree prowadzi do podwyższenia granicy Chandrasekhara-Clogstona.
- Zbadano wpływ pola magnetycznego na własności nadprzewodzące rozszerzonego modelu Hubbarda z $W < 0$ i $t^\uparrow = t^\downarrow$. Rozważono przypadek czystej symetrii parowania typu d . W $T = 0$, w obecności pola magnetycznego, stanem podstawowym jest przestrzennie jednorodny, spinowo spolaryzowany stan nadciekły, który ma bezszczelinowe widmo dla większościowego kierunku spinu i dwie powierzchnie Fermiego (BP-2), dla przypadku słabego przyciągania, w przeciwieństwie do przypadku symetrii parowania typu s w 2D. Rozszerzono także analizę do skończonych temperatur w 2D, wykorzystując scenariusz KT. W skończonych temperaturach, w reżimie słabego sprzężenia, w 2D występują następujące fazy w przypadku ustalonego μ : dla $h = 0$ – faza SC_0 ; w $T = 0$, $h \neq 0$ – spolaryzowany stan nadciekły z bezszczelinowym widmem dla większościowego kierunku spinu; w $T > 0$ – qSC($P \neq 0$) (poniżej T_c^{KT}); region par bez koherencji fazowej (poniżej temperatury

Hartree); region PS i NO. PS kończy się w punkcie trójkrytycznym wyznaczonym w przybliżeniu pola średniego (na diagramach w płaszczyźnie $(T - P)$).

- Szczegółowo zbadano także przypadek nierównych mas w spinowo spolaryzowanym modelu Hubbarda z jednocentrowym przyciąganiem i spinowo zależnymi całkami przeskoku ($t^\uparrow \neq t^\downarrow$, $t^\uparrow/t^\downarrow \equiv r$). Diagramy fazowe przejścia BCS-LP w obecności pola magnetycznego Zeemana wykazują ciekawe zachowanie. W przeciwieństwie do przypadku $t^\uparrow = t^\downarrow$, faza SC_M pojawia się w zerowej temperaturze, w przypadku silnego przyciągania. W ogólności, ten rodzaj rozwiązań (typu Sarma, z $\Delta(h)$) pojawia się (dla $r > 1$) kiedy $h > (\frac{r-1}{r+1})\bar{\mu} + 2\Delta\frac{\sqrt{r}}{r+1}$ (po stronie BCS) lub kiedy $h > \sqrt{(\bar{\mu} - \epsilon_0)^2 + |\Delta|^2} - D\frac{r-1}{r+1}$ (po stronie LP). Jeżeli $r \neq 1$, faza SC_M (lub BP-2) jest niestabilna w reżimie słabego sprzężenia w $T = 0$, ale faza BP-1 może być stabilna w granicy silnego sprzężenia (LP), zarówno dla 2D, jak i dla 3D. Zbadano wpływ członu Hartree na stabilność fazy SC_M w przypadku nierównych mas. Jeśli $t^\uparrow \neq t^\downarrow$, wyraz Hartree ogranicza występowanie fazy SC_M do niższych koncentracji nośników. Jednakże, nierówne masy mogą zmienić to zachowanie nawet dla 2D, ze względu na polaryzację spinową wynikającą z wyrazu kinetycznego.
- Zbadano, że faza BP-2 jest niestabilna w $T = 0$ w całym zakresie parametrów, zarówno w 2D, jak i w 3D jednopasmowym spinowo-spolaryzowanym modelu Hubbarda z jednocentrowym przyciąganiem. Faza ta może być jednak stabilna w przypadku parowania d . Można także przypuszczać, że faza BP-2 (Liu-Wilczka) może być zrealizowana w modelu dwupasmowym.
- Metodą transformacji kanonicznej wyprowadzono hamiltonian efektywny do 2. rzędu w $t/|U|$ i określono krytyczne wartości koncentracji nośników, powyżej której faza SC może współistnieć z uporządkowaniem ładunkowym (CO) w $h = 0$ i $r \neq 1$. SC/CO jest regionem separacji fazowej z domeną SC i domeną CO (z $n = 1$).
- Rozszerzono analizę przejścia BCS-LP do skończonych temperatur w 2D, w ramach spinowo spolaryzowanego modelu Hubbarda, wykorzystując scenariusz KT. Temperatury przejścia KT są znacznie niższe od temperatur Hartree-Focka. Polaryzacja spinowa ma silny niszczący wpływ na stan nadciekły KT, który występuje w reżimie słabego sprzężenia, zgodnie z rezultatami otrzymanymi dla przypadku continuum. W granicy silnego sprzężenia temperatury krytyczne KT nie zależą od pola magnetycznego (poniżej h_{c1}), ale są zależne od nierównowagi mas nośników – górna granica na te temperatury krytyczne: $k_B T_c^{KT} = 2\pi \frac{r}{(1+r)^2} \frac{t^2}{|U|} n(2-n)$ ($r > 0$). Dla $k_B T \ll |U|$, istnieją jedynie nierozzerwane pary lokalne, które mogą stworzyć niespolaryzowaną fazę qSC poniżej T_c^{KT} lub pozostać bez koherencji fazowej. Układ taki jest równoważny układowi gazu bozonów z twardym rdzeniem na sieci. Jeśli $r \neq 1$ w 2D, spinowo spolaryzowany stan nadciekły KT może być stabilny nawet w zakresie średniego i silnego sprzężenia.
- Zbadano również przejście BCS-BEC w skończonych temperaturach w 3D, w ramach spinowo spolaryzowanego modelu Hubbarda z $U < 0$ ($t^\uparrow = t^\downarrow$), wykraczając poza

przybliżenie pola średniego. Temperatury krytyczne przejścia nadprzewodzącego zostały wyznaczone metodą wielociałowej samouzgodnej macierzy T. Porównano wyniki uzyskane w ramach schematów $(GG_0)G_0$ i $(GG)G_0$, zarówno dla 3D modelu ciągłego z kontaktowym oddziaływaniem przyciągającym, jak i dla przyciągającego modelu Hubbarda przy niskich koncentracjach nośników. W skończonych temperaturach i zerowym polu, występują następujące fazy w układzie 3D: faza SC/SF (poniżej T_c), region pseudo-szczeliny (powyżej temperatury kondensacji par T_c , ale poniżej temperatury formowania się par T_p) i stan normalny (powyżej T_p). W regionie pseudo-szczeliny istnieją długożyjące pary, będące wzbudzeniami niekoherentnymi fazowo. Obliczenia w ramach schematów $(GG_0)G_0$ i $(GG)G_0$ prowadzą do bardzo podobnych wyników w dwóch skrajnych granicach: BCS i BEC (LP). Jednakże, krytyczne temperatury w reżimie unitarnym, określone w ramach schematu $(GG_0)G_0$ są wyższe niż te otrzymane w ramach schematu $(GG)G_0$, który jest bardziej zgodny z wynikami symulacji kwantowego Monte Carlo. Pokazano, że w granicy BEC istnieją wyraźne różnice pomiędzy rezultatami otrzymanymi w ramach przyciągającego modelu Hubbarda i w ramach 3D modelu ciągłego. Wynika to z faktu, że w granicy par lokalnych modelu Hubbarda, masa efektywna bozonów z twardym rdzeniem rośnie wraz z rosnącym $|U|$ – ta cecha modelu znajduje odzwierciedlenie w wynikach obliczeń w ramach T-macierzy.

- Otrzymano także temperaturowe diagramy przejścia BCS-BEC dla $d = 3$, w niezerowym polu magnetycznym. Temperatury krytyczne przejścia nadprzewodzącego zostały określone w ramach schematu $(GG_0)G_0$. Spinowo spolaryzowany stan nadciężły z bezszczelinowym widmem dla większościowego kierunku spinu może być stabilny w reżimie silnego sprężenia, w przeciwieństwie do układu 2D dla $r = 1$.

Appendix A

Attraction-repulsion Symmetry

Let us consider a bipartite lattice¹. For $t^\uparrow = t^\downarrow$ one can transform the Hamiltonian (2.14) (with $W = 0$):

$$H = \sum_{ij\sigma} (t_{ij} - \mu\delta_{ij}) c_{i\sigma}^\dagger c_{j\sigma} + U \sum_i n_{i\uparrow} n_{i\downarrow} - h \sum_i (n_{i\uparrow} - n_{i\downarrow}), \quad (\text{A.1})$$

with an attractive interaction $|U|$ ($U = -|U|$) into the repulsive Hubbard model, by means of the *canonical transformation* (particle-hole type) [27, 186]:

$$c_{i\downarrow}^\dagger \rightarrow b_{i\downarrow} e^{i\vec{Q} \cdot \vec{R}_i}, \quad c_{i\downarrow} \rightarrow b_{i\downarrow}^\dagger e^{-i\vec{Q} \cdot \vec{R}_i}, \quad (\text{A.2})$$

$$c_{i\uparrow}^\dagger \rightarrow b_{i\uparrow}^\dagger, \quad c_{i\uparrow} \rightarrow b_{i\uparrow}. \quad (\text{A.3})$$

The vector \vec{Q} is chosen so that it satisfies $\exp(i\vec{Q} \cdot \vec{R}) = -1$ for a translation vector \vec{R} connecting two sublattice sites. After using the above transformation, the Hamiltonian (A.1) for half-filling $\frac{1}{N} \sum_{i\sigma} \langle n_{i\sigma} \rangle = 1$, where $\mu = -|U|/2$ is given by:

$$\begin{aligned} H &= \sum_{ij\sigma} t_{ij} b_{i\sigma}^\dagger b_{j\sigma} + |U| \sum_i n_{i\uparrow} n_{i\downarrow} - \sum_{i\sigma} \left(h + \frac{|U|}{2} \right) n_{i\sigma} \\ &+ \left(h + \frac{|U|}{2} \right) N, \end{aligned} \quad (\text{A.4})$$

where: $n_{i\sigma} = b_{i\sigma}^\dagger b_{i\sigma}$. The magnetization per site $M = N^{-1} \sum_i \langle n_{i\uparrow} - n_{i\downarrow} \rangle$ in the half-filled negative U Hubbard model is mapped into a site filling $\langle n_{i\uparrow} + n_{i\downarrow} \rangle - 1 = \langle n \rangle - 1$. The half-filling condition for (A.1) is transformed to: $M = 0$.

Thus, the half-filled attractive Hubbard model in a Zeeman field has been transformed into the doped repulsive Hubbard model in which $h + |U|/2$ now plays the role of the chemical potential. Under this transformation, one can also see that the FFLO state

¹a lattice which can be decomposed into two sublattices such that each site of one sublattice is surrounded only by sites of the other sublattice.

Table A.1: Particle-hole transformation mapping the attractive ($U < 0$) Hubbard model onto the repulsive ($U > 0$) Hubbard model.

Operators and quantities	$U < 0$	$U > 0$
creation operator \downarrow	$c_{i\downarrow}^\dagger$	$b_{i\downarrow} e^{i\vec{Q} \cdot \vec{R}_i}$
creation operator \uparrow	$c_{i\uparrow}^\dagger$	$b_{i\uparrow}^\dagger$
annihilation operator \downarrow	$c_{i\downarrow}$	$b_{i\downarrow}^\dagger e^{-i\vec{Q} \cdot \vec{R}_i}$
annihilation operator \uparrow	$c_{i\uparrow}$	$b_{i\uparrow}$
number of particle \downarrow	$c_{i\downarrow}^\dagger c_{i\downarrow}$	$1 - b_{i\downarrow}^\dagger b_{i\downarrow}$
number of particle \uparrow	$c_{i\uparrow}^\dagger c_{i\uparrow}$	$b_{i\uparrow}^\dagger b_{i\uparrow}$
chemical potential	μ	$\mu = h + U /2$
external magnetic field	h	$h = \mu + U /2$
superfluid phase (SF)	$\langle c_{i\downarrow} c_{i\uparrow} \rangle$	SDW _{xy} : $\langle b_{i\downarrow}^\dagger b_{i\uparrow} \rangle e^{-i\vec{Q} \cdot \vec{R}_i}$
CDW order	$\langle c_{i\uparrow}^\dagger c_{i\uparrow} + c_{i\downarrow}^\dagger c_{i\downarrow} \rangle e^{i\vec{Q} \cdot \vec{R}_i}$	SDW _z : $(1 - \langle b_{i\downarrow}^\dagger b_{i\downarrow} - b_{i\uparrow}^\dagger b_{i\uparrow} \rangle) e^{i\vec{Q} \cdot \vec{R}_i} \propto \langle S_i^z \rangle e^{i\vec{Q} \cdot \vec{R}_i}$

becomes the striped, charge density ordered and π -phase shifted antiferromagnetic state of the doped positive $|U|$ Hubbard model [187].

The various correspondences between quantities and operators in the attractive and the repulsive Hubbard model are shown in Tab. A.1.

Appendix B

Zero-temperature equations

In Section 2.4 the general forms of the mean-field equations for the case of the finite temperatures were presented.

Here, the zero-temperature equations are shown both for the superconducting and the normal state explicitly.

If we set $T = 0$, the form of the order parameter equations changes in the following way:

$$\Delta_{\vec{k}} = \frac{1}{N} \sum_{\vec{k}'} V_{\vec{k}\vec{k}'}^s \frac{\Delta_{\vec{k}'}}{4\omega_{\vec{k}'}} \left(\text{sgn}(E_{\vec{k}'\uparrow}) + \text{sgn}(E_{\vec{k}'\downarrow}) \right). \quad (\text{B.1})$$

The particle number equation is:

$$n = 1 - \frac{1}{2N} \sum_{\vec{k}} \frac{-(t^\uparrow + t^\downarrow)\Theta_{\vec{k}} - \bar{\mu} - p \frac{\gamma_{\vec{k}}}{\gamma_0} W}{\omega_{\vec{k}}} \left(\text{sgn}(E_{\vec{k}\uparrow}) + \text{sgn}(E_{\vec{k}\downarrow}) \right). \quad (\text{B.2})$$

The equation for the magnetization takes the form:

$$M = \frac{1}{2N} \sum_{\vec{k}} \left(\text{sgn}(E_{\vec{k}\downarrow}) - \text{sgn}(E_{\vec{k}\uparrow}) \right). \quad (\text{B.3})$$

The Fock parameter equation:

$$p = -\frac{1}{N} \sum_{\vec{k}} \frac{1}{2} \gamma_{\vec{k}} \frac{-(t^\uparrow + t^\downarrow)\Theta_{\vec{k}} - \bar{\mu} - p \frac{\gamma_{\vec{k}}}{\gamma_0} W}{\omega_{\vec{k}}} \left(\text{sgn}(E_{\vec{k}\uparrow}) + \text{sgn}(E_{\vec{k}\downarrow}) \right). \quad (\text{B.4})$$

Finally, one obtains the grand canonical potential:

$$\begin{aligned} \frac{\Omega^{SC}}{N} &= \frac{1}{4} U n(2 - n) - \mu + \frac{1}{4} U M^2 + W \gamma_0 n - \frac{1}{2} W \gamma_0 n^2 \\ &- W p_\uparrow^2 / 2\gamma_0 - W p_\downarrow^2 / 2\gamma_0 + \frac{1}{N} \sum_{\vec{k}} \frac{|\Delta_{\vec{k}}|^2}{4\omega_{\vec{k}}} \left(\text{sgn}(E_{\vec{k}\uparrow}) + \text{sgn}(E_{\vec{k}\downarrow}) \right) \\ &- \frac{1}{2N} \sum_{\vec{k}\sigma} E_{\vec{k}\sigma} \text{sgn}(E_{\vec{k}\sigma}). \end{aligned} \quad (\text{B.5})$$

The corresponding equations for the normal phase ($\Delta = 0$) have the following forms:

$$n = 1 - \frac{1}{2N} \sum_{\vec{k}} \left(\text{sgn}(E_{\vec{k}\uparrow}^{NO}) + \text{sgn}(E_{\vec{k}\downarrow}^{NO}) \right), \quad (\text{B.6})$$

$$M = \frac{1}{2N} \sum_{\vec{k}} \left(\text{sgn}(E_{\vec{k}\downarrow}^{NO}) - \text{sgn}(E_{\vec{k}\uparrow}^{NO}) \right), \quad (\text{B.7})$$

$$p = -\frac{1}{N} \sum_{\vec{k}} \frac{1}{2} \gamma_{\vec{k}} \left(\text{sgn}(E_{\vec{k}\uparrow}^{NO}) + \text{sgn}(E_{\vec{k}\downarrow}^{NO}) \right), \quad (\text{B.8})$$

$$\begin{aligned} \frac{\Omega^{NO}}{N} &= \frac{1}{4} U n (2 - n) - \mu + \frac{1}{4} U M^2 + W \gamma_0 n - \frac{1}{2} W \gamma_0 n^2 \\ &- p_{\uparrow}^2 / 2 \gamma_0 - W p_{\downarrow}^2 / 2 \gamma_0 - \frac{1}{N} \sum_{\vec{k}} E_{\vec{k}}^{NO} \text{sgn}(E_{\vec{k}\sigma}^{NO}), \end{aligned} \quad (\text{B.9})$$

where: $E_{\vec{k}\downarrow,\uparrow}^{NO} = \pm(-t^{\downarrow} + t^{\uparrow})\Theta_{\vec{k}} \pm \frac{UM}{2} \pm \frac{1}{2}W(p_{\uparrow} - p_{\downarrow})\frac{\gamma_{\vec{k}}}{\gamma_0} \pm h + \omega_{\vec{k}}^{NO}$
and $\omega_{\vec{k}}^{NO} = (-t^{\uparrow} - t^{\downarrow})\Theta_{\vec{k}} - \bar{\mu} - p_{\gamma_0} \frac{\gamma_{\vec{k}}}{2} W$.

Appendix C

The analysis of the quasiparticle excitations spectrum: gapless region

In this Appendix, we determine, by analysis of the quasiparticle excitations spectrum, the critical magnetic field h_c above which the spin-polarized superfluidity arises at $T = 0$. There has been much work on the possibility of the existence of the spatially homogeneous spin-polarized superfluidity (breached pair (BP)) with one or two Fermi surfaces (BP-I or BP-II, respectively) and a gapless spectrum for the majority spin species. These kinds of pairing are very interesting not only in the context of superconductivity, but also in that of trapped unbalanced ultracold Fermi atomic gases and color superconductivity in quantum chromodynamics.

In our analysis, we take into account the isotropic pairing with the order parameter: $\Delta = -\frac{U}{N} \sum_i \langle c_{i\downarrow} c_{i\uparrow} \rangle = -\frac{U}{N} \sum_{\vec{k}} \langle c_{-\vec{k}\downarrow} c_{\vec{k}\uparrow} \rangle$. Therefore, the Hamiltonian (2.14) takes the form:

$$H = \sum_{ij\sigma} (t_{ij}^\sigma - \mu \delta_{ij}) c_{i\sigma}^\dagger c_{j\sigma} + U \sum_i n_{i\uparrow} n_{i\downarrow} - h \sum_i (n_{i\uparrow} - n_{i\downarrow}). \quad (\text{C.1})$$

Transforming the Hamiltonian (C.1) to the reciprocal space and applying the broken symmetry Hartree approximation, one can obtain two physical branches of quasiparticle excitations:

$$E_{\vec{k}\downarrow,\uparrow} = \pm(-t^\downarrow + t^\uparrow)\Theta_{\vec{k}} \pm \frac{UM}{2} \pm h + \omega_{\vec{k}}, \quad (\text{C.2})$$

where: $\omega_{\vec{k}} = \sqrt{((-t^\uparrow - t^\downarrow)\Theta_{\vec{k}} - \bar{\mu})^2 + |\Delta|^2}$, $\Theta_{\vec{k}} = \sum_{l=1}^d \cos(k_l a_l)$ (here $d = 2, 3$ for two- and three-dimensional lattices, respectively); a_l is the lattice constant in the l -th direction (we set $a_l = 1$ in further considerations).

Let us assume $t^\uparrow \geq t^\downarrow$ and $h > 0$. For clarity, let us introduce the following notation: $\bar{h} \equiv h + \frac{UM}{2}$, $t_\pm \equiv t^\uparrow \pm t^\downarrow$.

Therefore, the quasiparticle energies (C.2) can be rewritten as:

$$E_{\vec{k}\downarrow,\uparrow} = \pm t_- \Theta_{\vec{k}} \pm \bar{h} + \sqrt{(-t_+ \Theta_{\vec{k}} - \bar{\mu})^2 + |\Delta|^2}. \quad (\text{C.3})$$

The critical value of $\bar{h} = \bar{h}_c$ is determined from the condition that $E_{\vec{k}\uparrow}$ branch has one zero, i.e. $E_{\vec{k}\uparrow} = 0$. Then, we have the quadratic equation:

$$(t_-^2 - t_+^2)\Theta_k^2 + 2(t_- \bar{h} - t_+ \bar{\mu})\Theta_k + \bar{h}^2 - \bar{\mu}^2 + |\Delta|^2, \quad (\text{C.4})$$

which can be solved with respect to Θ_k . In this way:

$$\Theta_k^\pm = \frac{t_- \bar{h} - t_+ \bar{\mu} \pm \sqrt{(t_+ \bar{h} - t_- \bar{\mu})^2 - 4t^\uparrow t^\downarrow |\Delta|^2}}{4t^\uparrow t^\downarrow}. \quad (\text{C.5})$$

Therefore, above \bar{h}_c , the $E_{\vec{k}\uparrow}$ branch crosses the zero energy axis at two points. At the critical value of $\bar{h} = \bar{h}_c$, the two Fermi surfaces are equal $\Theta_k^+ = \Theta_k^- \equiv \Theta_c$:

$$\Theta_c = \frac{\bar{h}_c t_- - t_+ \bar{\mu}}{4t^\uparrow t^\downarrow}. \quad (\text{C.6})$$

In the weak coupling limit, the homogeneous magnetized superconducting phase (SC_M) (Sarma-type solution with $\Delta(h)$) occurs at the critical value of $\bar{h} = \bar{h}_c$:

$$\bar{h}_c = \left(\frac{r-1}{r+1}\right)\bar{\mu} + 2\Delta \frac{\sqrt{r}}{r+1}, \quad (\text{C.7})$$

where: $r \equiv t^\uparrow/t^\downarrow$. If $t^\uparrow = t^\downarrow$ ($r = 1$), then $\bar{h}_c = \Delta$, on the BCS side.

On the other hand, in the strong coupling limit (for $\vec{k} = 0$), the critical value of \bar{h} is:

$$\bar{h}_c = \sqrt{(\bar{\mu} - \epsilon_0)^2 + |\Delta|^2} - D \frac{r-1}{r+1}, \quad (\text{C.8})$$

where: $D = zt$, $z = 2d$ is the coordination number. If $t^\uparrow = t^\downarrow$ ($r = 1$), then $\sqrt{(\bar{\mu} - \epsilon_0)^2 + |\Delta|^2}$, on the BEC side.

It is worth mentioning that the transition from the non-polarized superfluid state (SC_0) to the polarized superfluid phase is a topological quantum phase transition (Lifshitz type [188]). As shown above, the quasiparticle excitation spectrum can change from gapped to gapless one. There is a change in the electronic structure. Therefore, we can identify the topological quantum phase transition as the appearance of zero energies in the energy excitation spectrum. Lifshitz type transitions take place in metals and alloys [189]. The topological phase transition also appears in non-s-wave superfluids [79, 80, 190, 191, 192, 193]. The $\text{SC}_0 \rightarrow \text{SC}_M$ transition is in some sense unusual, because it concerns the s-wave pairing symmetry case and occurs without a change in the order parameter symmetry [80].

For the BCS state, the momentum distribution in the Brillouin zone is given by [115]:

$$n_{\vec{k}} = |\nu_{\vec{k}}|^2, \quad (\text{C.9})$$

where $|\nu_{\vec{k}}|^2$ (2.46) is a measure of the probability that the $(\vec{k} \uparrow, -\vec{k} \downarrow)$ state is occupied.

In turn, for the SC_M state:

$$\begin{cases} \text{if } \Theta_{\vec{k}} \in [\Theta_{\vec{k}}^-, \Theta_{\vec{k}}^+] : & n_{\vec{k}\uparrow} = 1, \ n_{\vec{k}\downarrow} = 0 \\ \text{otherwise :} & n_{\vec{k}\uparrow} = n_{\vec{k}\downarrow} = |\nu_{\vec{k}}|^2. \end{cases} \quad (C.10)$$

The numbers of particles with spin up and spin down are equal in the BCS state. However, in the presence of the Zeeman magnetic field, in the SC_M phase, they differ. Therefore, this quantum phase transition is associated with the change in the Fermi sea topology and it appears at the point in which the Fermi sea is divided into two regions.

Appendix D

T-matrix approach. Functional derivatives technique

D.1 Functional derivatives technique

In this appendix a detail derivation of the T-matrix equations for the Hubbard model is presented using the functional derivative technique. In addition, we also obtain the mean-field equations derived in Chapter 4. We consider the Hubbard Hamiltonian:

$$H = H_0 + H_1, \quad (D.1)$$

$$H_0 = \sum_{i,j,\sigma} \bar{t}_{ij} c_{i\sigma}^\dagger c_{j\sigma}, \quad \bar{t}_{ij} = t_{ij} - \mu \delta_{ij} \quad (D.2)$$

$$H_1 = U \sum_i n_{i\uparrow} n_{i\downarrow}, \quad (D.3)$$

Introducing the Nambu representation: $\hat{\Psi}_i^\dagger = \begin{pmatrix} c_{i\uparrow}^\dagger & c_{i\downarrow} \end{pmatrix}$, $\hat{\Psi}_i = \begin{pmatrix} c_{i\uparrow} \\ c_{i\downarrow}^\dagger \end{pmatrix}$, we have: $n_{i\uparrow} = \frac{1}{2} \hat{\Psi}_i^\dagger (\tau_3 + \tau_0) \hat{\Psi}_i$, $n_{i\downarrow} = \frac{1}{2} \hat{\Psi}_i^\dagger (\tau_3 - \tau_0) \hat{\Psi}_i + 1$, $c_{i\uparrow}^\dagger c_{i\downarrow}^\dagger = \hat{\Psi}_i^\dagger \tau_+ \hat{\Psi}_i$, $c_{i\downarrow} c_{i\uparrow} = \hat{\Psi}_i^\dagger \tau_- \hat{\Psi}_i$, τ_α are the Pauli matrices ($\tau_\pm = \frac{1}{2}(\tau_1 \pm i\tau_2)$, τ_0 is the identity matrix).

The Hubbard Hamiltonian $H = H_0 + H_1$ can be rewritten in the following way:

$$H_0 = \sum_{i,j} t_{ij} \hat{\Psi}_i^\dagger \tau_3 \hat{\Psi}_j - \mu N, \quad (D.4)$$

$$H_1 = U \sum_i \left(\hat{\Psi}_i^\dagger \tau_+ \hat{\Psi}_i \right) \left(\hat{\Psi}_i^\dagger \tau_- \hat{\Psi}_i \right), \quad (D.5)$$

where N is the total number of sites.

We define the thermal (Matsubara) Green functions using the Nambu field representation:

$$\begin{aligned}\hat{\mathcal{G}}_{ij}(\tau, \tau') = -\langle T_\tau \hat{\Psi}_i(\tau) \hat{\Psi}_j^\dagger(\tau') \rangle &= \begin{pmatrix} -\langle T_\tau c_{i\uparrow}(\tau) c_{j\uparrow}^\dagger(\tau') \rangle & -\langle T_\tau c_{i\uparrow}(\tau) c_{j\downarrow}(\tau') \rangle \\ -\langle T_\tau c_{i\downarrow}^\dagger(\tau) c_{j\uparrow}^\dagger(\tau') \rangle & -\langle T_\tau c_{i\downarrow}^\dagger(\tau) c_{j\downarrow}(\tau') \rangle \end{pmatrix} = \\ &= \begin{pmatrix} G_{ij}^\uparrow(\tau, \tau') & F_{ij}(\tau, \tau') \\ F_{ij}^\dagger(\tau, \tau') & -G_{ji}^\downarrow(\tau', \tau) \end{pmatrix}, \end{aligned} \quad (\text{D.6})$$

The time dependence of the operators is given by $\hat{\Psi}_i(\tau) = e^{\tau H} \hat{\Psi}_i e^{-\tau H}$, $\hat{\Psi}_i^\dagger(\tau) = e^{\tau H} \hat{\Psi}_i^\dagger e^{-\tau H}$. The thermal average is given by: $\langle \cdots \rangle = \text{Tr}[\cdots \exp(-\beta H)] / \text{Tr}[\exp(-\beta H)]$.

In order to derive the equations for the Green functions, we use the functional derivative technique [194, 195, 196, 197]. We consider the Green functions written in the presence of the source fields, as given below:

$$\hat{G}_{ij}(\tau, \tau') = -\langle T_\tau \hat{\Psi}_i(\tau) \hat{\Psi}_j^\dagger(\tau') \rangle_S = -\frac{\langle T_\tau S \hat{\Psi}_i(\tau) \hat{\Psi}_j^\dagger(\tau') \rangle}{\langle T_\tau S \rangle} \equiv \langle \langle \hat{\Psi}_i(\tau); \hat{\Psi}_j^\dagger \rangle \rangle, \quad (\text{D.7})$$

where T_τ is the chronological ordering operator and the generating functional S is given by:

$$\begin{aligned}S &= \exp \left(- \int_0^\beta d\tau \sum_i [\xi_i(\tau) \hat{\Psi}_i^\dagger(\tau) \tau_3 \hat{\Psi}_i(\tau) + h_i(\tau) \hat{\Psi}_i^\dagger(\tau) \tau_0 \hat{\Psi}_i(\tau) + \right. \\ &\quad \left. + \eta_i(\tau) \hat{\Psi}_i^\dagger(\tau) \tau_- \hat{\Psi}_i(\tau) + \eta_i^*(\tau) \hat{\Psi}_i^\dagger(\tau) \tau_+ \hat{\Psi}_i(\tau)] \right) = \\ &= \exp \left(- \int d1 [\xi(1) \hat{\Psi}^\dagger(1) \tau_3 \hat{\Psi}(1) + h(1) \hat{\Psi}^\dagger(1) \tau_0 \hat{\Psi}(1) + \right. \\ &\quad \left. + \eta(1) \hat{\Psi}^\dagger(1) \tau_- \hat{\Psi}(1) + \eta^*(1) \hat{\Psi}^\dagger(1) \tau_+ \hat{\Psi}(1)] \right), \end{aligned} \quad (\text{D.8})$$

where we have introduced convenient shorthand notation: $1 \equiv (\vec{R}_i, \tau)$, $\int d1 \equiv \int_0^\beta d\tau \sum_i$. This functional of the external sources includes: $\xi_i(\tau)$ – charge field (that couples to the number of particles $n_{i\uparrow} + n_{i\downarrow}$), $h_i(\tau)$ – magnetic field (couples to the magnetization $n_{i\uparrow} - n_{i\downarrow}$), and $\eta_i(\tau), \eta_i^*(\tau)$ are the pairing fields (couple to products of operators $c_{i\downarrow} c_{i\uparrow}$ and $c_{i\uparrow}^\dagger c_{i\downarrow}^\dagger$, respectively). Explicitly, we have:

$$\hat{G}(1, 2) = \begin{pmatrix} G^\uparrow(1, 2) & F(1, 2) \\ F^\dagger(1, 2) & -G^\downarrow(2, 1) \end{pmatrix}. \quad (\text{D.9})$$

The equation of motion for $\hat{G}(1, 2)$ is the Heisenberg equation:

$$\frac{\partial \hat{\Psi}(1)}{\partial \tau} = [H + H', \hat{\Psi}(1)], \quad (\text{D.10})$$

where H' describes the source term. Explicitly:

$$\begin{aligned} & \sum_m \left\{ \left[-\frac{\partial}{\partial \tau} - h_m(\tau) \right] \tau_0 \delta_{im} - [\bar{t}_{im} + \xi_m(\tau) \delta_{im}] \tau_3 - [\eta_m(\tau) \tau_- + \eta_m^*(\tau) \tau_+] \delta_{im} \right\} \hat{G}_{mj}(\tau, \tau') \\ & = \tau_0 \delta_{ij} \delta(\tau - \tau') + U \langle \langle \tau_+ \hat{\Psi}(1) \left(\hat{\Psi}^\dagger(1) \tau_- \hat{\Psi}(1) \right); \hat{\Psi}^\dagger(2) \rangle \rangle + U \langle \langle \left(\hat{\Psi}^\dagger(1) \tau_+ \hat{\Psi}(1) \right) \tau_- \hat{\Psi}(1); \hat{\Psi}^\dagger(2) \rangle \rangle, \end{aligned} \quad (\text{D.11})$$

where we have used:

$$\left[\hat{\Psi}(1), \left(\hat{\Psi}^\dagger(1) \tau_\pm \hat{\Psi}(1) \right) \right] = \tau_\pm \hat{\Psi}(1) \quad (\text{D.12})$$

The first $\langle \langle \dots \rangle \rangle$ term on the RHS of Eq. (D.11) can be rewritten by means of functional derivatives as:

$$\langle \langle \tau_+ \hat{\Psi}(1) \left(\hat{\Psi}^\dagger(1) \tau_- \hat{\Psi}(1) \right); \hat{\Psi}^\dagger(2) \rangle \rangle = -\tau_+ \frac{\delta \hat{G}(1, 2)}{\delta \eta(1)} + \tau_+ \langle \hat{\Psi}^\dagger(1) \tau_- \hat{\Psi}(1) \rangle_S \hat{G}(1, 2), \quad (\text{D.13})$$

and the analogous formula holds for the second $\langle \langle \dots \rangle \rangle$ term of Eq.(D.11). The RHS of (D.11) is the given by

$$U \left[\tau_+ \langle \hat{\Psi}^\dagger(1) \tau_- \hat{\Psi}(1) \rangle_S + \tau_- \langle \hat{\Psi}^\dagger(1) \tau_+ \hat{\Psi}(1) \rangle_S \right] \hat{G}(1, 2) - U \left[\tau_+ \frac{\delta \hat{G}(1, 2)}{\delta \eta(1)} + \tau_- \frac{\delta \hat{G}(1, 2)}{\eta^*(1)} \right]. \quad (\text{D.14})$$

Defining the gap function as:

$$\Delta^*(1) = U \langle c_{i\uparrow}^\dagger(\tau) c_{i\downarrow}^\dagger(\tau) \rangle_S, \quad (\text{D.15})$$

the equation of motion takes the form:

$$\begin{aligned} & \sum_m \left\{ \left[-\frac{\partial}{\partial \tau} - h_m(\tau) \right] \tau_0 \delta_{im} - [\bar{t}_{im} + \xi_m(\tau) \delta_{im}] \tau_3 - [\eta_m(\tau) \tau_- + \eta_m^*(\tau) \tau_+] \delta_{im} \right\} \hat{G}_{mj}(\tau, \tau') = \\ & \tau_0 \delta_{ij} \delta(\tau - \tau') + (\tau_+ \Delta(1) + \tau_- \Delta^*(1)) \hat{G}(1, 2) - U \left[\tau_+ \frac{\delta \hat{G}(1, 2)}{\delta \eta(1)} + \tau_- \frac{\delta \hat{G}(1, 2)}{\eta^*(1)} \right]. \end{aligned} \quad (\text{D.16})$$

Let us now introduce the Dyson equation in Nambu space:

$$\hat{G}(1, 2) = \hat{G}_0(1, 2) + \int d\bar{3} \int d\bar{4} \hat{G}_0(1, \bar{3}) \hat{\Sigma}(\bar{3}, \bar{4}) \hat{G}(\bar{4}, 2). \quad (\text{D.17})$$

The inverse Green function is defined by:

$$\int d\bar{3} \hat{G}(1, \bar{3}) \hat{G}^{-1}(\bar{3}, 2) = \tau_0 \delta(1 - 2). \quad (\text{D.18})$$

In particular, the zeroth order Green function is explicitly given by:

$$[\hat{G}_{ij}^0(\tau, \tau')]^{-1} = \left\{ \left[-\frac{\partial}{\partial \tau} - h_i(\tau) \right] \tau_0 \delta_{ij} - [\bar{t}_{ij} + \xi_i(\tau) \delta_{ij}] \tau_3 \right. \\ \left. - [\eta_i(\tau) \tau_- + \eta_i^*(\tau) \tau_+] \delta_{ij} \right\} \delta(\tau - \tau'). \quad (\text{D.19})$$

The Dyson equation can be written as:

$$\hat{G}^{-1}(1, 2) = \hat{G}_0^{-1}(1, 2) - \hat{\Sigma}(1, 2). \quad (\text{D.20})$$

The self-energy is given by:

$$\hat{\Sigma}(1, 3) = [\tau_+ \Delta(1) + \tau_- \Delta^*(1)] \delta(1 - 3) \\ - U \int d\bar{2} \left[\tau_+ \frac{\delta \hat{G}(1, \bar{2})}{\delta \eta(1)} \hat{G}^{-1}(\bar{2}, 3) + \tau_- \frac{\delta \hat{G}(1, \bar{2})}{\delta \eta^*(1)} \hat{G}^{-1}(\bar{2}, 3) \right]. \quad (\text{D.21})$$

Using now the identity:

$$\delta \hat{G} = -\hat{G} \delta \hat{G}^{-1} \hat{G} = -\hat{G} \delta \hat{G}_0^{-1} \hat{G} + \hat{G} \delta \hat{\Sigma} \hat{G}, \quad (\text{D.22})$$

which follows from the definition of the inverse Green function (D.18), we can rewrite the functional derivatives in terms of $\hat{\Sigma}$. We get

$$\frac{\delta \hat{G}(1, 2)}{\delta \eta(1^+)} = \hat{G}(1, 1^+) \tau_- \hat{G}(1, 2) + \int d\bar{3} \int d\bar{4} \hat{G}(1, \bar{3}) \frac{\delta \hat{\Sigma}(\bar{3}, \bar{4})}{\delta \eta(1^+)} \hat{G}(\bar{4}, 2). \quad (\text{D.23})$$

Substituting (D.23) and using $\langle n_\sigma(1) \rangle_S = -\langle T_\tau c(1) c^\dagger(1^+) \rangle_S$, we obtain the equation for the matrix self-energy in the form:

$$\hat{\Sigma}(1, 2) = \begin{pmatrix} U \langle n_{\downarrow}(1) \rangle_S & \Delta(1) \\ \Delta^*(1) & -U \langle n_{\uparrow}(1) \rangle_S \end{pmatrix} \delta(1 - 2) \\ - U \int d\bar{3} \left[\tau_+ \hat{G}(1, \bar{3}) \frac{\delta}{\delta \eta(1)} + \tau_- \hat{G}(1, \bar{3}) \frac{\delta}{\delta \eta^*(1)} \right] \hat{\Sigma}(\bar{3}, 2). \quad (\text{D.24})$$

Or explicitly restoring space and time indices:

$$\hat{\Sigma}_{ij}(\tau, \tau') = \begin{pmatrix} U \langle n_{i\downarrow}(\tau) \rangle_S & \Delta_i(\tau) \\ \Delta_i^*(\tau) & -U \langle n_{i\uparrow}(\tau) \rangle_S \end{pmatrix} \delta_{ij} \delta(\tau - \tau') \\ - U \sum_l \int_0^\beta d\bar{\tau} \left[\tau_+ \hat{G}_{il}(\tau, \bar{\tau}) \frac{\delta}{\delta \eta_i(\tau)} + \tau_- \hat{G}_{il}(1, \bar{\tau}) \frac{\delta}{\delta \eta_i^*(\tau)} \right] \hat{\Sigma}_{lj}(\bar{\tau}, \tau'). \quad (\text{D.25})$$

The compact form of the above equation (D.24, D.25) gives an exact integro-differential equation for determining the self-energy $\hat{\Sigma}_{ij}(\tau, \tau')$. This equation can be solved in an

iterative way. The zeroth order self-energy, in which we set $\delta\hat{\Sigma} = 0$ and the source fields to zero, gives the Hartree-Fock-Bogoliubov approximation and leads to the BCS theory in the Nambu formulation.

Let us consider the case of non-zero Zeeman magnetic field, setting: $h_i(\tau) = -h$, $\xi_i(\tau) \rightarrow 0$, $\eta_i(\tau) \rightarrow 0$, $\eta_i^*(\tau) \rightarrow 0$ and $\delta\hat{\Sigma} = 0$. Using (D.19) and (D.24) in the Dyson equation (D.20), the inverse of the full Green function is given by:

$$[\hat{G}_{ij}(\tau, \tau')]^{-1} = \begin{pmatrix} [-\frac{\partial}{\partial\tau} + h - U\langle n_{i\downarrow} \rangle] \delta_{ij} - \bar{t}_{ij} & -\Delta_i \delta_{ij} \\ -\Delta_i^* \delta_{ij} & [-\frac{\partial}{\partial\tau} + h - U\langle n_{i\uparrow} \rangle] \delta_{ij} + \hat{t}_{ij} \end{pmatrix} \delta(\tau - \tau'). \quad (\text{D.26})$$

Assuming translational invariance, one can introduce the space-time Fourier transform:

$$\hat{G}_{ij}(\tau, \tau') = \frac{1}{\beta N} \sum_{\vec{k}, \omega_n} e^{i\vec{k} \cdot (\vec{R}_i - \vec{R}_j) - i\omega_n(\tau - \tau')} \hat{G}(\vec{k}, i\omega_n). \quad (\text{D.27})$$

Considering only homogeneous superconducting ordering and setting $\langle n_{i\sigma} \rangle = n_\sigma$, $\Delta_i = \Delta$ one gets for the Green function:

$$\begin{aligned} \hat{G}(\vec{k}, i\omega_n) &= \begin{pmatrix} G^\uparrow(\vec{k}, i\omega_n) & F(\vec{k}, i\omega_n) \\ F^\dagger(\vec{k}, i\omega_n) & -G^\downarrow(-\vec{k}, -i\omega_n) \end{pmatrix} = \\ &= \begin{pmatrix} i\omega_n + h - \epsilon_{\vec{k}} + \mu - Un_\downarrow & -\Delta \\ -\Delta^* & i\omega_n + h + \epsilon_{\vec{k}} - \mu + Un_\uparrow \end{pmatrix}^{-1}. \end{aligned} \quad (\text{D.28})$$

This yields explicit solutions in the following form:

$$\begin{aligned} G^\uparrow(\vec{k}, i\omega_n) &= \frac{i\omega_n + \bar{h} + \bar{\epsilon}_{\vec{k}}}{(i\omega_n + \bar{h} - \bar{\epsilon}_{\vec{k}})(i\omega_n + \bar{h} + \bar{\epsilon}_{\vec{k}}) - |\Delta|^2}, \\ G^\downarrow(\vec{k}, i\omega_n) &= \frac{i\omega_n - \bar{h} + \bar{\epsilon}_{\vec{k}}}{(i\omega_n - \bar{h} - \bar{\epsilon}_{\vec{k}})(i\omega_n - \bar{h} + \bar{\epsilon}_{\vec{k}}) - |\Delta|^2}, \\ F(\vec{k}, i\omega_n) &= \frac{\Delta}{(i\omega_n + \bar{h} - \bar{\epsilon}_{\vec{k}})(i\omega_n + \bar{h} + \bar{\epsilon}_{\vec{k}}) - |\Delta|^2}, \\ F^*(\vec{k}, i\omega_n) &= \frac{\Delta^*}{(i\omega_n - \bar{h} + \bar{\epsilon}_{\vec{k}})(i\omega_n - \bar{h} - \bar{\epsilon}_{\vec{k}}) - |\Delta|^2}, \end{aligned} \quad (\text{D.29})$$

where: $\bar{h} = h + UM/2$, $\bar{\epsilon}_{\vec{k}} = \epsilon_{\vec{k}} - \bar{\mu}$, $\bar{\mu} = \mu - Un/2$, $n = n_\uparrow + n_\downarrow$, $M = n_\uparrow - n_\downarrow$, $\epsilon_{-\vec{k}} = \epsilon_{\vec{k}}$ and $F^\dagger(\vec{k}, i\omega_n) = F^*(-\vec{k}, -i\omega_n)$. The quasiparticle spectrum is obtained upon analytic continuation $i\omega_n \rightarrow E + i\eta$ and is given by the four poles:

$$\begin{aligned} E_{\vec{k}\uparrow}^\pm &= -\bar{h} \pm E_{\vec{k}} \\ E_{\vec{k}\downarrow}^\pm &= \bar{h} \pm E_{\vec{k}} \\ E_{\vec{k}} &= \sqrt{\bar{\epsilon}_{\vec{k}}^2 + |\Delta|^2}, \end{aligned} \quad (\text{D.30})$$

among which it is sufficient to choose only two:

$$\begin{aligned} E_{\vec{k}\uparrow} &= -\bar{h} + E_{\vec{k}} \\ E_{\vec{k}\downarrow} &= \bar{h} + E_{\vec{k}}. \end{aligned} \quad (\text{D.31})$$

The equation (D.29) can be written as follows:

$$\begin{aligned} G^\uparrow(\vec{k}, i\omega_n) &= \frac{u_{\vec{k}}^2}{i\omega_n - E_{\vec{k}\uparrow}} + \frac{v_{\vec{k}}^2}{i\omega_n + E_{\vec{k}\downarrow}}, \\ G^\downarrow(\vec{k}, i\omega_n) &= \frac{u_{\vec{k}}^2}{i\omega_n - E_{\vec{k}\downarrow}} + \frac{v_{\vec{k}}^2}{i\omega_n + E_{\vec{k}\uparrow}}, \\ F(\vec{k}, i\omega_n) &= \frac{\Delta}{(i\omega_n - E_{\vec{k}\uparrow})(i\omega_n + E_{\vec{k}\downarrow})}, \end{aligned} \quad (\text{D.32})$$

where $u_{\vec{k}}^2 + v_{\vec{k}}^2 = 1$, $u_{\vec{k}}^2 = \frac{1}{2} \left(1 + \frac{\bar{\epsilon}_{\vec{k}}}{E_{\vec{k}}} \right)$ are the usual BCS coherence factors. In this way, one obtains the gap equation:

$$\Delta = U \frac{1}{\beta N} \sum_{\vec{k}, \omega_n} F(\vec{k}, i\omega_n) = -U \frac{1}{N} \sum_{\vec{k}} \frac{\Delta}{2E_{\vec{k}}} \left[1 - f(E_{\vec{k}\uparrow}) - f(E_{\vec{k}\downarrow}) \right] \quad (\text{D.33})$$

and the particle numbers are:

$$n_{\vec{k}\sigma} = \frac{1}{\beta} \sum_{\omega_n} G^\sigma(\vec{k}, i\omega_n) e^{i\omega_n 0^+} = u_{\vec{k}}^2 f(E_{\vec{k}\sigma}) + v_{\vec{k}}^2 f(-E_{\vec{k}, -\sigma}), \quad (\text{D.34})$$

where $f(x) = [e^x + 1]^{-1}$ is the Fermi function. Thus, the particle number equation and the magnetization equation are given by:

$$n = \frac{1}{N} \sum_{\vec{k}} \left[1 - \frac{\bar{\epsilon}_{\vec{k}}}{E_{\vec{k}}} \left[1 - f(E_{\vec{k}\uparrow}) - f(E_{\vec{k}\downarrow}) \right] \right], \quad (\text{D.35})$$

$$M = \frac{1}{N} \sum_{\vec{k}} \left[f(E_{\vec{k}\uparrow}) - f(E_{\vec{k}\downarrow}) \right], \quad (\text{D.36})$$

in complete agreement with the standard treatment (Eqs. (4.2), (4.4) and (4.5) for the gap parameter, particle number and magnetization, respectively).

The above scheme can be generalized to the hopping imbalance ($t^\uparrow \neq t^\downarrow$) case. The Hubbard Hamiltonian with asymmetric hopping takes the form:

$$H = H_0 + H_1, \quad (\text{D.37})$$

where:

$$H_0 = \sum_{i,j,\sigma} (t_{ij}^\sigma - \mu \delta_{ij}) c_{i\sigma}^\dagger c_{j\sigma}, \quad (\text{D.38})$$

$$H_1 = U \sum_i n_{i\uparrow} n_{i\downarrow}, \quad (\text{D.39})$$

$$t_{ij}^\sigma = t_{ji}^\sigma, t_{ii}^\sigma = 0.$$

After introducing the Nambu representation, the Hamiltonian (D.37)-(D.39) can be rewritten:

$$H_0 = \sum_{i,j} \left[\bar{t}_{ij} \hat{\Psi}_i^\dagger \tau_3 \hat{\Psi}_j - t_{ij}^- \hat{\Psi}_i^\dagger \tau_0 \hat{\Psi}_j \right] - \mu N, \quad (\text{D.40})$$

$$H_1 = U \sum_i \left(\hat{\Psi}_i^\dagger \tau_+ \hat{\Psi}_i \right) \left(\hat{\Psi}_i^\dagger \tau_- \hat{\Psi}_i \right), \quad (\text{D.41})$$

where: $\bar{t}_{ij} = t_{ij} - \mu \delta_{ij}$, $t_{ij} = \frac{1}{2}(t_{ij}^\uparrow + t_{ij}^\downarrow)$, $t_{ij}^- = \frac{1}{2}(t_{ij}^\downarrow - t_{ij}^\uparrow)$.

The inverse of the full Green function given by Eq. (D.26) in Hartree-Fock-Bogoliubov approximation for the asymmetric hopping case takes the form:

$$[\hat{G}_{ij}(\tau, \tau')]^{-1} = \begin{pmatrix} \left[-\frac{\partial}{\partial \tau} + h - U\langle n_{i\downarrow} \rangle + \mu \right] \delta_{ij} - t_{ij}^\uparrow & -\Delta_i \delta_{ij} \\ -\Delta_i^* \delta_{ij} & \left[-\frac{\partial}{\partial \tau} + h - U\langle n_{i\uparrow} \rangle - \mu \right] \delta_{ij} + t_{ij}^\downarrow \end{pmatrix} \delta(\tau - \tau'). \quad (\text{D.42})$$

After the use of the space-time Fourier transform (D.27) and considering only homogeneous superconducting ordering, one gets for the Green function:

$$\begin{aligned} \hat{G}(\vec{k}, i\omega_n) &= \begin{pmatrix} G^\uparrow(\vec{k}, i\omega_n) & F(\vec{k}, i\omega_n) \\ F^\dagger(\vec{k}, i\omega_n) & -G^\downarrow(-\vec{k}, -i\omega_n) \end{pmatrix} = \\ &= \begin{pmatrix} i\omega_n + h - \epsilon_{\vec{k}\uparrow} + \mu - Un_\downarrow & -\Delta \\ -\Delta^* & i\omega_n + h + \epsilon_{\vec{k}\downarrow} - \mu + Un_\uparrow \end{pmatrix}^{-1}, \end{aligned} \quad (\text{D.43})$$

where: $\epsilon_{\vec{k}\sigma} = -2t^\sigma \Theta_{\vec{k}}$. The solutions are:

$$\begin{aligned} G^\uparrow(\vec{k}, i\omega_n) &= \frac{i\omega_n + \bar{h} + \bar{\epsilon}_{\vec{k}\downarrow}}{(i\omega_n + \bar{h} - \bar{\epsilon}_{\vec{k}\uparrow})(i\omega_n + \bar{h} + \bar{\epsilon}_{\vec{k}\downarrow}) - |\Delta|^2}, \\ G^\downarrow(\vec{k}, i\omega_n) &= \frac{i\omega_n - \bar{h} + \bar{\epsilon}_{\vec{k}\uparrow}}{(i\omega_n - \bar{h} - \bar{\epsilon}_{\vec{k}\downarrow})(i\omega_n - \bar{h} + \bar{\epsilon}_{\vec{k}\uparrow}) - |\Delta|^2}, \\ F(\vec{k}, i\omega_n) &= \frac{\Delta}{(i\omega_n + \bar{h} - \bar{\epsilon}_{\vec{k}\uparrow})(i\omega_n + \bar{h} + \bar{\epsilon}_{\vec{k}\downarrow}) - |\Delta|^2}, \\ F^*(\vec{k}, i\omega_n) &= \frac{\Delta^*}{(i\omega_n - \bar{h} + \bar{\epsilon}_{\vec{k}\uparrow})(i\omega_n - \bar{h} - \bar{\epsilon}_{\vec{k}\downarrow}) - |\Delta|^2}, \end{aligned} \quad (\text{D.44})$$

where: $\bar{h} = h + UM/2$, $\bar{\epsilon}_{\vec{k}\sigma} = \epsilon_{\vec{k}\sigma} - \bar{\mu}$, $\bar{\mu} = \mu - Un/2$, $n = n_\uparrow + n_\downarrow$, $M = n_\uparrow - n_\downarrow$, $\epsilon_{-\vec{k}\sigma} = \epsilon_{\vec{k}\sigma}$ and $F^\dagger(\vec{k}, i\omega_n) = F^*(-\vec{k}, -i\omega_n)$.

The quasiparticle spectrum is given by the four poles:

$$\begin{aligned} E_{\vec{k}\uparrow}^{\pm} &= -\bar{h} + \bar{\epsilon}_{\vec{k}}^{\pm} \pm E_{\vec{k}} \\ E_{\vec{k}\downarrow}^{\pm} &= \bar{h} - \bar{\epsilon}_{\vec{k}}^{\pm} \pm E_{\vec{k}} \\ E_{\vec{k}} &= \sqrt{(\bar{\epsilon}_{\vec{k}}^+)^2 + |\Delta|^2}, \end{aligned} \quad (\text{D.45})$$

where: $\bar{\epsilon}_{\vec{k}}^{\pm} = \frac{\bar{\epsilon}_{\vec{k}\uparrow} \pm \bar{\epsilon}_{\vec{k}\downarrow}}{2}$, $\bar{\epsilon}_{\vec{k}}^+ = \bar{\epsilon}_{\vec{k}} = \epsilon_{\vec{k}} - \bar{\mu}$, $\epsilon_{\vec{k}} = -2t\Theta_{\vec{k}}$, $t = \frac{t^{\uparrow} + t^{\downarrow}}{2}$, among which it is sufficient to choose only two:

$$\begin{aligned} E_{\vec{k}\uparrow} &= -\bar{h} + \bar{\epsilon}_{\vec{k}}^+ + E_{\vec{k}} \\ E_{\vec{k}\downarrow} &= \bar{h} - \bar{\epsilon}_{\vec{k}}^+ + E_{\vec{k}}. \end{aligned} \quad (\text{D.46})$$

The equation (D.44) can be written analogously to the equal hopping integral case (see: Eq. (D.29)) as follows:

$$\begin{aligned} G^{\uparrow}(\vec{k}, i\omega_n) &= \frac{u_{\vec{k}}^2}{i\omega_n - E_{\vec{k}\uparrow}} + \frac{v_{\vec{k}}^2}{i\omega_n + E_{\vec{k}\downarrow}}, \\ G^{\downarrow}(\vec{k}, i\omega_n) &= \frac{u_{\vec{k}}^2}{i\omega_n - E_{\vec{k}\downarrow}} + \frac{v_{\vec{k}}^2}{i\omega_n + E_{\vec{k}\uparrow}}, \\ F(\vec{k}, i\omega_n) &= \frac{\Delta}{(i\omega_n - E_{\vec{k}\uparrow})(i\omega_n + E_{\vec{k}\downarrow})}, \end{aligned} \quad (\text{D.47})$$

where $u_{\vec{k}}^2 + v_{\vec{k}}^2 = 1$, $u_{\vec{k}}^2 = \frac{1}{2} \left(1 + \frac{\bar{\epsilon}_{\vec{k}}}{E_{\vec{k}}} \right)$ are the usual BCS coherence factors.

One can also derive the spin-dependent superconducting density of states, given by the formula:

$$g_{\sigma}(E) = \frac{-1}{\pi N} \sum_{\vec{k}} \text{Im} G^{\sigma}(\vec{k}, i\omega_n \rightarrow E + i0^+), \quad (\text{D.48})$$

which upon the use of (D.47) yields:

$$g_{\sigma}(E) = \frac{1}{N} \sum_{\vec{k}} \left[u_{\vec{k}}^2 \delta(E - E_{\vec{k}\sigma}) + v_{\vec{k}}^2 \delta(E + E_{\vec{k}-\sigma}) \right], \quad (\text{D.49})$$

i.e. Eq. (4.7).

After simple transformations, one can obtain a set of self-consistent equations, in analogy to Eqs. (D.33)-(D.35).

D.2 T-matrix scheme

Let us write the exact equation for the self-energy (D.24) in the form:

$$\hat{\Sigma}(1, 2) = \hat{\Sigma}^0(1, 2) + \hat{\Sigma}^1(1, 2), \quad (\text{D.50})$$

$$\hat{\Sigma}^0(1, 2) = \begin{pmatrix} U\langle n_{\downarrow}(1) \rangle_S & \Delta(1) \\ \Delta^*(1) & -U\langle n_{\uparrow}(1) \rangle_S \end{pmatrix} \delta(1-2), \quad (\text{D.51})$$

$$\hat{\Sigma}^1(1, 2) = - \int d\bar{3} \left[\tau_+ \hat{G}(1, \bar{3}) \hat{\Gamma}_1(\bar{3}, 2|1) + \tau_- \hat{G}(1, \bar{3}) \hat{\Gamma}_2(\bar{3}, 2|1) \right], \quad (\text{D.52})$$

where the vertex functions $\hat{\Gamma}_s(\bar{3}, 2|1)$, $s = 1, 2$ are:

$$\hat{\Gamma}_1(\bar{3}, 2|1) = U \frac{\delta \hat{\Sigma}(\bar{3}, 2)}{\delta \eta(1)}, \quad (\text{D.53})$$

$$\hat{\Gamma}_2(\bar{3}, 2|1) = U \frac{\delta \hat{\Sigma}(\bar{3}, 2)}{\delta \eta^*(1)}, \quad (\text{D.54})$$

The equation for the vertex function can be obtained by substituting again the Dyson equation: $\hat{\Sigma}(\bar{3}, 2) = \hat{G}^{-1}(\bar{3}, 2) - \hat{G}_0^{-1}(\bar{3}, 2)$ in (D.53) and (D.54). To a first iteration, we get:

$$\hat{\Gamma}_1(\bar{3}, 2|1) = \begin{pmatrix} U^2 \frac{\delta \langle n_{\downarrow}(2) \rangle_S}{\delta \eta(1)} & U \frac{\delta \Delta(2)}{\delta \eta(1)} \\ U \frac{\delta \Delta^*(2)}{\delta \eta(1)} & -U^2 \frac{\delta \langle n_{\uparrow}(2) \rangle_S}{\delta \eta(1)} \end{pmatrix} \delta(2 - \bar{3}), \quad (\text{D.55})$$

and analogously for $\hat{\Gamma}_2(\bar{3}, 2|1)$. Substituting (D.55) to (D.52) we have

$$\begin{aligned} \hat{\Sigma}^1(1, 2) = & \quad (\text{D.56}) \\ & \begin{pmatrix} -U^2 F^+(1, 2) \frac{\delta \langle n_{\downarrow}(2) \rangle_S}{\delta \eta(1)} + U G_{\downarrow}(2, 1) \frac{\delta \Delta^*(2)}{\delta \eta(1)} & -U^2 G_{\downarrow}(2, 1) \frac{\delta \langle n_{\downarrow}(2) \rangle_S}{\delta \eta(1)} - U F^{\dagger}(1, 2) \frac{\delta \Delta(2)}{\delta \eta(1)} \\ -U^2 G_{\uparrow}(1, 2) \frac{\delta \langle n_{\downarrow}(2) \rangle_S}{\delta \eta^*(1)} - U F(1, 2) \frac{\delta \Delta^*(2)}{\delta \eta^*(1)} & U^2 F(1, 2) \frac{\delta \langle n_{\uparrow}(2) \rangle_S}{\delta \eta^*(1)} - U G_{\uparrow}(1, 2) \frac{\delta \Delta(2)}{\delta \eta^*(1)} \end{pmatrix}. \end{aligned}$$

In this way, in this approach we included corrections up to second order in U .

From now on we consider only the normal state and set all the sources to zero as well as $t^{\uparrow} = t^{\downarrow}$. (At this stage, we also do not consider the effect of the Zeeman field). The self energy to a first iteration is then diagonal and given by:

$$\hat{\Sigma}(1, 2) = \begin{pmatrix} \Sigma_{11}(1, 2) & 0 \\ 0 & \Sigma_{22}(1, 2) \end{pmatrix}, \quad (\text{D.57})$$

$$\Sigma_{11}(1, 2) = U \langle n_{\downarrow}(1) \rangle \delta(1-2) + U G_{\downarrow}(2, 1) \left. \frac{\delta \Delta^*(2)}{\delta \eta(1)} \right|_0, \quad (\text{D.58})$$

$$\Sigma_{22}(1, 2) = -U \langle n_{\uparrow}(1) \rangle \delta(1-2) - U G_{\uparrow}(1, 2) \left. \frac{\delta \Delta(2)}{\delta \eta^*(1)} \right|_0. \quad (\text{D.59})$$

In the above, the terms given by functional derivatives generate the Cooper pair fluctuations. These terms are calculated from:

$$\frac{\delta \Delta^*(2)}{\delta \eta(1)} = U \frac{\delta F^{\dagger}(2, 2^+)}{\delta \eta(1)} = U \left. \frac{\delta \hat{G}(2, 2^+)}{\delta \eta(1)} \right|_{21}, \quad (\text{D.60})$$

by substituting the self-energy through (D.22). Keeping the terms involving the Cooper pair fluctuations to the same order of approximation, we have:

$$\left. \frac{\delta\Delta^*(2)}{\delta\eta(1)} \right|_0 = -UG_{\downarrow}(1,2)G_{\uparrow}(1,2) - U \int d\bar{4} G_{\downarrow}(\bar{4},2) \left. \frac{\delta\Delta^*(\bar{4})}{\delta\eta(1)} \right|_0 G_{\uparrow}(\bar{4},2), \quad (\text{D.61})$$

$$\left. \frac{\delta\Delta(2)}{\delta\eta^*(1)} \right|_0 = -UG_{\uparrow}(2,1)G_{\downarrow}(2,1) - U \int d\bar{4} G_{\uparrow}(2,\bar{4}) \left. \frac{\delta\Delta(\bar{4})}{\delta\eta^*(1)} \right|_0 G_{\downarrow}(2,\bar{4}). \quad (\text{D.62})$$

On the other hand:

$$\left. \frac{\delta\Delta^*(2)}{\delta\eta(1)} \right|_0 = -UG_2(1,2), \quad \left. \frac{\delta\Delta(2)}{\delta\eta^*(1)} \right|_0 = -UG_2(2,1), \quad (\text{D.63})$$

where $G_2(1,2) = \langle T_{\tau} \rho^-(1) \rho^+(2) \rangle$ is the two-particle Green function, $\rho^-(1) = c_{\downarrow}(1)c_{\uparrow}(1)$, $\rho^+(2) = c_{\uparrow}^{\dagger}(2)c_{\downarrow}^{\dagger}(2)$. Using (D.62), we obtain the equation satisfied by $G_2(1,2)$:

$$G_2(1,2) = G_{\downarrow}(1,2)G_{\uparrow}(1,2) - U \int d\bar{4} G_{\downarrow}(\bar{4},2)G_{\uparrow}(\bar{4},2)G_2(1,\bar{4}). \quad (\text{D.64})$$

We now define the T-matrix:

$$T_{\downarrow\uparrow}(1,2) = U\delta(1-2) + U \left. \frac{\delta\Delta^*(2)}{\delta\eta(1)} \right|_0, \quad (\text{D.65})$$

$$T_{\uparrow\downarrow}(2,1) = U\delta(2-1) + U \left. \frac{\delta\Delta(2)}{\delta\eta^*(1)} \right|_0, \quad (\text{D.66})$$

which leads to:

$$\left. \frac{\delta\Delta^*(2)}{\delta\eta(1)} \right|_0 = - \int d\bar{4} G_{\downarrow}(\bar{4},2)G_{\uparrow}(\bar{4},2)T_{\downarrow\uparrow}(1,\bar{4}), \quad (\text{D.67})$$

$$\left. \frac{\delta\Delta(2)}{\delta\eta^*(1)} \right|_0 = - \int d\bar{4} G_{\uparrow}(2,\bar{4})G_{\downarrow}(2,\bar{4})T_{\uparrow\downarrow}(\bar{4},1). \quad (\text{D.68})$$

$$(\text{D.69})$$

The T-matrix satisfies the equation:

$$T_{\downarrow\uparrow}(1,2) = U\delta(1-2) - U \int d\bar{4} G_{\downarrow}(\bar{4},2)G_{\uparrow}(\bar{4},2)T_{\downarrow\uparrow}(1,\bar{4}), \quad (\text{D.70})$$

$$T_{\uparrow\downarrow}(2,1) = U\delta(1-2) - U \int d\bar{4} G_{\uparrow}(2,\bar{4})G_{\downarrow}(2,\bar{4})T_{\uparrow\downarrow}(\bar{4},1). \quad (\text{D.71})$$

The self-energies in the T-matrix scheme are obtained from (D.57) and given by:

$$\Sigma_{11}(1,2) = G_{\downarrow}(2,1) \left[U\delta(1-2) + U \left. \frac{\delta\Delta^*(2)}{\delta\eta(1)} \right|_0 \right] = T_{\downarrow\uparrow}(1,2)G_{\downarrow}(2,1), \quad (\text{D.72})$$

$$\Sigma_{22}(1,2) = -G_{\uparrow}(1,2) \left[U\delta(1-2) + U \left. \frac{\delta\Delta(2)}{\delta\eta^*(1)} \right|_0 \right] = -T_{\uparrow\downarrow}(2,1)G_{\uparrow}(1,2), \quad (\text{D.73})$$

where we substituted $\langle n_\sigma(1) \rangle = G_\sigma(1, 2)\delta(1 - 2)$ in (D.58-D.59). Since in the absence of magnetic field, the normal state Green functions are spin symmetric, we simply set $T_{\downarrow\uparrow}(1, 2) = T(1, 2)$. Thus, for the electron Green function $G(1, 2) = -\langle T_\tau c_{i\sigma}(\tau) c_{j\sigma}^\dagger(\tau') \rangle$ in the T-matrix approximation, we have the following set of self-consistent equations:

$$G^{-1}(1, 2) = G_0^{-1}(1, 2) - \Sigma(1, 2), \quad (\text{D.74})$$

$$\Sigma(1, 2) = T(1, 2)G(2, 1), \quad (\text{D.75})$$

$$T(1, 2) = U\delta(1 - 2) - U \int d\bar{3} G(\bar{3}, 2)G(\bar{3}, 2)T(1, \bar{3}), \quad (\text{D.76})$$

$$G_0^{-1}(1, 2) = \left(-\frac{\partial}{\partial \tau} \delta_{ij} - \bar{t}_{ij} \right) \delta(\tau - \tau'), \quad (\text{D.77})$$

and the self-energy is expressed by fully dressed Green functions G . For the translationally invariant system, we go to the space-time Fourier representation using (D.27) and:

$$\Sigma_{ij}(\tau, \tau') = \frac{1}{\beta N} \sum_{\vec{k}, \omega_n} e^{i\vec{k} \cdot (\vec{R}_i - \vec{R}_j) - i\omega_n(\tau - \tau')} \Sigma(\vec{k}, i\omega_n), \quad (\text{D.78})$$

$$T_{ij}(\tau, \tau') = \frac{1}{\beta N} \sum_{\vec{q}, \nu_m} e^{i\vec{q} \cdot (\vec{R}_i - \vec{R}_j) - i\nu_m(\tau - \tau')} T(\vec{q}, i\nu_m), \quad (\text{D.79})$$

to obtain:

$$T(\vec{q}, i\nu_m) = \frac{U}{1 + U\chi(\vec{q}, i\nu_m)}, \quad (\text{D.80})$$

$$\Sigma(\vec{k}, i\omega_n) = \frac{1}{\beta N} \sum_{\vec{q}, \nu_m} T(\vec{q}, i\nu_m) G(\vec{q} - \vec{k}, i\nu_m - i\omega_n), \quad (\text{D.81})$$

$$\chi(\vec{q}, i\nu_m) = \frac{1}{\beta N} \sum_{\vec{k}, \omega_n} G(\vec{k}, i\omega_n) G(\vec{q} - \vec{k}, i\nu_m - i\omega_n), \quad (\text{D.82})$$

where $\nu_m = 2\pi m/\beta$, m integer, is the bosonic Matsubara frequency, $\chi(\vec{q}, i\nu_m)$ is the pairing susceptibility. The free Green function is given by $G_0(\vec{k}, i\omega_n) = [\omega_n - \epsilon_{\vec{k}} + \mu]^{-1}$ and has no Hartree term. In diagrammatic interpretation, the T-matrix approximation is equivalent to the summation of repeated particle-particle scatterings described by the ladder diagrams [198]. For the attractive interaction, it describes particle-particle correlations in the Cooper channel. It can also be considered as a ladder approximation to the full Bethe-Salpeter equation for the two-particle Green functions (compare (D.64)). The $G_2(q)$ is simply related to the T-matrix:

$$G_2(q) = \frac{\chi(q)T(q)}{U} = \frac{\chi(q)}{1 + U\chi(q)}. \quad (\text{D.83})$$

The so called $(GG_0)G_0$ T-matrix scheme follows as an approximation to the above equations (D.81), (D.82) by replacing on the RHS one dressed G by G_0 .

The T-matrix scheme goes beyond the standard mean-field, since includes the pairing fluctuations (effect of noncondensed pairs with $\vec{q} \neq 0$) and allows for description of the BEC regime of the crossover. In general, the method works best in a low density regime.

D.3 T-matrix approach for $h \neq 0$

We shall now consider the case of the Hubbard model in a Zeeman magnetic field and in the normal state. The matrix Green function is diagonal with the components given by:

$$G_{11}^{-1}(1, 2) = [G_{11}^0(1, 2)]^{-1} - \Sigma_{11}(1, 2) \quad (\text{D.84})$$

$$G_{22}^{-1}(1, 2) = [G_{22}^0(1, 2)]^{-1} - \Sigma_{22}(1, 2), \quad (\text{D.85})$$

where the self-energies are given by (D.72) and (D.73), i.e.:

$$\Sigma_{11}(1, 2) = T_{\downarrow\uparrow}(1, 2)G_{\downarrow}(2, 1), \quad (\text{D.86})$$

$$\Sigma_{22}(1, 2) = -T_{\uparrow\downarrow}(2, 1)G_{\uparrow}(1, 2), \quad (\text{D.87})$$

and $[G_0(1, 2)]^{-1} = \{[-\frac{\partial}{\partial\tau} - h] \tau_0 \delta_{ij} - \bar{t}_{ij} \tau_3\} \delta(\tau - \tau')$. We can also write:

$$G_{\uparrow}^{-1}(1, 2) = [G_{0\uparrow}(1, 2)]^{-1} - \Sigma_{11}(1, 2) \quad (\text{D.88})$$

$$G_{\downarrow}^{-1}(1, 2) = [G_{0\downarrow}(1, 2)]^{-1} + \Sigma_{22}(2, 1). \quad (\text{D.89})$$

Therefore, one has the Dyson equation for both σ :

$$G_{\sigma}^{-1}(1, 2) = [G_{0\sigma}(1, 2)]^{-1} - \Sigma_{\sigma}(1, 2), \quad (\text{D.90})$$

where:

$$\Sigma_{\uparrow}(1, 2) = T_{\downarrow\uparrow}(1, 2)G_{\downarrow}(2, 1), \quad (\text{D.91})$$

$$\Sigma_{\downarrow}(1, 2) = T_{\uparrow\downarrow}(1, 2)G_{\uparrow}(2, 1). \quad (\text{D.92})$$

Performing the Fourier transform, we obtain:

$$G_{\sigma}^{-1}(k) = G_{0\sigma}^{-1}(k) - \Sigma_{\sigma}(k), \quad (\text{D.93})$$

$$\Sigma_{\uparrow}(k) = \sum_q T_{\downarrow\uparrow}(q)G_{\downarrow}(q - k), \quad (\text{D.94})$$

$$\Sigma_{\downarrow}(k) = \sum_q T_{\uparrow\downarrow}(q)G_{\uparrow}(q - k), \quad (\text{D.95})$$

where we have used the four-vector notation: $k = (\vec{k}, i\omega_n)$, $q = (\vec{q}, i\nu_m)$, $\sum_q = \frac{1}{N} \sum_{\vec{q}} \frac{1}{\beta} \sum_{\nu_m}$. The free Green function is given by: $G_{0\sigma}^{-1}(k) = i\omega_n - (\epsilon_{\vec{k}} - \mu) + h\sigma$.

The corresponding T-matrix satisfies the equations:

$$T_{\downarrow\uparrow}^{-1}(q) = \frac{1}{U} + \chi_{\downarrow\uparrow}(q), \quad (\text{D.96})$$

$$T_{\uparrow\downarrow}^{-1}(q) = \frac{1}{U} + \chi_{\downarrow\uparrow}(q), \quad (\text{D.97})$$

where the pairing susceptibilities are given by:

$$\chi_{\sigma\bar{\sigma}}(q) = \sum_k G_{\sigma}(k)G_{\bar{\sigma}}(q-k), \quad \bar{\sigma} = -\sigma. \quad (\text{D.98})$$

One can check, by the change of summation variables, that $\chi_{\downarrow\uparrow}(q) = \chi_{\uparrow\downarrow}(q)$ and therefore we have $T_{\downarrow\uparrow}^{-1}(q) = T_{\uparrow\downarrow}^{-1}(q)$, and thus only one T-matrix for both spin directions. The effects of superconducting correlations in the normal state are described by the above spin-dependent self-energies. The above equations (D.93-D.97), supplemented by the number equation:

$$n = \sum_{k,\sigma} G_{\sigma}(k)e^{i\omega_n 0^+}, \quad (\text{D.99})$$

form the required set for the normal state.

For calculations of the critical temperature, one resorts to the Thouless criterion of the divergent T-matrix:

$$\frac{1}{U} + \chi_{\downarrow\uparrow}(\vec{q}, 0, T_c) = 0, \quad (\text{D.100})$$

which in general can yield instability of the normal state for $\vec{q} = 0$ or $\vec{q} \neq 0$, if $h \neq 0$. For the free case, one gets for the pairing susceptibilities:

$$\chi_{\downarrow\uparrow}^0(q) = \sum_k G_{0\downarrow}(k)G_{0\uparrow}(q-k) = \frac{1}{N} \sum_{\vec{k}} \frac{1 - f(\epsilon_{\vec{k}} - \mu + h) - f(\epsilon_{\vec{q}-\vec{k}} - \mu - h)}{\epsilon_{\vec{k}} + \epsilon_{\vec{q}-\vec{k}} - 2\mu - i\nu_m}, \quad (\text{D.101})$$

$$\chi_{\uparrow\downarrow}^0(q) = \sum_k G_{0\uparrow}(k)G_{0\downarrow}(q-k) = \frac{1}{N} \sum_{\vec{k}} \frac{1 - f(\epsilon_{\vec{k}} - \mu - h) - f(\epsilon_{\vec{q}-\vec{k}} - \mu + h)}{\epsilon_{\vec{k}} + \epsilon_{\vec{q}-\vec{k}} - 2\mu - i\nu_m}, \quad (\text{D.102})$$

and indeed $\chi_{\downarrow\uparrow}^0(q) = \chi_{\uparrow\downarrow}^0(q)$, as it is seen, by a change of the variable in the momentum summation. The unique solution which follows from the Thouless criterion is in agreement with the expression for T_c in a simple BCS theory:

$$\begin{aligned} 0 &= \frac{1}{U} + \chi_{\downarrow\uparrow}^0(\vec{0}, 0, T_c) = \frac{1}{U} + \frac{1}{N} \sum_{\vec{k}} \frac{1 - f(\epsilon_{\vec{k}} - \mu + h) - f(\epsilon_{\vec{k}} - \mu - h)}{2(\epsilon_{\vec{k}} - \mu)} = \\ &= \frac{1}{U} + \frac{1}{N} \sum_{\vec{k}} \frac{1 - 2\bar{f}(\epsilon_{\vec{k}} - \mu)}{2(\epsilon_{\vec{k}} - \mu)}, \end{aligned} \quad (\text{D.103})$$

where $\bar{f}(x)$ is the symmetrized Fermi function:

$$\bar{f}(x) = \frac{1}{2} [f(x+h) + f(x-h)]. \quad (\text{D.104})$$

For approximate solutions, one can use the $(GG_0)G_0$ scheme, where we replace one dressed $G_{\bar{\sigma}}(q-k)$ by $G_{0\bar{\sigma}}(q-k)$ in the self-energies (D.94), (D.95) and pairing susceptibilities (D.98). However, for consistency one has to use a T-matrix which is the same for

both spin directions. A solution has been suggested by the Levin group and consists in the use of the symmetrized pairing susceptibility:

$$\bar{\chi}(q) = \frac{1}{2} [\chi_{\downarrow\uparrow}(q) + \chi_{\uparrow\downarrow}(q)]. \quad (\text{D.105})$$

The corresponding T-matrix is, according to (D.96-D.97):

$$T^{-1}(q) = \frac{1}{U} + \bar{\chi}(q). \quad (\text{D.106})$$

Finally, in the $(GG_0)G_0$ scheme, one has the following equations:

$$G_{\sigma}^{-1}(k) = G_{0\sigma}^{-1}(k) - \Sigma_{\sigma}(k), \quad (\text{D.107})$$

$$\Sigma_{\sigma}(k) = \sum_q T(q) G_{0\bar{\sigma}}(q - k), \quad (\text{D.108})$$

$$T^{-1}(q) = \frac{1}{U} + \bar{\chi}(q), \quad (\text{D.109})$$

$$\bar{\chi}(q) = \frac{1}{2} [\chi_{\downarrow\uparrow}(q) + \chi_{\uparrow\downarrow}(q)], \quad (\text{D.110})$$

$$\chi_{\sigma,\bar{\sigma}}(q) = \sum_k G_{\sigma}(k) G_{0\bar{\sigma}}(q - k). \quad (\text{D.111})$$

It is clear that this scheme arises as an approximation to the fully self-consistent T-matrix approach. An attractive feature of the above formulation is that the structure of equations is much similar to the case without magnetic field (only the Fermi function is replaced by the symmetrized Fermi function) and numerical computations are feasible.

Appendix E

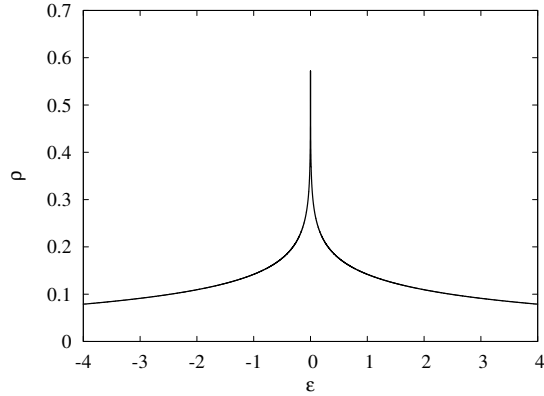
Density of states

In this Appendix, the densities of states [112] which have been used for numerical calculations in this thesis are shown.

- 2D square lattice:

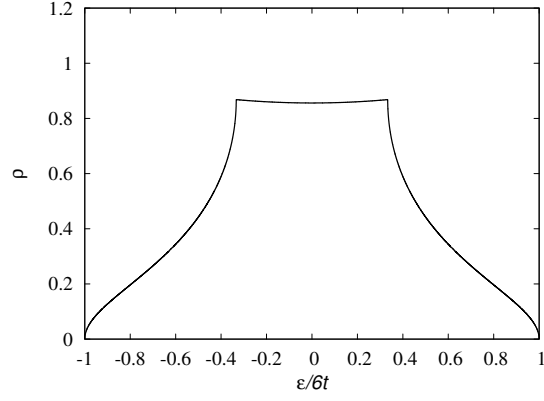
$$\rho_{2D} = \begin{cases} \frac{2}{4\pi^2} K(1 - (\epsilon/4t)^2) & |\epsilon/t| \leq 4 \\ 0 & |\epsilon/t| > 4 \end{cases} \quad (\text{E.1})$$

The density of states for the 2D square lattice is expressed by the complete elliptic integral of the first kind $K(x) = \int_0^{\pi/2} \frac{dt}{\sqrt{1-x^2 \sin^2 t}}$.



- simple cubic lattice (sc):

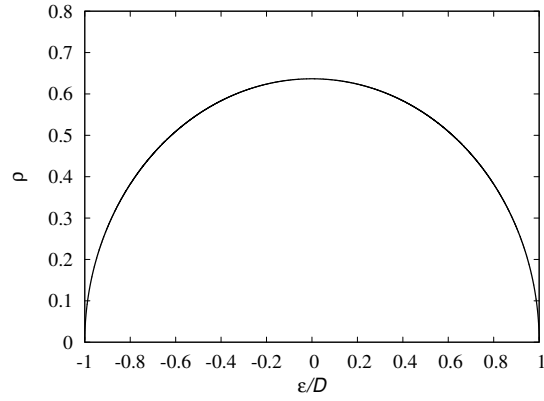
$$\rho_{sc} = \frac{3}{8\pi^3} \begin{cases} 70.7801 + 1.0053|3\epsilon/6t|^2 & |\epsilon/6t| < 1/3 \\ \sqrt{3 - 3|\epsilon/6t|}(80.3702 - 16.3846(3 - 3|\epsilon/6t|) \\ + 0.78978(3 - 3|\epsilon/6t|)^2 + \sqrt{3|\epsilon/6t| - 1}(-44.2639 \\ + 3.66394(3 - 3|\epsilon/6t|) - 0.17248(3 - 3|\epsilon/6t|)^2)) & 1 \geq |\epsilon/6t| \geq 1/3 \\ 0 & \text{otherwise} \end{cases} \quad (\text{E.2})$$



- semicircular DOS (s-circ):

$$\rho_{s-circ} = \frac{2}{\pi D} \sqrt{(\epsilon/D + 1)(2 - (\epsilon/D + 1))}, \quad (\text{E.3})$$

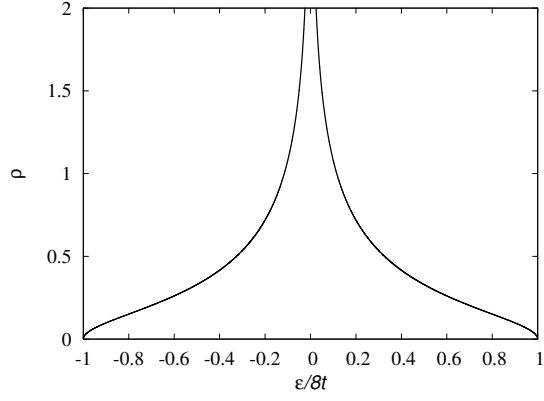
where $D = 10.80732t$ is the half bandwidth.



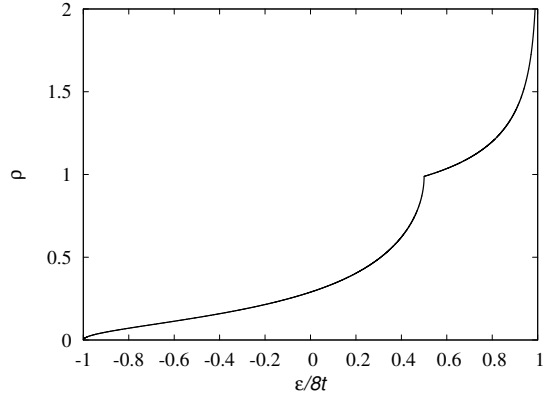
- body-centered cubic lattice (BCC):

$$\rho_{BCC} = \begin{cases} \frac{1}{8t}(2\sqrt{1 - |\epsilon/8t|} \ln^2(5.845/|\epsilon/8t|)(16.6791 \\ + 3.636|\epsilon/8t| + 2.4880|\epsilon/8t|^2)) & |\epsilon/8t| < 1 \\ 0 & \text{otherwise} \end{cases} \quad (\text{E.4})$$

- face-centered cubic lattice (FCC):



$$\rho_{FCC} = \frac{2}{8\pi^3} \begin{cases} \frac{1}{4t}(4(122.595 - 19.4100(2\epsilon/8t - 1) \\ + 1.76011((2\epsilon/8t - 1)^2 \\ + (-44.8100 + 7.18628(2\epsilon/8t - 1)) \ln(1 - (2\epsilon/8t - 1)))) \\ \frac{1}{4t}(4\sqrt{3 + (2\epsilon/8t - 1)}((-85.9325 \\ + 101.103(3 + (2\epsilon/8t - 1)) \\ - 16.2885(3 + (2\epsilon/8t - 1))^2 \\ + (56.8683 - 47.1215(3 + (2\epsilon/8t - 1)) \\ + 2.9045(3 + (2\epsilon/8t - 1))^2)\sqrt{|2\epsilon/8t - 1|}))) \\ 0 \end{cases} \begin{matrix} 0.5 < \epsilon/8t \leq 1 \\ \\ -1 \leq \epsilon/8t \leq 0.5 \\ \text{otherwise} \end{matrix} \quad (\text{E.5})$$



Bibliography

- [1] Onnes H. K., On the sudden rate at which the resistance of mercury disappears, *Akad van Wetenschappen* **14** (**113**), 818 (1911).
- [2] Meissner, W., R. Ochsenfeld, *Naturwissenschaften* **21** (**44**), 787 (1933).
- [3] Castin Y., Bose-Einstein condensates in atomic gases: simple theoretical results, *cond-mat/0105058*, Les Houches Summer School 1999.
- [4] Bose S. N., *Zeitschrift für Physik* **26**, 178 (1924).
- [5] Einstein A., *Sitzungsberichte der Preussischen Akademie der Wissenschaften* **1**, 3 (1925).
- [6] London F., *Phys. Rev.* **54**, 947 (1938).
- [7] Allen J. F., A. D. Misener, *Nature* **141**, 75 (1938).
- [8] Kapitza P., *Nature* **141**, 74 (1938).
- [9] Osheroff D. D., R. C. Richardson, D. M. Lee, *Phys. Rev. Lett.* **28**, 885 (1972).
- [10] Penrose O., L. Onsager, *Phys. Rev.* **104**, 576 (1956).
- [11] Landau L. D., *J. Phys. USSR* **5**, 71 (1941).
- [12] Landau L. D. *Phys. Rev.* **60**, 356 (1941).
- [13] Bogolyubov N. N., *Izv. Akademii Nauk USSR* **11** (**1**), 77 (1947).
- [14] Bogolyubov N. N., *Journal of Physics* **11** (**1**), 23 (1947).
- [15] Huang K., A. Rhys, *Proc. Roy. Soc.* **A204**, 406 (1950).
- [16] Cooper L. N., *Phys. Rev.* **104**, 1189 (1956).
- [17] Bardeen J., L. N. Cooper, and J. R. Schrieffer, *Phys. Rev.* **106**, 162 (1957).
- [18] Bardeen J., L. N. Cooper, and J. R. Schrieffer, *Phys. Rev.* **108**, 1175 (1957).
- [19] Bednorz J. G., K. Müller, *Z. Physik* **B64**, 189 (1986).

- [20] Uemura Y. J., et al., *Phys. Rev. Lett.* **62**, 2317 (1989); *Phys. Rev. Lett.* **66**, 2665 (1991).
- [21] A.J. Leggett, *J. Phys. (Paris) Colloq.* **41**, C7-19 (1980).
- [22] Nozières P, S. Schmitt-Rink, *J. Low Temp. Phys.* **59**, 195 (1985).
- [23] Robaszkiewicz S., R. Micnas, K. A. Chao, *Phys. Rev. B* **23**, 1447 (1981).
- [24] Robaszkiewicz S., R. Micnas, K. A. Chao, *Phys. Rev. B* **24**, 4018 (1981); *Phys. Rev. B* **26** 3915 (1982).
- [25] Micnas R., J. Ranninger, S. Robaszkiewicz, S. Tabor, *Phys. Rev. B* **37**, 9410 (1988).
- [26] Micnas R., J. Ranninger, S. Robaszkiewicz, *Phys. Rev. B* **39**, 11653 (1989).
- [27] Micnas R., J. Ranninger, S. Robaszkiewicz, *Rev. Mod. Phys.* **62**, 113 (1990).
- [28] Randeria M., „Bose-Einstein Condensation”, *Cambridge University Press*, 355 (1995).
- [29] Micnas R., T. Kostyrko, „Recent Progress in High Temperature Superconductivity”, *Springer Lecture Notes in Physics* 475, 221 (1996).
- [30] Micnas R., S. Robaszkiewicz, *High- T_c superconductivity 1996: Ten Years after the Discovery* (Kluwer Academic Publishers) ed. E Kaldias, E. Liarokapis, K. A. Müller, NATO ASI Series E **342**, 31 (1997).
- [31] Bąk M. R. Micnas, *J. Phys.: Cond. Matt.* **10**, 9029 (1998).
- [32] Micnas R., S. Robaszkiewicz, B. Tobijaszewska, *J. Supercond.* **12**, 79 (1999).
- [33] Chen Q. J., J. Stajic, S. N. Tan, K. Levin, *Phys. Rep.* **412**, 1 (2005).
- [34] Micnas R., S. Robaszkiewicz, *Cond. Mat. Phys* Vol. **1**, No 1(13), 89 (1998).
- [35] Chien Ch., Q. Chen, Y. He, K. Levin, *Phys. Rev. Lett.* **98**, 110404 (2007).
- [36] Fano U., *Phys. Rev.* **124**, 1866 (1961).
- [37] Feshbach H., *Ann. Phys.* **19**, 287 (1962).
- [38] S. Jochim, M. Bartenstein, A. Altmeyer, G. Hendl, S. Riedl, C. Chin, J. Hecker Denschlag, R. Grimm, *Science* **302**, 20101 (2003).
- [39] Chin C., M. Bartenstein, A. Altmeyer, S. Riedl, S. Jochim, J. H. Denschlag, R. Grimm, *Science* **305**, 1128 (2004).
- [40] M. W. Zwierlein, C. A. Stan, C. H. Schunck, S. M. F. Raupach, S. Gupta, Z. Hadzibabic, W. Ketterle, *Phys. Rev. Lett.* **91**, 250401 (2003).

- [41] Zwierlein M. W., C. A. Stan, C. H. Schunck, S. M. F. Raupach, A. J. Kerman, W. Ketterle *Phys. Rev. Lett.* **92**, 120403 (2004).
- [42] M. Greiner, C. A. Regal, D. S. Jin, *Nature* **426**, 537 (2003).
- [43] Regal C. A., M. Greiner, D. S. Jin, *Phys. Rev. Lett.* **92**, 040403 (2004).
- [44] Kinast J., S. L. Hemmer, M. E. Gehm, A. Turlapov, J. E. Thomas, *Phys. Rev. Lett.* **92**, 150402 (2004).
- [45] Bourdel T., L. Khaykovich, J. Cubizolles, J. Zhang, F. Chevy, M. Teichmann, L. Tarruell, S. Kokkelmans, C.
- [46] M. W. Zwierlein, J. Abo-Shaeer, A. Schirotzek, C. Schunck, W. Ketterle, *Nature* **435**, 1047 (2005).
- [47] Zwierlein M. W., J. Abo-Shaeer, A. Schirotzek, C. Schunck, W. Ketterle, *Nature* **435**, 1047 (2005).
- [48] Zwierlein M. W., A. Schirotzek, C. H. Schunck, W. Ketterle, *Science* **311**, 492 (2006).
- [49] Zwierlein M. W., W. Ketterle, *cond-mat/0603489* (2006).
- [50] Partridge G. B., W. Li, R. I. Kamar, Y. Liao, R. G. Hulet, *Science* **311**, 503 (2006).
- [51] Stöferle T., H. Mortiz, K. Günter, M. Köhl, T. Esslinger, *Phys. Rev. Lett.* **96**, 030401 (2006).
- [52] Chandrasekhar B. S., *Appl. Phys. Lett.* **1**, 7 (1962).
- [53] Clogston A. M., *Phys. Rev. Lett.* **9**, 266 (1962).
- [54] Zwierlein M. W., C. H. Schunck, A. Schirotzek, W. Ketterle, *Nature* **442**, 54 (2006).
- [55] Fulde P., R. A. Ferrell, *Phys. Rev.* **135**, A550 (1964).
- [56] Larkin A. I., Y. N. Ovchinnikov, *Zh. Eksp. Teor. Fiz.* **47**, 1136 (1964).
- [57] Bianchi A., R. Movshovich, C. Capan, P. G. Pagliuso, J. L. Sarrao, *Phys. Rev. Lett.* **91**, 187004 (2003).
- [58] Casalbuoni R., G. Nardulli, *Rev. Mod. Phys.* **76**, 263 (2004).
- [59] Matsuda Y., H. Shimahara, *J. Phys. Soc. Jpn.* **76**, 051005 (2007).
- [60] Koponen T. K., T. Paananen, J.-P. Martikainen, P. Torma, *Phys. Rev. Lett.* **99**, 120403 (2007).
- [61] Mierzejewski M., A. Ptok, M. M. Maška, *Phys. Rev. B* **80**, 174525 (2009).

- [62] Feiguin A., R. Heidrich-Meisner, *Phys. Rev. B* **76**, 220508 (2007).
- [63] Batrouni G. G., M. H. Huntley, V. G. Rousseau, R. T. Scalettar, *Phys. Rev. Lett.* **100**, 116405 (2008).
- [64] Lüscher A., R. M. Noack, A. M. Läuchli *Phys. Rev. A* **78**, 013637 (2008).
- [65] Rizzi M., M. Polini, M. A. Cazalilla, M. R. Bakhtiari, M. P. Tosi, R. Fazio, *Phys. Rev. B* **77**, 245105 (2008).
- [66] Tezuka M., M. Ueda, *Phys. Rev. Lett* **100**, 110403 (2008).
- [67] Sheehy D. E., L. Radzihovsky, *Phys. Rev. Lett* **96**, 060401 (2006).
- [68] Radzihovsky L., D. E. Sheehy, *Ann. Phys.* **322**, 1790-1924 (2007).
- [69] Radzihovsky L., D. E. Sheehy, *Rep. Prog. Phys.* **73**, 076501 (2010).
- [70] Sarma G., *J. Phys. Chem. Solids* **24**, 1029 (1963).
- [71] W. Ketterle, Y. Shin, A. Schirotzek, C. H. Schunk, *J. Phys.: Condens. Matter* **21** (2009).
- [72] Sá de Melo C. A. R., *Physics Today* **61**, 45 (2008).
- [73] Liu W. V., F. Wilczek, *Phys.Rev.Lett.* **90**, 047002 (2003).
- [74] Gubankova E, W. V. Liu, F. Wilczek, *Phys. Rev. Lett.* **91**, 032001 (2003).
- [75] Liu W. V., F. Wilczek, P. Zoller, *Phys. Rev. A* **70**, 033603 (2004).
- [76] Forbes M. M., E. Gubankova, W. V. Liu, F. Wilczek, *Phys. Rev. Lett.* **94**, 017001 (2005).
- [77] Gubankova E., E. G. Mishchenko, F. Wilczek, *Phys. Rev. Lett.* **94**, 110402 (2005).
- [78] Gubankova E., A. Schmitt, F. Wilczek, *Phys. Rev. B* **74**, 064505 (2006).
- [79] Iskin M., C. A. R. Sá de Melo, *Phys. Rev. Lett.* **97**, 100404 (2006).
- [80] Iskin M., C. A. R. Sá de Melo, *Phys. Rev. A* **76**, 013601 (2007).
- [81] Parish M. M., F. M. Marchetti, A. Lamacraft and B. D. Simons, *Phys. Rev. Lett.* **98**, 160402 (2007).
- [82] Parish M. M., F. M. Marchetti, A. Lamacraft and B. D. Simons, *Nature Physics* **3**, 124 (2007)
- [83] Fazekas P., *Lectures Notes on Electron Correlation and Magnetism*, World Scientific 1999.

- [84] Hubbard J., *Proc. R. Soc. London A* **276**, 238-257 (1963).
- [85] Micnas R., *On the Crossover from BCS Superconductivity to Bose Condensation*, arXiv: cond-mat/0211561 (2003).
- [86] Miyake K., *Prog. Theor. Phys.* **72**, 1063 (1984).
- [87] Tobijaszevska B., Ph.D. thesis, Solid State Theory Division, Faculty of Physics, Adam Mickiewicz University, Poznań 2001; Micnas. R, B. Tobijaszevska, *J. Phys.: Condens. Matter* **14**, 9631 (2002).
- [88] Cuoco M., P. Gentile, C. Noce, *Phys. Rev. Lett.* **91**, 197003 (2002).
- [89] Mermin N. D., H. Wagner, *Phys. Rev. Lett.* **22**, 1133 (1966).
- [90] Hohenberg P. C., *Phys. Rev. B* **158**, 383 (1967).
- [91] Kosterlitz J. M., D. J. Thouless, *J. Phys. C: Solid State Phys.* **6**, 1181 (1973).
- [92] Kosterlitz J.M., *J. Phys. C* **7**, 1046 (1974).
- [93] Bishop D. J., J. D. Reppy, *Phys. Rev. Lett.* **40**, 1727 (1978).
- [94] Resnick D. J., J. C. Garland, J. T. Boyd, S. Shoemaker, R. S. Newrock, *Phys. Rev. Lett.* **47**, 1542 (1981).
- [95] Petrov D. S., M. Holtzmann, G. V. Shlyapnikov, *Phys. Rev. Lett.* **84**, 2551 (2000).
- [96] Bagnato V., D. Kleppner, *Phys. Rev. A* **44**, 7439 (1991).
- [97] Prokof'ev N., B. Svistunov, *Phys. Rev. A* **66**, 043608 (2002).
- [98] Sachdev S., E. Demler, *Phys. Rev. B* **69**, 144504 (2004).
- [99] Hadzibabic Z., P. Krüger, M. Cheneau, B. Battelier, J. Dalibard, *Nature (London)* **441**, 1118 (2006).
- [100] Krüger P., Z. Hadzibabic, J. Dalibard, *Phys. Rev. Lett.* **99**, 040402 (2007).
- [101] Alvarez J. J. V., C. A. Balseiro, *Solid Stat. Comm.* **98**, 313 (1996).
- [102] De Paolo S., C. Castellani, C. Di Castro, B. K. Chakraverty, *Phys. Rev. B* **60**, 564 (1999).
- [103] Halperin B. I., D. R. Nelson, *Jour. of Low Temp. Phys.* **36**, 599 (1979).
- [104] Fisher M., M. N. Barber, D. Jasnow, *Phys. Rev. A* **8**, 1111 (1973).
- [105] Ohta T., Jasnow D., *Phys. Rev. B* **20**, 139 (1979).

- [106] Denteneer P. J. H., Guozhong An, J. M. J. van Leeuwen, *Europhys. Lett* **16**, 5 (1991).
- [107] Denteneer P. J. H., Guozhong An, J. M. J. van Leeuwen, *Phys. Rev. B* **47**, 6256 (1993).
- [108] Van Leeuwen J. M. J., M. S. L. du Croo de Jongh, P. J. H. Denteneer, *J. Phys. A* **29**, 41 (1996).
- [109] Cichy A., *Acta Phys. Pol. A* **121**, No 2., 824 (2012).
- [110] Kujawa A., R. Micnas, *Acta. Phys. Pol. A* **114**, 43 (2008).
- [111] Kujawa A., R. Micnas, *Acta. Phys. Pol. A* **115**, 138 (2009).
- [112] Jelitto R. J. *J. Phys. Chem. Solids* **30**, 609 (1969).
- [113] Randeria M., J. Duan, L.-Y. Shieh *Phys. Rev. Lett.* **62**, 981 (1999).
- [114] Randeria M., J. Duan, L.-Y. Shieh *Phys. Rev. B* **41**, 327 (1990).
- [115] Tinkham M., *Introduction to Superconductivity*, McGraw-Hill, New York (1975).
- [116] Landau L. D., E. M. Lifshitz, *Statistical Physics*, 3rd ed., p. I, Pergamon Press, Oxford (1980).
- [117] Ginzburg W. Ł., L. D. Landau, *Ž. Eksp. Tior. Fiz.* **20**, 1064 (1950).
- [118] Gor'kov L. P., *Ž. Eksp. Tior. Fiz.* **36**, 1918 (1959).
- [119] Schneider T., J. M. Singer, *Europhys. Lett.* **40**, 79 (1997).
- [120] Maple M. B., cond-mat/9802202 (1998).
- [121] Shen Z.-X., , D. S. Dessau, B. O. Wells, D. M. King, W. E. Spicer, A. J. Arko, D. Marshall, L. W. Lombardo, A. Kapitulnik, P. Dickinson, S. Doniach, J. DiCarlo, T. Loeser, C. H. Park, *Phys. Rev. Lett.* **70**, 1553 (1993).
- [122] Tsuei C. C., J. R. Kirtley, C. C. Chi, Lock See Yu-Jahnes, A. Gupta, T. Shaw, J. Z. Sun, M. B. Ketchen, *Phys. Rev. Lett.* **73**, 593 (1994).
- [123] Harlingen D. J. V., *Rev. Mod. Phys.* **67**, 503 (1995).
- [124] Annett J., N. Goldenfeld, A. J. Leggett in: *Physical Properties of High Temperature Superconductors*, vol 5, ed. G. M. Ginsberg, World Scientific, Singapore (1996).
- [125] Bulut N., D. J. Scalapino, *Phys. Rev. Lett.* **67**, 2898 (1991).
- [126] Bulut N., D. J. Scalapino, S. R. White, *Phys. Rev. B* **47**, 14599 (1993).

- [127] Tempere J. S. N. Klimin, J. T. Devreese, V. V. Moshchalkov, *Phys. Rev. B* **77**, 134502 (2008).
- [128] Yang K., S. L. Sondhi, *Phys. Rev. B* **57**, 8566 (1998).
- [129] Zhou C., H. J. Schultz, *Phys. Rev. B* **45**, 7397 (1992).
- [130] Gruenberg L. W., L. Gunther, *Phys. Rev. Lett.* **16**, 996 (1966).
- [131] Kujawa A., *Acta Phys. Pol. A* **118**, 423 (2010).
- [132] Kujawa-Cichy A., R. Micnas, *Europhysics Letters EPL* **95**, 37003 (2011).
- [133] He L., P. Zhuang, *Phys. Rev. A* **78**, 033613 (2008).
- [134] Du J.-j., C. Chen, J.-j. Liang, *Phys. Rev. A* **80**, 023601 (2009).
- [135] Tempere J., M. Wouters, J. T. Devreese, *Phys. Rev. A* **75**, 184526 (2007).
- [136] Pilati S., S. Giorgini, *Phys. Rev. Lett.* **100**, 030401 (2008).
- [137] Pistolesi F., G. C. Strinati, *Phys. Rev. B* **49**, 6356 (1994).
- [138] Misawa S., *Phys. Rev. B* **51**, 11791 (1995).
- [139] Privitera A., M. Capone, C. Castellani, *Phys. Rev. B* **81** 014523 (2010).
- [140] For an analysis of the KT transition in 2D continuum Fermi gas with the *s*-wave pairing and population imbalance see: Tempere J., S. N. Klimin, J. T. Devreese, *Phys. Rev. A* **79**, 053637 (2009).
- [141] Chorowska B., Master thesis, Solid State Theory Division, Faculty of Physics, Adam Mickiewicz University, Poznań (1995).
- [142] Bąk M., Ph.D. thesis, Solid State Theory Division, Faculty of Physics, Adam Mickiewicz University, Poznań (1999).
- [143] Wille E. et al., *Phys. Rev. Lett.* **100**, 053201 (2008).
- [144] Eagles D. M., *Phys. Rev.* **186**, 456 (1969).
- [145] Micnas R., M. H. Pedersen, S. Schafroth, T. Schneider, J. J. Rodriguez-Nunez, H. Beck, *Phys. Rev. B* **52**, 16223 (1995).
- [146] Janko B., J. Maly, K. Levin, *Phys. Rev. B* **56**, R11407 (1997).
- [147] Kosztin I., Q. Chen, B. Janko, K. Levin, *Phys. Rev. B* **58**, R5936 (1998).
- [148] Chen Q., I. Kosztin, B. Janko, K. Levin, *Phys. Rev. Lett.* **81**, 4708 (1998).

- [149] Kadanoff L. P., P. C. Martin, *Phys. Rev.* **124**, 670 (1961).
- [150] Patton B. R., PhD thesis, Cornell University, 1971; *Phys. Rev. Lett* **27**, 1273 (1971).
- [151] Thouless D. J., *Ann. Phys.* **10**, 553 (1960).
- [152] Micnas R., *unpublished*.
- [153] Ozawa T., G. Baym, *Phys. Rev. A* **82**, 063615 (2010).
- [154] Chen Q., Y. He, Ch. Chien, K. Levin, *Phys. Rev. B* **75**, 014521 (2007).
- [155] Burovski E., N. Prokof'ev, B. Svistunov, M. Troyer, *Phys. Rev. Lett.* **96**, 160402 (2006).
- [156] Bulgac A., J. E. Drut, P. Magierski, *Phys. Rev. A* **78**, 023625 (2008).
- [157] Chen Q., Y. He, Ch. Chin, K. Levin, *Phys. Rev. A* **74**, 063603 (2006).
- [158] Kujawa-Cichy A., R. Micnas, *in preparation*.
- [159] Kujawa-Cichy A., accepted for publication in *Acta. Phys. Pol.*
- [160] Cichy A., R. Micnas, presented at XXXIV International Conference of Theoretical Physics: Correlations and Coherence in different scales in Ustroń 2010, unpublished.
- [161] Spałek J., J. Kaczmarczyk, *J. Phys.: Condens. Matter* **22**, 355702 (2010).
- [162] Schrieffer J. R., P. A. Wolff, *Phys. Rev. B* **149**, 491 (1966).
- [163] Cazalilla M. A., A. F. Ho, T. Giamarchi, *Phys. Rev. Lett.* **95**, 226402 (2005).
- [164] Baskaran G., Z. Zou, P. W. Anderson, *Solid State Commun.* **63**, 973 (1987).
- [165] Harris A. B., R. V. Lange, *Phys. Rev.* **157**, 295 (1967).
- [166] Chao K. A., J. Spałek, A. M. Oleś, *J. Phys. C: Solid State Phys.* **10**, L271 (1977).
- [167] MacDonald A. H., S. M. Grivin, D. Yoshioka, *Phys Rev. B* **37**, 9753 (1988).
- [168] Gros C., R. Joynt, T. M. Rice, *Phys. Rev. B* **36**, 381 (1987).
- [169] Oleś A. M., *Phys. Rev. B* **41**, 2562 (1990).
- [170] Kolley E., W. Kolley, *Ann. Phys.* **47**, 150 (1990).
- [171] Kulik I. O., A. G. Pedan, *Zh. Eksp. Teor. Fiz.* **79**, 1469 (1980).
- [172] Kulik I. O., A. G. Pedan, *Fiz. Nizk. Temp.* **8**, 236 (1982).
- [173] Oppermann R., *Z. Phys. B.* **75**, 149.

- [174] Micnas R., S. Robaszkiewicz, *Phys. Rev. B* **45**, 9900 (1992).
- [175] Micnas. R., S. Robaszkiewicz, T. Kostyrko, *Phys. Rev. B* **52**, 6863 (1995).
- [176] Yunoki S., *Phys. Rev. B* **65**, 092402 (2002).
- [177] Dao T.-L., A. Georges, M. Capone, *Phys. Rev. B* **76**, 104517 (2007).
- [178] Falicov L. M., J. C. Kimball, *Phys. Rev. Lett.* **22**, 997 (1969).
- [179] Tamaki H., K. Miyake, Y. Ohashi, *J. Phys. Soc. Jpn.* **78**, 073001 (2009).
- [180] Shimahara H., *J. Phys. Soc. Jpn.* **67**, 1872 (1998).
- [181] Micnas R., *Phys. Rev. B* **76**, 184507 (2007).
- [182] Krzyszczak J., T. Domański, K. I. Wysokiński, *Acta Phys. Pol. A* **114**, 165 (2008).
- [183] Krzyszczak J., T. Domański, K. I. Wysokiński, R. Micnas, S. Robaszkiewicz, *J. Phys.: Condens. Matter* **22**, 255702 (2010).
- [184] Maška M., M. Mierzejewski, *Phys. Rev. B* **69**, 054502 (2004).
- [185] Micnas R., A. Kujawa-Cichy *in preparation*.
- [186] Shiba H., *Prog. Theor. Phys.* **48**, 2171 (1972).
- [187] Moreo A., D. J. Scalapino, *Phys. Rev. Lett.* **98**, 216402 (2007).
- [188] Lifshitz I. M., *Sov. Phys. JETP* **11**, 1130 (1960).
- [189] Blanter Y. M., M. I. Kaganov, A. V. Pantsulaya, A. A. Varlamov, *Phys. Rep.* **245**, 160 (1994).
- [190] Volovik G. E., *Exotic Properties of Superfluid ^3He* , World Scientific, Singapore (1992).
- [191] Duncan R. D., C. A. R. Sá de Melo, *Phys. Rev. B* **62**, 9675 (2000).
- [192] Botelho S. S., C. A. R. Sá de Melo, *Phys. Rev. B* **71**, 134507 (2005).
- [193] Tobijaszewska B., R. Micnas, *Phys. Stat. Sol. (b)* **243**, No 1, 159-164 (2006).
- [194] Kadanoff L. P., G. Baym, *Quantum Statistical Mechanics*, W. A. Benjamin, New York (1962).
- [195] Teubel A., E. Kolley, W. Kolley, *Phys. Stat. Sol. B* **157**, 389 (1990).
- [196] Pedersen M. H. *et al*, *Z. Phys. B* **103**, 21 (1997).
- [197] Micnas R., unpublished.

- [198] Fetter A.L., J.D. Walecka, *Quantum Theory of Many-Particle Systems*, McGraw-Hill Book Co. (1971).

List of Tables

A.1	Particle-hole transformation mapping the attractive ($U < 0$) Hubbard model onto the repulsive ($U > 0$) Hubbard model.	158
-----	---	-----

List of Figures

1.1	Schematic phase diagram for systems in which the BCS-BEC crossover takes place [34].	17
1.2	Chemical potential behavior in units of the Fermi energy at $T = 0$ in three regimes: BCS, BCS-BEC crossover (PG) and BEC [35].	18
1.3	Schematic diagram (temperature-interaction strength-spin polarization) in which various possible phases of two-component Fermi gas are illustrated [71].	20
4.1	Dependence of the order parameter (a) and the grand canonical potential (b) on the magnetic field at $T = 0$, $d = 2$, $U = -2$, for fixed $\mu \approx -1.358$	45
4.2	Dependence of the grand canonical potential on the order parameter at $T = 0$ and fixed $\mu \approx -1.358$. (a) $h = 0$, (b) $h = 0.2$ (red, dashed line), $h = 0.23$ (green, dotted line), $h = 0.26$ (blue, dash-dotted line) and $h = 0.3$ (black, solid line). t is used as the unit.	46
4.3	Density of states for two-dimensional s-wave pairing symmetry case, $T = 0$, $\mu \approx -1.358$, $U = -2$, (a) $h = 0$, (b) $h = 0.15$ (the stable branch solution), (c) $h = 0.223$ (the unstable branch solution).	47
4.4	Plots of momentum occupation numbers $n_{\vec{k}\uparrow}$ (red points), $n_{\vec{k}\downarrow}$ (black points) vs. $k \equiv k_x = k_y $ and corresponding quasiparticle spectra $E_{\vec{k}\uparrow}$, $E_{\vec{k}\downarrow}$ (insets) for $U = -2$, $\mu \approx -1.358$, (a) $h = 0$, (b) $h = 0.15$, (c) $h = 0.223$	48
4.5	Critical magnetic field vs. the chemical potential for the first order SC ₀ -NO transition, at $T = 0$, three different values of the attractive interaction; (a) square lattice, (b) simple cubic lattice.	50
4.6	Critical magnetic field vs. electron concentration for the first order SC ₀ -NO transition, at $T = 0$; (a) square lattice, (b) simple cubic lattice.	52
4.7	Dependence of the order parameter on the magnetic field (a) and temperature (b), $d = 2$, $U = -2$, for a fixed $\mu \approx -1.358$. The grand canonical potential vs. temperature for $h = 0.24$: (c) the first order phase transition to the normal state, (d) the details of the reentrant transition: second order transition from NO to SC and from SC to NO (inset).	54
4.8	Magnetization vs. temperature, $d = 2$, $U = -2$, for a fixed $\mu \approx -1.358$. (a) $h = 0.23$, (b) $h = 0.24$	55
4.9	Dependence of the order parameter on the magnetic field (a) and temperature (b), $d = 3$, $U = -4$, for a fixed $\mu \approx -2.4439$	55

4.10	Grand canonical potential vs. temperature, $d = 3$, $U = -4$, for a fixed $\mu \approx -2.4439$, at $h = 0.96$ and $h = 0.972$	56
4.11	Dependence of the grand canonical potential on the order parameter, $d = 3$, $U = -4$, for a fixed $\mu \approx -2.4439$, at $h = 0.96$, $T = 0.06$ (solid line) $T = 0.09$ (dashed line) (a), $T = 0.16$ (b) and for $h = 0.972$, $T = 0.12$ (c), $T = 0.24$ (d).	57
4.12	Magnetization vs. temperature for fixed $h = 0.96$ (a) and $h = 0.972$ (b); $d = 3$, $U = -4$, fixed $\mu \approx -2.4439$	58
4.13	Superfluid density vs. temperature (a) and magnetic field (b) for the square lattice, $\mu \approx -1.358$, $U = -2$. The Kosterlitz-Thouless temperatures in 2D are found from the intersection point of the straight line $\frac{2}{\pi}k_B T$ with the curve $\rho_s(T)$	59
4.14	Superfluid density vs. temperature (a) and magnetic field (b) for the simple cubic lattice, $\mu \approx -2.4439$, $U = -4$	60
4.15	Temperature vs. magnetic field phase diagrams for $d = 2$, $U = -2$ and fixed chemical potential $\mu \approx -1.358$. (a) diagram with Hartree term, (b) without Hartree term (blue color). (c) phase diagrams for $d = 3$, $U = 4$, $\mu \approx -2.4439$	64
4.16	Temperature vs. magnetic field (a) and polarization (b) phase diagrams for square lattice, (c) T vs. P phase diagrams for simple cubic lattice; fixed $U = -2$ and $n = 0.75$	65
4.17	Temperature vs. magnetic field (a) and polarization (b) phase diagrams with Hartree term, for square lattice, fixed $U = -1$ and $n = 0.75$	66
4.18	Dependence of Δ_η on the magnetic field (a) and temperature (b), $W/t = -2$, $U = 0$, for a fixed $\mu = -1.25$. (c) The grand canonical potential (Ω) vs. h at $T = 0$ (first order phase transition); (d) Ω vs. T at $h = 0.2$	68
4.19	Density of states for $W = -2$, $U = 0$, $\mu = -1.25$, (a) $h = 0$ and (b) $h = 0.19$ at $T = 0$	70
4.20	Plots of momentum occupation numbers $n_{\vec{k}\uparrow}$ (red points), $n_{\vec{k}\downarrow}$ (black points) vs. $k \equiv k_x = k_y $ and the corresponding quasiparticle spectra $E_{\vec{k}\uparrow}$, $E_{\vec{k}\downarrow}$ (inset) for $W = -2$, $\mu = -1.25$, $h = 0$ (a) and $h = 0.18$ (b).	71
4.21	Critical magnetic field vs. chemical potential (a) and electron concentration (b) for the first order SC($P \neq 0$)-NO transition, at $T = 0$; three different values of the attractive interaction.	73
4.22	Superfluid density vs. temperature (a) and magnetic field (b) for 2D d-wave pairing symmetry, $\mu = -1.25$, $W = -2$, $U = 0$	74
4.23	Temperature vs. magnetic field (a) and polarization (b) phase diagrams for $W = -2$, $U = 0$, three values of μ	76
4.24	Temperature vs. magnetic field (a) and polarization (b) phase diagrams for $W = -2$, $U = 0$, $n = 0.75$	77
5.1	Magnetic field vs. on-site attraction (a) and polarization (b) phase diagrams, at $T = 0$ and fixed $n = 0.2$, for the square lattice.	80

5.2	Magnetic field vs. binding energy (a) and polarization (b) phase diagrams both with and without the Hartree term (inset), in units of the lattice Fermi energy, at $T = 0$ and fixed $n = 0.01$ for $d = 2$	81
5.3	Magnetic field vs. on-site attraction (a) and polarization (b) phase diagrams, at $T = 0$ and fixed $n = 0.2$, for the simple cubic lattice.	83
5.4	Critical magnetic field vs. chemical potential for $d = 3$, $U = -12$ on LP side.	84
5.5	Dependence of the order parameter (a), chemical potential (inset) and the polarization (b) on the magnetic field for $d = 3$, at $T = 0$, fixed $n = 0.01$ and three values of the attraction.	85
5.6	Critical magnetic field vs. $ U $ for fixed $n = 0.01$ (a) and electron concentration for fixed $U = -12$ (b) phase diagrams, $T = 0$, $d = 3$	85
5.7	h/E_F (a) and polarization (b) vs. $1/k_F a_s = \left(\frac{1}{ U_c ^{d=3}} - \frac{1}{ U } \right) \frac{8\pi}{\sqrt{E_F}}$, where $ U_c ^{d=3}/12t = 0.659$, for the sc lattice.	86
5.8	Polarization vs. on-site attraction phase diagrams, at $T = 0$ and fixed $n = 0.001$ (a), $n = 0.03$ (b), $n = 0.05$ (c), $n = 0.1$ (d), for the simple cubic lattice.	87
5.9	Dependence of the coherence length ξ (in units of the lattice constant) on h (a) and $ U $ (b). ξ is computed for finite but small T ($T = 5 \times 10^{-3}$). Fraction of pairs in condensate n_0/n vs. h (inset (a)) and $ U $ (inset (b)); $d = 3$, $n = 0.01$	88
5.10	Density of states for $d = 3$, $n = 0.01$, $U = -12$, $h = 0$ and two different values of the magnetic field.	90
5.11	Polarization vs. $ U $ ground state phase diagrams for (a) sc lattice $n = 0.005$, (b) semicircular DOS $n = 0.005$, (c) semicircular DOS $n = 0.01$. Diagrams without the Hartree term.	91
5.12	Polarization vs. $ U $ ground state phase diagrams, at fixed $n = 0.1$, for (a) semicircular DOS, (b) BCC lattice, (c) FCC lattice. Diagrams without the Hartree term.	92
5.13	Polarization vs. $ U $ ground state phase diagrams, at fixed $n = 0.18$, for (a) BCC lattice (b) FCC lattice. Diagrams without the Hartree term.	93
5.14	Critical values of the attraction, for which the SC_M state arises stable and tricritical points at $T = 0$ vs. electron concentration.	93
6.1	Temperature vs. binding energy phase diagrams in units of the lattice Fermi energy at $h = 0$, (a) $n = 0.01$, (b) $n = 0.2$ and T vs. $ U $ phase diagram (inset of (b)).	98
6.2	Temperature vs. binding energy phase diagrams in units of the lattice Fermi energy at (a) $h/E_F = 0.35$ (inset – details of a region around TCP), (b) $h/E_F = 0.6$, (c) $h/E_F = 1$ (inset – diagram without the Hartree term) and (d) $h/E_F = 2$	99
6.3	Temperature vs. polarization at (a) $E_b/E_F = 0.131$ ($U = -2.8$), (b) $E_b/E_F = 0.235$ ($U = -3$), (c) $E_b/E_F = 0.766$ ($U = -3.5$) and (d) $E_b/E_F = 33.58$ ($U = -8$).	100

6.4	Temperature vs. binding energy phase diagrams in units of the lattice Fermi energy at (a) $P = 0.02$, (b) $P = 0.1$ (inset – diagram without the Hartree term).	102
6.5	(a) $k_B T/E_F$ (E_F – lattice Fermi energy) vs. $1/k_F a_s$ phase diagram of the AHM at fixed $n = 0.005$ for the sc lattice. (b) the analogous diagram for the 3D continuum model with contact attraction; $h = 0$.	112
6.6	h vs. $ U $ ground state phase diagram of spin polarized AHM (a) and critical magnetic field in units of the lattice Fermi energy E_F vs. $1/k_F a_s$ (b).	114
6.7	T vs. h and T vs. P phase diagrams in units of the lattice Fermi energy, at fixed $n = 0.005$ for the sc lattice.	115
6.8	T vs. h and T vs. P (insets) phase diagrams in units of the lattice Fermi energy, at fixed $n = 0.01$ (a) and $n = 0.2$ (b) for the sc lattice, $U = -12$.	116
6.9	T_c determined from the $(GG_0)G_0$ scheme vs. h for three values of n at $U = -12$ (a) and at fixed $n = 0.005$ for six values of $ U $ (b). Inset of (b) shows the behavior of Δ_{pg} vs. h for fixed $n = 0.005$ and $U = -11$.	118
7.1	The critical n (n_c) (within the mean field (MF) approximation) above which superconductivity can coexist with commensurate CO for different values of r . Inset – n_c vs. $z = \left \frac{r-1}{r+1} \right $ above which superconductivity can coexist with commensurate CO. The results from the Quantum Monte Carlo (QMC) method for the anisotropic Heisenberg model (Yunoki [176]) are also shown – for 2D and 3D.	126
7.2	Ground state phase diagrams for the $d = 2$ square lattice: mass imbalance vs. E_b/E_F (where E_F is the lattice Fermi energy of unpolarized, non-interacting fermions with hopping t) for $n = 0.01$, (a) $h = 0$ with and without Hartree term (inset), (b) $h/E_F = 16.1$ (inset – r vs. $ U $, $h = 1$).	127
7.3	Ground state phase diagrams r vs. $ U $ for $n = 0.1$, $h = 0$ (a) without the Hartree term, (b) with Hartree term.	128
7.4	Magnetic field vs. attractive interaction phase diagrams for three values of r : (a) $r = 5$, (b) $r = 7$, $r = 10$ and $n = 0.2$, without Hartree term.	129
7.5	Critical magnetic field vs. molecular chemical potential diagrams for $d = 2$ at fixed $U = -12$ (a) $r = 7$ ($r = 3$ – inset), (b) $r = 10$. (c), (d) h vs. n phase diagrams.	130
7.6	Polarization vs. on-site attraction ground state phase diagram at fixed $n = 0.1$ and $r = 7$, for the square lattice.	131
7.7	Temperature vs. $ U $ phase diagrams, at fixed $n = 0.1$, $h = 0$ for the square lattice. (a) $r = 1$, (b) $r = 2$, (c) $r = 4$ (inset – $h = 1$) (d) $r = 7$ (inset – $P(T_c^{KT})$ vs. $ U $).	132
7.8	Temperature vs. r phase diagrams, at fixed $n = 0.1$, $h = 0$ for the square lattice. (a) $U = -7$, (b) $U = -11$.	133
7.9	Temperature vs. magnetic field (a) and polarization (b)-(d) phase diagrams without the Hartree term, at fixed $n = 0.1$, $r = 7$, for the square lattice. (a)-(b) $U = -3$, (c) $U = -6.429$, (d) $U = -11.5$.	135

7.10	Critical magnetic field vs. chemical potential for $d = 3$, $U = -12$ on LP side, (a) $r = 2$ and (b) $r = 5$. Diagram without the Hartree term.	136
7.11	Dependence of the order parameter (a) and the grand canonical potential (b) on the magnetic field in the units of the binding energy E_b at $T = 0$, $d = 3$, $U = -12$, $r = 2$, for three values of $\mu_m = \mu - \epsilon_0 + \frac{1}{2}E_b$	137
7.12	Ground state phase diagrams of AHM r vs. $ U $ for $d = 3$, $n = 0.1$, (a) $h = 0$ (b) $h = 2$	138
7.13	Polarization vs. $ U $ ground state phase diagrams, at fixed $n = 0.1$, for (a) $r = 2$, (b), (c) $r = 5$, (d) $r = 10$	140
7.14	Plots of momentum occupation numbers $n_{\vec{k}\uparrow}$ (red points), $n_{\vec{k}\downarrow}$ (black points) vs. $k \equiv k_x = k_y = k_z$ and the corresponding quasiparticle spectra $E_{\vec{k}\uparrow}$, $E_{\vec{k}\downarrow}$ (inset) for $d = 3$, $n = 0.1$, $r = 5$ $U = -12$	141
7.15	Critical values of the attraction for which the SC_M state becomes stable at $T = 0$ vs. electron concentration. A comparison of two cases: $r = 1$ vs. $r = 2$ with and without the Hartree term.	142

List of publications

1. A. Kujawa, “The BCS-BEC Crossover and Superconductivity in a Lattice Fermion Model with Hard Core Repulsion,” *Acta Phys. Polon. A* **111** (2007) 745 [arXiv:0808.1374 [cond-mat.str-el]].
2. K. Cichy, J. Gonzalez Lopez, K. Jansen, A. Kujawa and A. Shindler, “Cutoff effects for Wilson twisted mass fermions at tree-level of perturbation theory,” *PoS LAT* **2007** (2007) 098 [arXiv:0710.2036 [hep-lat]].
3. A. Kujawa, R. Micnas, “On the Phase Diagram of the Spin-Polarized Attractive Hubbard Model: Weak Coupling Limit,” *Acta Phys. Polon. A* **114** (2008) 43 [arXiv:0808.1578 [cond-mat.str-el]].
4. K. Cichy, J. Gonzalez Lopez, K. Jansen, A. Kujawa and A. Shindler, “Twisted Mass, Overlap and Creutz Fermions: Cut-off Effects at Tree-level of Perturbation Theory,” *Nucl. Phys. B* **800** (2008) 94 [arXiv:0802.3637 [hep-lat]].
5. A. Kujawa, R. Micnas, “Some Properties of the Spin-Polarized Attractive Hubbard Model,” *Acta Phys. Polon. A* **115** (2009) 138 [arXiv:0809.1420 [cond-mat.str-el]].
6. K. Cichy, J. Gonzalez Lopez and A. Kujawa, “A Comparison of the cut-off effects for Twisted Mass, Overlap and Creutz fermions at tree-level of Perturbation Theory,” *Acta Phys. Polon. B* **39** (2008) 3463 [arXiv:0811.0572 [hep-lat]].
7. A. Kujawa-Cichy, “On the BCS-BEC Crossover in the Spin-Polarized Attractive Hubbard Model at $T = 0$,” *Acta Phys. Polon. A* **118** (2010) 423.
8. A. Kujawa, “Teoria superstrun jako zunifikowana teoria fizyki,” in: Antoni Szczuciński, Zdzisław Błaszczak (eds.), “Wokół ewolucjonizmu. Dylematy filozofów i fizyków,” Oficyna Wydawnicza Batik, Poznań 2010.
9. A. Kujawa-Cichy and R. Micnas, “Stability of superfluid phases in the 2D spin-polarized attractive Hubbard model,” *Europhys. Lett.* **95** (2011) 37003.
10. A. Kujawa-Cichy, “On the Imbalanced d-wave Superfluids within the Spin Polarized Extended Hubbard Model: Weak Coupling Limit,” *Acta Phys. Polon. A* **121** (2012) 824.
11. A. Kujawa-Cichy, “On the BCS-BEC crossover in the 2D Asymmetric Attractive Hubbard Model,” *Acta Phys. Polon. A* **121** (2012), 1066.

List of conferences and schools

1. Physics of Magnetism 2005, Poznań, Poland, June 2005, poster: “The quantum spin-1/2 Heisenberg antiferromagnet on a triangular lattice with some bonds removed in a translationally invariant manner - ground state and lowest excitations,” in collaboration with: K. Cichy, J. Richter and P. Tomczak.
2. XII National School on Superconductivity, Ustroń, Poland, September 2006, poster: “BCS-BEC crossover in a lattice fermion model. The 3D case with infinite on-site repulsion”.
3. Cosmological Dilemmas of Physics and Philosophy, Adam Mickiewicz University, Poznań, Poland, November 2006, presentation: “Superstring theory as a unified theory of physics”
4. XXV International Symposium on Lattice Field Theory LATTICE 2007, Regensburg, Germany, July 2007, poster: “Cutoff effects for Wilson twisted mass fermions at tree-level of perturbation theory,” in collaboration with: K. Cichy, J. Gonzalez Lopez, K. Jansen and A. Shindler.
5. Les Houches Predoctoral School in Statistical Physics, Les Houches, France, 26 August – 7 September 2007.
6. XIII National School on Superconductivity, Łądek Zdrój, Poland, November 2007, poster: “Phase Diagram of Spin-Polarized Attractive Hubbard Model.”
7. Physics Of Magnetism 2008, Poznań, Poland , June 2008, poster: “Superconducting Properties of the Spin-Polarized Attractive Hubbard Model,” in collaboration with: R. Micnas.
8. Physics Of Magnetism 2008, Poznań, Poland , June 2008, poster: “Quantum Monte Carlo study of the repulsive Hubbard model on a Sierpinski gasket”, in collaboration with: K. Cichy, P. Tomczak.
9. Lattice Practices 2008, Zeuthen, Germany, October 2008.
10. XIV National School on Superconductivity, Ostrów Wlkp., Poland, October 2009, poster and presentation: “On the BCS-BEC crossover in the Spin-Polarized Attractive Hubbard Model,” in collaboration with: R. Micnas.
11. Modern perspectives in lattice QCD: Quantum field theory and high performance computing, Les Houches Summer School, Les Houches, France, 3-28 August 2010.
12. XXXIV International Conference of Theoretical Physics “Correlations and coherence at different scales”, Ustroń, Poland, September 2010, poster: “BCS-BEC crossover in the Spin-Polarized Attractive Hubbard Model.”
13. Workshop on Frontiers in Ultracold Fermi Gases, Abdus Salam International Centre for Theoretical Physics, Trieste, Italy, June 2011, poster: “Superfluid phases in the 2D Spin-Polarized Attractive Hubbard Model.”
14. Physics Of Magnetism 2011, Poznań, Poland, June 2011, poster: “Superfluid phases in the 2D Spin-Polarized Attractive Hubbard Model.”

15. XIV National School on Superconductivity, Kazimierz Dolny, Poland, October 2011, poster: “On the Imbalanced d-wave Superfluids within the Spin-Polarized Extended Hubbard Model: Weak Coupling Limit.”